Spectroscopic infrared ellipsometry on functional polymer films

Spektroskopische Infrarotellipsometrie an funktionalen Polymerfilmen

Promotionsschrift
zur Erlangung des akademischen Grades
Doctor rerum naturalium
(Dr. rer. nat.)

eingereicht an der
Fakultät II – Mathematik und Naturwissenschaften
der Technischen Universität Berlin

vorgelegt von
Diplom-Physiker
Andreas Furchner

Genehmigte Dissertation

Promotionsausschuss:
- Vorsitzender: Prof. Dr. Heinz-Wilhelm Hübers, TU Berlin
- 1. Gutachter: Prof. Dr. Norbert Esser, TU Berlin
- 2. Gutachter: Prof. Dr. Svetlana Santer, Universität Potsdam
- 3. Gutachter: PD Dr. Karsten Hinrichs, TU Dresden

Eingereicht am: 20. Dezember 2013
Tag der wissenschaftlichen Aussprache: 7. April 2014

Berlin 2014

D 83

List of publications and book contributions:

1. Furchner, A.; Bittrich, E.; Rauch, S.; Uhlmann, P.; Hinrichs, K., "Temperature-Sensitive Swelling Behavior of Thin Poly(*N*-isopropylacrylamide) Brushes Studied by In-situ Infrared Spectroscopic Ellipsometry," *Polymeric Materials: Science & Engineering* **2012**, 107, 372–373, ISBN: 978-0-8412-2777-4.
2. Hinrichs, K.; Bittrich, E.; Aulich, D.; Furchner, A.; Minko, S.; Luzinov, I.; Stamm, M.; Uhlmann, P.; Eichhorn, K.-J., "Ellipsometry for Study of Smart Polymer Brushes," *Polymeric Materials: Science & Engineering* **2012**, 107, 655–656, ISBN: 978-0-8412-2777-4.
3. Hinrichs, K.; Furchner, A.; Rappich, J.; Oates, T. W. H., "Polarization-dependent and ellipsometric infrared microscopy for analysis of anisotropic thin films," *The Journal of Physical Chemistry C* **2013**, 117 (26), 13557–13563, DOI: 10.1021/jp401576r.
4. Furchner, A.; Bittrich, E.; Uhlmann, P.; Eichhorn, K.-J.; Hinrichs, K., "In-situ characterization of the temperature-sensitive swelling behavior of poly(*N*-isopropylacrylamide) brushes by infrared and visible ellipsometry," *Thin Solid Films* **2013**, 541, 41–45, DOI: 10.1016/j.tsf.2012.10.135.
5. Bittrich, E.; Uhlmann, P.; Eichhorn, K.-J.; Hinrichs, K.; Aulich, D.; Furchner, A., "Smart polymer surfaces and films" in *Ellipsometry of Functional Organic Surfaces and Films*, Eichhorn, K.-J.; Hinrichs, K. (Editors), Springer Berlin 2014, ISBN: 978-3-642-40127-5, DOI: 10.1007/978-3-642-40128-2_5.
6. Furchner, A.; Aulich, D., "Common Polymers and Proteins" in *Ellipsometry of Functional Organic Surfaces and Films*, Eichhorn, K.-J.; Hinrichs, K. (Editors), Springer Berlin 2014, ISBN: 978-3-642-40127-5, DOI: 10.1007/978-3-642-40128-2_17.
7. Furchner, A.; Aulich, D., "Organic Materials for Optoelectronic Applications" in *Ellipsometry of Functional Organic Surfaces and Films*, Eichhorn, K.-J.; Hinrichs, K. (Editors), Springer Berlin 2014, ISBN: 978-3-642-40127-5, DOI: 10.1007/978-3-642-40128-2_18.
8. Hinrichs, K.; Furchner, A.; Sun, G.; Gensch, M; Rappich, J.; Oates, T. W. H., "Infrared ellipsometry for improved laterally resolved analysis of thin films," *Thin Solid Films*, in press 2014, DOI: 10.1016/j.tsf.2014.02.006.

Selected contributions at academic conferences and meetings:

1. A. Furchner, D. Aulich, E. Bittrich, S. Rauch, K. Hinrichs, "Characterization of optical properties of PNIPAAm brushes via ex-situ infrared spectroscopic ellipsometry," Poster presentation at the **6th Workshop Ellipsometry**, February 21–24, 2011, Berlin, Germany.
2. A. Furchner, D. Aulich, E. Bittrich, K. Hinrichs, "Characterization of temperature-sensitive swelling behavior of PNIPAAm brushes via in-situ infrared ellipsometry," Poster presentation at the **DPG spring meeting**, March 13–18, 2011, Dresden, Germany.

3. A. Furchner, D. Aulich, S. Pop, G. Sun, N. Esser, K. Hinrichs, "Analysis of thin organic films by infrared ellipsometry (IRSE)," Oral presentation and poster presentation at the **26. Tag der Chemie**, August 13, 2011, Berlin, Germany.
4. A. Furchner, D. Aulich, E. Bittrich, S. Rauch, P. Uhlmann, K. Hinrichs, "Temperature-sensitive swelling behavior of poly(N-isopropylacrylamide) brushes characterized by in-situ infrared spectroscopic ellipsometry," Poster presentation at the **7th Workshop Ellipsometry**, March 5–7, 2012, Leipzig, Germany.
5. A. Furchner, D. Aulich, E. Bittrich, S. Rauch, P. Uhlmann, K. Hinrichs, "In-situ characterization of temperature-sensitive poly(N-isopropylacrylamide) brushes by in-situ infrared spectroscopic ellipsometry," Oral presentation at the **E-MRS spring meeting**, Symposium W (Current Trends in Optical and X-Ray Metrology of Advanced Materials for Nanoscale Devices III), May 13–18, 2012, Strasbourg, France.
6. A. Furchner, D. Aulich, E. Bittrich, S. Rauch, P. Uhlmann, K. Hinrichs, "Temperature-sensitive poly(N-isopropylacrylamide) brushes investigated by in-situ infrared spectroscopic ellipsometry," Oral presentation at the **E-MRS spring meeting**, Symposium G (Functional Biomaterials), May 13–18, 2012, Strasbourg, France.
7. A. Furchner, E. Bittrich, P. Uhlmann, K.-J. Eichhorn, K. Hinrichs, "Combined studies of in-situ infrared and VIS ellipsometry on temperature-sensitive poly(N-isopropylacrylamide) brushes," Poster presentation at the **Leibniz-Doktoranden-Forum der Sektion D**, June 7, 2012, Berlin, Germany.
8. A. Furchner, D. Aulich, S. Pop, G. Sun, N. Esser, K. Hinrichs, "Organic-thin-film analysis by infrared ellipsometry (IRSE)," Poster presentation at the **27. Tag der Chemie**, June 28, 2012, Berlin, Germany.
9. A. Furchner, E. Bittrich, S. Rauch, P. Uhlmann, K. Hinrichs, "Temperature-Sensitive Swelling Behavior of Thin Poly(N-isopropylacrylamide) Brushes Studied by In-situ Infrared Spectroscopic Ellipsometry," Poster presentation at the **244th Annual ACS Meeting**, PMSE (Polymeric Matrials: Science and Engineering), August 19–23, 2012, Philadelphia, USA.
10. A. Furchner, A. Kroning, E. Bittrich, S. Rauch, M. König, P. Uhlmann, K.-J. Eichhorn, K. Hinrichs, "Studies on the Swelling Behavior of Thin Polymer Brush Films with In situ Infrared Spectroscopic Ellipsometry," Poster presentation at the **245th Annual ACS Meeting**, PMSE (Polymeric Matrials: Science and Engineering), April 7–11, 2013, New Orleans, USA.
11. K. Hinrichs, A. Furchner, J. Rappich, T. W. H. Oates, "Towards ellipsometric infrared microscopy of new materials," Poster presentation at the **6th International Conference on Spectroscopic Ellipsometry** (ICSE-VI), May 26–31, 2013, Kyoto, Japan.
12. A. Furchner, D. Aulich, E. Bittrich, S. Rauch, P. Uhlmann, K.-J. Eichhorn, K. Hinrichs, "Towards controlled protein adsorption on smart polymer surfaces," Oral presentation at the **6th International Conference on Spectroscopic Ellipsometry** (ICSE-VI), May 26–31, 2013, Kyoto, Japan.

Dem inneren Schweinehund . . .

Contents

„Das Rauschen im Walde und kleine Wubbel im Signal.“

1. Introduction

1.1. Motivation

Spectroscopic infrared ellipsometry [1–4] is a powerful optical technique that combines the many advantages of ellipsometry with those of infrared spectroscopy. Ellipsometry [5–10] measures the change of polarization state upon reflection or transmission of light at a sample. It is a non-destructive method that allows one to determine absolute sample properties without the need for a reference standard. Probing the infrared range with ellipsometry gives quantitative access to the molecular vibrations of organic material systems, which in turn contain valuable information about, for instance, chemical composition, structural properties, and interactions [11–15]. Infrared ellipsometry shows its high potential for in-situ investigations of film properties at the solid–liquid interface in aqueous environments. Among others, applications range from biosensing [16], the monitoring of growth or etching processes [17–19], to the study of functional polymer films or brushes [20–25], the latter of which is the main interest of this thesis.

Functional polymer films—and stimuli-responsive polymer brushes in particular—are of high technological interest. External stimuli like temperature [26], pH [27], salinity [28], or electric fields [29] can induce changes in structure and chemistry of these films, which often results in switching between states of distinctly different surface characteristics. By adjusting the sample parameters of film or brush, such as composition, grafting density, end-functionalization, or molecular weight, the switching behavior can be tuned towards the needs of the desired application. Polymer brushes are either prepared as mono brushes made from a single polymer species, or as mixed brushes made from two or more polymer species with different properties and switching behaviors upon external stimuli. Both types of brushes can lead to attractive surface functionalizations and promising applications like miniaturized sensors [30–32], tunable surface wetting [29, 33], controlled cell adhesion [34–37] and adsorption of biomolecules [24, 38–40], as well as drug delivery systems [41, 42].

One of the most extensively studied and important representatives for temperature-sensitive polymers is poly(*N*-isopropylacrylamide) [PNIPAAm]. In aqueous environment, it undergoes a coil-to-globule phase transition around its lower critical solution temperature (LCST) at about 32 °C [43–45]. For polymer brushes made of end-grafted PNIPAAm chains, the transition temperature can be shifted, for instance, by changes in grafting density [26], rendering these brushes especially useful for bioapplications like controlled protein adsorption or cell growth [46–49]. Swelling behavior and hydration states of PNIPAAm in solution [45, 50–54] as well as of PNIPAAm hydrogels [55–60] and microgels [61–63] are very well investigated. Few studies, however, exist on the LCST behavior of PNIPAAm mono brushes [26, 47, 64] and

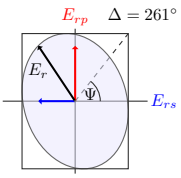

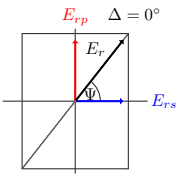

possible conformational changes [26, 47, 65] during the phase transition. A deep knowledge of both is necessary, though, in order to successfully tune more complex mixed-brush systems that are based on PNIPAAm as the temperature-sensitive component. Such mixed PNIPAAm brushes that contain, for example, poly(2-vinylpyridine) [P2VP] [46, 66] or poly(acrylic acid) [PAA] [67] are particularly promising candidates for controlling protein adsorption and cell adhesion. The same is true for mixed P2VP/PAA brushes [20, 21, 27, 38].

In this work, in-situ infrared ellipsometry is used as an appropriate tool for studying swelling and deswelling effects of PNIPAAm brushes as well as changing interactions at the solid–liquid interface. A custom-made in-situ flow cell [20], together with the convenient geometry of the set-up, enables the quantitative evaluation of measured spectra on the basis of physical models according to the sample properties. This yields valuable information about temperature-dependent polymer–water and polymer–polymer interactions within the brushes. To achieve this aim and to obtain physically meaningful results from the modeling process, systematic investigations of PNIPAAm films and brushes in dry, humid, and wet state are needed. The results of these quantitative studies are the foundation for interpreting in-situ spectra of protein-adsorption on polymer brushes. With regard to protein adsorption on mixed PNIPAAm/PAA brushes, the long-term goal is to better understand brush–protein interactions, changes in brushes structure and chemistry upon protein adsorption and desorption, as well as conformational changes of the protein.

The outline of this thesis is as follows: After an introduction to polymer brushes in Section 1.2., the experimental methods used in this work are described in Sections 2.1. and 2.2. These methods are infrared and visible ellipsometry, infrared microscopy and transmission spectroscopy, as well as atomic force microscopy. Extended correction formulae are derived that allow for accurate ellipsometric measurements needed for quantitative spectra evaluation. General aspects of data analysis, optical layer models, and the fitting procedure are discussed in Section 2.3. In Section 2.4., an overview is given on the material systems of interest as well as on sample preparation and pre-characterization.

Results are discussed in six parts. In the first part, Section 3.1., spin-coated PNIPAAm films are thoroughly investigated for their optical properties. After pre-characterization and several homogeneity tests, the optical constants of these films are determined in dry state with infrared ellipsometry. In a subsequent systematic study, humidity effects on PNIPAAm films are analyzed qualitatively as well as quantitatively. Lastly, temperature effects in dry state are studied. In the second part, Section 3.2., similar investigations are performed on various PNIPAAm brushes. Furthermore, polymer–polymer interactions in dry state are studied with time-dependent deuteration experiments. Qualitative and semi-quantitative studies on the temperature-dependent swelling behavior of PNIPAAm brushes in aqueous solutions are presented in Section 3.3. The influence of changing interactions around the LCST is discussed, and hysteresis effects are addressed.

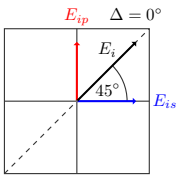

The next two parts aim at the quantitative modeling of in-situ PNIPAAm-brush spectra below and above the LCST. In the first step, Section 3.4., the optical constants of water and heavy water are determined in dependence of temperature using special transmission cells with micrometer-short path lengths. In the second step, Section 3.5., swelling and water content of PNIPAAm brushes are modeled. Most importantly, different interactions at the brush–water interface are identified and quantified. In the last part, Section 3.6., the model protein *human serum albumin* (HSA) is analyzed pH-dependently in solution and in adsorbed state on several substrates. PNIPAAm mono brushes are studied for their HSA-repelling properties. Lastly, controlled pH-dependent HSA adsorption and desorption at PAA mono brushes are investigated in a time-resolved way with in-situ infrared ellipsometry. Complementary measurements with visible ellipsometry allow the determination of buffer content and amount of adsorbed protein within the swollen brush. In a semi-quantitative analysis, the switching behavior of a pure PAA brush [23] is compared to the switching behavior in the presence of bound protein. The findings of this thesis are summarized in Section 4.

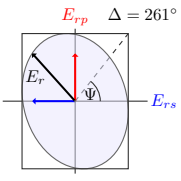

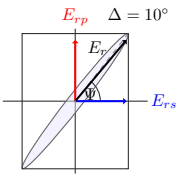

1.2. Polymer brushes

This section gives a brief overview on the terminology of polymer brushes as well as important brush parameters used for pre-characterization. Various structural definitions of polymer brushes exist in the literature [68–71]. In this thesis, the term *polymer brush* describes layers of densely grafted polymer chains, the behavior of which is dominated by strong interactions between the chains [68]. In aqueous environment, these interactions can cause swelling effects, as illustrated in Fig. 1.1, which often occur in dependence on external stimuli like temperature or pH. Examples of swellable brushes are PNIPAAm and PAA brushes, which respectively react upon changes in temperature and pH.

PNIPAAm brushes are neutral water-soluble brushes [69] that undergo a phase transition between a swollen and a collapsed state around their lower critical solution temperature of about 32 °C [43–45, 69, 72]. Swelling behavior and transition temperature are depending on grafting density and molecular weight, but are also strongly influenced by the solvent quality [26, 68–70]. Polymer–polymer and polymer–water interactions seem to play an important role during the phase transition [26, 50, 60, 65]. Figure 1.2 shows how interactions between PNIPAAm's amide groups and surrounding water molecules are expected to change towards intra- and interchain amide–amide interactions above the LCST.

PAA brushes, on the other hand, are weak polyelectrolyte brushes [69, 73] with ionizable carboxylic groups at each monomer unit. The swelling of PAA brushes strongly depends on the salt concentration. In this respect, the terms *osmotic-brush regime* and *salted-brush regime* are often used in order to distinguish whether the swelling behavior is dominated by osmotic pressure or excluded-volume interactions [69, 70, 73], respectively.

Polymer brushes investigated in this thesis were exclusively prepared with the *grafting-to* method [74] in a two-step process shown in Fig. 1.3. In the first step, the *linker polymer* poly(glycidylmethacrylate) [PGMA], which is equipped with epoxy groups, is attached to a

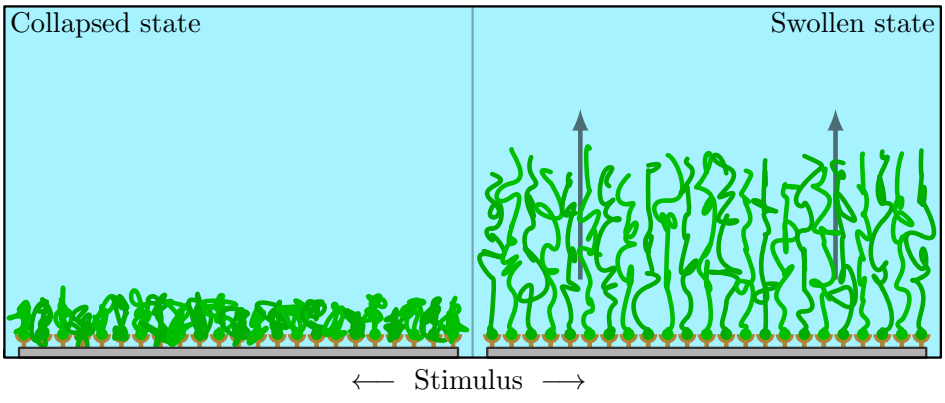

Figure 1.1: Swelling and collapsing of a stimuli-responsive polymer brush upon external stimuli.

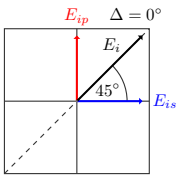

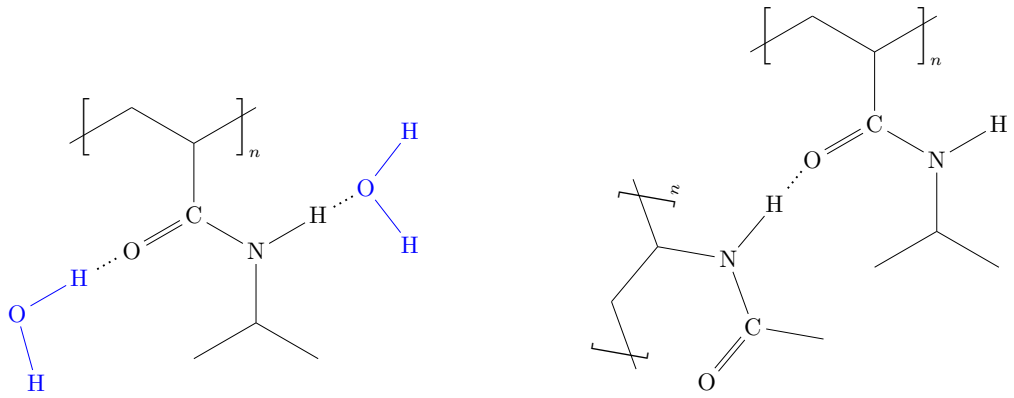

Figure 1.2: Changing interactions of temperature-responsive (grafted) PNIPAAm chains in aqueous environment. The swelling behavior depicted in Fig. 1.1 is related to polymer–water interactions, which dominate below the LCST. Above the LCST, polymer–polymer interactions become relevant. The brush is getting more hydrophobic and deswells.

silicon substrate via epoxy-ring-opening reactions that results in ether bonds between PGMA and substrate. PGMA serves as an anchoring layer for the subsequently grafted brush layer. In the second step, PAA or COOH-functionalized PNIPAAm is reacted with the linker layer via ester-bond formation between PGMA's epoxy groups and the carboxylic groups of the polymer. The actual grafting process takes place in a vacuum oven, which allows one to adjust the grafting density of the polymer-brush top-layer by choosing appropriate values for annealing time and temperature [75].

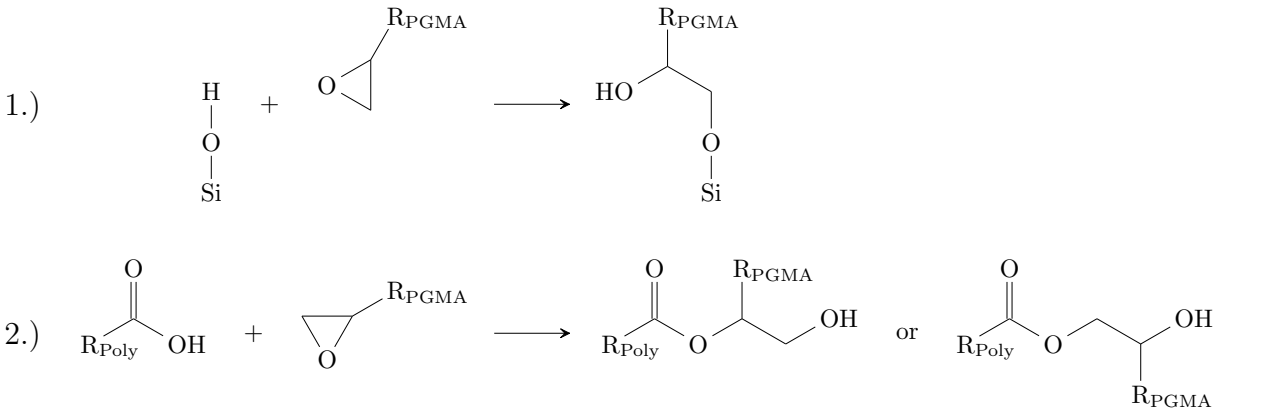

Figure 1.3: Two-step grafting process. 1.) Attachment of the PGMA anchoring layer to the silicon substrate via epoxy-ring-opening reactions, resulting in ether bonds. 2.) Grafting of the polymer-brush top-layer via reactions between the carboxylic groups of the COOH-functionalized polymer and PGMA's epoxy groups, resulting in ester bonds [76].

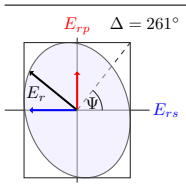

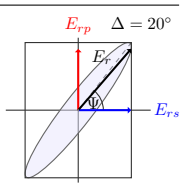

Characteristic parameters of polymer brushes are [26, 68, 70] the surface concentration

$$\Gamma = \varrho \cdot d\,, \tag{1.1}$$

the distance d_g between grafting sites,

$$d_g = \sqrt{\frac{\overline{M}_n}{\Gamma \cdot N_A}}\,, \tag{1.2}$$

and the grafting density

$$\sigma = \frac{\Gamma \cdot N_A}{\overline{M}_n} = d_g^{-2}\,, \tag{1.3}$$

where ϱ is the density of the grafted polymer, d denotes the thickness of the brush layer in dry state, N_A is the Avogadro constant, and $\overline{M}_n$ is the number-average molecular weight of the polymer. These parameters are very useful in order to determine the conformational state of the prepared polymer systems. At low grafting densities, the polymer chains usually exist in the so-called mushroom regime and behave more or less like individual chains. If the distance between grafting sites, however, approaches the size of the grafted polymer chains, then interactions between different chains become relevant, and the polymer system undergoes a transition towards the brush regime with stretched chains [68]. A more detailed discussion on brush preparation, pre-characterization, and brush conformation is presented in Sections 2.4. and 3.2.1.a).

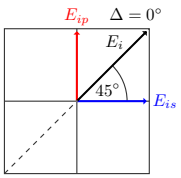

2. Experimental section

2.1. Ellipsometry

Ellipsometry [5–10] is a non-invasive optical measurement technique. It is known for its ability to determine thicknesses and dielectric functions of thin layers with very high accuracy, thereby providing access to fundamental physical parameters of the sample. Ellipsometry offers many insights, ranging from characterization of substrate properties, surface roughness, and multi-layer systems to detailed analysis of structural properties, such as anisotropy, molecular orientation, chemical composition, and interactions.

An advancing field of ellipsometry is in-situ infrared [19–25, 77] and visible ellipsometry [24–26, 46, 67, 77–82] on organic samples in contact with aqueous solutions. While changing the environmental conditions like temperature, pH, or solvent, in-situ ellipsometry allows one to monitor and quantify, for example, conformational changes, water content, degree of swelling, interactions at the solid–liquid interface, as well as adsorption processes of biomolecules, such as cells or proteins. In the last years—besides its traditional applications in silicon technology and optoelectronics—ellipsometry has thereby gained more and more importance in biochemistry and biomedicine [12, 16, 83–89].

Spectroscopic ellipsometry is widely used in the infrared, the visible, and the ultraviolet spectral range, but also for vibrational spectroscopy in the Terahertz and microwave regions. Visible ellipsometry has its strength, among others, in using high-intensity light sources that allow for very short measurement times in the range of minutes or even seconds. On the other hand, it is very sensitive to smallest changes in refractive indices and layer thicknesses, including, for instance, changes in water content of solid–liquid interfaces [26]. This sensitivity is imperative for studying potential bioapplications like the controlled adsorption and desorption of proteins on organic surfaces [66, 82].

Owing to its high spectral contrast, infrared-spectroscopic ellipsometry (IR-SE) is particularly suited for studying organic material systems, such as polymer brushes [20, 21, 23, 25] and protein adsorption thereon [90]. This is because the infrared spectral range reveals the vibrational bands associated with the chemical structure of the various organic components under investigation. IR-SE is highly sensitive to structural and chemical changes of the sample [21, 23]. It is therefore the primary experimental method used in this work to investigate polymer-film and polymer-brush systems, stimuli-induced changes, protein adsorption processes, as well as interactions between organic constituents and solvent.

In the following, a brief introduction to the principle of ellipsometry is given. Afterwards, visible ellipsometry and the in-situ set-up at the IPF Dresden are presented. The main focus, though, lies on infrared ellipsometry. Details on the various in-situ set-ups as well as

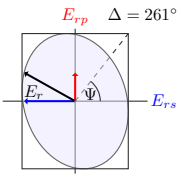

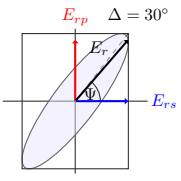

the measuring principle are shown. Imperfect optical components are discussed, and correction formulae for the measured ellipsometric parameters are derived. Lastly, methods of data analysis are outlined with details on optical modeling, the fitting procedure, and error estimation.

2.1.1. Fundamentals

Ellipsometry [5, 6, 8, 91, 92] measures how light changes its state of polarization when it is reflected off or transmitted through a sample. The name *ellipsometry* is derived from the fact that the final state is usually elliptical polarization [93]. Figure 2.1 depicts the basic set-up of an ellipsometer in reflection mode. It consists of a light source that emits radiation over a certain desired spectral range, two (linear) polarizers called *polarizer* and *analyzer* that are respectively placed before and after the sample, an optional phase-shifting compensator, as well as a photo-sensitive detector. The sample is irradiated under a (variable) incidence angle φ_0, while the detector is positioned at the appropriate reflection or transmission angle according to the sample geometry.

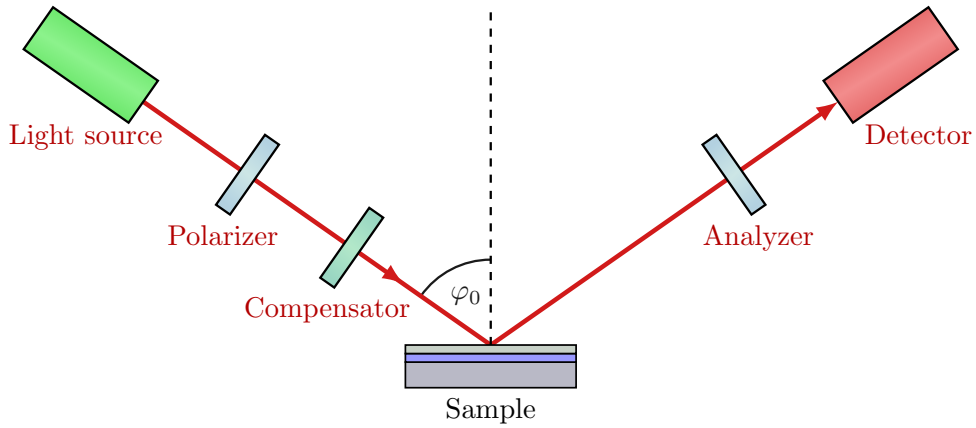

Figure 2.1: Schematic set-up of a variable-angle ellipsometer with two polarizers and an optional phase-shifting compensator. The compensator can also be placed behind the sample, or two compensators may be used to measure the whole Müller matrix of the sample [94].

Figure 2.2 illustrates the measuring principle of ellipsometry. The azimuth angle of the first polarizer defines the incoming state of polarization with respect to the plane of incidence, which is the plane spanned by the propagation direction of the light and the surface normal. Depending on the polarizer azimuth, the light exhibits a component E_{ip} parallel and a component E_{is} perpendicular to the plane of incidence. Sample properties like thickness and dielectric function cause the light to be reflected in a defined elliptically polarized state with components E_{rp} and E_{rs} that usually differ in amplitude and show phase shifts δ_p and δ_s, respectively. Ratios of intensities measured at various analyzer positions allow

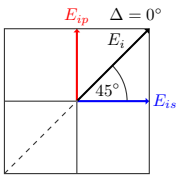

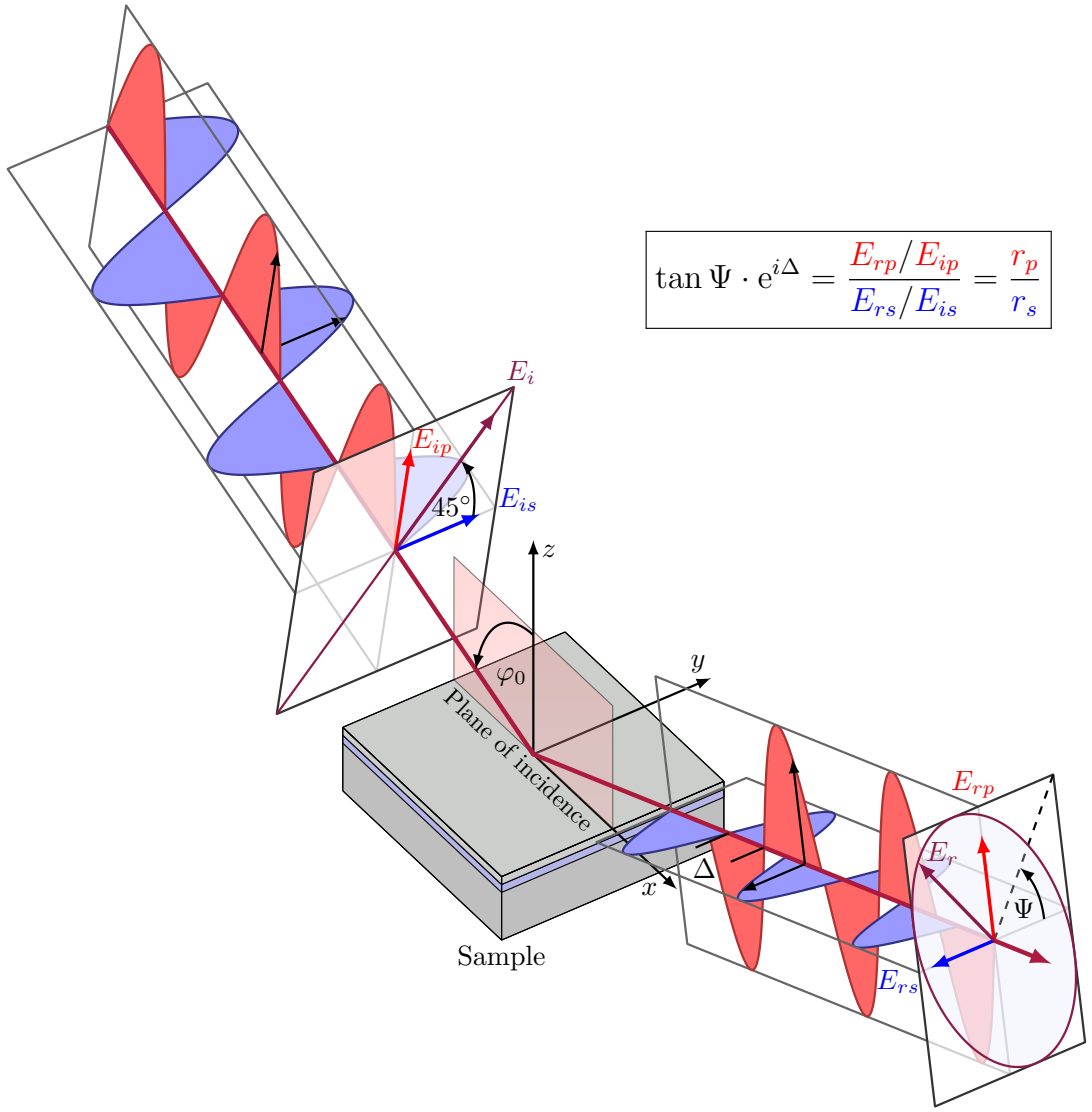

Figure 2.2: Visualization of the characteristic changes in the polarization state of light upon reflection off the sample. The changes from linear polarization with electric-field strengths E_{ip} and E_{is} to elliptical polarization with E_{rp} and E_{rs} are captured by the amplitude ratio $\tan\Psi$ and the phase difference Δ between parallel and perpendicular component with respect to the plane of incidence.

one to characterize the ellipse, that is, to determine the changes in amplitude ($\tan\Psi$) and phase difference (Δ) between parallel and perpendicular component. This is expressed in the fundamental equation

$$\rho = \tan\Psi \cdot e^{i\Delta} = \frac{E_{rp}/E_{ip}}{E_{rs}/E_{is}} = \frac{r_p}{r_s} \tag{2.1}$$

with

$$\tan\Psi = \frac{|r_p|}{|r_s|} \qquad \text{and} \qquad \Delta = \delta_p - \delta_s\,. \tag{2.2}$$

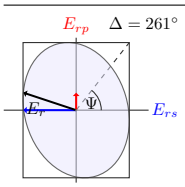

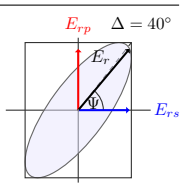

Here, r_p and r_s are the p- and s-polarized complex reflection coefficients. Although the absolute phases δ_p and δ_s are not accessible in a standard ellipsometry set-up, their difference Δ can be obtained from the complex ellipsometric ratio ρ. If $|\cos\Delta| \approx 1$ or if Δ must be determined unambiguously between $0° \leq \Delta < 360°$, then a compensator (retarder) is required that causes an additional phase shift between p and s component. The compensator can be placed either before or after the sample, depending on the experimental situation, as will be discussed later.

The above equations are sufficient to describe the samples investigated in this thesis, which are all isotropic. In principle, generalized ellipsometry [8, 95] allows one to measure anisotropic samples. Müller-matrix ellipsometry [94, 96] is usually applied for depolarizing and/or optically active samples. Equation (2.1) already hints at the many advantages of ellipsometry [97] compared to other techniques like standard reflection intensity measurements. Ellipsometry directly accesses at least two independent sample-specific parameters per wavelength. In this respect, it is an absolute technique, because no reference sample is needed. Since ellipsometers used in this work measure intensity ratios, the results are also less prone to changes in atmospheric conditions. This is especially useful in the infrared where absorption due to water vapor poses an intrinsic measurement problem [4, 20]. Via appropriate optical modeling [5, 6, 8], presented in Section 2.3., ellipsometry is capable of determining the real as well as the imaginary part of the sample's dielectric function.

2.1.2. (In-situ) VIS ellipsometry

Sample pre-characterization after preparation was performed with an SE 402 visible ellipsometer (Sentech Instruments GmbH, Berlin, Germany) and a Woollam alpha-SE (J. A. Woollam Co., Inc., Lincoln NE, USA) by Eva Bittrich [75] and Sebastian Rauch [98] at the IPF Dresden. The final pre-characterization was done at ISAS Berlin using a Sentech SE 801, a rotating-analyzer ellipsometer that measures Ψ and Δ according to Fig. 2.1 in the spectral range between 240–930 nm. Additionally, a Sentech SE 850 ellipsometer was used for thickness-homogeneity maps of polymer samples. This ellipsometer is equipped with microfocus apertures that allow measuring spots of $250 \times 250\ \mu m^2$.

In-situ measurements were performed by Eva Bittrich at the IPF Dresden. The experimental set-up is shown in Fig. 2.3. An M-2000 diode-array rotating-compensator ellipsometer (J. A. Woollam Co., Inc., Lincoln NE, USA) is combined with a custom-made in-situ cell [26, 99] (IPF Dresden) that resolves a spectral range of 371–800 nm. The polymer-brush sample, usually prepared on a polished single-crystal silicon wafer of {100} orientation, is attached inside a batch cuvette (TSL Spectrosil, Hellma, Müllheim, Germany) that is mounted on a heating plate for temperature-dependent measurements. The cuvette is irradiated normal to its sides with an incidence angle of 68°. The large angle makes for a very high phase

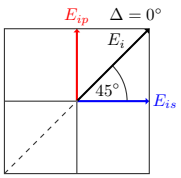

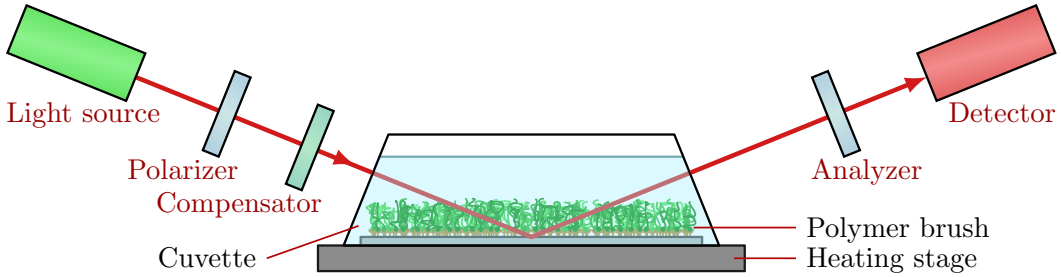

Figure 2.3: Schematic of the heatable in-situ cuvette used for temperature-dependent VIS-ellipsometric measurements at the IPF Dresden.

sensitivity and consequently a high thickness sensitivity [26]. This enables in-situ VIS ellipsometry to quantify, for instance, the pH- or temperature-dependent swelling degree of such brush systems in short measurement times and with very high precision [26, 67].

2.1.3. FT-IR ellipsometry

a) The Fourier-transform spectrometer

Ellipsometry in the infrared is strongly limited by the low intensity of available light sources. To overcome this problem, the ellipsometer is coupled to a Fourier-transform spectrometer [1, 2], as shown in Fig. 2.5. Basically, the spectrometer is a Michelson interferometer [100] consisting of a globar as radiation source, a beamsplitter, as well as a movable and a stationary mirror. Depending on the displacement z of the movable mirror, the recombined light beam at the exit of the spectrometer exhibits wavelength-dependent constructive or destructive interference, which results in an intensity interferogram $\mathcal{I}(z)$ measured at the detector. The corresponding intensity spectrum $\mathcal{I}(\tilde{\nu})$ in energy space, then, is given by the Fourier transform of $\mathcal{I}(z)$, displayed schematically in Fig. 2.4. This already indicates one of many advantages of utilizing a Fourier-transform spectrometer, for example, the high throughput and an increased signal-to-noise ratio due to the absence of dispersive optical elements. Details on Fourier-transform spectrometers and spectra acquisition are given in Appendix A.

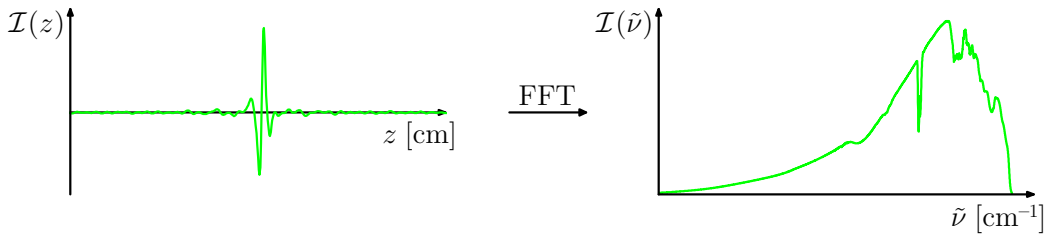

Figure 2.4: Interferogram and corresponding single-channel intensity spectrum in energy space after apodization (see Appendix A.) and Fast-Fourier transform (FFT) [101].

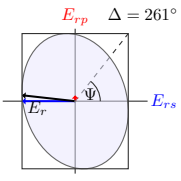

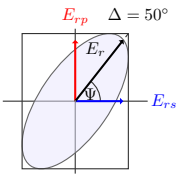

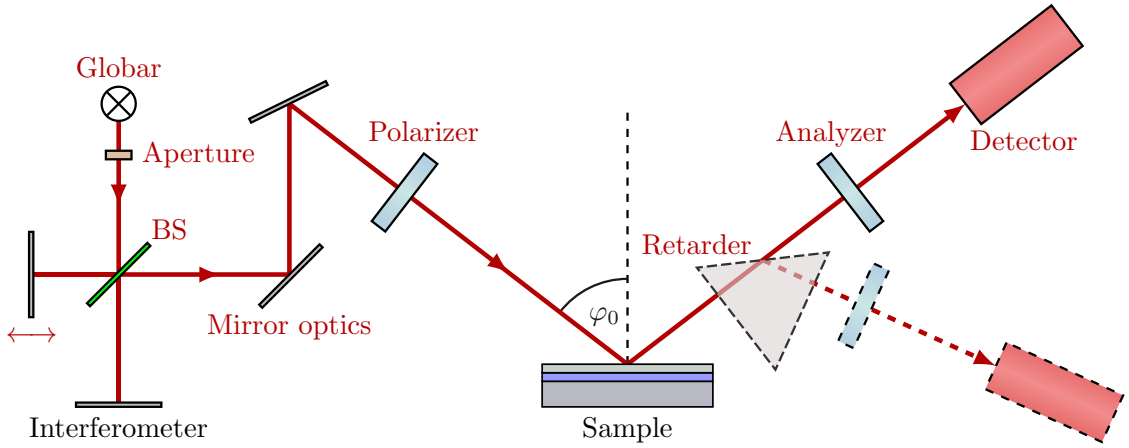

Figure 2.5: Schematic set-up of a Fourier-transform infrared ellipsometer. The interferometer on the left comprises a globar as the lightsoure, an adjustable Jacquinot aperture, a beamsplitter (BS), and a movable as well as a stationary mirror. A mirror optics couples the light to the ellipsometer on the right. An optional retarder prism can be inserted into the optical train for sensitive phase measurements.

b) The infrared ellipsometer

An infrared ellipsometer that is coupled to a Fourier-transform spectrometer (see Fig. 2.5) is usually set up like a standard ellipsometer, with the main difference being the materials used for the compensator. There exist various kinds of infrared compensators or *retarders* in the literature [1, 15, 102, 103]. In the present work, total-reflection retarder prisms cut from KBr or KRS-5 crystals are used, because they are easily calibrated, as will be shown in Section 2.1.4., and they exhibit an almost constant retardation over the extended mid-infrared spectral range of 7000–400 cm^{-1} [1, 3]. For accurate phase measurements of the sample, the retarder is inserted into the optical train and the corresponding ellipsometer arm is pivoted according to the base angle of the retarder.

Although the use of a Fourier-transform spectrometer speeds up the measurement process significantly, full ellipsometric measurements of $\tan\Psi$ and Δ can still take several minutes or even hours, depending on the choice of resolution and detector, sample thickness, intensity of the molecular vibrations, and desired signal-to-noise ratio. In order to keep the measurement time as short as possible, the spectral resolution and the kind of detector have to be selected carefully. Furthermore, the atmospheric conditions have to be held constant to ensure that the final spectra contain vibrational information of the sample only.

For most polymer and protein samples, it is sufficient to measure with a standard spectral resolution of 4 cm^{-1}. If very narrow vibrational bands need to be resolved, though, then the resolution must be increased accordingly [104]. The left panel of Fig. 2.6 shows the CH_x-bending modes of a PNIPAAm polymer film measured with infrared microscopy at 2 cm^{-1}

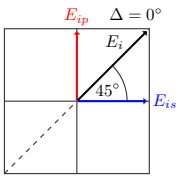

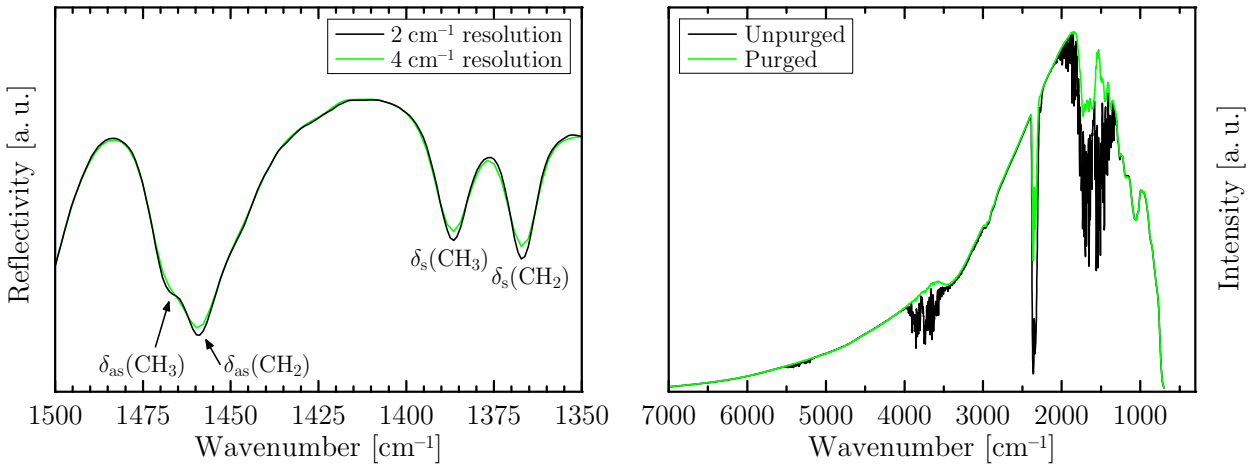

Figure 2.6: Left: Reflectivity spectra of a PNIPAAm polymer film in the CH_x-bending region measured with infrared microscopy at $2\,cm^{-1}$ and $4\,cm^{-1}$ resolution. Right: Empty-channel FT-IR spectra at $4.0\,cm^{-1}$ resolution *with* and *without* purging of the ellipsometer chamber with dry air. The spectrum in purged state resembles that of a black-body radiator, except for the cut-off at $700\,cm^{-1}$ caused by the barium fluoride window of the MCT detector.

and $4\,cm^{-1}$ resolution. The bending vibrations exhibit band widths of about $10\,cm^{-1}$. Clearly, the correct band amplitudes and shapes can only be resolved accurately at higher resolutions.

The right panel of Fig. 2.6 demonstrates the effects of CO_2 and water vapor on an infrared intensity spectrum if the ellipsometer is exposed to normal air conditions with a relative humidity of $\approx 20\%$. Water in particular is a strong infrared absorber over a large spectral range, which is very unfavorable for measuring organic samples. The amide vibrational bands of proteins, for instance, become completely inaccessible if masked by water-vapor absorption. For this reason, the ellipsometer is placed inside a plexiglas chamber with small defined openings, and the whole set-up, that is, ellipsometer as well as spectrometer, is constantly purged with dry air. This not only leads to stable atmospheric conditions with reduced water content, but it also increases the signal-to-noise ratio because more photons are reaching the detector. Besides purging, a special measurement protocol [4], introduced in Section 2.1.4., decreases the effects of slight time-dependent environmental variations.

The final point addresses the choice of detectors [3, 105–107]. Various types of detectors with different characteristics are commercially available. In the present work, DTGS and MCT detectors were used. Pyroelectric detectors based on DTGS (deuterated triglycine sulfate) are thermal detectors that exhibit a high linearity of the detected signals. This is crucial for measurements involving a Fourier-transform spectrometer, because intensity variations in the interferogram require a very high dynamic range. Since TGS crystals are hygroscopic, the detector must be sealed with an appropriate window, which in turn narrows the accessible spectral range. KBr is a typical window material with a lower transmission

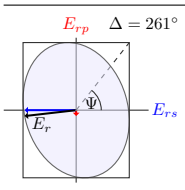

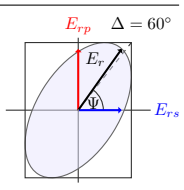

limit of about 350 cm^{-1}. DTGS detectors were utilized in this work for quantitative ex-situ reference measurements of spin-coated polymer films and thin polymer brushes as well as for infrared-transmission measurements (see Section 2.2.1.) of water, heavy water, and protein solutions. Photovoltaic MCT detectors (mercury cadmium telluride, HgCaTe) cooled with liquid nitrogen are the preferred choice if higher sensitivity paired with high linearity is required, for example, in in-situ experiments. MCT detectors used in this work exhibit a spectral cut-off at 700 cm^{-1}, which also coincides with the transmission limit of the BaF_2 windows installed in the detectors. All reference measurements were performed in a home-built ellipsometer (ISAS Berlin) externally attached to a Bruker IFS 55 Fourier-transform spectrometer. In-situ measurements, on the other hand, were executed in a second custom-built ellipsometer attached to a Bruker Vertex 70 Fourier-transform spectrometer.

Prior to the actual sample measurement, the signal-to-noise is usually assessed by two short consecutive sample measurements, the ratio of which gives a 100% line [105] with corresponding noise fluctuations. Measurement time (number of repetitive cycles × scans), Jacquinot aperture of the spectrometer, and other parameters are set accordingly.

The next two sections introduce the in-situ flow cells for non-ATR and ATR measurements that respectively involve wedge-shaped and prism-shaped silicon substrates.

c) In-situ set-up for temperature- and pH-dependent measurements

In-situ measurements in the infrared are challenging for at least two major reasons. First, the sample cannot be probed through the aqueous solution, since infrared radiation has a penetration depth of only a few micrometers in water [108]. Second, measurement times are usually quite long due to the small intensity of infrared light sources. Typical times range from 5 min to 60 min or even up to several hours if high resolution and/or high signal-to-noise ratio is required. This sets very high standards for the stability of the experimental conditions.

Figure 2.7 shows how in-situ infrared ellipsometry is facilitated using a custom-made flow cell (ISAS Berlin) [20]. Samples are prepared on highly polished infrared-transparent wedge-shaped silicon (111) substrates (26 × 20 mm^2, Vario GmbH, Wildau, Germany). In contrast to plane-parallel substrates, the wedge suppresses interferences that would otherwise arise from multiple internal reflections. Moreover, inner and outer reflex are well separated, since their angular difference is larger than twice the opening angle of ±4° in the optical set-up.

The small wedge angle of 1.5° offers many advantages compared to standard attenuated-total-reflection (ATR) geometries. Sample preparation is the same as for normal flat substrates. Absorption effects inside the substrate are almost negligible due to the short optical path length of about 2.35 mm through the wedge. This makes it possible to extend the accessible spectral region well below 1000 cm^{-1}. Also phase coherence is nearly unaffected, which allows for straightforward phase measurements Δ.

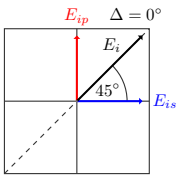

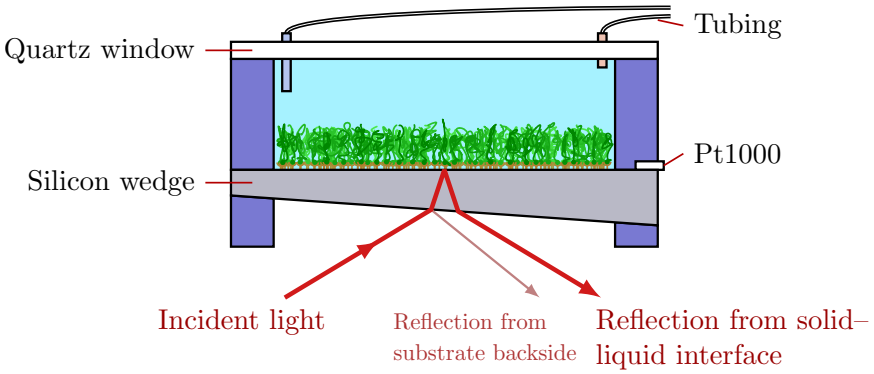

Figure 2.7: Schematic of the temperature-controlled in-situ flow cell used for infrared-ellipsometric measurements. The wedge-shaped sample substrates allows the separation of inner and outer reflex.

A metal frame secures the sample to the actual flow cell, which consists of polyether ether ketone (PEEK), an organic polymer with excellent chemical resistance properties needed for measurements in low- or high-pH solutions. A quartz window at the back of the cell (also secured by a metal frame) allows visual inspection of the cell content and, in principle, the possibility to implement additional simultaneous optical techniques like reflection anisotropy spectroscopy (RAS) [109].

In-situ measurements require that temperature, pH, and other possibly influential parameters are controlled precisely. Temperature regulation of the cell is accomplished by Peltier heating/cooling at the rear metal frame. A PID controller (PS01, OsTech GmbH i. G., Berlin, Germany) triggered by a Pt1000 sensor at the inner side of the sample wedge adjusts the temperature in the range of 20 °C to 50 °C without overshoots and with a stability of ±0.05 °C. This precision is imperative since the optical properties of solvents like water change dramatically with temperature [110] and thereby cover the spectral information of the actual sample [25]. Properties like pH or salt concentration of the solution can be changed via inlet and outlet tubes made from polytetrafluorethylen (PTFE) that are connected to a peristaltic pump. The whole set-up is purged with dry air to ensure constant atmospheric conditions and to reduce absorption of infrared radiation due to atmospheric water vapor.

Sample alignment takes place in two steps. At first, the wedge is autocollimated and aligned with respect to the outer reflex. Under an incidence angle of about 50°, rotation of the sample holder is then adjusted for the inner reflex until maximum intensity is reached at the detector. At the substrate/film interface, internal incidence angles between 5° and 16° are feasible, depending on the refractive index of the substrate as well as the external angle of incidence.

Photovoltaic MCT detectors offer a high enough sensitivity for in-situ measurements at a standard resolution of 4 cm^{-1}. If necessary, measured spectra are low-pass filtered and smoothed using cubic interpolating splines [111] or Savitzky–Golay filters [112, 113].

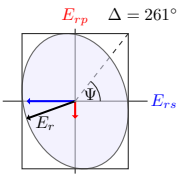

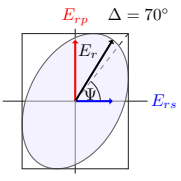

d) ATR FT-IR ellipsometry

For in-situ attenuated-total-reflection (ATR) measurements, the wedge-shaped silicon substrate is replaced by a silicon ATR prism (Vario GmbH, Wildau, Germany), as shown in Fig. 2.8. The prisms used in this work are infrared-transparent down to at least 1200 cm^{-1}, allowing to spectrally resolve the vibrational bands of organic samples, such as proteins. After securing the prism by evenly tensioning the metal frame to avoid stress and twisting, horizontal rotation of the sample holder and vertical tilt of the prism with respect to its side faces are adjusted. With $\varphi_0 = 45°$, the incidence angle of the infrared beam is set slightly offorthogonal to the side faces, which have a base angle of 49°, thus preventing backreflections towards the spectrometer. Temperature stability of the cell slightly reduces to ±0.10 °C, which is due to the larger mass of the ATR crystal compared to the thin silicon wedges.

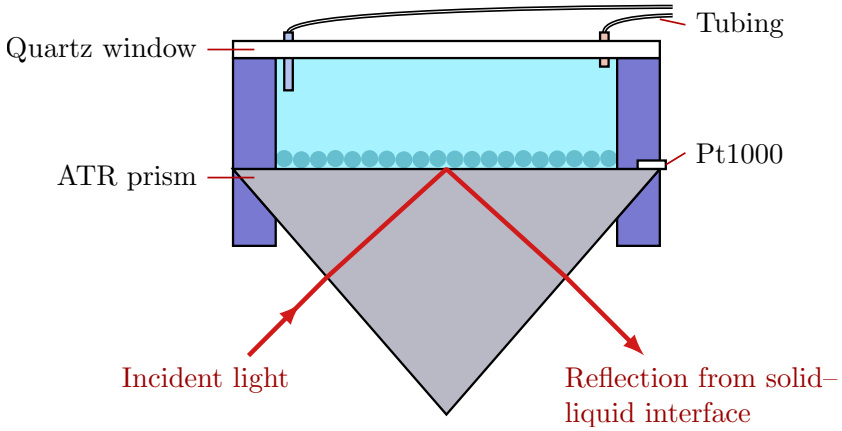

Figure 2.8: Schematic of the attenuated-total-reflection (ATR) in-situ flow cell used for infrared-ellipsometric ATR measurements. Adsorbates like proteins are detectable down to sub-monolayer thickness.

2.1.4. tan Ψ and Δ measurements

This section covers three topics concerning ellipsometric measurements. In part a), the basic concept behind tan Ψ and Δ acquisition is presented. Part b) deals with imperfect optical components of the set-up and derives correction formulae for tan Ψ and Δ. Part c) addresses the correction procedure for in-situ spectra measured through wedge-shaped substrates.

a) Quasi-ideal optical components

The basic concept behind ellipsometric measurements of tan Ψ and Δ is best demonstrated within the Jones formalism [114] in a simple arrangement of a light source that emits natural unpolarized light with field strength E_0, an ideal polarizer with fixed azimuth α_1, a reflecting isotropic sample with complex reflection coefficients r_p and r_s, and a rotating analyzer with variable azimuth α_2, followed by an ideal detector [1].

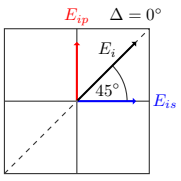

From the incoming unpolarized light, the first polarizer generates linearly polarized light with components

$$E_{ip} = E_0 \cos\alpha_1 \qquad \text{and} \qquad E_{is} = E_0 \sin\alpha_1 \tag{2.3}$$

parallel (p) and perpendicular (s) to the plane of incidence, respectively. After reflection off the sample, the corresponding electric-field strengths read

$$E_{rp} = r_p E_{ip} = |r_p|\,\mathrm{e}^{i\delta_p} E_{ip} \qquad \text{and} \qquad E_{rs} = r_s E_{is} = |r_s|\,\mathrm{e}^{i\delta_s} E_{is}\,. \tag{2.4}$$

The analyzer, then, polarizes according to

$$E = E_{rp}\cos\alpha_2 + E_{rs}\sin\alpha_2 = (r_p\cos\alpha_1\cos\alpha_2 + r_s\sin\alpha_1\sin\alpha_2)E_0\,. \tag{2.5}$$

Finally, the detector measures the intensity

$$\begin{aligned}\mathcal{I}(\alpha_1,\alpha_2) &= |E|^2 = EE^* \\ &= |E_{rp}|^2\cos^2\alpha_2 + |E_{rs}|^2\sin^2\alpha_2 + 2\,\mathrm{Re}(E_{rp}E_{rs}^*)\cos\alpha_2\sin\alpha_2 \\ &= |E_0|^2\left(|r_p|^2\cos^2\alpha_1\cos^2\alpha_2 + |r_s|^2\sin^2\alpha_1\sin^2\alpha_2 + \frac{1}{2}\mathrm{Re}(r_p r_s^*)\sin 2\alpha_1\sin 2\alpha_2\right) \\ &= \frac{1}{2}(s_0 + s_1\cos 2\alpha_2 + s_2\sin 2\alpha_2)\,,\end{aligned} \tag{2.6}$$

which is the second harmonic of the analyzer azimuth α_2. The Fourier coefficients s_j ($j = 0$, 1, 2, 3) are the Stokes parameters [115] that define total intensity, linear polarization in p/s direction, linear polarization in $\pm 45°$ direction, as well as circular polarization:

$$s_0 = |E_{rp}|^2 + |E_{rs}|^2 \quad = \left(|r_p|^2\cos^2\alpha_1 + |r_s|^2\sin^2\alpha_1\right)|E_0|^2 \tag{2.7}$$

$$s_1 = |E_{rp}|^2 - |E_{rs}|^2 \quad = \left(|r_p|^2\cos^2\alpha_1 - |r_s|^2\sin^2\alpha_1\right)|E_0|^2 \tag{2.8}$$

$$s_2 = \quad 2\,\mathrm{Re}(E_{rp}E_{rs}^*) = \quad \sin 2\alpha_1\mathrm{Re}(r_p r_s^*)\,|E_0|^2 \tag{2.9}$$

$$s_3 = -2i\,\mathrm{Im}(E_{rp}E_{rs}^*) = -i\sin 2\alpha_1\mathrm{Im}(r_p r_s^*)\,|E_0|^2 \tag{2.10}$$

Essentially, ellipsometry measures the Stokes parameters by analyzing the detector intensities $\mathcal{I}(\alpha_1,\alpha_2)$ at different azimuths α_1 and α_2. The third parameter s_3 can be accessed by placing a phase-shifting retarder before or after the sample.

The third line of Eq. (2.6) shows that the measured intensities are, in principle, symmetric in α_1 and α_2, and it should therefore be possible to rotate either the polarizer or the analyzer. In a real experimental situation, however, non-idealities like polarization sensitivity of the detector or source polarization restrict this freedom and dictate to fix the corresponding polarizer. Details on this subject are covered in Section 2.1.4.b).

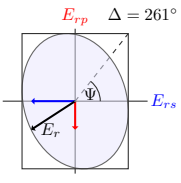

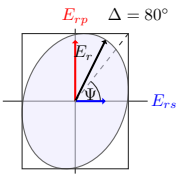

For historical reasons, the more intuitive parameterization of *amplitude ratio* $\tan\Psi$ and *phase difference* Δ between parallel and perpendicular component is widely used. This parameterization is very convenient for the qualitative interpretation of ellipsometric measurements, especially in the infrared, as will become apparent. With the trigonometric relations

$$\tan\Psi' \equiv \frac{\tan\Psi}{\tan\alpha_1}\,, \quad \cos 2\Psi = \frac{1-\tan^2\Psi}{1+\tan^2\Psi}\,, \quad \text{and} \quad \sin 2\Psi = \frac{2\tan\Psi}{1+\tan^2\Psi}\,, \tag{2.11}$$

Eq. (2.6) yields [1]

$$\mathcal{I}(\alpha_1,\alpha_2) = \frac{1}{2}s_0 \cdot \Big(1 - \cos 2\Psi' \cos 2\alpha_2 + \sin 2\Psi' \cos\Delta \sin 2\alpha_2\Big)\,, \tag{2.12}$$

with the ellipsometric parameters

$$\tan\Psi \cdot \mathrm{e}^{i\Delta} = \frac{E_{rp}/E_{ip}}{E_{rs}/E_{is}} = \frac{r_p}{r_s}\,, \qquad \tan\Psi = \frac{|r_p|}{|r_s|}\,, \qquad \text{and} \qquad \Delta = \delta_p - \delta_s\,. \tag{2.13}$$

In terms of Stokes parameters, this reads

$$-s_1 = s_0\ \cos 2\Psi'\,, \tag{2.14}$$

$$s_2 = s_0\ \sin 2\Psi' \cos\Delta\,, \tag{2.15}$$

$$s_3 = s_0\ \sin 2\Psi' \sin\Delta\,. \tag{2.16}$$

s_3 is obtained from measurements $\widetilde{\mathcal{I}}(\alpha_1,\alpha_2)$ with an additional retarder in the optical train that introduces a phase shift δ_{Ret}. The second Stokes parameter $\tilde{s}_2$, then, is proportional to $\cos(\Delta+\delta_{\mathrm{Ret}})$:

$$\widetilde{\mathcal{I}}(\alpha_1,\alpha_2) = \frac{1}{2}(\tilde{s}_0 + \tilde{s}_1\cos 2\alpha_2 + \tilde{s}_2 \sin 2\alpha_2) \tag{2.17}$$

Since non-ideal retarders influence the transmission of light [1, 116], it is necessary to account for changes in the total intensity $s_0 \to \tilde{s}_0$ as well as in $s_1 \to \tilde{s}_1$. It is useful to remember the addition theorem

$$\frac{\tilde{s}_2}{\tilde{s}_0} = \sin 2\Psi' \cos(\Delta+\delta_{\mathrm{Ret}}) = \sin 2\Psi'(\cos\Delta\cos\delta_{\mathrm{Ret}} - \sin\Delta\sin\delta_{\mathrm{Ret}})\,. \tag{2.18}$$

Together with Eqs. (2.15) and (2.16), this relates $\tilde{s}_2$ to s_2 and s_3,

$$\frac{\tilde{s}_2}{\tilde{s}_0} = \frac{s_2}{s_0}\cos\delta_{\mathrm{Ret}} - \frac{s_3}{s_0}\sin\delta_{\mathrm{Ret}}\,, \tag{2.19}$$

and thereby leads to

$$\sin 2\Psi' \sin\Delta = \frac{\dfrac{s_2}{s_0}\cos\delta_{\mathrm{Ret}} - \dfrac{\tilde{s}_2}{\tilde{s}_0}}{\sin\delta_{\mathrm{Ret}}}\,. \tag{2.20}$$

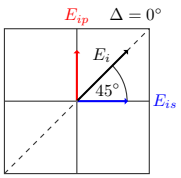

The determination of $\tan\Psi$ and Δ after Eq. (2.12) takes place from measurements $\mathcal{I}(\alpha_2)$ with fixed polarizer, typically $\alpha_1 = 45°$, at analyzer azimuths $\alpha_2 = 0°$, 90°, 45°, and 135°:

$$\cos 2\Psi' = \frac{\mathcal{I}(90°) - \mathcal{I}(0°)}{\mathcal{I}(90°) + \mathcal{I}(0°)}\,, \qquad \sin 2\Psi' \cos\Delta = \frac{\mathcal{I}(45°) - \mathcal{I}(135°)}{\mathcal{I}(45°) + \mathcal{I}(135°)} \tag{2.21}$$

To reduce influences from instrumental drift and changing atmospheric conditions on the ellipsometric parameters in the infrared, intensities at 0° and 90° are alternatingly measured for a given number of cycles and then averaged before the equivalent sequence of measurements at 45° and 135° is performed [4].

If $|\cos\Delta| \approx 1$ or if Δ needs to be determined unambiguously over the whole range between $0° \leq \Delta < 360°$, retarder measurements $\widetilde{\mathcal{I}}(\alpha_2)$ are performed at the same azimuths, which yields $\sin\Delta$ after Eq. (2.20). In practice, additional empty-channel measurements $\mathcal{E}(\alpha_2)$ without a sample, carried out at the same azimuths, have to be performed in order to compensate for possible imperfections of polarizers, retarder, and interferometer. In Eqs. (2.21), then, the intensities $\mathcal{I}(\alpha_2)$ have to be replaced by $\mathcal{I}(\alpha_2)/\mathcal{E}(\alpha_2)$, in first-order approximation. How imperfections of optical elements are treated in a rigorous way is presented in the next section.

With the four Stokes parameters at hand, the degree of polarization P can be defined according to [1, 3, 4]

$$P = \frac{\sqrt{s_1^2 + s_2^2 + s_3^2}}{s_0} = \sqrt{\cos^2 2\Psi' + \sin^2 2\Psi' \left(\cos^2\Delta + \sin^2\Delta\right)} \leqq 1\,. \tag{2.22}$$

Ideally, P should reach unity. In real experiments, however, depolarization effects can occur either at the sample or at other optical elements in the set-up. Depending on the size of these effects, they must be considered within a proper theoretical framework, e. g., the Müller matrix formalism, which is also introduced in Section 2.1.4.b). Note that measured $(\cos^2\Delta + \sin^2\Delta)$ usually differs from unity, too. This is due to lateral variations in Δ, over which the actual measurement is averaging. The so-called degree of phase polarization

$$P_{\mathrm{ph}} = \sqrt{\langle\cos\Delta\rangle^2 + \langle\sin\Delta\rangle^2} = \left[\frac{s_2^2 + s_3^2}{s_0^2 - s_1^2}\right]_{\mathrm{exp}}^{1/2} \leqq 1 \tag{2.23}$$

is an important quantity for assessing the quality of the measurement [1, 116]. Among others, P_{ph} is strongly affected by scattering at the sample surface, inside the sample (for example, in ATR crystals), or inside the retarder [3], by variations in thickness or refractive index across the illuminated area, or by interference patterns of optically thick transparent samples. A correction according to

$$\sin 2\Psi' \cos\Delta = \frac{s_2}{s_0 P_{\mathrm{ph}}} \qquad \text{and} \qquad \sin 2\Psi' \sin\Delta = \frac{s_3}{s_0 P_{\mathrm{ph}}} \tag{2.24}$$

can prove fruitful for the correct determination of Δ in the presence of these effects.

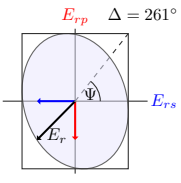

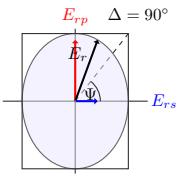

b) Imperfect optical components – The Müller matrix formalism

Typical infrared ellipsometers suffer from polarizing effects of the interferometer and from non-ideal polarizers with degree of polarization much smaller than unity [1]. Wire-grid polarizers used in the infrared also show a generic phase shift between transmitted and attenuated component [117, 118]. In order to minimize these effects on the measured ellipsometric parameters, a calibration protocol [1, 119] has to be followed that allows one to quantify the non-idealities and reincorporate them in correction formulae yielding ellipsometer-independent tan Ψ and Δ spectra. The derivation of these formulae is based on the Müller matrix formalism [120, 121], which—in contrast to the Jones formalism [114]—enables the characterization of optical systems with partial polarization.

The general procedure is presented, extending the original calculations of A. Röseler [1] towards arbitrary source and interferometer polarization as well as independent polarizer and analyzer imperfections, including phase retardation. Exemplarily, interferometer and polarizer parameters are determined for a laboratory ellipsometer. In the end, correction formulae are obtained for different relevant experimental scenarios, including ellipsometry with strongly direction-dependent source polarization found, for instance, at a synchrotron.

The polarization state of electromagnetic radiation can be characterized by the four Stokes parameters s_0, s_1, s_2, and s_3 [115], which, for convenience, are usually combined into a Stokes vector S [120]:

$$S = \begin{bmatrix} s_0 \\ s_1 \\ s_2 \\ s_3 \end{bmatrix} = \begin{bmatrix} I_x + I_y \\ I_x - I_y \\ I_{+\pi/4} - I_{-\pi/4} \\ I_r - I_l \end{bmatrix} \tag{2.25}$$

The virtual intensities I describe the polarization components in the respective directions. x and y are horizontal and vertical direction, $\pm\pi/4$ are the azimuths $\pm 45°$, and r and l represent right- and left-circular polarization. The total intensity is given by the zeroth component of the Stokes vector, $I_0 = s_0 = I_x + I_y$.

How Stokes vectors behave when interacting with optical elements is described by the Müller matrix formalism [6, 89, 120, 121]. Each element is characterized by a 4×4 matrix $\mathcal{M}_n$ under which a Stokes vector S transforms into a new vector $S' = \mathcal{M}_n \cdot S$. The Müller matrix $\mathcal{M}$ of the whole system, then, is the ordered product of its N single-component matrices,

$$\mathcal{M} = \mathcal{M}_N \cdot \mathcal{M}_{N-1} \cdot \ldots \cdot \mathcal{M}_2 \cdot \mathcal{M}_1 \,. \tag{2.26}$$

Altogether, the Stokes vector S_{in} of the incident radiation transforms as

$$S^{\text{D}} = \mathcal{M} \cdot S_{\text{in}} \,. \tag{2.27}$$

In that way, the system Müller matrix $\mathcal{M}$ relates the intensity s_0^{D} measured at a detector

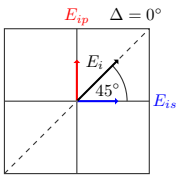

with the properties of the optical system. Within the Müller calculus, a typical infrared ellipsometer comprising the following optical components can now be described:

Globar	$S_{\text{in}} = [s_0, 0, 0, 0]^T$
Interferometer / window / mirror optics	$\mathcal{M}_{\text{Interferometer}}$
Polarizer	$\mathcal{M}_{\text{Pol}}$
Sample	$\mathcal{M}_{\text{Sample}}$
Retarder	$\mathcal{M}_{\text{Ret}}$
Analyzer	$\mathcal{M}_{\text{Pol}}$
Focusing mirror	$\mathcal{M}_{\text{Mirror}}$
Detector window	$\mathcal{M}_{\text{Det}}$
Detector	$S^{\text{D}} = [s_0^{\text{D}}, s_1^{\text{D}}, s_2^{\text{D}}, s_3^{\text{D}}]^T$

Before the light passes through the first polarizer, it can be parameterized by a Stokes vector

$$\bar{S} = [\bar{s}_0, \bar{s}_1, \bar{s}_2, \bar{s}_3]^T = \mathcal{M}_{\text{Interferometer}} \cdot S_{\text{in}} \tag{2.28}$$

that represents the optical response of the globar radiation with the interferometer and the mirror optics. After the analyzer, an ellipsoidal gold or aluminium mirror focuses the light onto the detector. Normally, the mirror is aligned at a small angle $\lesssim 45°$ with respect to the light beam. Its Müller matrix can therefore be approximated by the identity matrix $\mathcal{M}_{\text{Mirror}} = \text{diag}(1, 1, 1, 1)$. The same holds true for ideal detectors with carefully installed windows, which minimizes stress-induced birefringence. These simplifications lead to the detector intensity

$$S^{\text{D}}(\alpha_1, \alpha_2) = \mathcal{M}_{\text{Pol}}(\alpha_2) \cdot \mathcal{M}_{\text{Ret}} \cdot \mathcal{M}_{\text{Sample}} \cdot \mathcal{M}_{\text{Pol}}(\alpha_1) \cdot \bar{S}\,. \tag{2.29}$$

The required Müller matrices for polarizers, retarder, and isotropic sample are summarized in Appendix B. They contain the ellipsometric parameters tan Ψ and Δ of the sample, the retarder parameters $\tan\psi_{\text{Ret}}$ and δ_{Ret}, as well as the polarization degrees $c_i = \cos\vartheta_i$ and the phase retardations δ_i of polarizer ($i = 1$) and analyzer ($i = 2$). Infrared ellipsometers used in this work are set up with polarizers as the only rotating elements. The corresponding Müller matrices need to be derived in dependence of the azimuth angles α_1 and α_2. In contrast, the retarder is fixed in its orientation with respect to the plane of incidence. Other types of ellipsometers also make use of rotating retarders, for instance, at the IRIS beamline at BESSY II [15, 22, 122, 123].

Full ellipsometric measurements of tan Ψ and Δ require knowledge about the retarder phase δ_{Ret}, the imperfection parameters ψ_{Ret}, c_i, and δ_i, as well as the radiation-characterizing Stokes parameters $\bar{s}_0$, $\bar{s}_1$, $\bar{s}_2$, and $\bar{s}_3$. These parameters are determined from empty-channel calibration measurements with and without retarder. After calibration, the sample is usually measured without retarder to obtain tan Ψ, and additionally with retarder to accurately

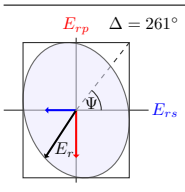

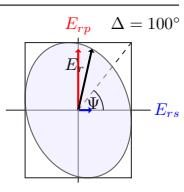

determine the phase Δ. The small intensity of infrared light sources, compared to the visible range, limits the possible realistic number of measurements at different polarizer/analyzer settings. A minimum number of four azimuth combinations (α_1, α_2) with at least one non-parallel setting is required, though, to determine both Ψ and Δ accurately. For practical reasons, the azimuths $\alpha_i = 0°$, 45°, 90°, and 135° are chosen, which simplifies the polarizer Müller matrices significantly. tan Ψ and Δ are usually deduced from measurements at 0°/0°, 90°/90° and 45°/45°, 135°/45° polarizer/analyzer positions, respectively.

The measured detector intensities for full ellipsometry are given below:

$$\begin{aligned}
\mathcal{E}(\alpha_1,\alpha_2) &\equiv \mathcal{M}_{\mathrm{Pol}}(\vartheta_2,\delta_2,\alpha_2)\cdot\mathcal{M}_{\mathrm{Pol}}(\vartheta_1,\delta_1,\alpha_1)\cdot\bar{S}\,,\\
\mathcal{R}(\alpha_1,\alpha_2) &\equiv \mathcal{M}_{\mathrm{Pol}}(\vartheta_2,\delta_2,\alpha_2)\cdot\mathcal{M}_{\mathrm{Ret}}(\psi_{\mathrm{Ret}},\delta_{\mathrm{Ret}})\cdot\mathcal{M}_{\mathrm{Pol}}(\vartheta_1,\delta_1,\alpha_1)\cdot\bar{S}\,,\\
\mathcal{I}(\alpha_1,\alpha_2) &\equiv \mathcal{M}_{\mathrm{Pol}}(\vartheta_2,\delta_2,\alpha_2)\cdot\mathcal{M}_{\mathrm{Sample}}(\Psi,\Delta)\cdot\mathcal{M}_{\mathrm{Pol}}(\vartheta_1,\delta_1,\alpha_1)\cdot\bar{S}\,,\\
\widetilde{\mathcal{I}}(\alpha_1,\alpha_2) &\equiv \mathcal{M}_{\mathrm{Pol}}(\vartheta_2,\delta_2,\alpha_2)\cdot\mathcal{M}_{\mathrm{Ret}}(\psi_{\mathrm{Ret}},\delta_{\mathrm{Ret}})\cdot\mathcal{M}_{\mathrm{Sample}}(\Psi,\Delta)\cdot\mathcal{M}_{\mathrm{Pol}}(\vartheta_1,\delta_1,\alpha_1)\cdot\bar{S}
\end{aligned} \tag{2.30}$$

Equations (2.30) are now written in explicit form for the azimuths $\alpha_i = 0°$, 90°, 45°, and 135° using the symbolic notation $\left[\begin{smallmatrix}\vert\\ \text{–}\end{smallmatrix}\right] \equiv \left[\begin{smallmatrix}0°\\ 90°\end{smallmatrix}\right]$ and $\left[\begin{smallmatrix}/\\ \backslash\end{smallmatrix}\right] \equiv \left[\begin{smallmatrix}45°\\ 135°\end{smallmatrix}\right]$. For brevity, sample detector intensities are only shown for azimuth combinations of 0° and 90° as well as 45° and 135°. Other combinations for rotating-polarizer/-analyzer measurements can be found in Appendix B.

Empty-channel detector intensities *without* retarder

$$\mathcal{E}\left(\left[\begin{smallmatrix}\vert\\ \text{–}\end{smallmatrix}\right],\left[\begin{smallmatrix}\vert\\ \text{–}\end{smallmatrix}\right]\right) = K_1K_2\Big\{\bar{\mathrm{s}}_0\Big(1+[\pm c_1][\pm c_2]\Big)+\bar{\mathrm{s}}_1\,[\pm c_1 \pm c_2]\Big\} \tag{2.31}$$

$$\mathcal{E}\left(\left[\begin{smallmatrix}/\\ \backslash\end{smallmatrix}\right],\left[\begin{smallmatrix}/\\ \backslash\end{smallmatrix}\right]\right) = K_1K_2\Big\{\bar{\mathrm{s}}_0\Big(1+[\pm c_1][\pm c_2]\Big)+\bar{\mathrm{s}}_2\,[\pm c_1 \pm c_2]\Big\} \tag{2.32}$$

$$\mathcal{E}\left(\left[\begin{smallmatrix}\vert\\ \text{–}\end{smallmatrix}\right],\left[\begin{smallmatrix}/\\ \backslash\end{smallmatrix}\right]\right) = K_1K_2\Big\{\bar{\mathrm{s}}_0+\bar{\mathrm{s}}_1\,[\pm c_1]+\bar{\mathrm{s}}_2\,[s_1][\pm c_2]\cos\delta_1+\bar{\mathrm{s}}_3\,[\pm s_1][\pm c_2]\sin\delta_1\Big\} \tag{2.33}$$

$$\mathcal{E}\left(\left[\begin{smallmatrix}/\\ \backslash\end{smallmatrix}\right],\left[\begin{smallmatrix}\vert\\ \text{–}\end{smallmatrix}\right]\right) = K_1K_2\Big\{\bar{\mathrm{s}}_0+\bar{\mathrm{s}}_2\,[\pm c_1]+\bar{\mathrm{s}}_1\,[s_1][\pm c_2]\cos\delta_1-\bar{\mathrm{s}}_3\,[\pm s_1][\pm c_2]\sin\delta_1\Big\} \tag{2.34}$$

$[\pm c_1]$ and $[\pm s_1]$ refer to the two different polarizer positions given in the first argument of $\mathcal{E}$, while $[\pm c_2]$ refers to the two analyzer positions given in the second argument. As will be discussed later in more detail, Eqs. (2.31)–(2.34) allow one to determine the polarization degrees c_1 and c_2, s_1, the phase shift δ_1, as well as the normalized Stokes parameters $\bar{\mathrm{s}}_1/\bar{\mathrm{s}}_0$, $\bar{\mathrm{s}}_2/\bar{\mathrm{s}}_0$, and $\bar{\mathrm{s}}_3/\bar{\mathrm{s}}_0$ in front of the first polarizer. The constants K_i, c_i, s_i, and δ_i are given by

$$K_i = \frac{\tau_{\mathrm{M}}^i+\tau_{\mathrm{m}}^i}{2}\,,\quad c_i = \cos 2\vartheta_i = \frac{\tau_{\mathrm{M}}^i-\tau_{\mathrm{m}}^i}{\tau_{\mathrm{M}}^i+\tau_{\mathrm{m}}^i}\,,\quad s_i = \sin 2\vartheta_i = \frac{2\sqrt{\tau_{\mathrm{M}}^i\tau_{\mathrm{m}}^i}}{\tau_{\mathrm{M}}^i+\tau_{\mathrm{m}}^i}\,,\quad \delta_i = \delta_{\mathrm{M}}^i-\delta_{\mathrm{m}}^i\,, \tag{2.35}$$

where τ_{M}^i and τ_{m}^i are maximum and minimum transmittances of polarizer and analyzer.

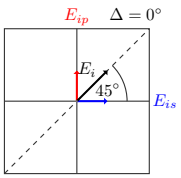

Detector intensities of sample *without* retarder

$$\mathcal{I}\Big(\big[\tfrac{\square}{-}\big],\big[\tfrac{\square}{-}\big]\Big) = K_1K_2K_\mathrm{S}\Big\{\bar{\mathrm{s}}_0\big(1+[\pm c_1][\pm c_2]\big)+\bar{\mathrm{s}}_1\,[\pm c_1\pm c_2] \\ -\cos 2\Psi\Big[\bar{\mathrm{s}}_0\,[\pm c_1\pm c_2]+\bar{\mathrm{s}}_1\big(1+[\pm c_1][\pm c_2]\big)\Big]\Big\} \tag{2.36}$$

$$\mathcal{I}\Big(\big[\tfrac{\diagup}{\diagdown}\big],\big[\tfrac{\diagup}{\diagdown}\big]\Big) = K_1K_2K_\mathrm{S}\Big\{\bar{\mathrm{s}}_0+\bar{\mathrm{s}}_2\,[\pm c_1]-\cos 2\Psi\Big[\bar{\mathrm{s}}_1\,[s_1]\cos\delta_1-\bar{\mathrm{s}}_3\,[\pm s_1]\sin\delta_1\Big] \\ +\sin 2\Psi\cos\Delta\Big[\bar{\mathrm{s}}_0\,[\pm c_1][\pm c_2]+\bar{\mathrm{s}}_2\,[\pm c_2]\Big] \\ +\sin 2\Psi\,\sin\Delta\Big[\bar{\mathrm{s}}_1\,[\pm s_1][\pm c_2]\sin\delta_1+\bar{\mathrm{s}}_3\,[s_1][\pm c_2]\cos\delta_1\Big]\Big\} \tag{2.37}$$

Here, $K_\mathrm{S}=(|r_p|^2+|r_s|^2)/2$. With polarizer imperfections and Stokes parameters known from calibration, $\tan\Psi$ and $\cos\Delta$ are determined from Eqs. (2.36) and (2.37).

Empty-channel detector intensities *with* retarder

Retarder calibration measurements of ψ_Ret and δ_Ret correspond to a sample measurement in which the retarder acts as the sample. Detector intensities $\mathcal{R}(\alpha_1,\alpha_2)$ can therefore be obtained from Eqs. (2.36) and (2.37) using the substitution

$$\mathcal{R}(\alpha_1,\alpha_2)=\mathcal{I}(\alpha_1,\alpha_2)\Big|_{\Psi\to\psi_\mathrm{Ret},\,\Delta\to\delta_\mathrm{Ret},\,K_\mathrm{S}\to K_\mathrm{R}}. \tag{2.38}$$

K_R is given in Appendix B., Eq. (B.7).

Detector intensities of sample *with* retarder

$$\widetilde{\mathcal{I}}\Big(\big[\tfrac{\square}{-}\big],\big[\tfrac{\square}{-}\big]\Big) = K_1K_2K_\mathrm{S}K_\mathrm{R}\Big\{\big(1+\cos 2\Psi\cos 2\psi_\mathrm{Ret}\big)\big[\bar{\mathrm{s}}_0\big(1+[\pm c_1][\pm c_2]\big)+\bar{\mathrm{s}}_1\,[\pm c_1\pm c_2]\big] \\ -\big(\cos 2\Psi+\cos 2\psi_\mathrm{Ret}\big)\big[\bar{\mathrm{s}}_0\,[\pm c_1\pm c_2]+\bar{\mathrm{s}}_1\big(1+[\pm c_1][\pm c_2]\big)\big]\Big\} \tag{2.39}$$

$$\widetilde{\mathcal{I}}\Big(\big[\tfrac{\diagup}{\diagdown}\big],\big[\tfrac{\diagup}{\diagdown}\big]\Big) = K_1K_2K_\mathrm{S}K_\mathrm{R}\Big\{\big(1+\cos 2\Psi\cos 2\psi_\mathrm{Ret}\big)\big[\bar{\mathrm{s}}_0+\bar{\mathrm{s}}_2\,[\pm c_1]\big] \\ -\big(\cos 2\Psi+\cos 2\psi_\mathrm{Ret}\big)\big[\bar{\mathrm{s}}_1\,[s_1]\cos\delta_1-\bar{\mathrm{s}}_3\,[\pm s_1]\sin\delta_1\big] \\ +\sin 2\Psi\sin 2\psi_\mathrm{Ret}\cos(\Delta+\delta_\mathrm{Ret})\big[\bar{\mathrm{s}}_0\,[\pm c_1][\pm c_2]+\bar{\mathrm{s}}_2\,[\pm c_2]\big] \\ +\sin 2\Psi\sin 2\psi_\mathrm{Ret}\,\sin(\Delta+\delta_\mathrm{Ret})\big[\bar{\mathrm{s}}_1\,[\pm s_1][\pm c_2]\sin\delta_1+\bar{\mathrm{s}}_3\,[s_1][\pm c_2]\cos\delta_1\big]\Big\} \tag{2.40}$$

With $\cos 2\psi_\mathrm{Ret}$ and δ_Ret determined from calibration, $\tan\Psi$ can also be calculated from Eq. (2.39), similar to measurements without retarder. Equation (2.40) allows the computation of $\cos(\Delta+\delta_\mathrm{Ret})$, which yields $\sin\Delta$ and thereby $0°\le\Delta<360°$, as will be shown in the following Subsection 4.

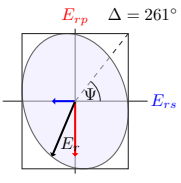

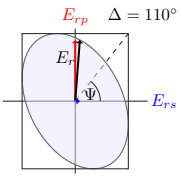

With equations for the various detector intensities at hand, it is now possible to quantify the polarizer imperfections and the incident Stokes parameters by combining the intensities $\mathcal{E}(\alpha_1, \alpha_2)$ into convenient differences, sums, and ratios. After that, correction formulae for tan Ψ and Δ for different experimental situations will be given.

1. Polarizer imperfections and incident Stokes parameters:

Combinations of empty-channel intensities

$$2\bar{s}_0\,[1 - c_1c_2]\;\; K_1K_2 = \mathcal{E}(\,\mathbb{I}\,,\,\mathbb{=}) + \mathcal{E}(\mathbb{=},\,\mathbb{I}\,) = \mathcal{E}(\mathbb{/},\mathbb{\backslash}) + \mathcal{E}(\mathbb{\backslash},\mathbb{/}) \tag{2.41}$$

$$2\bar{s}_0\,[1 + c_1c_2]\;\; K_1K_2 = \mathcal{E}(\,\mathbb{I}\,,\,\mathbb{I}\,) + \mathcal{E}(\mathbb{=},\mathbb{=}) = \mathcal{E}(\mathbb{/},\mathbb{/}) + \mathcal{E}(\mathbb{\backslash},\mathbb{\backslash}) \tag{2.42}$$

$$2\bar{s}_1\,[c_1 + c_2]\;\; K_1K_2 = \mathcal{E}(\,\mathbb{I}\,,\,\mathbb{I}\,) - \mathcal{E}(\mathbb{=},\mathbb{=}) \tag{2.43}$$

$$2\bar{s}_2\,[c_1 + c_2]\;\; K_1K_2 = \mathcal{E}(\mathbb{/},\mathbb{/}) - \mathcal{E}(\mathbb{\backslash},\mathbb{\backslash}) \tag{2.44}$$

$$2\bar{s}_1\,[c_1 - c_2]\;\; K_1K_2 = \mathcal{E}(\,\mathbb{I}\,,\mathbb{=}) - \mathcal{E}(\mathbb{=},\,\mathbb{I}\,) \tag{2.45}$$

$$2\bar{s}_2\,[c_1 - c_2]\;\; K_1K_2 = \mathcal{E}(\mathbb{/},\mathbb{\backslash}) - \mathcal{E}(\mathbb{\backslash},\mathbb{/}) \tag{2.46}$$

$$4\bar{s}_0\;\; K_1K_2 = \mathcal{E}(\,\mathbb{I}\,,\mathbb{/}) + \mathcal{E}(\mathbb{=},\mathbb{\backslash}) + \mathcal{E}(\mathbb{/},\,\mathbb{I}\,) + \mathcal{E}(\mathbb{\backslash},\mathbb{=}) = \mathcal{E}(\,\mathbb{I}\,,\mathbb{\backslash}) + \mathcal{E}(\mathbb{=},\mathbb{/}) + \mathcal{E}(\mathbb{/},\mathbb{=}) + \mathcal{E}(\mathbb{\backslash},\,\mathbb{I}\,) \tag{2.47}$$

$$\frac{\mathcal{E}(\mathbb{\backslash},\mathbb{\backslash}) - \mathcal{E}(\mathbb{/},\mathbb{\backslash})}{\mathcal{E}(\mathbb{\backslash},\mathbb{\backslash}) + \mathcal{E}(\mathbb{/},\mathbb{\backslash})} = \frac{c_1c_2 - \frac{\bar{s}_2}{\bar{s}_0}c_1}{1 - \frac{\bar{s}_2}{\bar{s}_0}c_2}, \qquad \frac{\mathcal{E}(\,\mathbb{I}\,,\mathbb{\backslash}) - \mathcal{E}(\mathbb{=},\mathbb{\backslash})}{\mathcal{E}(\,\mathbb{I}\,,\mathbb{\backslash}) + \mathcal{E}(\mathbb{=},\mathbb{\backslash})} = \frac{\frac{\bar{s}_1}{\bar{s}_0}c_1 - \frac{\bar{s}_3}{\bar{s}_0}s_1c_2\sin\delta_1}{1 - \frac{\bar{s}_2}{\bar{s}_0}s_1c_2\cos\delta_1} \tag{2.48}$$

$$\frac{\mathcal{E}(\mathbb{/},\mathbb{/}) - \mathcal{E}(\mathbb{\backslash},\mathbb{/})}{\mathcal{E}(\mathbb{/},\mathbb{/}) + \mathcal{E}(\mathbb{\backslash},\mathbb{/})} = \frac{c_1c_2 + \frac{\bar{s}_2}{\bar{s}_0}c_1}{1 + \frac{\bar{s}_2}{\bar{s}_0}c_2}, \qquad \frac{\mathcal{E}(\,\mathbb{I}\,,\mathbb{/}) - \mathcal{E}(\mathbb{=},\mathbb{/})}{\mathcal{E}(\,\mathbb{I}\,,\mathbb{/}) + \mathcal{E}(\mathbb{=},\mathbb{/})} = \frac{\frac{\bar{s}_1}{\bar{s}_0}c_1 + \frac{\bar{s}_3}{\bar{s}_0}s_1c_2\sin\delta_1}{1 + \frac{\bar{s}_2}{\bar{s}_0}s_1c_2\cos\delta_1}$$

$$\frac{\mathcal{E}(\mathbb{/},\mathbb{/}) - \mathcal{E}(\mathbb{/},\mathbb{\backslash})}{\mathcal{E}(\mathbb{/},\mathbb{/}) + \mathcal{E}(\mathbb{/},\mathbb{\backslash})} = \frac{c_1c_2 + \frac{\bar{s}_2}{\bar{s}_0}c_2}{1 + \frac{\bar{s}_2}{\bar{s}_0}c_1}, \qquad \frac{\mathcal{E}(\mathbb{/},\,\mathbb{I}\,) - \mathcal{E}(\mathbb{/},\mathbb{=})}{\mathcal{E}(\mathbb{/},\,\mathbb{I}\,) + \mathcal{E}(\mathbb{/},\mathbb{=})} = \frac{\left(\frac{\bar{s}_1}{\bar{s}_0}\cos\delta_1 - \frac{\bar{s}_3}{\bar{s}_0}\sin\delta_1\right)s_1c_2}{1 + \frac{\bar{s}_2}{\bar{s}_0}c_1}$$

$$\frac{\mathcal{E}(\mathbb{\backslash},\mathbb{\backslash}) - \mathcal{E}(\mathbb{\backslash},\mathbb{/})}{\mathcal{E}(\mathbb{\backslash},\mathbb{\backslash}) + \mathcal{E}(\mathbb{\backslash},\mathbb{/})} = \frac{c_1c_2 - \frac{\bar{s}_2}{\bar{s}_0}c_2}{1 - \frac{\bar{s}_2}{\bar{s}_0}c_1}, \qquad \frac{\mathcal{E}(\mathbb{\backslash},\,\mathbb{I}\,) - \mathcal{E}(\mathbb{\backslash},\mathbb{=})}{\mathcal{E}(\mathbb{\backslash},\,\mathbb{I}\,) + \mathcal{E}(\mathbb{\backslash},\mathbb{=})} = \frac{\left(\frac{\bar{s}_1}{\bar{s}_0}\cos\delta_1 + \frac{\bar{s}_3}{\bar{s}_0}\sin\delta_1\right)s_1c_2}{1 - \frac{\bar{s}_2}{\bar{s}_0}c_1}$$

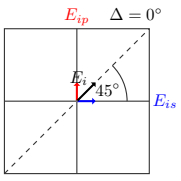

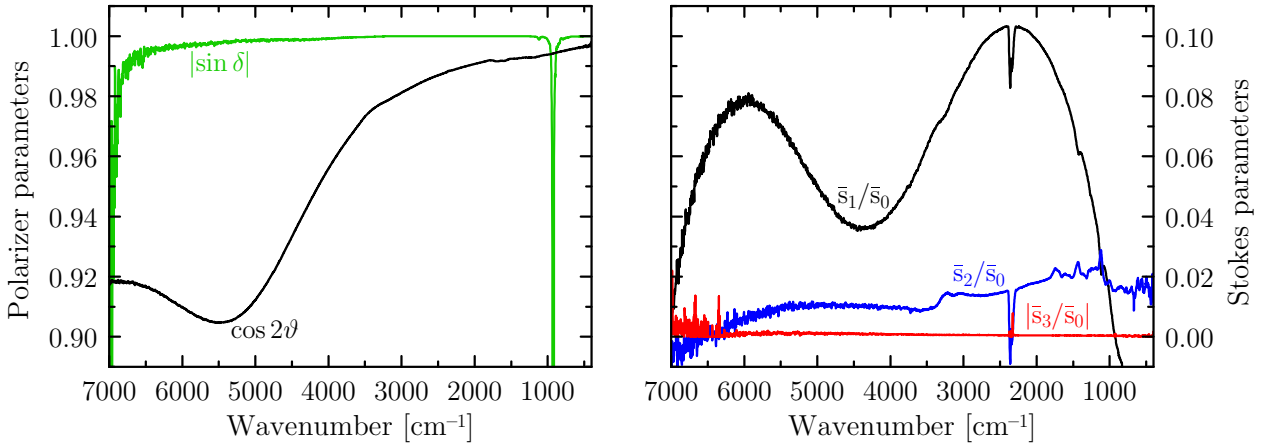

Figure 2.9: Degree of polarization $\cos 2\vartheta$ and absolute sine of the phase shift δ between transmitted and attenuated component of a KRS-5 polarizer (left) as well as normalized Stokes parameters $\bar{s}_1/\bar{s}_0$, $\bar{s}_2/\bar{s}_0$, and $|\bar{s}_3/\bar{s}_0|$ of the incident radiation in front of the first polarizer (right), measured in a custom-built infrared ellipsometer attached to a Bruker IFS55 FT-IR spectrometer.

Equations (2.41)–(2.48) are easily solved for c_1, s_1, c_2, $|\sin\delta_1|$, $\bar{s}_1/\bar{s}_0$, $\bar{s}_2/\bar{s}_0$, and $|\bar{s}_3/\bar{s}_0|$. The sign of $\bar{s}_3/\bar{s}_0$ and $\sin\delta_1$ has to be determined from additional retarder measurements (see Appendix B.) or from theoretical considerations about the phase shift in wire-grid polarizers [117]. The above equations have a rather obvious meaning: With crossed polarizers in Eq. (2.41), a deviation from zero is a direct measure of the polarizers' degree of polarization c_1 and c_2, or, in other words, a measure of the leaking unpolarized part that passes the polarizers due to $c_1 c_2 < 1$. Equations (2.42)–(2.44) reflect the definition (2.25) of a Stokes vector. The intensity sums and differences $\mathcal{E}(\,\mathbb{I}\,,\,\mathbb{I}\,)+\mathcal{E}(⥊,⥊)$, $\mathcal{E}(\,\mathbb{I}\,,\,\mathbb{I}\,)-\mathcal{E}(⥊,⥊)$, and $\mathcal{E}(⥋,⥋)-\mathcal{E}(⥍,⥍)$ respectively measure the total intensity $\bar{s}_0$ of the incident radiation, linear polarization $\bar{s}_1$ in x/y direction, and linear polarization $\bar{s}_2$ in $\pm 45°$ direction. Measurements that involve only the polarizer positions 45° and 135°—the left column of Eqs. (2.48)—are sensitive to $\bar{s}_2$. Combining 0° and 90° with 45° or 135° positions—the right column of Eqs. (2.48)—one is sensitive to circular polarization ($\bar{s}_3$) and the phase shift δ_1 of the first polarizer. For ideal detectors, the phase shift δ_2 of the analyzer has no influence on the measured intensities.

KRS-5 polarizer imperfections $\cos 2\vartheta$ and $|\sin\delta|$ as well as the normalized Stokes parameters $\bar{s}_1/\bar{s}_0$, $\bar{s}_2/\bar{s}_0$, and $|\bar{s}_3/\bar{s}_0|$ measured in a custom-built infrared ellipsometer are shown in Fig. 2.9. The ellipsometer was attached to a Bruker IFS55 FT-IR spectrometer. Between $400\,\mathrm{cm}^{-1}$ and $2000\,\mathrm{cm}^{-1}$, the degree of polarization $\cos 2\vartheta$ is larger than 99%. The relative phase shift δ between transmitted and attenuated component is approximately 90°, in agreement with measurements by den Boer et al. [118]. The Stokes parameters were normalized to the total intensity $\bar{s}_0$. Their magnitude therefore shows their relative importance in future correction formulae. $\bar{s}_3/\bar{s}_0$ is de facto zero, which is not unexpected since there are no elliptically polarizing elements inside the interferometer. $\bar{s}_2/\bar{s}_0$ is almost negligible, whereas

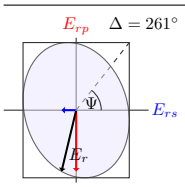

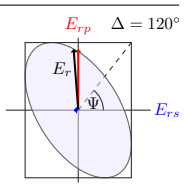

$\bar{s}_1/\bar{s}_0$ is definitely non-negligible. Depending on the sample, $\bar{s}_2/\bar{s}_0$ plays an important role for the correct measurement of Δ.

When comparing the polarizer parameters with the Stokes parameters, one finds a slight spectral interdependence; the phase shift δ, for example, exhibits a steep drop at about $900\,\mathrm{cm}^{-1}$ where $\bar{s}_1/\bar{s}_0$ has a zero-crossing. This is, to some extent, unphysical, since interferometer and polarizers are separate optical elements. However, it hints at small—but negligible—oversimplifications of the used Müller matrix model. Typical possible reasons are non-uniform illumination of the polarizers, stress-induced birefringence of the detector window, the wedge-shaped geometry of the wire-grid polarizers, multiple reflections within the polarizers, or polarizer-stress due to the mounting mechanism [3]. In principle, these effects are readily implementable into the calculations by including the appropriate Müller matrices [6, 89, 124]. Calibration becomes more complicated, though, because the number of imperfection parameters exceeds the number of empty-channel intensity equations at 4×4 azimuth combinations. While it is, of course, possible to measure at additional different combinations, one must bear in mind that the signal-to-noise ratio in the final tan Ψ and Δ spectra will suffer with an increasing number of free imperfection parameters that are to be determined by calibration. Hence, accuracy has to be balanced against precision, given a certain S/N ratio. One might circumvent this problem by using a sample with known optical properties as a calibration standard.

A method to reduce the propagation of polarizer imperfections into the ellipsometric parameters is using tandem wire-grid polarizers [125], at the expense of intensity though. With two polarizers in sequence and aligned axes of maximum transmission, the degree of polarization $\cos 2\vartheta$ improves according to the better attenuation, $\tan\vartheta_{\mathrm{single}} \approx 0.01 \rightarrow (\tan\vartheta_{\mathrm{tandem}})^2 \approx 0.0001$. Since $c_i = \cos 2\vartheta_i \rightarrow 1$ and $s_i = \sin 2\vartheta_i \rightarrow 0$, Eqs. (2.31)–(2.48) for the measured detector intensities simplify significantly. As a consequence, correction formulae for tan Ψ and Δ become much more convenient, as is shown in Appendix B.

2. tan Ψ from parallel-polarizer measurements *without* retarder:
From the ratios of sample to empty-channel intensities at 0°/0° and 90°/90° polarizer/analyzer positions, it follows that

$$(\tan\Psi_{\mathrm{uncorr.}})^2 \equiv \frac{\mathcal{I}(\,\mathbb{I}\,,\,\mathbb{I}\,)\,/\,\mathcal{E}(\,\mathbb{I}\,,\,\mathbb{I}\,)}{\mathcal{I}(\,\mathbb{=}\,,\,\mathbb{=}\,)\,/\,\mathcal{E}(\,\mathbb{=}\,,\,\mathbb{=}\,)} = \frac{1-\cos 2\Psi\cdot E_+}{1+\cos 2\Psi\cdot E_-}\,, \qquad E_\pm = \pm\frac{\frac{\bar{s}_1}{\bar{s}_0}\,(1+c_1c_2)\pm(c_1+c_2)}{(1+c_1c_2)\pm\frac{\bar{s}_1}{\bar{s}_0}\,(c_1+c_2)}\,. \tag{2.49}$$

For ideal polarizers, $\vartheta_1 = \vartheta_2 = 0$, i. e., $c_1 = c_2 = 1$ and $E_\pm = 1$. Thus, one directly measures $|r_p|$ and $|r_s|$, even in the presence of source or interferometer polarization. Equation (2.49)

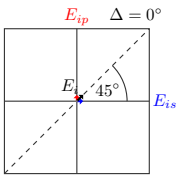

simplifies to

$$\tan\Psi_{\text{ideal}} = \frac{|r_p|}{|r_s|} = \sqrt{\left.\frac{\mathcal{I}(\,\square\,,\,\square\,)\,/\,\mathcal{E}(\,\square\,,\,\square\,)}{\mathcal{I}(\,\square\,,\,\square\,)\,/\,\mathcal{E}(\,\square\,,\,\square\,)}\right|_{\vartheta_1=\vartheta_2=0}}\,. \tag{2.50}$$

In the case of imperfect polarizers, i. e., $c_1, c_2 < 1$, a correction formula for $\tan\Psi$ is obtained from Eq. (2.49) by solving for $\cos 2\Psi$:

$$\tan\Psi_{\text{corr.}} = \sqrt{\frac{1-\cos 2\Psi}{1+\cos 2\Psi}}\,, \quad \cos 2\Psi = \frac{1-(\tan\Psi_{\text{uncorr.}})^2}{E_+ + E_-\,(\tan\Psi_{\text{uncorr.}})^2} \tag{2.51}$$

At small wavenumbers, typically $< 2000\,\text{cm}^{-1}$, mid-infrared polarizers exhibit $\cos 2\vartheta_i \approx 1$, for which $E_\pm \to 1$ in Eq. (2.49). At higher wavenumbers, on the other hand, the degree of polarization usually drops down—for example, to approximately 0.9 for KRS-5 polarizers (see Fig. 2.9)—and thus, a correction of $\tan\Psi$ after Eq. (2.51) becomes necessary.

3. $\tan\Psi$ from parallel-polarizer measurements *with* retarder:
For various reasons like stability of the set-up or quickness of spectra acquisition in in-situ measurements, it is often desirable to skip the measurements without retarder and measure solely with retarder in the optical train. Similar to the previous case without retarder, the corresponding intensity ratios read

$$\overline{\mathcal{I}} \equiv \frac{\widetilde{\mathcal{I}}(\,\square\,,\,\square\,)\,/\,\mathcal{E}(\,\square\,,\,\square\,)}{\widetilde{\mathcal{I}}(\,\square\,,\,\square\,)\,/\,\mathcal{E}(\,\square\,,\,\square\,)} = \frac{(1+\cos 2\Psi\cos 2\psi_{\text{Ret}}) - (\cos 2\Psi + \cos 2\psi_{\text{Ret}})\cdot E_+}{(1+\cos 2\Psi\cos 2\psi_{\text{Ret}}) + (\cos 2\Psi + \cos 2\psi_{\text{Ret}})\cdot E_-}\,. \tag{2.52}$$

Again for ideal polarizers, one obtains

$$\left.\frac{\widetilde{\mathcal{I}}(\,\square\,,\,\square\,)\,/\,\mathcal{E}(\,\square\,,\,\square\,)}{\widetilde{\mathcal{I}}(\,\square\,,\,\square\,)\,/\,\mathcal{E}(\,\square\,,\,\square\,)}\right|_{\vartheta_1=\vartheta_2=0} = \frac{(1-\cos 2\Psi)\,(1-\cos 2\psi_{\text{Ret}})}{(1+\cos 2\Psi)\,(1+\cos 2\psi_{\text{Ret}})} = (\tan\Psi)^2\cdot(\tan\psi_{\text{Ret}})^2\,. \tag{2.53}$$

Solving Eq. (2.52) for $\tan\Psi$ yields an appropriate correction formula for imperfect polarizers:

$$\tan\Psi_{\text{corr.}} = \sqrt{\frac{1-\cos 2\Psi}{1+\cos 2\Psi}}\,, \quad \cos 2\Psi = \frac{1-\overline{\mathcal{I}}-\cos 2\psi_{\text{Ret}}(E_+ + E_-)}{E_+ + \overline{\mathcal{I}}E_- + \cos 2\psi_{\text{Ret}}\big(1-\overline{\mathcal{I}}\big)} \tag{2.54}$$

Before applying this formula, $\cos 2\psi_{\text{Ret}}$ has to be determined from calibration measurements $\mathcal{R}(\alpha_1,\alpha_2)$ with retarder, that is, by Eqs. (2.49) and (2.51) with $\mathcal{I}(\alpha_1,\alpha_2) \to \mathcal{R}(\alpha_1,\alpha_2)$ and $\Psi \to \psi_{\text{Ret}}$.

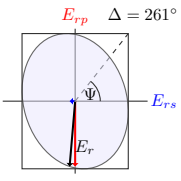

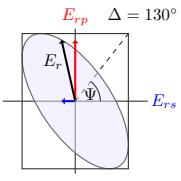

4. cos Δ and sin Δ from 45° and 135° measurements:
Measuring at polarizer combinations of 45° and 135° allows one to determine cos Δ, or equivalently, $0° \leq \Delta \leq 180°$:

$$\frac{\mathcal{I}(\diagdown,\diagdown)-\mathcal{I}(\diagup,\diagdown)}{\mathcal{I}(\diagdown,\diagdown)+\mathcal{I}(\diagup,\diagdown)} = \frac{c_1\left[\frac{\bar{s}_2}{\bar{s}_0} - \sin 2\Psi\cos\Delta\, c_2\right] + s_1\sin\delta_1\left[\frac{\bar{s}_3}{\bar{s}_0}\cos 2\Psi - \frac{\bar{s}_1}{\bar{s}_0}\sin 2\Psi\sqrt{1-\cos^2\Delta}\, c_2\right]}{-1+\frac{\bar{s}_2}{\bar{s}_0}\sin 2\Psi\cos\Delta\, c_2 + s_1\cos\delta_1\left[\frac{\bar{s}_1}{\bar{s}_0}\cos 2\Psi + \frac{\bar{s}_3}{\bar{s}_0}\sin 2\Psi\sqrt{1-\cos^2\Delta}\, c_2\right]} \tag{2.55}$$

With the known imperfection and Stokes parameters from calibration as well as tan Ψ from 0°/0° and 90°/90° measurements, Eq. (2.55) can be solved for cos Δ. Correction parameters of very small absolute values can be neglected in correction formulae. For infrared ellipsometers used in this work, this concerns terms proportional to $\bar{s}_3/\bar{s}_0$ and $s_1\cos\delta_1$. Equation (2.55) then simplifies to

$$\frac{\mathcal{I}(\diagdown,\diagdown)-\mathcal{I}(\diagup,\diagdown)}{\mathcal{I}(\diagdown,\diagdown)+\mathcal{I}(\diagup,\diagdown)} \approx \frac{c_1\left[\frac{\bar{s}_2}{\bar{s}_0} - \sin 2\Psi\cos\Delta\, c_2\right] - \frac{\bar{s}_1}{\bar{s}_0}\sin 2\Psi\sqrt{1-\cos^2\Delta}\, s_1 c_2\sin\delta_1}{-1+\frac{\bar{s}_2}{\bar{s}_0}\sin 2\Psi\cos\Delta\, c_2}\,, \tag{2.56}$$

which yields a quadratic equation in cos Δ. To unambiguously quantify Δ in the full range between $0° \leq \Delta < 360°$, cos Δ *and* sin Δ must be known. This requires additional measurements with retarder. With $\frac{\tilde{\mathcal{I}}(\diagdown,\diagdown)-\tilde{\mathcal{I}}(\diagup,\diagdown)}{\tilde{\mathcal{I}}(\diagdown,\diagdown)+\tilde{\mathcal{I}}(\diagup,\diagdown)}$ according to Eq. (2.40), one measures the phase $\cos(\Delta+\delta_{\mathrm{Ret}})$. Using the retarder phase shift δ_{Ret} as determined from calibration, sin Δ is then calculated with the help of the addition theorem

$$\sin\Delta = \frac{\cos\Delta\cos\delta_{\mathrm{Ret}} - \cos(\Delta+\delta_{\mathrm{Ret}})}{\sin\delta_{\mathrm{Ret}}}\,. \tag{2.57}$$

Measurements with retarder are also necessary if $|\cos\Delta| \approx \pm 1$, because small errors in cos Δ then propagate into large errors in Δ.

As discussed in Section 2.1.3.a), the complete set of ellipsometer-independent ellipsometric parameters tan Ψ, cos Δ, and sin Δ—calculated from Eqs. (2.51)/(2.54), (2.56), and (2.57)—finally enables one to determine the sample's degree of polarization

$$P = \sqrt{\langle\cos 2\Psi\rangle^2 + \langle\sin 2\Psi\rangle^2\,\left(\langle\cos\Delta\rangle^2 + \langle\sin\Delta\rangle^2\right)} \tag{2.58}$$

as well as degree of phase polarization

$$P_{\mathrm{ph}} = \sqrt{\langle\cos\Delta\rangle^2 + \langle\sin\Delta\rangle^2}\,, \tag{2.59}$$

which, for unknown samples, are crucial quantities for assessing the quality of the measurement [1, 116].

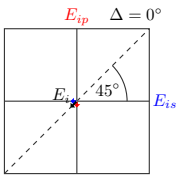

5. Rotating polarizer and rotating analyzer:
In contrast to tan Ψ, the ellipsometric phase Δ must be determined from measurements with at least one non-parallel polarizer combination. If the detector, however, exhibits polarization-dependent properties, it is advantageous to measure both tan Ψ and Δ with a fixed analyzer, commonly set to 45° or 135°, and a rotating polarizer at different positions. For strong or varying source polarization, on the other hand, the polarizer is held fixed at 45°, while the analyzer is being rotated. This measuring mode is important, for example, for measurements at a synchrotron (BESSY II), where the beam properties vary with time and usually show direction-dependent pre-polarization [126–128].

Equations for rotating polarizer and rotating analyzer set-ups are given in Appendix B.

c) Correction procedure for in-situ spectra

Probing the sample through the backside of a silicon wedge is a very elegant method from a methodological point of view. Quantitative interpretation of measured in-situ spectra requires special care, though. Two kinds of measurements have to be distinguished. The first are in-situ experiments performed on a single sample. Recorded tan Ψ spectra are then analyzed with respect to the initial sample conditions, $\tan\Psi/\tan\Psi_{\text{initial}}$. This method of *self-referencing* automatically takes care of systematic errors like sample misalignment or beam divergence. Protein adsorption on PAA brushes in dependence of pH, for instance, is studied in this way (see Section 3.6.4.). The second kind are measurements that have to be repeated on two different samples. This concerns, for example, temperature-dependent experiments on PNIPAAm brushes (see Section 3.5.), where a separate reference substrate without brush is measured ($\tan\Psi_{\text{ref}}$) to compensate for the T-dependent bulk-water contributions that would otherwise mask the much smaller spectral signatures of the brush [25]. A quantitative evaluation of in-situ spectra obtained with this method is not straightforward, since small differences in the optical paths as well as different tensions of the substrates due to the metal-frame mounting mechanism cause baseline distortions in $\tan\Psi/\tan\Psi_{\text{ref}}$.

In order to remove these distortions, both brush and reference sample are also measured in dry state within the in-situ cell before performing the actual in-situ measurements. The ratio $\tan\Psi_{\text{dry}}/\tan\Psi_{\text{ref, dry}}$ is then used for baseline compensation. Since the dry-state sample spectrum also contains contributions from the film-side of the substrate, $\tan\Psi_{\text{dry}}$ is first interpolated between the non-absorbing regions of the film. This approach works very well for films with dry-state thicknesses below ≈ 20 nm. For thicker films, effects from thin-film interference [129] become non-negligible. These effects are accounted for by simulating the corresponding ratio $\tan\Psi^{\text{simul}}_{\text{dry}}/\tan\Psi^{\text{simul}}_{\text{ref, dry}}$ in an appropriate optical model (see Section 2.3.) and multiplying the result with the dry-state-corrected spectra. The correction formula, then, reads $\tan\Psi/\tan\Psi_{\text{ref}} \rightarrow (\tan\Psi/\tan\Psi_{\text{ref}})/(\tan\Psi_{\text{dry}}/\tan\Psi_{\text{ref, dry}}) \cdot (\tan\Psi^{\text{simul}}_{\text{dry}}/\tan\Psi^{\text{simul}}_{\text{ref, dry}})$.

Phase differences $\Delta - \Delta_{\text{ref}}$ are corrected similarly by substituting "$/ \rightarrow -$" and "$\cdot \rightarrow +$".

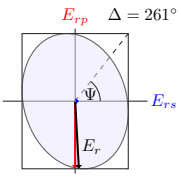

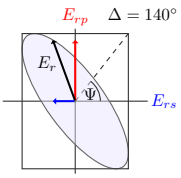

2.2. Complementary methods

This section presents three experimental methods, namely infrared microscopy, infrared transmission spectroscopy, and atomic force microscopy, that were used for complementary qualitative and quantitative measurements.

2.2.1. Infrared microscopy

Compared to standard laboratory ellipsometers, infrared microscopes usually offer higher lateral resolution down to a few 10 µm, which is very useful for characterizing sample homogeneity and thickness. Another appealing aspect is the capability to quickly switch between different types of objectives with different beneficial properties, for example, a Cassegrain objective [105, 130, 131] employed in standard reflection or transmission mode, a grazing-incidence objective [130, 131] for higher sensitivity with respect to thin films on metal substrates, or an ATR objective [131, 132] that is helpful for samples with low reflectivity or transmittance and for achieving higher lateral resolution. Also the wide variety of commercially available easy-to-use sample stages render infrared microscopy a very attractive experimental method.

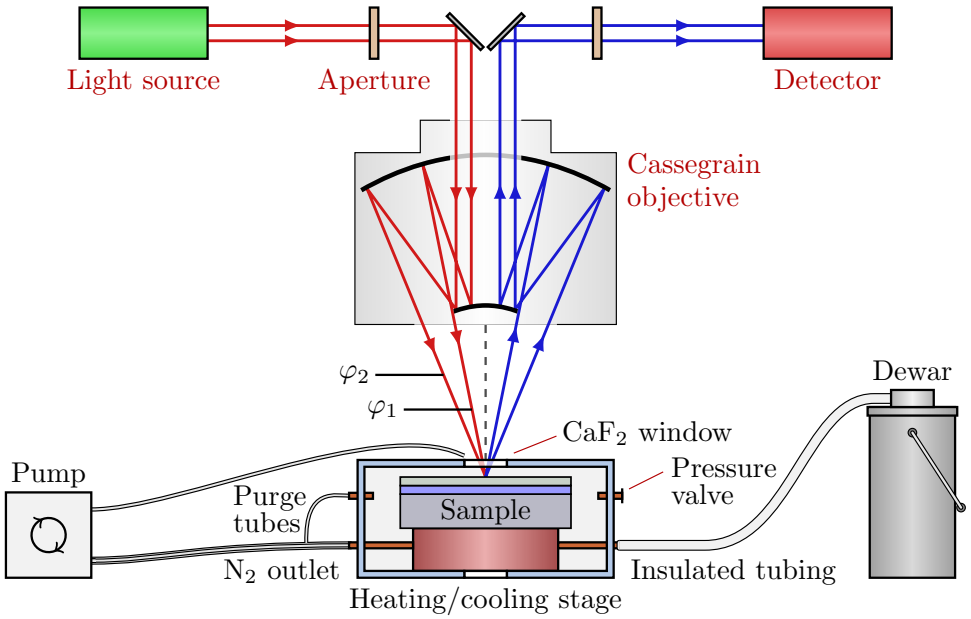

Figure 2.10: Schematic of the infrared-microscopy set-up for temperature-dependent reflection measurements.

Figure 2.10 displays the optical train in a Bruker Hyperion 3000 FT-IR microscope with Cassegrain objective (15x, numerical aperture = 0.4) that was used in this work. The microscope is externally attached to a Bruker Vertex 70 FT-IR spectrometer and uses a photovoltaic MCT detector. The small active detector area and two knife-edge apertures in front

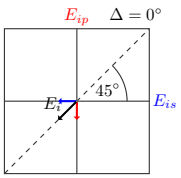

of objective and detector restrict the lateral resolution to values below $160 \times 160\,\mu m^2$. The Cassegrain objective comprises two parabolic mirrors that define a range of incidence angles between $\varphi_1 = 9.8°$ and $\varphi_2 = 23.6°$. Influences of water vapor and CO_2 on the measurements are reduced by dry-air purging of spectrometer and microscope, the latter of which is enclosed within a sealed plexiglas chamber to maintain constant atmospheric conditions.

Optionally, the sample can be mounted on a heating/cooling stage for temperature-sensitive measurements (THMS600 + LNP95, Linkam Scientific Instruments, Surrey, England). The Pt1000-controlled silver heating stage reaches temperatures of up to 600 °C with a temperature stability of ±0.1 °C without overshoots. Additional connections to a reservoir of liquid nitrogen also enable low-temperature measurements down to −196 °C. The exhaust dry nitrogen is recycled through a pumping system in order to purge the sample chamber, to avoid condensation at the CaF_2 window, and to keep the tubing flexible. Purging is crucial because water vapor shows a highly temperature-sensitive infrared absorption signature that is difficult to remove from the final spectra.

Some measurements were intentionally performed under changing atmospheric conditions (see Section 3.1.5.). If necessary, reflectivity spectra were corrected for water-vapor and CO_2 absorption using the correction algorithm provided by the OPUS spectroscopy software (Bruker, Leipzig, Germany). Possible correction artifacts need to be evaluated carefully.

Thin-layer samples are usually measured in reflection, but standard transmission measurements are also possible through a small tapered hole in the heating stage. In general, relative reflectivity spectra with respect to a reference surface are obtained with the reference sample placed on the same mapping stage. Measurements on wedge-shaped samples are performed on a modified mapping table that compensates for the wedge angle. Importantly for infrared-transparent substrates, the table has a small recess below the sample in order to prevent backside reflections from an otherwise present wedge/table interface, which would arise due to the small incidence angles of the Cassegrain objective.

A grazing-incidence objective (Bruker, Leipzig, Germany), shown in Fig. 2.11, is beneficial for measurements of polymer films on gold substrates owing to the higher film sensitivity at larger incidence angles [130, 131]. The optical train of the objective [133] is similar to the standard Cassegrain objective in Fig. 2.10, except for three additional mirrors that cause the light beam to be reflected twice off the sample surface under much higher incidence angles. This double reflection increases the sensitivity by a factor of about 2.

Infrared microscopy can also be upgraded to full polarization-dependent ellipsometric infrared microscopy [134, 135]. For this purpose, a polarizer is placed before the objective, and an analyzer is placed before the detector. The otherwise ill-defined optical plane is established by inserting an optical-plane-aperture (a circular disc with a centered slit) into the standard thread of the Cassegrain objective. Also, a retarder may be placed in front of the analyzer for higher phase sensitivity.

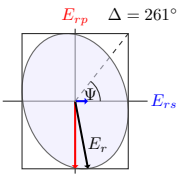

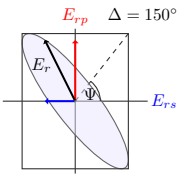

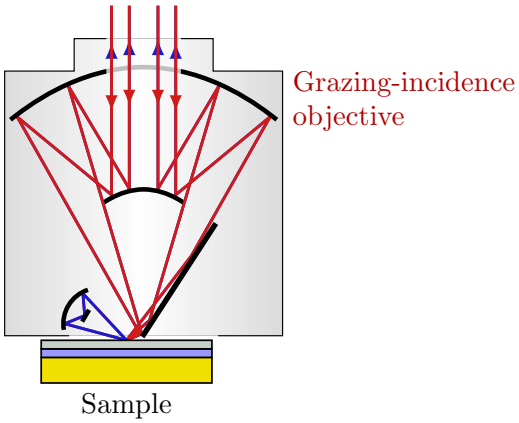

Figure 2.11: Schematic of the grazing-incidence objective for high-sensitivity infrared-microscopy measurements of thin films on gold substrate. The geometry of microscope and objective is such that incident and reflected light beams illuminate the front and back hemisphere, respectively.

Among others, applications of quantitative ellipsometric infrared microscopy cover thickness maps of thin films, the determination of in-plane and out-of-plane properties of nanometer-thin silicon-oxide films, laterally resolved mobility studies of thin conducting films that exhibit plasmon resonances in the mid-infrared, as well as measurements of tilt-angle variations in ordered organic films.

Optical simulations:
In order to quantitatively evaluate reflectivity spectra obtained from infrared microscopy, some parts of the optical-modeling process had to be adjusted. A spin-coated PNIPAAm film (on gold substrate) with known optical properties (see Section 3.1.4.) served as a reference sample. It was measured with both the Cassegrain objective and the grazing-incidence objective. For the Cassegrain objective, measured spectra were successfully reproduced by averaging forward-simulated spectra under several incidence angles between φ_1 and φ_2. Alternatively, simulations at the mean incidence angle of about 16° resulted in almost identical spectra.

Modeling grazing-incidence spectra is more involved due to the double reflection and the asymmetrical range of incidence angles. Nanometer-thin polymer films on gold have a reflectivity close to 1. The double reflection of the objective can therefore be approximated by a factor of 2 in reflectivity band amplitudes. For polymers used in this work, this approximation holds for thicknesses up to about 200 nm. Observed band amplitudes are strongly dependent on the incidence angle as well as the wavenumber positions of the vibrational bands. This allows one to estimate the objective's range of incidence angles. Unlike for the Cassegrain objective, the angle distribution is asymmetrical, and presumably not every angle is weighed the same. It is, thus, not sufficient to use a mean incidence angle. It turns out that simulations of averaged spectra between $\varphi_0 = 54°$ and 72° agree very well with measured spectra.

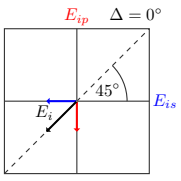

2.2.2. Infrared transmission spectroscopy

Infrared ellipsometry is very sensitive to the refractive index n and to large extinction coefficients k of the measured material. Owing to the limited precision of Δ measurements, however, it is rather insensitive to small k values, typically to $k \lesssim 0.01$, depending on sample thickness and measuring conditions. In this case, transmission measurements are a preferable complementary method.

In principle, ellipsometry can also be performed in transmission mode, and the sample properties can be evaluated with standard optical models. Indeed, this approach is used in this work to determine the extinction coefficient of infrared-transparent silicon substrates and wedges. When it comes to measuring k of water or other liquids, unpolarized transmission is usually favourable due to the low penetration depth of infrared radiation and the consequently low signal-to-noise ratio. In the stretching and bending regions of water, infrared radiation is totally absorbed in water after a path length of approximately 6–20 µm. Nevertheless, special transmission cells with window spacings in the micrometer range still enable an accurate determination of k.

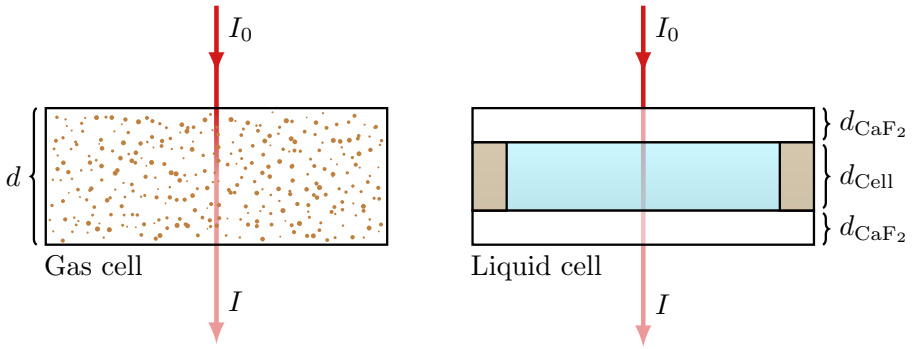

Figure 2.12: Schematic of transmission cells for gases and liquids.

The extinction coefficient k is measured according to Lambert–Beer's law [136, 137], as visualized in Fig. 2.12. If light of an initial intensity I_0 travels through a medium over a certain distance d, then the absorption coefficient α of this medium is related to the final intensity I by the negative-exponential dependence

$$\overline{T} = \frac{I}{I_0} = \mathrm{e}^{-\alpha \cdot d}. \tag{2.60}$$

The wavenumber-dependent $k(\tilde{\nu})$, then, is given by $\alpha = 4\pi\,\tilde{\nu}\,k$. Instead of the transmittance $\overline{T}$, the absorbance $A = -\ln \overline{T}$ is often a more convenient representation for liquids with large k values. Note that absorbance is sometimes defined with a logarithmic base of 10 instead of e, which leads to differently scaled absorption coefficients by a factor of $\ln 10$.

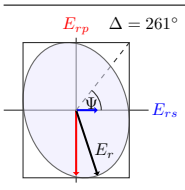

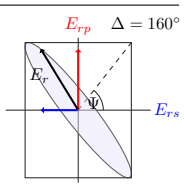

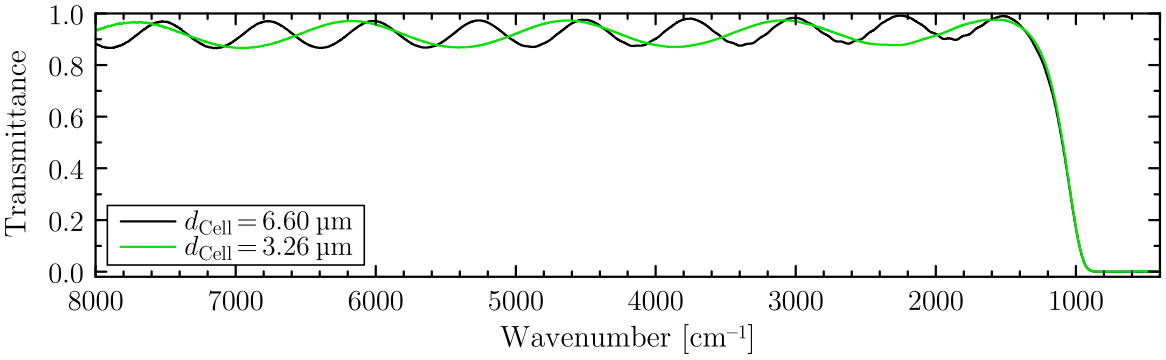

Figure 2.13: Measured transmittances of two empty transmission cells with different path lengths d_{Cell}.

When dealing with gases, the respective transmission cells, as shown in Fig. 2.12, usually have a large path length d of some millimeters. Optical effects due to the window spacing play only a minor role in the determination of k. For liquids, and especially for water, however, the windows have to be separated by only a few micrometers, resulting in multiple reflections that cause interference fringes in the mid-infrared. Figure 2.13 shows measured transmittances of two empty cells with different path lengths d_{Cell}. The path lengths can be estimated by the fringe method [138], that is, by counting the number of complete interference fringes between two wavenumbers $\tilde{\nu}_1$ and $\tilde{\nu}_2$ in the transmittance spectra:

$$d_{\mathrm{Cell}} = \frac{\#\mathrm{Fringes}}{2n(\tilde{\nu}_2 - \tilde{\nu}_1)} \tag{2.61}$$

Here, n denotes the refractive index of the cell content, which is equal to 1 for air. Interference fringes are damped if the cell is filled with a liquid, but they are still non-negligible in regions of small absorption.

Several procedures exist in the literature to deal with these fringes in order to extract the true values of $k(\tilde{\nu})$ of the liquid. These methods range from naïve averaging of the data to deconvolution techniques that damp the fringes by removing the corresponding frequency in Fourier space [139]. More elaborate methods include the actual cell and window geometry—also considering non-parallel windows—and then calculate a generalized relation between $\overline{T}$ and k based on the optical path in this extended optical model [140].

A simpler method is to use a window material with a refractive index similar to the one of the liquid under investigation. The transmission coefficients at the window/cell interfaces, then, are close to 1, and multiple reflections are largely suppressed. In the mid-infrared region, the refractive index of water varies around $n \approx 1.33$. A suitable window material for investigations of aqueous solutions, therefore, is calcium flouride (CaF_2) [141] with $n_{CaF_2} \approx 1.30 \ldots 1.42$ between 1000–4000 cm^{-1} [142]. CaF_2 reduces interference fringes significantly, but does not eliminate them completely in regions of small absorption. For

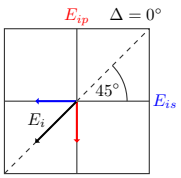

this reason, transmission spectra were simulated in an optical layer model consisting of Air/Window/Liquid/Window/Air using the Abelès method (see Appendix C.). This automatically accounts for multiple reflections within the transmission cell and allows one to access k (and n) of the liquid. Details on the modeling process are given in Section 3.4.

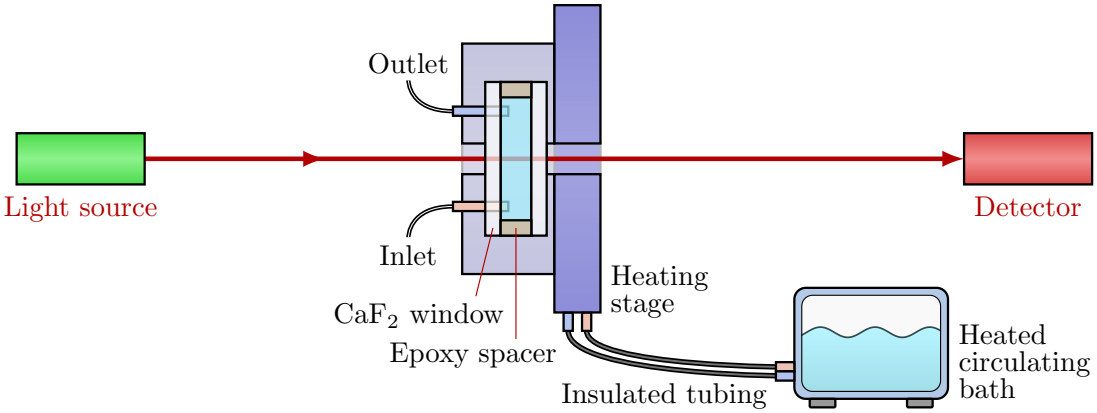

Figure 2.14: Schematic of the transmission set-up for temperature-dependent measurements of liquids.

Figure 2.14 shows the transmission set-up used in this work to measure the temperature-dependent extinction coefficients of water and heavy water as well as the pH-dependent properties of human serum albumin solved in water. The *AquaSpec* transmission cells [143] (micro-biolytics GmbH, Esslingen am Neckar, Germany) consist of two 4 mm thick CaF_2 windows separated by an epoxy spacer ($d_{\mathrm{Cell}} = 6.6\,\mu\mathrm{m}$ or $3.2\,\mu\mathrm{m}$). A syringe connected to an injection port allows for a quick exchange of the cell content. The inner cell itself is enclosed by a stainless-steel cylinder in contact with a heating stage that is temperature-controlled by a heated circulating bath. For reference measurements of I_0, the cylinder is replaced by a steel cylinder of the same geometry, but without the actual transmission cell [144]. The whole cell is placed inside the internal compartment of a Bruker Vertex 70 FT-IR spectrometer. Intensity spectra were measured with a DTGS detector at $4\,\mathrm{cm}^{-1}$ resolution.

2.2.3. Atomic force microscopy

An essential pre-characterization method for sample quality and film homogeneity is atomic force microscopy. Its basic measuring concept is depicted in Fig. 2.15, which shows a schematic of an XE-100 atomic force microscope (Park Systems Corp., Suwon, Korea) used in this work.

The sample is mounted on a two-dimensional mapping table that is controlled by piezo motors in x and y direction. In a totally decoupled piezo-driven z stage, a cantilever with a sharp tip is then used to measure the surface topography of the sample upon scanning along x and y based on the changing interaction forces between cantilever and sample surface.

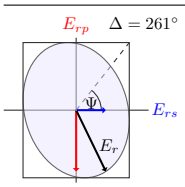

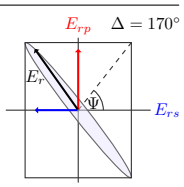

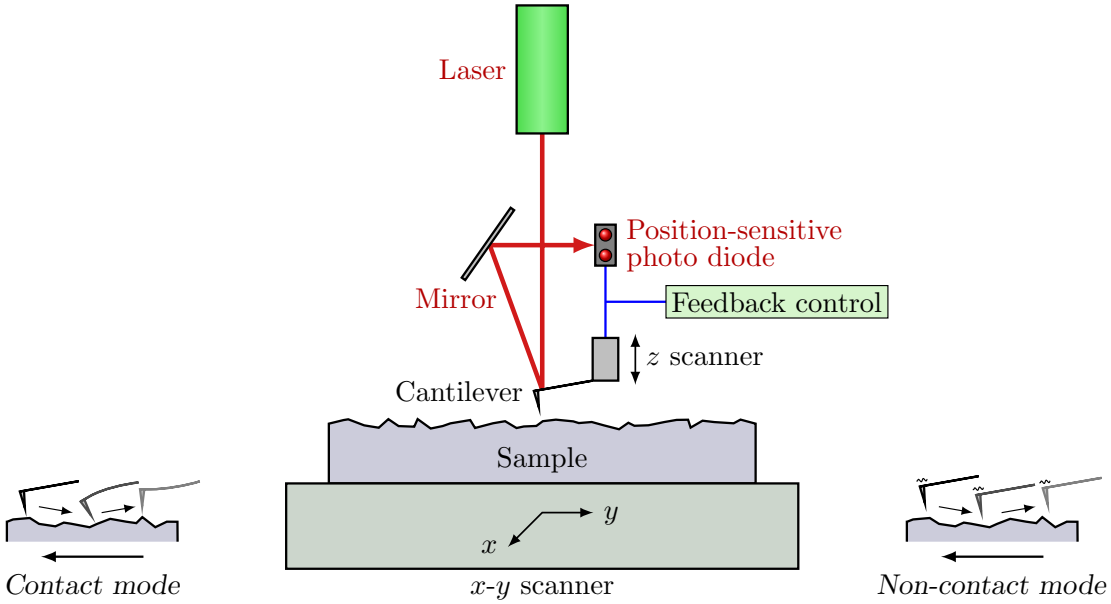

Figure 2.15: Schematic of the atomic force microscope used for surface-topography measurements.

Two measuring modes have to be distinguished. In so-called *contact mode*, a bendable cantilever is positioned closely to the sample surface. Its tip position is monitored with a position-sensitive photo diode that detects a reflected laser beam. If the interaction forces change due to changes in the sample's height profile, the cantilever will bend either towards the surface or away from it. This deflection is measured at the photo diode, and, consequently, a feedback control is adjusting the vertical position of the z scanner, aiming for a constant force between tip and surface. The surface topography is then derived from the current x, y, and z positions. A drawback of contact mode is tip wearout that occurs on samples with large height differences over small lateral distances.

Non-contact mode makes use of a piezoelectric bimorph that vibrates a stiff cantilever near its intrinsic resonance frequency with an amplitude of a few nanometers. Changes in *van der Waals* forces between tip and sample surface are measured via shifts in amplitude or frequency of the resonance. By adjusting the tip-to-sample distance at the z stage, a feedback loop compensates for these changes to maintain a constant amplitude. Again, the current x, y, and z positions yield the surface topography of the sample.

Although contact mode offers high scanning speed and atomic resolution, non-contact mode is the preferred method for soft and biological samples [145], because even for thin adsorbed fluid layers, the distance between tip and sample surface remains constant, which reduces tip wearout and sample damage. Non-contact mode is also less prone to image distortions. For these reasons, all measurements were performed in non-contact mode.

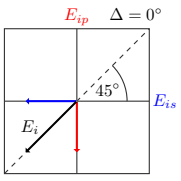

2.3. Data analysis

Ellipsometry is an indirect method. Except for a few simple cases, the ellipsometric parameters $\tan\Psi$ and Δ cannot be related to physical sample properties in a closed analytical form. These properties have to be extracted with the help of optical-model simulations [6, 8]. The standard procedure is to calculate $\tan\Psi$ and Δ based on the model using sample parameters like layer thicknesses and dielectric functions as input parameters. In an iterative best-fit routine, these parameters are then varied—and thereby determined—until measured and simulated spectra match within the uncertainties of the experiment.

Since optical models are based on the dielectric function $\varepsilon(\tilde{\nu})$ of the sample, this section at first overviews the origins of $\varepsilon(\tilde{\nu})$, its relation to the refractive index, as well as the interdependence of its real and imaginary part via Kramers–Kronig relations. Then, different models of dielectric functions are presented, and optical layer models used in this work are introduced. Finally, details on the fitting process as well as on error estimation are given.

2.3.1. Dispersion models of dielectric functions

Before going into details about models of dielectric functions $\varepsilon(\tilde{\nu})$, it is helpful to establish the physical context in which ε appears. The dielectric function or *dielectric constant* arises from the Maxwell equations of electrodynamics in the presence of a macroscopic continuous medium. ε connects the dielectric displacement $\vec{D}$ with the macroscopic electric-field strength $\vec{E}$ [146, 147]:

$$\begin{aligned}\vec{D}(\tilde{\nu}) &= \varepsilon_0 \vec{E}(\tilde{\nu}) + \vec{P}(\tilde{\nu}) \\ &= \varepsilon_0 \left[1 + \chi_\mathrm{e}(\tilde{\nu})\right] \vec{E}(\tilde{\nu}) \\ &= \varepsilon_0 \, \varepsilon(\tilde{\nu}) \, \vec{E}(\tilde{\nu})\end{aligned} \tag{2.62}$$

Here, ε_0 is the vacuum permittivity, and $\chi_\mathrm{e}(\tilde{\nu})$ denotes the electric susceptibility of the material. $\vec{P}$ is the macroscopic polarization density or electric-dipole density of the dielectric material,

$$\vec{P}(\tilde{\nu}) = N_p \left\langle \vec{p}(\tilde{\nu}) \right\rangle , \tag{2.63}$$

with N_p being the average number of dipole moments $\vec{p}$ per unit volume. In the linear-optics approximation [146, 147], higher-order multipole moments in $\vec{P}$ are usually negligible.

Solving Maxwell's wave equations results in transversal plane waves. For isotropic materials at space-time coordinates (r, t), one finds

$$E(r,t) = E_0 \cdot \mathrm{e}^{i\omega(t - \frac{n}{c}r + \delta)} \mathrm{e}^{-\omega \frac{k}{c} r} = E_0 \cdot \mathrm{e}^{i\omega(t - \frac{N}{c}r + \delta)} , \tag{2.64}$$

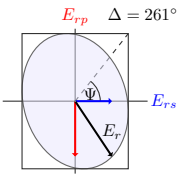

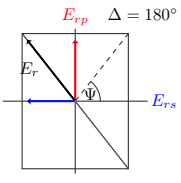

with the vacuum speed of light c, the angular frequency ω (related to the optical frequency f by $f = \omega/2\pi$), the phase δ, and the complex refractive index $N = n - ik$, which comprises the real refractive index n as well as the extinction coefficient k. In the literature, the wavenumber-dependent $n(\tilde{\nu})$ and $k(\tilde{\nu})$ are often also referred to as the *optical constants* of the material.

The dielectric function $\varepsilon(\tilde{\nu})$ is related to the complex refractive index by

$$\varepsilon = \varepsilon_1 - i\varepsilon_2 = N^2 = (n - ik)^2 = n^2 - k^2 - 2ink\,. \tag{2.65}$$

From this equation, the following useful conversion formulae are found:

$$\varepsilon_1 = n^2 - k^2, \qquad \varepsilon_2 = 2nk \tag{2.66}$$

$$n = \left[\frac{1}{2}\left(\sqrt{\varepsilon_1^2 + \varepsilon_2^2} + \varepsilon_1\right)\right]^{1/2}, \qquad k = \left[\frac{1}{2}\left(\sqrt{\varepsilon_1^2 + \varepsilon_2^2} - \varepsilon_1\right)\right]^{1/2} \tag{2.67}$$

Note that $\varepsilon(\tilde{\nu})$ and $\chi_\mathrm{e}(\tilde{\nu})$ are scalars for isotropic and second-rank tensors for anisotropic materials.

Real and imaginary part of the dielectric function are *not* independent. They are, in fact, related by Kramers–Kronig (K–K) integral relations [148, 149] based on the principle of causality,

$$\varepsilon_1(\tilde{\nu}) = \varepsilon_\infty + \frac{2}{\pi}\mathcal{P}\int_0^\infty \frac{\xi\,\varepsilon_2(\xi)}{\xi^2 - \tilde{\nu}^2}\,\mathrm{d}\xi\,, \qquad \varepsilon_2(\tilde{\nu}) = -\frac{2\tilde{\nu}}{\pi}\mathcal{P}\int_0^\infty \frac{\varepsilon_1(\xi) - \varepsilon_\infty}{\xi^2 - \tilde{\nu}^2}\,\mathrm{d}\xi\,, \tag{2.68}$$

where $\mathcal{P}$ denotes the Cauchy principal value of the integral. The high-frequency dielectric constant ε_∞ contains all contributions to the dielectric function above a given cut-off frequency $\tilde{\nu}_\infty$. Similar equations hold for p- and s-polarized reflectivity [150] and also for n and k using the replacements $\varepsilon_1 \to n$ and $\varepsilon_2 \to k$. If k is known over the whole spectral range from $0\,\mathrm{cm}^{-1}$ to infinity, then n can be calculated directly using the above K–K relation, and vice versa. In practice, however, measurement resolution is finite, and the optical properties of spectrometer and other elements restrict the feasible spectral limits. Therefore, the integral has to be replaced by a finite sum, whereby K–K conversion becomes potentially problematic. If, though, the energy limits of the sum are far away from regions of strong absorption, then K–K conversion still yields valid results [150, 151]. Since physical models of dielectric functions have to obey the Kramers–Kronig relations, it is, in general, best practice to perform a K–K consistency check in order to test the validity of the applied model.

Figure 2.16 displays the real part ε_1 of a typical polymer dielectric function over a large energy range. Electronic transitions are usually observed in the VIS/UV region, whereas molecular vibrations appear in the infrared spectral range. Effects of orientational polarization as, e. g., libration vibrations of water are found in the THz/microwave range of the

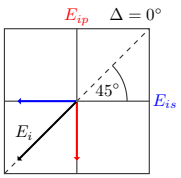

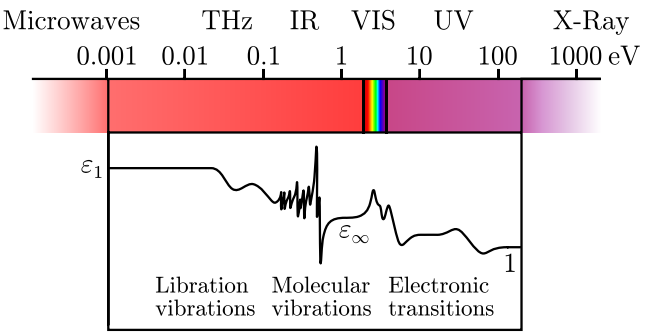

Figure 2.16: Real part ε_1 of a typical polymer dielectric function with electronic transitions in the VIS/UV, molecular vibrations in the infrared, and libration vibrations in the THz/microwave spectral range. The high-frequency dielectric constant ε_∞, arbitrarily set in this example between the infrared and visible range, sums up all contributions to the dielectric function above the said cutoff.

spectrum. At infinitely high frequency, ε_1 approaches unity because the corresponding vibrations or transitions can no longer follow the oscillations of incoming light [8]. In the figure, ε_∞ denotes the high-energy contributions to the dielectric function above the accessible energy range from the viewpoint of infrared-spectroscopic measurements. In simulations of molecular vibrations, ε_∞ is an important quantity for setting the correct baseline in the real part of the dielectric function.

Models of dielectric functions are necessary if the dielectric functions themselves are unknown or if tables of optical constants are likely not to reflect the actual sample properties. Bulk dielectric constants, for instance, are tabulated for many materials but usually differ from the corresponding thin-film dielectric constants [108, 152, 153]. In these cases, or in general for unknown samples, the dielectric functions have to be determined either empirically or by appropriate optical modeling. Empirical models tend to be restricted to a small spectral range and have to be used with caution, since they can produce potentially unphysical dispersion. Physical optical models, on the other hand, characterize the optical properties according to the underlying physics that describe the interaction of electromagnetic radiation with the material.

Constant n and k:
For infrared-transparent silicon substrates, it is often sufficient to approximate the optical properties in the mid-infrared by constant values $n = 3.42$ and $k = 0.00$ [154], especially when modeling in-situ spectra that have to be referenced to some initial spectrum at the beginning of the in-situ experiment or to a reference sample with equivalent substrate. From experience, minor differences in accuracy that would arise from using the true optical constants obtained from separate substrate measurements are in the sub-percent range compared to other spectral features stemming, for example, from an in-situ switching process of a polymer.

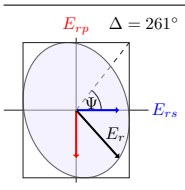

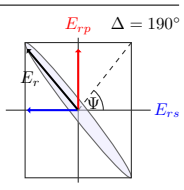

Cauchy dispersion:
Many polymers exhibit regions of negligibly small absorption. Typically, there is a transparent window in the visible spectral range between about 800–400 nm (12500–25000 cm^{-1}) and also in the mid-infrared between 2000–2700 cm^{-1}, depending on the molecular composition of the polymer. In these regions, the refractive index can be modeled according to Cauchy [155] after

$$n(\lambda) = a_0 + \frac{a_2}{\lambda^2} + \frac{a_4}{\lambda^4} - a_{-2} \cdot \lambda^2 \,, \qquad \lambda = \text{wavelength [nm]} \,, \tag{2.69}$$

where the first three terms are due to absorption in the ultraviolet and X-ray regions, while the last term is due to infrared absorption [150]. A similar equation with a different set of coefficients is used to model small absorptions $k(\lambda)$. Note that the Cauchy model does not obey Kramers–Kronig consistency. Cauchy dispersions are used in this work to determine the thicknesses and high-frequency dielectric constants ε_∞ of polymer films and brushes, which is necessary for the quantitative evaluation of infrared-ellipsometric spectra.

Lorentz and Gaussian oscillators:
Electromagnetic radiation $\vec{E}$ can be absorbed by molecules if the radiation excites a vibration that correlates with a change in the molecule's electric dipole moment $\vec{p}$, that is, if the vibration is connected with a non-vanishing transition dipole moment M_{ij} between initial state i and final state j [147, 156],

$$k \propto M_{ij} = |\langle j|\, \vec{E} \cdot \vec{p}\, |i\rangle|^2 \approx |E|^2\, |\langle j|\, \partial p/\partial q\, |i\rangle|^2 \cos^2\theta. \tag{2.70}$$

Here, $\vec{q}$ is the molecular distortion and θ is the angle between $\vec{E}$ and $\vec{p}$. Obviously, absorption of infrared radiation is anisotropic. The distribution of electric dipoles in the material, though, determines the kind of anisotropy (biaxially, uniaxially). In isotropic materials, the electric dipoles are distributed randomly.

The interaction between radiation and molecules is usually derived in analogy to Lorentz' considerations [157, 158] of electrons, bound to fixed nuclei, that constitute an ensemble of harmonic oscillators [146, 147]. Newton's equation of motion of an oscillator exposed to an external time-varying electromagnetic field $\vec{E}(\omega, t) = \vec{E}_0 \cdot \mathrm{e}^{i\omega t}$ with angular frequency $\omega = 2\pi\, c\, \tilde{\nu}$ is given by

$$m^* \left[\frac{\mathrm{d}^2\vec{r}}{\mathrm{d}t^2} + \gamma \frac{\mathrm{d}\vec{r}}{\mathrm{d}t} + \omega_0^2\, \vec{r} \right] = -e^* \vec{E}(\omega, t) \,, \tag{2.71}$$

where the three terms on the left-hand side denote kinetic, damping, and restoring force. $\vec{r}$ is the displacement of the oscillator with respect to its equilibrium position, γ is the damping constant, and e^* and m^* are the effective charge and reduced mass of the dipole, respectively. In the linear-optics approximation, the external field $\vec{E}$ induces an electric dipole moment $\vec{p} = -e^*\, \vec{r}$, and at the same time, the oscillator becomes polarized, that is, $\vec{p} = \hat{\alpha}\, \varepsilon_0\, \vec{E}$, which

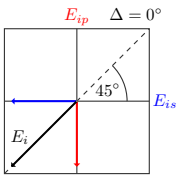

is characterized by the electric polarizability $\hat{\alpha}$. Via Eq. (2.63), this microscopic polarization $\vec{p}$ contributes to the overall electric-dipole density $\vec{P}$ on a macroscopic scale: $\vec{P} = N_p\,\hat{\alpha}\,\varepsilon_0\,\vec{E}$. From Eq. (2.62), one finds the relation $\varepsilon = 1 + N_p\,\hat{\alpha}$, which links the macroscopic dielectric function ε to the microscopic polarizability $\hat{\alpha}$. Integrating Eq. (2.71) and combining the result for the displacement $\vec{r}$ with these equations then yields

$$\varepsilon(\omega) = 1 + \frac{S\,\omega_0^2}{\omega_0^2 - \omega^2 + i\omega\gamma} \quad \text{with} \quad S = \frac{N_p\,e^{*2}}{\varepsilon_0 m^* \omega_0^2}\,. \tag{2.72}$$

Written in wavenumbers, the above equation reads

$$\varepsilon(\tilde{\nu}) = 1 + \frac{F}{\tilde{\nu}_0^2 - \tilde{\nu}^2 + i\tilde{\Gamma}\tilde{\nu}}\,, \tag{2.73}$$

with the reparameterization

$$F = \frac{S\,\omega_0^2}{(2\pi\,c)^2} = S\,\tilde{\nu}_0^2 \qquad \text{and} \qquad \tilde{\Gamma} = \frac{\gamma}{2\pi\,c}\,. \tag{2.74}$$

The dielectric function of a single Lorentz vibration can thereby be characterized by three parameters: the oscillator strength F, the center frequency $\tilde{\nu}_0$, and the dampening constant $\tilde{\Gamma}$.

Lorentz oscillators are used in this work for modeling the majority of molecular vibrations. Some vibrations, however, are strongly influenced by hydrogen bonding. This concerns mainly vibrations of C=O and N−H groups, which can form hydrogen bonds with one another and with water. As a result of microscopically varying Gaussian-distributed strengths of hydrogen bonding, the band shapes become Gaussian as well [150, 159, 160]. The imaginary part of the corresponding dielectric function is given by

$$\varepsilon_2(\tilde{\nu}) = \tilde{F} \sum_{k=\pm 1} k \cdot \exp\left\{ -\left(\frac{\tilde{\nu} - k \cdot \tilde{\nu}_0}{\tilde{\sigma}} \right)^2 \right\}, \tag{2.75}$$

and the real part $\varepsilon_1(\tilde{\nu})$ is obtained by Kramers–Kronig transform. Similar to the Lorentz oscillator, the Gaussian oscillator is parameterized by the oscillator strengths $\tilde{F}$, the center frequency $\tilde{\nu}_0$, as well as the dampening $\tilde{\sigma}$.

Multiple molecular vibrations $\varepsilon_{\text{vib}}(\tilde{\nu})$ within a material are modeled by assuming that the dielectric function can be written as a sum of the various oscillator contributions [147]:

$$\varepsilon(\tilde{\nu}) = \varepsilon_\infty + \sum_j \varepsilon_{\text{vib}}^{(j)}(\tilde{\nu}) \tag{2.76}$$

If Gaussian oscillators are used together with Lorentz oscillators, then the sum is calculated in $\varepsilon_2(\tilde{\nu})$, and the real part is computed by Kramers–Kronig transform.

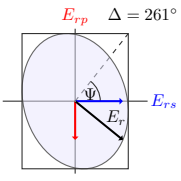

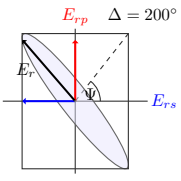

Modified effective-medium approximation (mEMA):
Dielectric functions of mixtures of different materials can be described by effective-medium theories. In this thesis, the effective-medium approximation after Bruggeman [97, 161, 162] is used, which allows one to calculate an effective dielectric function $\varepsilon_{\text{eff}}(\tilde{\nu})$ according to

$$0 = \sum_{i=1}^{M} f_i \frac{\varepsilon_i - \varepsilon_{\text{eff}}}{\varepsilon_i + 2\varepsilon_{\text{eff}}} \qquad \text{with} \qquad \sum_{i=1}^{M} f_i = 1\,. \tag{2.77}$$

The Bruggeman EMA assumes a random mixture of the M constituents with variable volume fractions f_i. Inversion of Eq. (2.77) in order to solve for ε_{eff} yields an algebraic equation of degree M. Care must be taken in the computational implementation in order to find the correct complex roots, especially for three or more components.

Protein adsorption on PAA polymer brushes measured with VIS ellipsometry is modeled with a three-component EMA of brush, buffer solution, and protein. Humidity-dependent swelling of polymer films as well as swelling of polymer brushes in aqueous environment are evaluated quantitatively using polymer–water mEMA layers. In these *modified EMA* layers, changing polymer–polymer and polymer–water interactions are taken into account by adjusting the corresponding oscillator parameters of the polymer constituent.

2.3.2. Optical layer models and matrix formalisms

a) General considerations

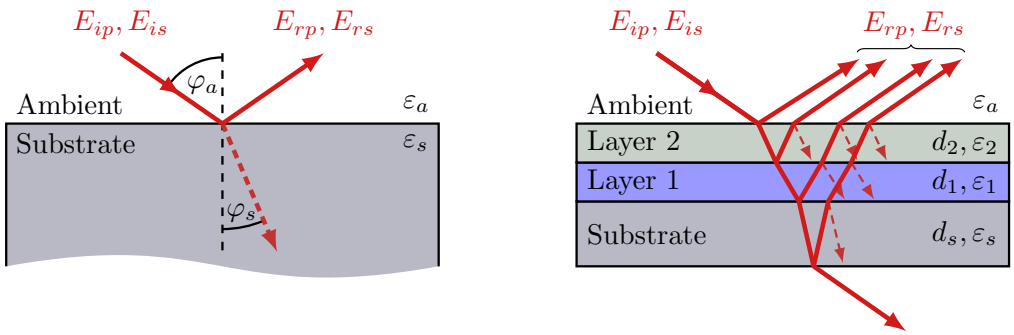

Figure 2.17: Reflection and transmission in a semi-infinite ambient/substrate system (left) and a stratified layer system (right) with multiple reflections between the various interfaces.

With suitable models of dielectric functions at hand, optical layer models of the sample are now briefly introduced. They allow one to simulate the ellipsometric parameters $\tan\Psi$ and Δ, based on the sample's dielectric functions, and compare them with experimental data. The simplest experimental situation is an isotropic bulk substrate with perfect surface in contact with an isotropic ambient, as represented in the left panel of Fig. 2.17. In this case, the

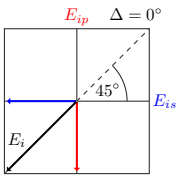

well-known Fresnel equations are used to calculate the complex p- and s-polarized reflection coefficients r_p and r_s as well as transmission coefficients t_p and t_s at the a/s interface between top medium a and bottom medium s:

$$r_p^{as} = \frac{N_s \cos\varphi_a - N_a \cos\varphi_s}{N_s \cos\varphi_a + N_a \cos\varphi_s}, \qquad r_s^{as} = \frac{N_a \cos\varphi_a - N_s \cos\varphi_s}{N_a \cos\varphi_a + N_s \cos\varphi_s} \tag{2.78}$$

$$t_p^{as} = \frac{2N_a \cos\varphi_a}{N_s \cos\varphi_a + N_a \cos\varphi_s}, \qquad t_s^{as} = \frac{2N_a \cos\varphi_a}{N_a \cos\varphi_a + N_s \cos\varphi_s} \tag{2.79}$$

$\varphi_a = \varphi_0$ and φ_s are the reflection and transmission angles, which are related by Snell's law:

$$N_a \sin\varphi_a = N_s \sin\varphi_s \tag{2.80}$$

The ellipsometric ratio $\rho = \tan\Psi \cdot \mathrm{e}^{i\Delta} = r_p/r_s$ is easily computed by inserting the corresponding complex refractive indices N_a and N_s of ambient and substrate into the above equations. With a little bit of algebra, one can also invert $\rho(\tilde{\nu})$, which results in an expression for the substrate dielectric function [6, 8]:

$$\varepsilon_s(\tilde{\nu}) = \sin^2\varphi_0 \left[1 + \tan^2\varphi_0 \left(\frac{1-\rho(\tilde{\nu})}{1+\rho(\tilde{\nu})}\right)^2\right] \tag{2.81}$$

For measured $\tan\Psi$ and Δ and with the incidence angle φ_0, this allows one to calculate $\varepsilon_s(\tilde{\nu})$ directly without the use of any dielectric-function model. Equation (2.81) is used in this work to determine the dielectric functions of gold and etched silicon substrates, which are necessary for the subsequent evaluations of polymer dielectric functions.

In the case of more complicated sample geometries, it is common to consider a stack of layers with ideal interfaces on top of the substrate, as represented in the right panel of Fig. 2.17. If the sample consists of only one or two layers, it is fairly simple to calculate the reflection coefficients at each interface—again using the Fresnel equations—and sum up the contributions from multiple reflections within the layers. The results are the so-called Airy equations [6, 8] for the p- and s-polarized component. This approach, however, becomes very tedious for multi-layer samples and even more complicated if anisotropy has to be considered. A more general procedure are matrix formalisms that calculate so-called transfer matrices $\mathcal{T}_j$ for each layer. Similar to the Müller matrix formalism, the whole optical system, i. e., the whole sample, is represented by a characteristic matrix

$$\mathcal{T} = \mathcal{T}_{\mathrm{Amb}} \cdot [\mathcal{T}_z \cdot \mathcal{T}_{z-1} \cdot \ldots \cdot \mathcal{T}_2 \cdot \mathcal{T}_1] \cdot \mathcal{T}_{\mathrm{Sub}} \tag{2.82}$$

from which reflection and transmission coefficients are extracted. Isotropic samples can be treated with the Abelès method [163], a 2×2 matrix formalism based on the 2×2 Jones

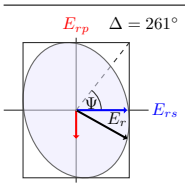

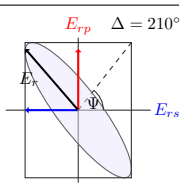

formalism [114]. Generalized cases of anisotropic stratified layers are described by Azzam and Bashara [5] in a 4×4 formalism after Berreman [164]. A rigorous treatment of arbitrarily anisotropic systems is provided by Schubert [7, 165]. For a computational implementation of his formalism, the corresponding equations from Ref. [7] should be used, because the original paper [165] contains some typing errors in Eqs. (20) and (22).

In the present work, most optical-layer-model simulations were performed using Abelès' method, which is presented in detail in Appendix C. Nevertheless, Schubert's equations were also used to check for possibly existing anisotropy in polymer samples. Both methods were coded in Matlab® (R2011a). However, Abelès' equations are preferred in the case of isotropic samples for reasons of computational speed.

b) Box models for quantitative spectra evaluation

In the following, the most important optical layer models used in this work are presented. These models are applied for simulating and fitting ellipsometric parameters $\tan\Psi$ and Δ as well as reflectivities R measured with infrared microscopy and transmittances $\overline{T}$ measured with infrared spectroscopy. In all models, ambient and substrate are depicted at the top and bottom, respectively. $n = 1$ and $k = 0$ are used for air. Silicon substrates are modeled with $n = 3.42$ and $k = 0$ [154], with literature data of n and k for the oxide layer [18]. The material systems investigated with these models are introduced in Section 2.4.

Each model is based on some parameters obtained from preceding modeling processes. Starting point are the optical constants of spin-coated polymer films determined in dry state, which are then used to model thin polymer brushes. Humidity effects on polymer films and brushes are investigated using literature data for n and k of water at room temperature [166]. Finally, temperature-dependent swelling effects of polymer brushes are analyzed. For these, dispersions $n(T)$ and $k(T)$ of water and heavy water are determined from separate transmission measurements with a model according to Fig. 2.12.

Spin-coated polymer films in dry state:

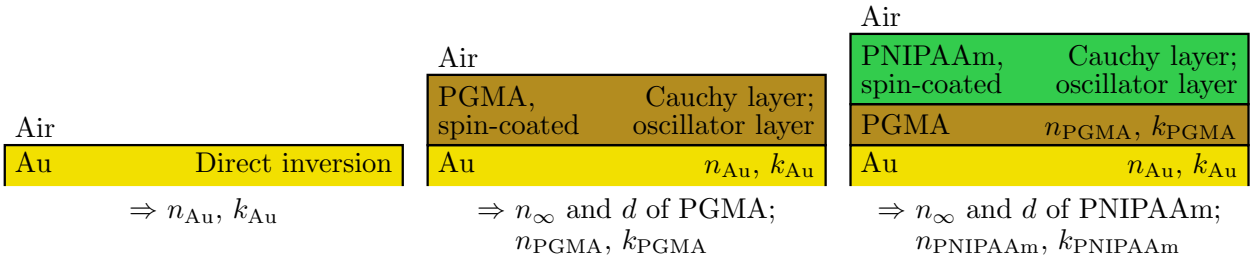

Figure 2.18: Optical layer models for determining the optical constants n and k of gold substrates by inversion of $\tan\Psi$ and Δ after Eq. (2.81), and of spin-coated PGMA and PNIPAAm films by using Cauchy dispersions in the visible range to obtain n_∞ and d as well as oscillator fits in the infrared to model the vibrational bands. Applied in Sections 3.1.2. and 3.1.4.

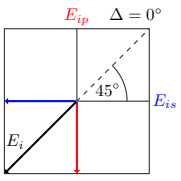

Polymer brushes in dry state:

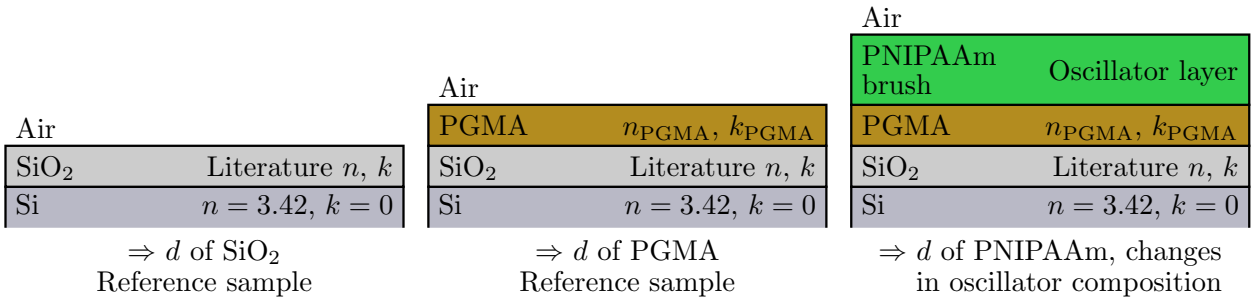

Figure 2.19: Optical layer models for PNIPAAm brushes to determine the thicknesses of silicon oxide, PGMA linker, and brush top-layer. Deuteration effects on PNIPAAm are studied by analyzing changes in the oscillator composition of the brush layer. Applied in Sections 3.2.1. and 3.2.3.b).

Polymer films and brushes in humid state:

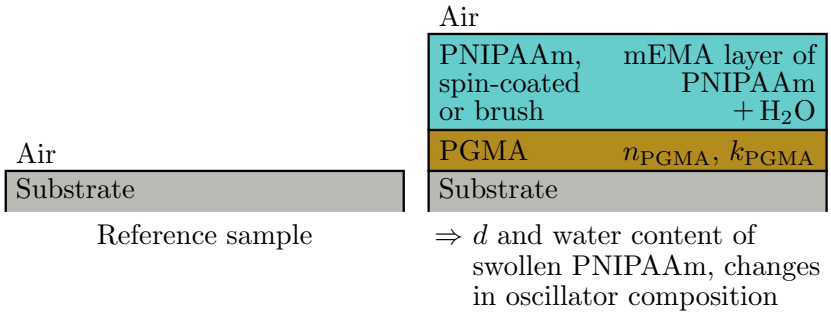

Figure 2.20: Box model for studying humidity effects on PNIPAAm films and brushes using a mEMA for the polymer–water layer. The substrate is Au or Si + SiO_2. Applied in Sections 3.1.5.b) and 3.2.4.

Polymer films and brushes in wet state:

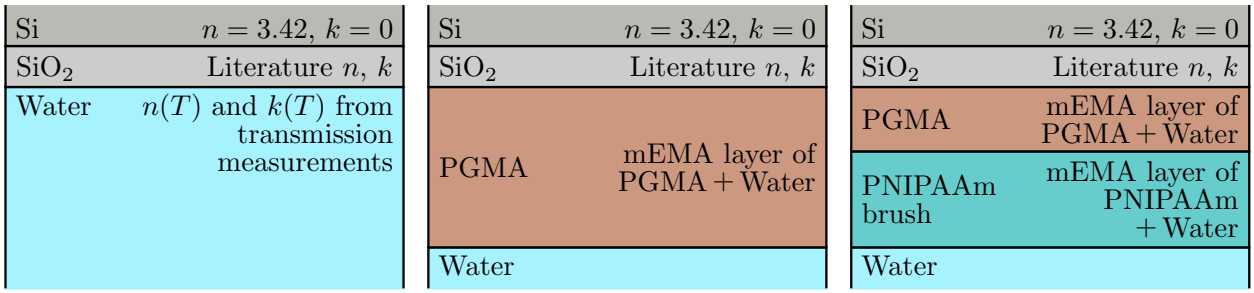

Figure 2.21: Box models for studying temperature-dependent swelling effects of spin-coated PGMA films and of PNIPAAm brushes in water measured through silicon wedges. mEMA layers are used to determine swollen-film thicknesses, water contents, as well as changing interactions, which cause alterations in the oscillator composition of the polymer components. Applied in Section 3.5.

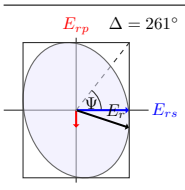

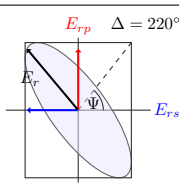

2.3.3. Fitting procedure and error estimation

Optical modeling consists of two steps: selecting an appropriate layer model and fitting the actual measured data. In the first step, the number of layers is fixed and dielectric functions are assigned to each layer. The dielectric functions are either taken from tabulated data sets, or they are described by model functions with a certain number of free parameters. In order to minimize the absolute difference between measured and simulated spectra, the free parameters are then fitted in the second step using the reduced χ^2 or *biased estimator* [167, 168]. For ellipsometric measurements, the estimator is given by

$$\chi^2 = \frac{1}{2M-K-1}\sum_{i=1}^{M}\left[\left(\frac{\tan\Psi_{\mathrm{exp}}(\tilde{\nu}_i)-\tan\Psi_{\mathrm{calc}}(\tilde{\nu}_i)}{\bar{\sigma}_{\tan\Psi}(\tilde{\nu}_i)}\right)^2+\left(\frac{\Delta_{\mathrm{exp}}(\tilde{\nu}_i)-\Delta_{\mathrm{calc}}(\tilde{\nu}_i)}{\bar{\sigma}_{\Delta}(\tilde{\nu}_i)}\right)^2\right], \quad (2.83)$$

where M denotes the number of spectral data points, K is the number of real-valued fit parameters, $(\tan\Psi_{\mathrm{exp}}, \Delta_{\mathrm{exp}})$ and $(\tan\Psi_{\mathrm{calc}}, \Delta_{\mathrm{calc}})$ are experimental and calculated $\tan\Psi$ and Δ data, and $(\bar{\sigma}_{\tan\Psi}, \bar{\sigma}_{\Delta})$ are the corresponding experimental errors. Equivalent expressions for χ^2 are used for reflectivity or transmittance measurements by substituting measured and calculated data for $R_{\mathrm{exp}}(\tilde{\nu}_i)$ and $R_{\mathrm{calc}}(\tilde{\nu}_i)$ as well as $\overline{T}_{\mathrm{exp}}(\tilde{\nu}_i)$ and $\overline{T}_{\mathrm{calc}}(\tilde{\nu}_i)$, respectively.

Including the errors, or weight factors, into the fit is essential for obtaining physically meaningful fit results. These errors contain statistical as well as systematic contributions. While the statistical errors in the infrared are correlated with the energy-dependent intensity distribution of the globar radiation, the systematic ones are not that easy to estimate [169]. The degree of polarization of polarizer and analyzer was chosen as a first weight factor. Additionally, Δ values in the vicinity of 0° and 180° were weighed less. Furthermore, Δ spectra were rescaled by a factor between 150 and 180 in order to match the absolute values of $\tan\Psi$.

Minimization of χ^2 itself is then performed using the Levenberg–Marquardt algorithm for non-linear curve fitting [169, 170], which is provided by a predefined Matlab® routine. This returns the fitted parameters, residual between measured and fitted spectra, as well as the Jacobian matrix, from which fit errors and correlations between fit parameters are computed [169, 170]. The goodness of the fit is then evaluated by the absolute value of χ^2 as well as the cross correlations between fit parameters, which should be small. Additional, and potentially larger, upper and lower bounds for fit errors are estimated by varying the corresponding fit parameters and judging the impact on the deviation between measurement and simulation.

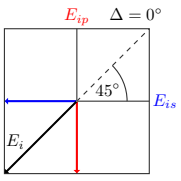

2.4. Materials and sample preparation

This section summarizes the polymers that were used in this thesis for the preparation of polymer brushes and spin-coated polymer films. Furthermore, model proteins and buffer solutions are discussed, and details on sample preparation are described.

2.4.1. Overview of polymers, model proteins, and buffer solutions

In the present work, three types of polymers were investigated by means of infrared and visible ellipsometry, namely carboxy-terminated poly(*N*-isopropylacrylamide) [PNIPAAm], poly(acrylic acid) [PAA], and poly(glycidylmethacrylate) [PGMA]. Their molecular structures are shown in Fig. 2.22. PNIPAAm and PAA are stimuli-responsive polymers that are mainly used in temperature- and pH-dependent switching experiments, respectively. PGMA provides an anchoring layer that serves as a linker between substrate and stimuli-responsive polymer top-layer. All polymers were purchased from Polymer Source Inc. (Dorval, Canada).

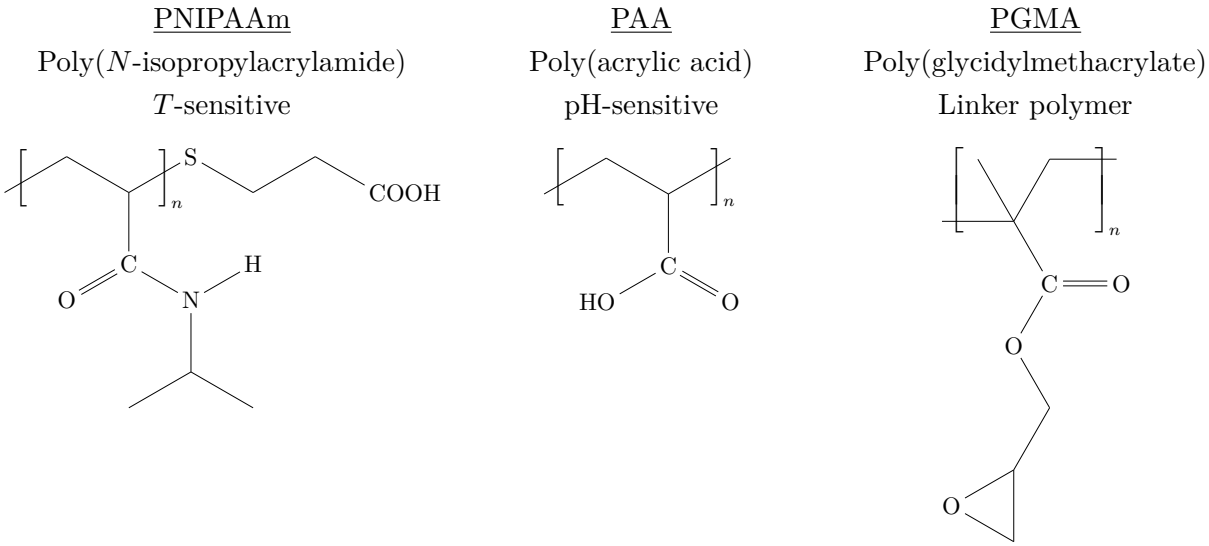

Figure 2.22: Chemical structure of the polymers used in this work.

Characteristic polymer properties of PNIPAAm, PAA, and PGMA are listed in Tab. 2.1. These properties [171] are the number-average molecular weight $\overline{M}_n$, the heterogeneity index or *polydispersity index* $\overline{M}_w/\overline{M}_n$ (PDI), which is the ratio between weight-average molecular weight $\overline{M}_w$ and $\overline{M}_n$, the number of monomers N_{mono} per chain, the length d_{chain} of a fully stretched chain, as well as the glass-transition temperature T_{g}. The monomer number N_{mono} is calculated from the ratio between $\overline{M}_n$ and the molecular weight of one monomer (113.16 g/mol for PNIPAAm, 72.06 g/mol for PAA, and 142.15 g/mol for PGMA). The

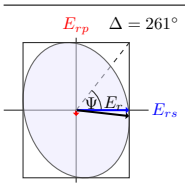

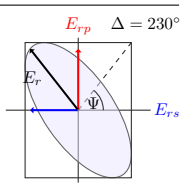

length d_{chain} is computed by

$$d_{\text{chain}} = N_{\text{mono}} \cdot \sqrt{n_{\text{cc}} \cdot a_{\text{cc}}^2 (1 - \cos \gamma_{\text{cc}})}\,, \tag{2.84}$$

with $a_{\text{cc}} = 0.154\,\text{nm}$ being the C−C bond length [172], $\gamma_{\text{cc}} = 109.45°$ the angle of a C−C bond, and n_{cc} the number of C−C bonds per monomer. The glass-transition temperatures were determined with differential scanning calorimetry by Eva Bittrich at the IPF Dresden [75]. Note that the unit *Dalton* is often used for molecular masses ($1\,\text{Da} \equiv 1\,\text{g/mol}$).

Polymer	Acronym	$\overline{M}_n$ [g/mol]	$\overline{M}_w/\overline{M}_n$	N_{mono}	d_{chain} [nm]	T_{g} [°C]
Poly(glycidylmethacrylate)	PGMA	17 500	1.70	123	31	59
Poly(acrylic acid)	PAA	26 500	1.12	368	93	105
Poly(*N*-isopropylacrylamide)	PNIPAAm					
	PN56k	56 000	1.22 (1.40)	495	124	
	PN94k	94 000	1.27	831	209	
	PN132k	132 000	1.28	1166	293	140

Table 2.1: Overview of the utilized polymers with characteristic parameters (number-average molecular weight $\overline{M}_n$, polydispersity index $\overline{M}_w/\overline{M}_n$, monomer number N_{mono}, stretched-chain length d_{chain}, glass-transition temperature T_{g}). PN56k (PDI = 1.40) was used for spin-coated PNIPAAm films.

Proteins:

Human serum albumin (HSA) [173] was utilized in this thesis as a model protein to study protein ad- and desorption on PNIPAAm and PAA brushes. It is a globular protein that constitutes about 55–60% of the total protein content in human blood plasma [174–177] with a typical concentration of about 50 mg/ml. HSA is important for maintaining the colloid osmotic pressure, for buffering the pH, and for transporting less water-soluble substances like fatty acids, trace elements, and certain hormons [178]. Furthermore, it is especially significant for biomedical applications due to its extraordinary ligand-binding properties [178, 179].

HSA is a single-stranded polypeptide with known amino acid sequence [173, 180]. In crystal state, it has a heart-shaped form with dimensions $3 \times 8 \times 8\,\text{nm}^3$ as determined from X-ray diffraction experiments [179], whereas HSA in solved state exhibits an ellipsoidal shape with dimensions $4 \times 4 \times 14\,\text{nm}^3$ [173]. It is characterized by a repeating pattern of three α-helical homologous domains, numbered I, II, and III, with each domain being divided into two subdomains A and B [177, 178] (see Fig. 2.23). Different information about the helical secondary structure of HSA is found in the literature [173, 174, 179, 181–184]. Dockal et al. [174] report 66% α-helix, 2% β-sheets, 2% β-turns, and 26% random coil for defatted human serum albumin with slight variations within the three domains [173, 174, 179, 182].

The protein exists in different isomeric forms depending on the pH value of the solution [178, 181, 184]. HSA has a molecular weight of 66 430 g/mol and an isoelectric point (IEP) of 4.7 in the lipid-bound [185] and 5.7 in the defatted case [186].

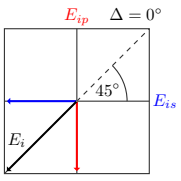

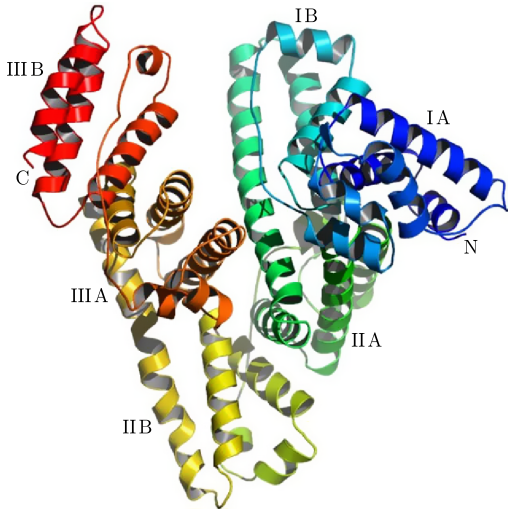

Figure 2.23: Three-domain structure (I, II, III) of HSA with sub-domains A and B, connected by random coil. N-terminus and C-terminus (start and end of the amino acid chain terminated by a free NH_2 and COOH group, respectively) are marked in the figure. The protein secondary structure is shown in different colors. For further details, see Refs. [177, 178]. Reprinted from Il Farmaco 60 (6–7), Roberto Artali, Gabriella Bombieri, Luisella Calabi, and Antonio Del Pra, "A molecular dynamics study of human serum albumin binding sites", pages 485–495, © 2005, with kind permission from Elsevier.

Substrates:

Samples were prepared on various substrates for different purposes. While flat Si (100) substrates are used for temperature-dependent infrared-microscopy measurements as well as (in-situ) VIS-ellipsometric investigations on polymer brushes and films, wedge-shaped Si (111) substrates (1.5°) are mainly employed for in-situ infrared-ellipsometry experiments. Reference measurements of spin-coated polymer films with very high optical contrast are possible using Au substrates. Owing to the metal-surface selection rule [187–190] for thin layers, though, only transition dipole components perpendicular to the substrate surface can be observed in the spectra. Si (100) substrates, Si (111) wedges, and gold-coated microscope slides (200 nm) were purchased from Silicon Materials (Kaufering, Germany), Vario GmbH (Wildau, Germany), and Ssens BV (Enschede, The Netherlands), respectively.

Buffer solutions:

Infrared-ellipsometric swelling experiments on PNIPAAm brushes were performed using purified water (H_2O) from a Millipore Direct-Q 3 UV system (Merck Millipore, Billerica, USA) as solvent. All VIS-ellipsometry measurements and experiments involving PAA brushes and/or proteins, on the other hand, were carried out in pH-stabilizing buffer solutions. Monosodium dihydrogen phosphate (NaH_2PO_4) and disodium hydrogen phosphate (Na_2HPO_4) were used to prepare buffers with different pH values and a constant salt concentration of 10 mM.

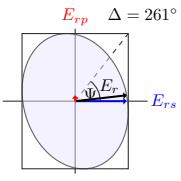

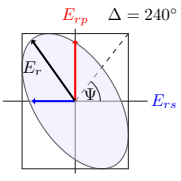

During in-situ experiments, the pH of the solutions was constantly monitored with a membrane pH meter (HI 8314, HANNA instruments, Kehl am Rhein, Germany) within an error of ±0.05. Purified water from a Milli-Q Direct 8 system (EMD Millipore Corporation, Billerica, USA) was used for VIS-ellipsometry experiments at the IPF Dresden.

2.4.2. Preparation of polymer brushes and spin-coated polymer films

a) Polymer brushes

Polymer mono brushes are usually prepared in three steps: cleaning of the substrate, grafting of the anchoring layer, and grafting of the stimuli-responsive polymer top-layer. All polymer-brush samples investigated in this work were prepared either on silicon (100) substrates or on silicon (111) wedges at the IPF Dresden by Eva Bittrich [75] and Sebastian Rauch [98], who also performed pre-characterization measurements using visible ellipsometry.

1. *Cleaning:* Several cleaning protocols exist that ensure the formation of high amounts of free OH groups on top of the silicon substrate, leading to a very hydrophilic interface that is necessary for the following grafting process. In the first method, which was used here prior to the grafting of PAA, the substrate is cleaned with hot piranha solution (3 : 1, H_2SO_4 : 30% H_2O_2) for 1 h, rinsed with H_2O, and dried under nitrogen flux. In the second method, used prior to the grafting of PNIPAAm, the silicon substrate is treated with absolute ethanol (EtOH) in an ultrasonic bath for 15 min and dried under nitrogen flux. Afterwards, they are exposed to a cleaning solution of NH_4OH / H_2O_2 / H_2O (1:1:5) at 70 °C for 20 min, rinsed twice with H_2O, and dried again.

2. *Anchoring layer:* In the next step of brush preparation, a thin layer of PGMA is deposited by spin-coating (Spin 150, SPS Coating, Putten, The Netherlands) a solution of 0.02 wt% PGMA in $CHCl_3$ with subsequent annealing at 100 °C in a vacuum oven for 20 min in order to react the silanol groups of the substrate with a fraction of PGMA's epoxy groups. The formed anchoring layer is thus equipped with remaining epoxy groups for the following *grafting-to* process [74].

3.1 *Preparation of PNIPAAm mono brushes:* A PNIPAAm solution in THF (1 wt%) is spin-coated onto the anchoring layer and annealed at 150 °C in a vacuum oven. The annealing temperature is chosen slightly above the glass-transition temperature of PNIPAAm, thereby increasing the mobility of the polymer chains in order for the COOH groups of PNIPAAm to form ester bondings with PGMA. The grafting density is controlled by choosing an appropriate annealing time, typically between 5 min and 20 h [75]. To remove noncovalently bonded polymer, the resulting films are first immersed in THF, then extracted in THF for 6 h, rinsed with EtOH, and finally dried under nitrogen flux.

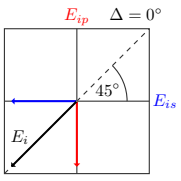

3.2 *Preparation of PAA Guiselin brushes:* Onto the formed PGMA anchoring layer, a PAA solution in EtOH (1 wt%) is spin-coated and annealed at 80 °C in a vacuum oven for 30 min to react the COOH groups of PAA with the remaining epoxy groups of PGMA. The annealing temperature is chosen well below the glass-transition temperature of PAA, which restricts chain mobility and consequently the maximum number of bonds between PAA and PGMA, thereby increasing the possible swelling degree of the brush [75]. After the annealing process, the PAA chains have an average of 1–2 anchoring points [75, 82], thus forming so-called Guiselin brushes [191, 192]. Ungrafted PAA is removed by extraction in 96% EtOH.

VIS ellipsometry (SE 402, Sentech Instruments GmbH, Berlin, Germany; and Woollam alpha-SE, J. A. Woollam Co., Inc., Lincoln NE, USA) was employed after each preparation step at the IPF Dresden to pre-characterize the individual layers of the samples. The final pre-characterization of PNIPAAm brushes was performed at ISAS Berlin via atomic force microscopy and visible ellipsometry (Sentech SE 801), as will be discussed in Section 3.2.1.

b) Pre-characterization of PAA brushes

PAA Guiselin brushes are used in this work for pH-dependent swelling and protein-adsorption experiments monitored with in-situ visible and infrared ellipsometry. For this purpose, four brushes were prepared on silicon wafers and wedges. Layer thicknesses as determined by VIS ellipsometry are given in Tab. 2.2.

	S1: VIS	S2: IR	S3: IR	S4: IR
d_{SiO_2} [nm]	1.4 ± 0.1	2.5 ± 0.1	1.9 ± 0.1	2.9 ± 0.1
d_{PGMA} [nm]	2.3 ± 0.2	2.5 ± 0.2	2.8 ± 0.2	2.7 ± 0.2
d_{PAA} [nm]	4.7 ± 0.3	6.9 ± 0.3	7.4 ± 0.3	5.1 ± 0.3
σ [nm^{-2}]	0.15 ± 0.01	0.22 ± 0.01	0.23 ± 0.01	0.16 ± 0.01

Table 2.2: VIS-ellipsometry results for dry-layer thicknesses d and grafting densities σ of the four PAA brushes used for in-situ VIS and IR measurements. Data from Ref. [99] were used for the dispersion relations of substrate and SiO_2. In order to determine the single-layer thicknesses, the refractive index of PGMA was set to $n_{PGMA} = 1.525$, while a two-parameter Cauchy dispersion relation $n_{PAA}(\lambda) = a_0 + a_2/\lambda^2$ was used for the PAA layer. The bulk density $\varrho_{PAA} = 1.4\,g/cm^3$ [193] was used to calculate the grafting densities after Eq. (1.3). Sample pre-characterization by Eva Bittrich.

Owing to the different crystal orientations, the silicon wedges and wafers exhibit different surface roughnesses after the chemical cleaning. This results in slightly different self-crosslinking and thicknesses of the PGMA layer and thereby of the top PAA-brush layer.

It is known that the swelling and dissociation behavior of PAA Guiselin brushes is qualitatively the same as that of end-grafted brushes [23, 192]. Also pH-sensitive HSA adsorption is showing similar trends [194]. Results from protein experiments are therefore expected to be comparable with existing literature on end-grafted PAA brushes [39, 195–198].

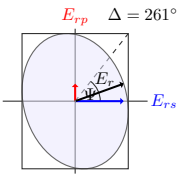

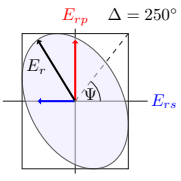

c) Spin-coated polymer films

For reference measurements and for the determination of thin-film polymer optical constants, polymer films of PNIPAAm and PGMA with thicknesses between 55–140 nm were spin-coated onto silicon substrates (flat and wedge-shaped) as well as gold substrates. PNIPAAm with $\overline{M}_n = 56\,000$ g/mol and PDI = 1.40 as well as PGMA with $\overline{M}_n = 17\,500$ g/mol and PDI = 1.70 were used. Sample preparation is basically the same as for regular polymer-brush samples but *without* annealing. PGMA and PNIPAAm films were also prepared *with* annealing to have reference films that reproduce the conditions in polymer brushes as closely as possible. After annealed spin-coated films have been measured ex-situ or in-situ, they can, in principle, be converted to thin polymer brushes by extracting the non-covalently bonded polymer film in an appropriate solvent. All spin-coated films were also pre-characterized with VIS ellipsometry (Sentech SE 801). Details are given in Section 3.1.2.

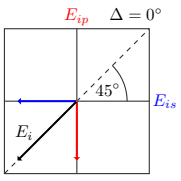

3. Results and discussion

3.1. Optical properties of 55–135 nm thick spin-coated polymer films

The aim of this section is to determine the optical constants n and k of spin-coated PGMA and PNIPAAm films using infrared ellipsometry. This is the foundation for further quantitative studies of polymer films and brushes in dependence of external stimuli like temperature. Priorly, a general discussion on the vibrational bands observed in polymer reference spectra is given. In order to evaluate film quality and homogeneity, the films are afterwards pre-characterized with visible ellipsometry, atomic force microscopy, and infrared microscopy. It turns out that PNIPAAm films show swelling effects in humid air that affect the spectral composition of the characteristic polymer vibrational bands. In a systematic study under H_2O- and D_2O-atmospheric conditions, these effects are investigated thouroughly by means of infrared microscopy and corresponding optical simulations. In the end, the influence of temperature on the structural properties of a spin-coated PNIPAAm film is studied.

3.1.1. Reference measurements

Spin-coated and annealed PNIPAAm and PGMA films on gold substrates were measured with infrared microscopy, as shown in Fig. 3.1, to obtain reference spectra that are necessary for future discussions of vibrational bands. Most important bands are labeled, and band positions are marked in the case of PNIPAAm. Small-intensity bands were identified by second-derivative analysis [199]. For PGMA, the focus lies on the prominent epoxy and ester vibrations, which are relevant for studying effects of grafting density and annealing time on polymer brushes. Such is the case, for instance, for the amide A, I, and II bands of PNIPAAm and the ν(C=O) band of PGMA.

a) PGMA

In polymer brushes investigated in this thesis, PGMA provides the anchoring layer between substrate and functional polymer top-layer. Since PGMA layers are comparably thin, it is sufficient to analyze only the most prominent vibrational bands that might contribute to polymer-brush spectra as well as bands that are possibly involved in the grafting process of the brush layer. This concerns the vibrational bands associated with PGMA's epoxy and ester groups. Corresponding band assignments according to references [200–203] are listed in Tab. 3.1.

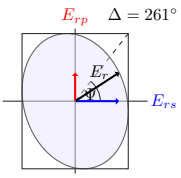

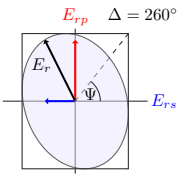

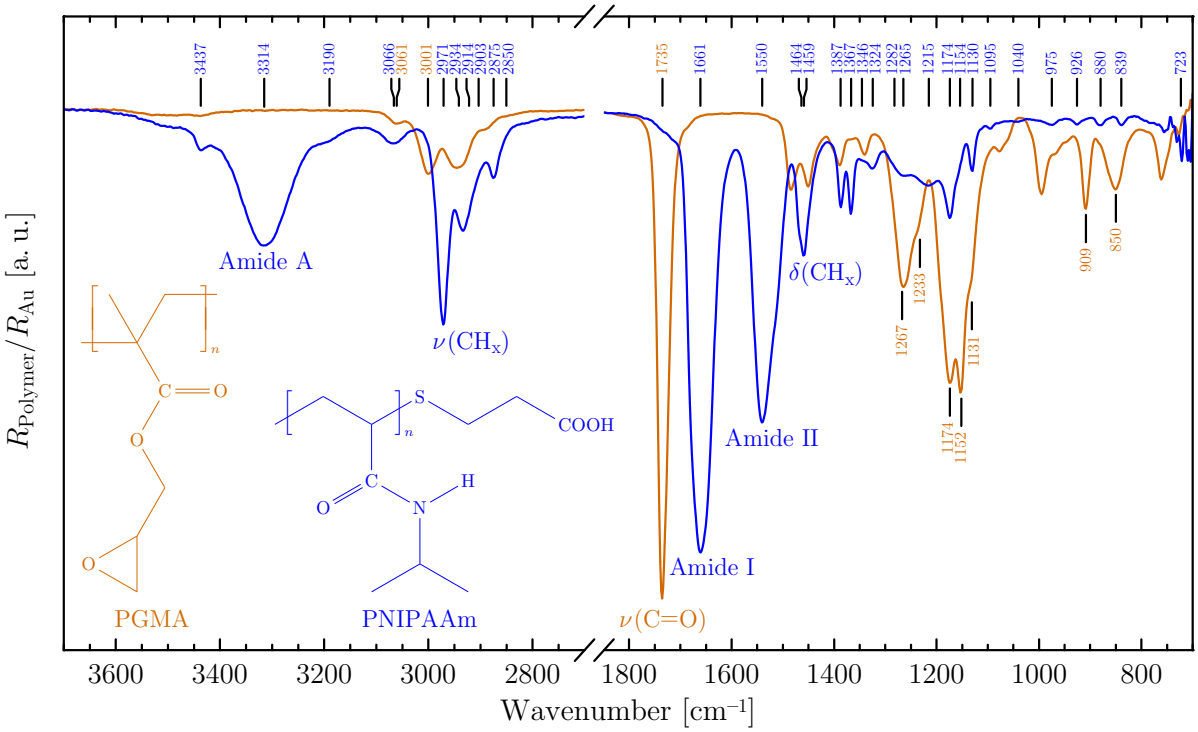

Figure 3.1: Infrared-microscopic reference measurements of a spin-coated and annealed 105 nm thick PGMA film (orange) and a 116 nm thick PNIPAAm film (blue) on Au using a grazing-incidence objective.

Epoxy rings of glycidyl groups

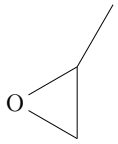

show characteristic ring-breathing as well as asymmetric and symmetric deformation modes, which in the case of PGMA are observed at 1267 cm^{-1}, 909 cm^{-1}, and 850 cm^{-1}, respectively. Furthermore, CH_x-stretching vibrations of the ring's methylene and methyne groups are found at respectively 3061 cm^{-1} and 3001 cm^{-1}. Below 3000 cm^{-1}, other CH_x-stretching vibrations of the polymer are, of course, also visible.

The ester groups

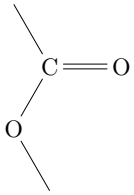

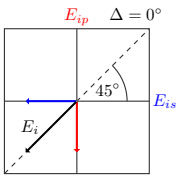

of PGMA make for the prominent sharp carbonyl-stretching vibration at 1735 cm^{-1} and the characteristic C−O−C-stretching vibration at 1233 cm^{-1}, which appears as a shoulder of the epoxy ring-breathing mode at 1267 cm^{-1}.

Details on how epoxy- and ester-specific vibrational bands change when grafting a polymer top-layer will be discussed in Section 3.2.2.

$\tilde{\nu}$ [cm^{-1}]	Band assignment – PGMA	Reference
3061	$\nu(CH_2)$ of epoxy-methylene group ($-CH_2{\cdot}O-$)	[200]
3001	$\nu(CH)$ of epoxy-methyne group ($>CH{\cdot}O-$)	[200]
1735	$\nu(C{=}O)$ of ester group	[203]
1267	Breathing mode of epoxy ring	[201, 202]
1233	$\nu(C-O-C)$ of ester group	
1131	$\omega(CH_2)$, wagging of epoxy-methylene group	[201]
909	$\gamma_{as}(C-O-C)$, asymmetric deformation of epoxy ring	[201, 202]
850	$\gamma_{s}(C-O-C)$, symmetric deformation of epoxy ring	[201, 202]

Table 3.1: Band assignments of annealed spin-coated PGMA films ($\overline{M}_n$ = 17 500 g/mol, PDI = 1.70) according to references [200–203].

b) PNIPAAm

Table 3.2 presents a detailed overview of PNIPAAm's vibrational bands with band assignments according to references [50, 51, 203–215]. The vibrations were categorized into six groups: skeletal vibrations (800–1200 cm^{-1}), the amide III region (1200–1320 cm^{-1}), CH_x-bending vibrations (1320–1480 cm^{-1}), the amide II and I regions (1480–1750 cm^{-1}), CH_x-stretching vibrations (2800–3020 cm^{-1}), and combination bands (3020–3600 cm^{-1}).

The main functional groups of PNIPAAm are—as the name poly(*N*-isopropylacrylamide) already implies—amide groups

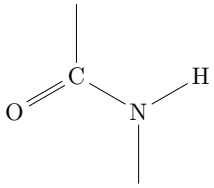

that are connected to the main chain of the polymer. The nitrogen atoms of each amide group are in turn connected to isopropyl groups. Amide groups involve several combinations of transition dipole moments that make for characteristic spectral features in the vibrational spectrum. In order of decreasing frequency, the corresponding vibrational bands are named amide A, B, I, II, III, IV, V, VI, and VII [206].

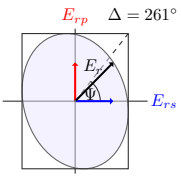

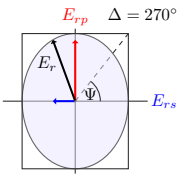

In the resolved spectral range of 3600–700 cm^{-1}, the lowest observed band is the amide V vibration at 723 cm^{-1}, which consists mainly of out-of-plane N−H-bending. The amide III region consists of complicated combination bands comprising the in-phase vibration of in-plane N−H-bending and C−N-stretching with small contributions from C−C-stretching and in-plane C=O-bending. Amide II contains primarily the out-of-phase vibration of in-plane N−H-bending (60%) and C−N-stretching (≈ 40%) with smaller contributions from in-plane C=O-bending as well as C−C- and N−C-stretching. Amide I arises mainly from C=O-stretching (80%) with minor contributions from out-of-phase C−N-stretching, C−C−N-deformation, and in-plane N−H-bending. C=O-stretching of PNIPAAm occurs at lower frequencies compared to ν(C=O) of PGMA. This is due to the strong mesomeric electron-releasing tendencies of the amide group's nitrogen atom, which causes an increase in electron density on the C=O bonds and, thus, a weakening of the ν(C=O) force constant [215, 216].

Amide A and B constitute a Fermi resonance doublet between N−H-stretching and the first overtone of amide II (mainly N−H-bending). N−H-stretching is observed at 3437 cm^{-1} and 3314 cm^{-1}, which respectively correspond to *free* and *bonded* N−H, where *bonded* refers to hydrogen bonding of the H atoms to oxygen atoms of neighboring C=O groups. The N−H-stretching band is particularly broad and exhibits a Gaussian shape [150, 159, 160] owing to microscopically varying strengths of hydrogen bonding within the polymer film. In general, hydrogen bonding plays an important role in the vibrational composition of PNIPAAm's amide bands, both in dry state as well as in aqueous environment or humid state. Different hydration states of PNIPAAm also affect the CH_x-bending and -stretching regions [50]. Details on hydrogen bonding and hydration states will be discussed in Section 3.1.5.

The relatively broad band at about 1720 cm^{-1} arises mainly from different overlapping stretching vibrations associated with free and hydrogen-bonded C=O groups. These C=O vibrations originate primarily from ester groups of the PGMA anchoring layer between substrate and PNIPAAm film. Additional contributions are due to ester groups formed between PGMA and the telechelic COOH groups of the carboxy-terminated PNIPAAm chain ends [26] as well as due to carboxylic groups of non-covalently bonded PNIPAAm. The latter two contributions, however, are small comparing the overall chain length of approximately 500 monomer units (Tab. 2.1) to one COOH unit. A detailed analysis of the vibrational band at 1720 cm^{-1} is given in Section 3.2.2.

Another broad band is visible at about 3500 cm^{-1}. Although samples are normally measured in dried air, it is likely that this band is associated with small amounts of water bound within the polymer layer. This hypothesis is supported by the findings in Section 3.1.5., which show the water-binding capabilities of PNIPAAm films under humid conditions.

Importantly for the analysis of thin polymer brushes, the amide I/II and amide A regions are not overlapped by any characteristic spectral features of the PGMA sublayer. This is of special relevance when studying the effects of deuteration on the amide I and II bands.

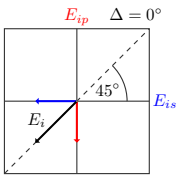

$\tilde{\nu}$ [cm^{-1}]	Band assignment – PNIPAAm	Reference
3437	ν(N−H)$_f$	[208]
3314	Amide A: ν(N−H)$_b$	[207, 208]
3190	Amide I + Amide II	[208]
3066	Amide B: Fermi resonance (see text)	[207, 208, 215]
2971	ν_{as}(CH$_3$)	[50]
2934	ν_{as}(CH$_2$)	[50]
2914	ν(CH)	[50]
2903	ν(CH)	[50]
2875	ν_s(CH$_3$)	[50]
2850	ν_s(CH$_2$)	[50]
1661	Amide I: mainly ν(C=O)	[204]
1550	Amide II: mainly δ_{ip}(N−H) + ν(C−N)	[204]
1467	δ_{as}(CH$_3$)	[50]
1459	δ_{as}(CH$_2$)	[50]
1387	δ_s(CH$_3$)	[50]
1367	δ_s(CH$_2$)	[50]
1346	δ(CH)?	[203]
1324	δ(CH)?, Amide III region	[203], [50, 204, 213, 215]
1282	Amide III region	[50, 204, 213, 215]
1265	Amide III region	[50, 204, 213, 215]
1215	Amide III region	[50, 204, 213, 215]
1174	Unclear	[50, 210]
1154	Skeletal ν(C−CH$_3$) or ρ(N−C)?	[50, 214], [204]
1130	ρ(CH$_3$)	[50, 210]
1095	Skeletal ν(N−C) or C−C vibration	[204], [214]
1040	Likely a skeletal C−C vibration	[203, 204]
975	Likely a skeletal C−C vibration	[203, 204]
926	Likely a skeletal C−C vibration	[203, 204]
880	Skeletal ν(C−C) + δ(O=C−N)	[204]
839	Likely a skeletal C−C vibration	[203, 204]
723	Amide V: δ_{op}(N−H)	[204, 205]

Table 3.2: Band assignments of annealed spin-coated PNIPAAm films ($\overline{M}_n$ = 56 000 g/mol, PDI = 1.40) according to references [50, 51, 203–215].

The CH$_x$-stretching region comprises three distinct bands at 2971 cm^{-1}, 2934 cm^{-1}, and 2875 cm^{-1} that are associated with ν_{as}(CH$_3$), ν_{as}(CH$_2$), and ν_s(CH$_3$), respectively, with smaller shoulders related to ν_a(CH$_2$) and ν(CH) vibrational modes. ν_{as}(CH$_3$) and ν_{as}(CH$_2$) might be involved in Fermi resonances, partly with overtones of CH$_x$-bending modes, thereby giving rise to another small contribution at about 2950 cm^{-1} [211, 217].

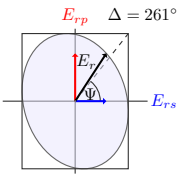

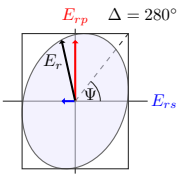

3.1.2. Overview and pre-characterization with VIS ellipsometry

Spin-coated PGMA and PNIPAAm films with different thicknesses were prepared on silicon (111) and (100) as well as on gold substrates. Table 3.3 gives an overview of the samples with corresponding layer thicknesses as determined by VIS ellipsometry.

Substrate	d_{SiO_2} [nm]	Polymer	d_{PGMA} [nm]	d_{Film} [nm]	$d_{Film,\,off}$ [nm]
Si (100)	1.3 ± 0.1	PGMA	2.2 ± 0.3		
	1.1 ± 0.1	PNIPAAm	2.5 ± 0.3	132.0 ± 0.5	
Si (111)	1.4 ± 0.1				
	1.2 ± 0.1	PGMA	119.2 ± 0.5		
	1.2 ± 0.1	PGMA	69.0 ± 1.2		
	1.4 ± 0.1	PNIPAAm	2.4 ± 0.3	119.0 ± 0.5	117.2 ± 0.5
	1.4 ± 0.1	PNIPAAm	2.5 ± 0.3	62.5 ± 0.5	—
Au	—	PGMA	105.6 ± 0.5		
	—	PGMA	55.8 ± 0.5		
	—	PNIPAAm	2.5 ± 0.3	117.8 ± 0.5	116.0 ± 0.5
	—	PNIPAAm	2.5 ± 0.3	60.7 ± 1.5	53.5 ± 0.5

Table 3.3: Overview of spin-coated polymer films with layer thicknesses determined by VIS ellipsometry. PNIPAAm films were measured near the center of the samples (d_{Film}) and also off-center ($d_{Film,\,off}$). Samples on Si (100) are used for temperature-dependent measurement with infrared microscopy (see Section 3.1.6.). Samples on Si (111) and Au are used for determining the optical constants of PGMA and PNIPAAm (Section 3.1.4.) as well as for humidity-dependent swelling experiments (Section 3.1.5.).

For the modeling process of VIS-ellipsometric spectra, literature data for silicon [218] were used, and a Cauchy model with $n_{SiO_2}(\lambda) = 1.452 + 3600/\lambda^2$ was assumed for silicon oxide. The optical constants of gold were determined by inversion of corresponding ellipsometric spectra using Eq. (2.81). All polymer films were modeled with Cauchy layers. Films on Si (111) and Au were prepared from the same batches of polymers. Therefore, a joint fit on Cauchy parameters and film thicknesses was performed on the ellipsometric spectra of the corresponding four PGMA and the four PNIPAAm samples (see Fig. D.1 in Appendix D.). With regard to infrared ellipsometry, the resulting high-frequency refractive indices are found to be

$$\begin{aligned} \text{PGMA:} \quad & n_\infty = 1.502 \pm 0.005, \\ \text{PNIPAAm:} \quad & n_\infty = 1.478 \pm 0.005. \end{aligned} \tag{3.1}$$

Layer thicknesses of PNIPAAm films show small variations when measured either directly after preparation or after a few days. This is due to swelling effects in humid air, which will be discussed in Section 3.1.5. For the same reason, the value of n_∞ of PNIPAAm in Eq. (3.1) is slightly smaller than the true dry-state value derived in Section 3.1.4.

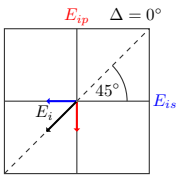

3.1.3. Homogeneity tests with mapping VIS ellipsometry, AFM, IR microscopy, and IR ellipsometry

Inspection of spin-coated polymer samples with visible microscopy hints at certain film inhomogeneities, as illustrated in Fig. 3.2 by a 23 000 µm × 670 µm map of the 116 nm thick PNIPAAm film on gold.

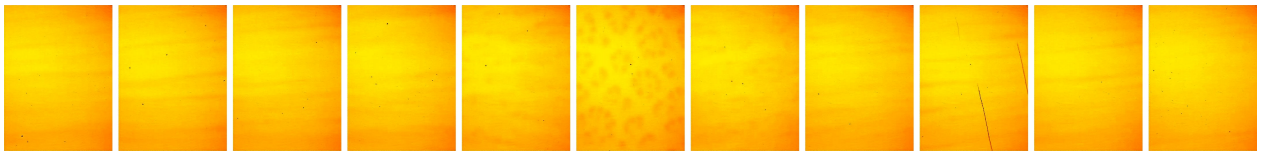

Figure 3.2: Visible-microscopy map (11 · 500 µm × 670 µm, 1000 µm separation) of the 116 nm thick PNIPAAm film on Au.

The center of the sample seems to be covered in a clustered way, whereas the polymer appears to be distributed more evenly towards the sample edges. This varying density or thickness distribution can be explained by the spin-coating process itself. Non-Newtonian shear thinning can occur if the film is spun from a highly concentrated polymer solution, leading to a decreasing film thickness with increasing radial distance from the center [219].

AFM measurements, shown in Fig. 3.3, support this hypothesis. Film thickness varies up to 30 nm in the very center of the sample, but the film becomes much more homogeneous away from the center area of about $3 \times 3\,\mathrm{mm}^2$.

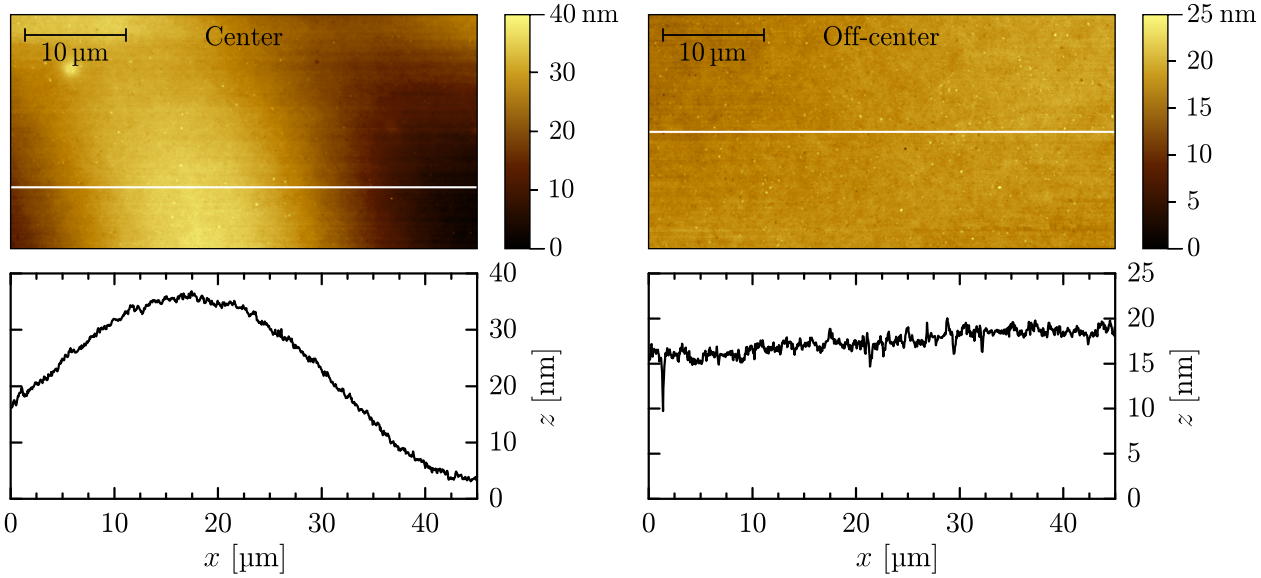

Figure 3.3: AFM maps of thickness variations z of the 116 nm thick PNIPAAm film on Au. The left and right map respectively correspond to spots within the 6th and 8th visually mapped fields in Fig. 3.2.

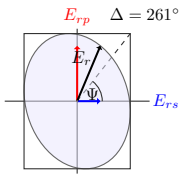

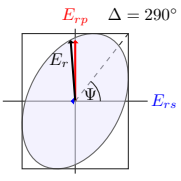

Mapping VIS ellipsometry (see Fig. 3.4) as well as linescans with infrared microscopy (Fig. E.1 in Appendix E.) also confirm these thickness trends. All subsequent measurements were therefore performed off-center where the film is most homogenous. This is essential for a quantitative evaluation of infrared-ellipsometric spectra, which relies on ideal interfaces.

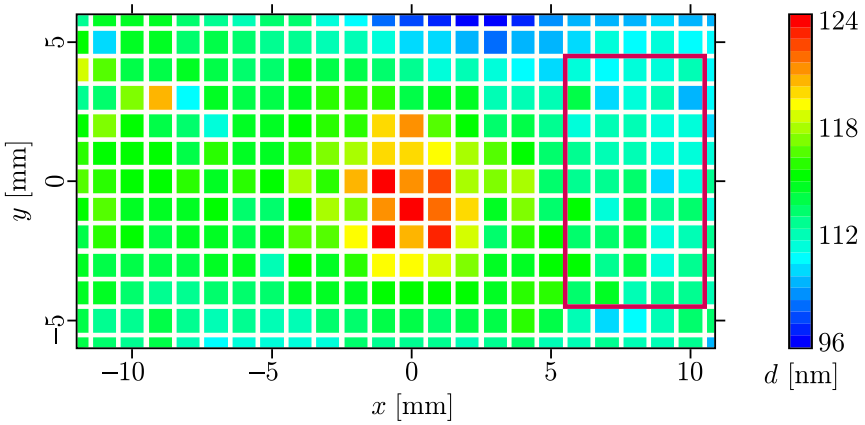

Figure 3.4: VIS-ellipsometric thickness map of the $d_{\mathrm{mean}} = 116\,\mathrm{nm}$ thick PNIPAAm film on Au over an area of $20 \times 10\,\mathrm{mm}^2$ around the center of the sample. Micro-focus apertures allowed for spot sizes of $250 \times 250\,\mu\mathrm{m}^2$. The purple rectangle marks the approximate sample area that was probed with infrared ellipsometry in Section 3.1.4.

Thickness maps of spin-coated PNIPAAm films on silicon (111) wedges (see Appendix E.) show similar thickness trends. Film homogeneity, however, is not as good towards the edges, which poses potential problems for measurements of the ellipsometric phase Δ. Figure 3.5 compares the ellipsometrically determined degrees of phase polarization P_{ph} of two PNIPAAm films on silicon and gold substrates. Deviations from unity in the silicon spectra confirm the stronger film inhomogeneities. These spectra were therefore not used for quantitative evaluation. Spin-coated PGMA films on silicon and gold were also investigated with infrared microscopy and ellipsometry. These films show slight thickness variations in the nanometer

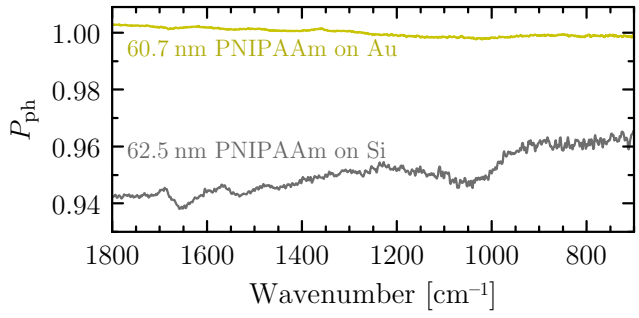

Figure 3.5: Degree of phase polarization P_{ph} of the 62.5 nm thick PNIPAAm film on Au and the 60.7 nm thick PNIPAAm film on Si, measured at $\varphi_0 = 65°$.

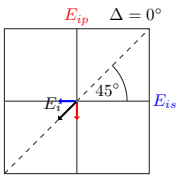

range as well. In contrast to PNIPAAm films, these variations seem to occur non-uniformly over the whole sample area rather than in a monotonic decrease towards the edges.

To conclude, outside the center area of the samples, the thickness variations of spin-coated PNIPAAm and PGMA films on gold—though demonstrable—are very small compared to the overall film thicknesses. They are therefore negligible with regard to upcoming infrared ellipsometry measurements, which probe the sample with a much larger spot size.

3.1.4. Optical constants in the infrared from spectroscopic ellipsometry

In order to determine the optical constants n and k of PGMA and PNIPAAm in the mid-infrared, spin-coated polymer films on gold substrates were measured ellipsometrically under three angles of incidence. The optical model for fitting these spectra consisted of gold substrate—with optical constants determined by inversion of gold reference measurements according to Eq. (2.81)—and isotropic oscillator layers for the polymer films with initial values for high-frequency refractive indices n_∞ as determined by VIS ellipsometry in Section 3.1.2. Each vibrational band was described by a Lorentzian oscillator with three free parameters: center frequency $\tilde{\nu}_0$, oscillator strength F, and dampening constant $\tilde{\Gamma}$. Bands like ν(NH) or subcomponents of amide bands that are strongly influenced by hydrogen bonding were

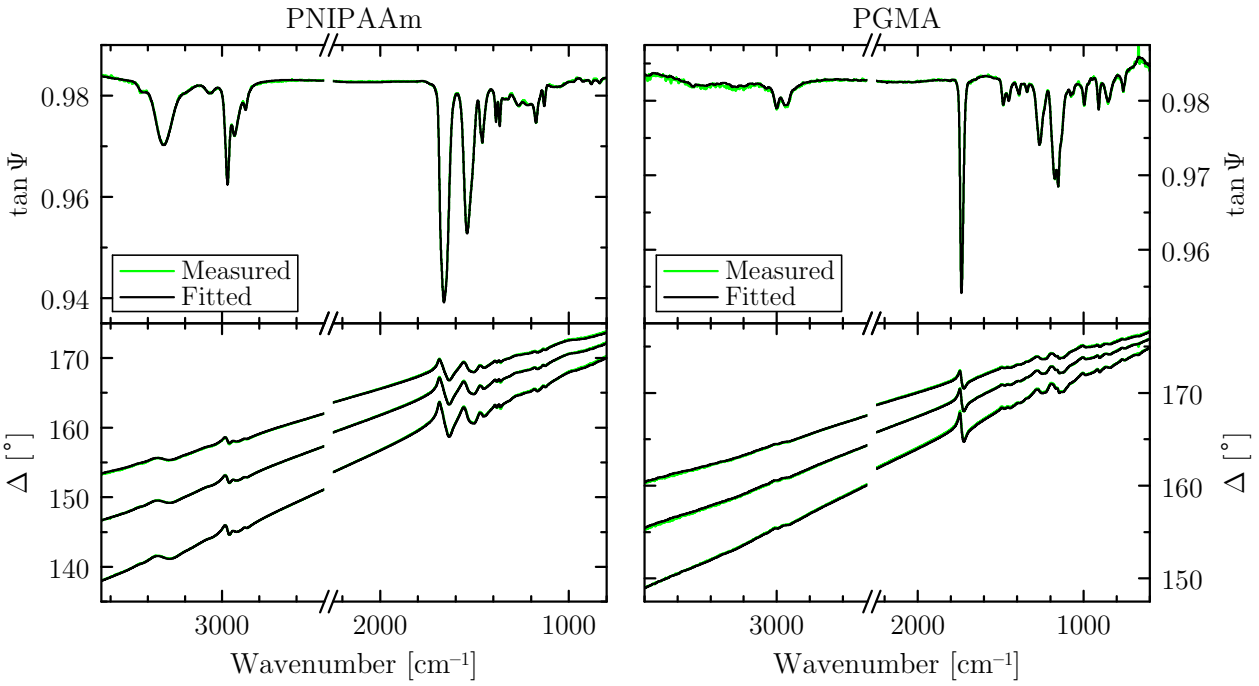

Figure 3.6: Measured and fitted $\tan\Psi$ at $\varphi_0 = 55°$ and Δ at $\varphi_0 = 55°$, 60°, and 65°, 2 cm^{-1} resolution, of the spin-coated 116 nm thick PNIPAAm film and the 55 nm thick PGMA film on Au substrate.

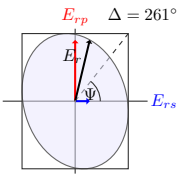

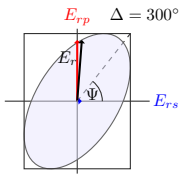

modeled using Gaussian oscillators [150, 159, 160] with analogous parameters $\tilde{\nu}_0$, $\tilde{\sigma}$, and $\tilde{F}$. A joint fit on layer thicknesses, high-frequency refractive index, and oscillator parameters was performed on the two PGMA samples and then on the two PNIPAAm samples using the PGMA fit results for the PGMA anchoring sublayer. Results for n_∞ are

$$\begin{aligned} \text{PGMA:} \quad & n_\infty = 1.5007 \pm 0.0070, \\ \text{PNIPAAm:} \quad & n_\infty = 1.4832 \pm 0.0060. \end{aligned} \tag{3.2}$$

Figure 3.6 exemplarily shows measured and fitted tan Ψ and Δ spectra of the 116 nm thick PNIPAAm film and the 55 nm thick PGMA film on gold substrate. Measurements and fit are in very good agreement. No uniaxial anisotropy was found. In-plane anisotropy was ruled out by transmission measurements of spin-coated PNIPAAm films on flat silicon (100) wafers. Importantly for the isotropic fit, the amide I and II bands could be described by respectively three and two subcomponents. These correspond to free and hydrogen-bonded C=O and N−H groups, details of which will be discussed in Section 3.1.5.

The optical constants of PNIPAAm and PGMA derived from the oscillator parameters of the fit are displayed in Fig. 3.7. They serve as the starting input parameters for optical simulations concerning PNIPAAm brushes, temperature-dependent in-situ studies, and also humidity effects on PNIPAAm films, which are investigated in the next section.

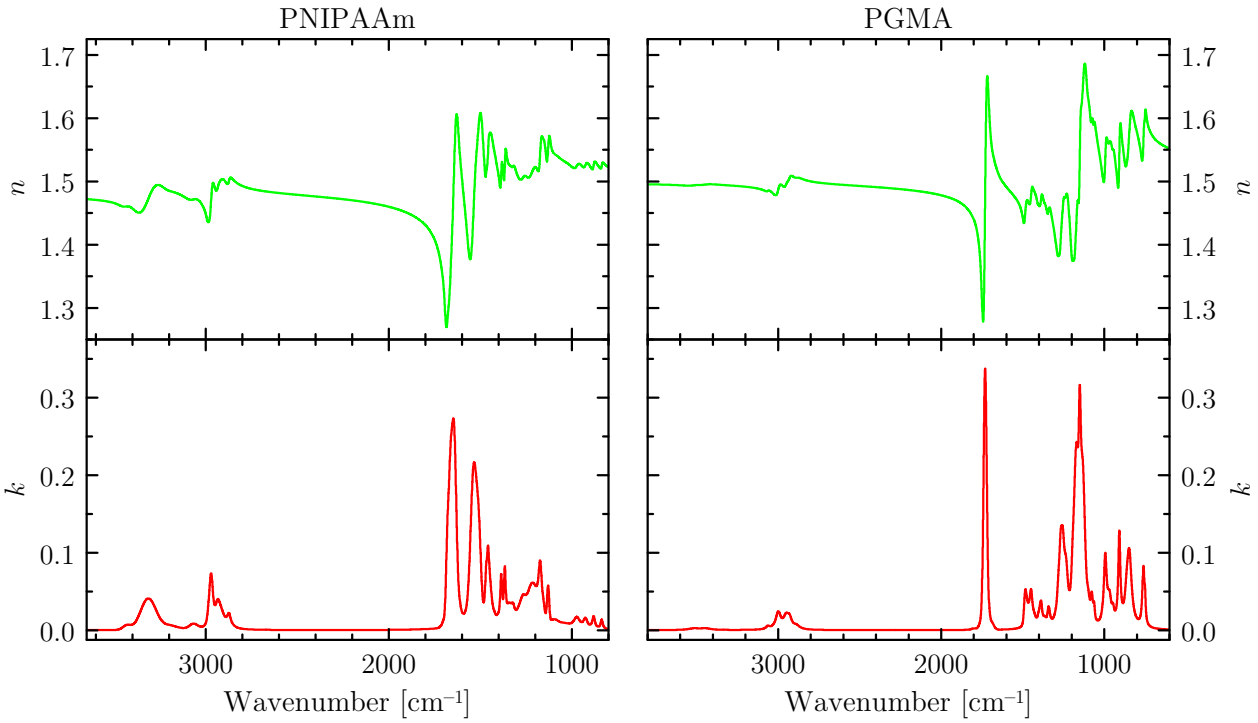

Figure 3.7: Optical constants n and k of spin-coated and annealed PNIPAAm and PGMA films in the mid-infrared as determined by infrared-spectroscopic ellipsometry at 2 cm^{-1} resolution.

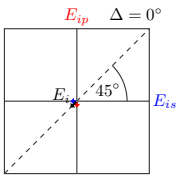

3.1.5. Humidity effects on PNIPAAm films

The hydration state of PNIPAAm in aqueous solutions is depending on temperature and other parameters [45, 50, 54, 60, 220]. Deswelling of solvated PNIPAAm chains, for example, can be induced by temperature changes around the LCST, leading to a coil-to-globule transition. Furthermore, PNIPAAm hydrogels and microgels are known to be swelling when being exposed to water or saturated water vapor [56–59, 61, 63]. It seems therefore natural to ask whether swelling is also possible for spin-coated PNIPAAm films in humid air. If so, characteristic changes in the polymer vibrational bands should enable one to draw conclusions about different polymer–water and polymer–polymer interactions. As will be shown in this section, swelling can occur in the supposedly *dry state* if the humidity is sufficiently high. This drastic effect was investigated with infrared microscopy for PNIPAAm films on gold and silicon substrates, and also for PNIPAAm brushes, as will be shown in Section 3.2.4.

Two typical reflectivity spectra of a PNIPAAm film in humid and dry state are shown in Fig. 3.8. Humidity affects positions and/or shapes of literally every vibrational band of PNIPAAm between 4000–1000 cm^{-1}. The potential causes for this are manyfold and include, for instance, changing polymer–water interactions, changes of water content within the film, as well as alterations of structural properties like swelling or deswelling. In order to understand the origin of these effects, a systematic study concerning interactions within the film is necessary. PNIPAAm films were therefore investigated in H_2O atmosphere as well as D_2O atmosphere at different humidities. This allows one to identify the various vibrational components associated with different polymer–polymer and polymer–water interactions. Furthermore, evaporating H_2O and D_2O drops were used to achieve higher water contents of the films and to confirm the results of the qualitative band analysis. After this, measured spectra are evaluated quantitatively to gain information about water content and—most importantly—humidity-dependent polymer–water interactions.

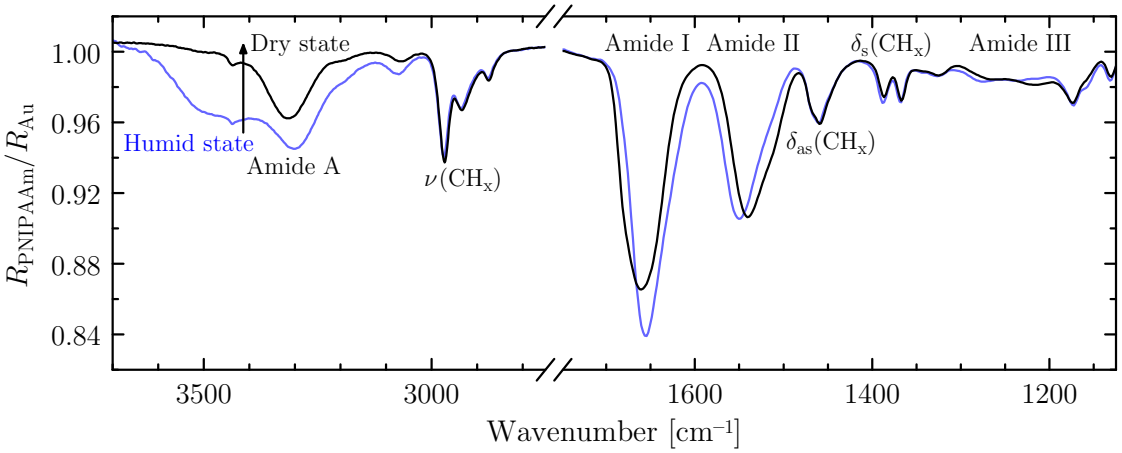

Figure 3.8: Effects of high (35%) and low humidity (< 2%) on the 116 nm thick PNIPAAm film on Au.

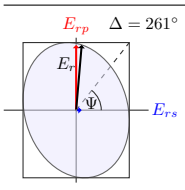

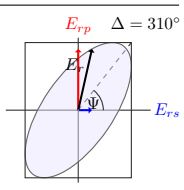

a) Qualitative band analysis

Measurements in H_2O atmosphere:

Figure 3.9 displays reflectivity spectra of the 116 nm thick PNIPAAm film on gold substrate in dependence of humidity (35% . . . < 2%). The stretching region $\nu(H_2O)$ of liquid water is visible as a broad asymmetric band at about 3450 cm^{-1} in humid state. With decreasing humidity, this band diminishes, thus proving the release of water from the film. $\nu(H_2O)$ is overlapping and thereby changing the apparent band positions and amplitudes in the ν(NH) region of PNIPAAm. Similarly, the bending vibration $\delta(H_2O)$ of water is masking the amide I vibration, partly shifting it to lower wavenumbers and also distorting its amplitude.

Interactions between water and polymer within the polymer film manifest themselves in changes in frequency and shape of the amide bands as well as the CH_x vibrational bands, similar to PNIPAAm in aqueous solutions [45, 50, 60]. The vibrational components of amide I, II, and III are strongly affected by interactions. The amide I band arises primarily from C=O-stretching, while the amide II band contains mainly a coupling between in-plane N−H-bending and C−N-stretching [50, 204, 205, 213]. C=O and N−H groups can form hydrogen bonds with one another and with neighboring water molecules [221, 222]. Alterations in the spectral composition of the amide bands are therefore a direct measure of the hydration state, correlating with hydrogen-bond strength and electron density on the bonds [50, 215]. In dry state, intra- and interchain hydrogen bonding >C=O · · · H−N< can occur. If water is present, additional >N−H · · · OH_2 and >C=O · · · H_2O bonding is possible [223, 224] and may even be favored energetically, at least at temperatures below the LCST.

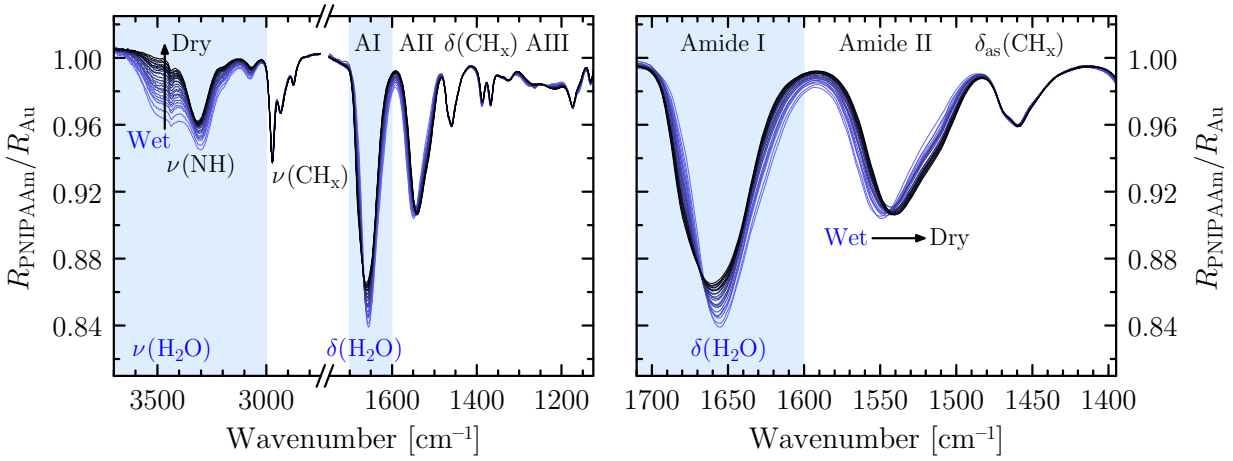

Figure 3.9: Effects of changing humidity on the 116 nm thick PNIPAAm film on Au measured with infrared microscopy. Regions of prominent liquid-water absorption are marked in light blue. The right plot shows a zoom of the amide I (AI) and amide II (AII) bands. Humidity was constantly reduced (starting at 35%) by increasing the rate of dry-air purging of the microscope chamber. All reflectivity spectra were baseline-corrected and also corrected for water-vapor absorption.

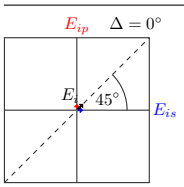

In general, hydrogen bonding lowers the frequency of stretching vibrations [ν(C=O), ν(NH)], since it lowers the corresponding restoring force, but it increases the frequency of bending vibrations [δ(NH)], because it introduces an additional restoring force [215]. In Fig. 3.9, the amide II band is shifting from 1549 cm^{-1} at 35% humidity to 1539 cm^{-1} in dry air (humidity < 2%). Specifically, Fig. 3.10 illustrates three amide II subcomponents as revealed by second-derivative analysis, shown in Fig. 3.11, all three of which are present in humid state, but only two of which are observed in dry state. The first component at 1544 cm^{-1} is found in both states and can therefore be assigned to N−H groups that are hydrogen-bonded to C=O groups. The second component at 1554 cm^{-1} is only present in humid state. It is, thus, reasonable to assign it to N−H groups hydrogen-bonded to water. At higher humidity, this component slightly shifts to higher wavenumbers, in agreement with ν(NH) at 3314 cm^{-1}, which shifts to lower wavenumbers. The third component at 1509 cm^{-1} is also visible in both states, with less intensity at increasing humidity though. Different possible assignments are proposed in the literature [50, 60, 210, 225], but it is plausible to attribute it to *free* N−H groups [225], since it is not present in dilute PNIPAAm solutions [50, 225]. The aforementioned frequency shifts of amide II subcomponents induced by hydrogen bonding are visualized in Fig. 3.10.

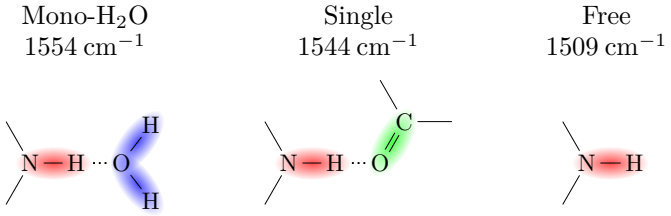

Figure 3.10: Frequency shifts of amide II subcomponents (N−H-bending) due to hydrogen bonding of N−H groups to O=C groups and water molecules.

Assignments of vibrational bands and band shifts in the amide I region are more complicated owing to effects of the overlapping water-bending vibration $\delta(H_2O)$ at about 1650 cm^{-1}. Next to this *free*-water contribution, which is too broad to be accessible with second-derivative analysis, one would expect at least eight other components in humid state that add to the amide I envelope. The first two components stem from stretching vibrations of C=O groups that form hydrogen bonds with either water, >C=O · · · H_2O<, or neighboring amide groups, >C=O · · · H−N<. Since oxygen atoms in C=O groups can form up to two hydrogen bonds, two additional respective components should occur. A fifth component arises from C=O groups that form *mixed* hydrogen bonds, that is, one with water and one with H−N. The sixth component is due to stretching vibrations of *free* C=O groups that are not involved in any hydrogen bonding. Finally, the last two components arise from water-bending vibrations for which changes in the force constant are caused by OH_2 · · · O=C or H_2O · · · H−N hydrogen bonding.

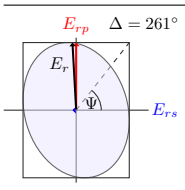

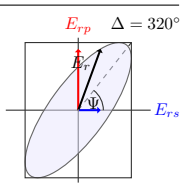

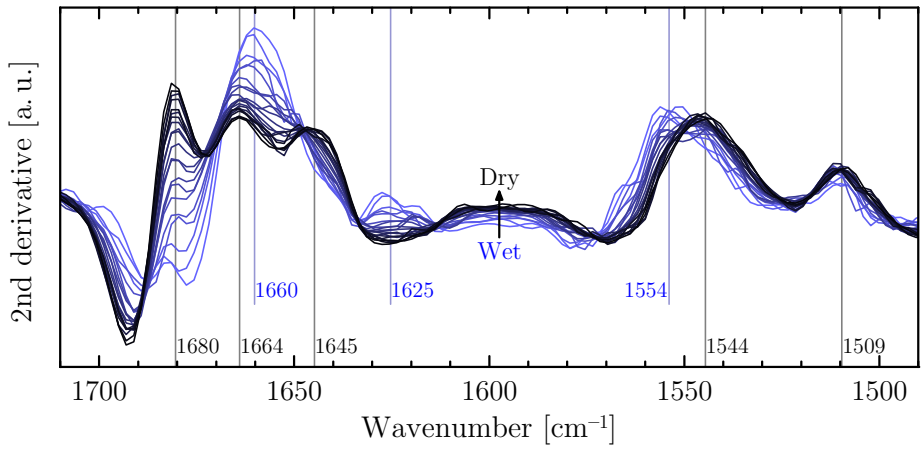

Figure 3.11: Second-derivative spectra corresponding to the 116 nm thick PNIPAAm film on Au in Fig. 3.9 showing band-component changes in the amide I and II region during changing humidity.

Five components are observable in the second-derivative spectra at wavenumber positions 1680 cm^{-1}, 1664 cm^{-1}, 1660 cm^{-1}, 1645 cm^{-1}, and 1625 cm^{-1}. Three further minor contributions at 1698 cm^{-1}, 1684 cm^{-1}, and 1654 cm^{-1} are visible in humid state. They are, however, not reliable for interpretation, considering the signal-to-noise ratio of the original spectra and possible 2nd-derivative artifacts due to residual water-vapor absorption. Also, the components at 1664 cm^{-1} and 1660 cm^{-1} are overlapping closely, that is, the latter might actually occur at slightly lower wavenumbers.

Katsumoto et al. [225] performed quantum chemical calculations for NIPAAm dimers in dry and solved state. They found various vibrational components corresponding to free and hydrogen-bonded C=O groups as well as two vibrations that are likely to be due to O−H bending of water molecules bonded to amide groups. These findings coincide with the single-bonded components found in the 2nd-derivative spectra of Fig. 3.11, meaning that at a certain humidity level, polymer–water interactions start to resemble these of PNIPAAm in solution. It is, however, not clear how their results translate to polymer chains in which C=O groups can form more than one hydrogen bond to neighboring N−H groups.

Similar to Hashimoto et al. [60], it is temptative to assign the bands at respectively 1680 cm^{-1}, 1664 cm^{-1}, and 1645 cm^{-1} to free (non-bonded), single-bonded, and double-bonded C=O groups in dry state, whereas the bands at 1660 cm^{-1} and 1625 cm^{-1} might be assigned to C=O groups that are involved in mono- or dihydrogen bonding with water, respectively (this nomenclature must not be confused with dihydrogen bonds of the type $X_1{-}H\cdots H{-}X_2$ [226, 227]). With increasing humidity, the free-water contribution at about 1650 cm^{-1} begins to influence the observed band positions at 1660 cm^{-1} and 1625 cm^{-1}, shifting the former to lower and the latter to higher wavenumbers. Given the relative amplitude of $\delta(H_2O)$ compared to $\nu(H_2O)$ [228] and its contribution to the amide I envelope, the

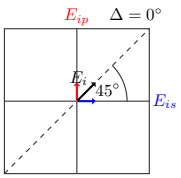

signatures of the two additional water-bending vibrations might be too small to be observable at the current signal-to-noise ratio and the used resolution of 4 cm^{-1}. It is also unclear at this moment whether the band at 1660 cm^{-1} originates solely from C=O groups with mixed hydrogen bonds ("C=O $\cdots$ H−N hydrogen bond weakened by hydration" in Hashimoto's nomenclature [60]) or if it also contains contributions from monohydrogen-bonded C=O groups (>C=O $\cdots$ H_2O) with a free lone pair of electrons. The small component at 1654 cm^{-1}, which is visible at low humidity, might be ascribable to the latter contributions.

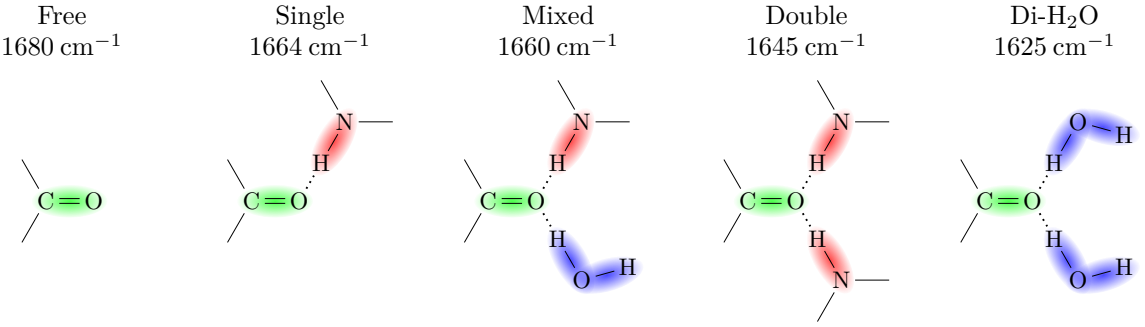

Figure 3.12: Frequency shifts of amide I subcomponents (C=O-stretching) due to hydrogen bonding of C=O groups to H−N groups and water molecules.

The above assignments, visualized in Fig. 3.12, are supported by comparing the relative peak intensities of the several second-derivative amide I and II components. It is known for NIPAAm monomers in aqueous solutions that isolated free N−H groups still exist up to certain water concentrations [60]. One would therefore expect only small changes in the corresponding band at 1509 cm^{-1} upon increasing humidity. Furthermore, C=O groups of PNIPAAm can form two hydrogen bonds, whereas N−H groups can form only one. The same holds for oxygen and hydrogen atoms of water molecules. Therefore, the amount of free C=O groups (1680 cm^{-1}) should decrease significantly, preceding the decrease of free N−H groups and the nearly isosbestic conversion between amide–amide-bonded (1544 cm^{-1}) and amide–water-bonded (1554 cm^{-1}) N−H groups with increasing humidity. Starting at low humidity, hydration of C=O groups should result at first in the formation of monohydrogen or mixed hydrogen bonds (1660 cm^{-1}), since there are not enough water molecules available to form a water-hydrogen bond network that allows for dihydrogen bonding (1625 cm^{-1}). All of the aforementioned effects are observed in the spectra.

For unambiguous band assignments, complementary theoretical considerations and measurements at higher humidity seem necessary, though. Because the latter are not feasible at the current experimental conditions, the PNIPAAm film was also investigated under D_2O atmosphere subsequent to deuteration, which sheds more light onto the nature of hydrogen bonding within the film in the presence of water.

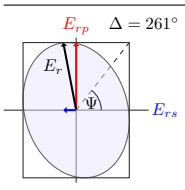

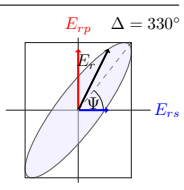

Lastly, it has to be mentioned that the binding of water from the atmosphere is a reversible process. Repeated measurements also show that changes in water content can occur within several minutes, provided a quick change in humidity. *Complete* drying, however, is observed only after at least 24 h. Even then, small amounts of water still seem to be bound within the film. It is not possible, though, to distinguish whether this residual water is due to the strength of the hydrogen bonds or due to residual water vapor within the microscope chamber.

Measurements in D_2O atmosphere:
N-deuteration [229, 230] (>N−H → >N−D) of the PNIPAAm film was achieved by pipetting a small drop of heavy water with a diameter of about 10 mm onto the polymer layer. Since the water-soluble PNIPAAm was not grafted completely to the PGMA bottom-layer, it accumulated in the center of the water drop upon evaporation, thus forming a film with a certain thickness gradient. After ca. 90 min, full *N*-deuteration of the dried film was verified by the absence of N−H-specific vibrations, such as the amide A and II bands. For comparability of spectra to measurements in H_2O atmosphere (Figs. 3.9 and 3.11), a sample position was chosen that lead to similar band amplitudes in the CH_x-stretching and amide I regions. Paper towels placed inside the purged microscope chamber (H_2O humidity < 2%) were then soaked with D_2O, which upon evaporation created D_2O-atmospheric conditions. Humidity was estimated to be approximately 20% by comparing the amplitudes of water-vapor-specific D_2O and H_2O bands in the respective gold-reference single-channel spectra.

Reflectivity spectra and corresponding second-derivative spectra obtained between humid and dry state are shown in Figs. 3.13 and 3.14. Deuteration of amide groups causes obvious alterations in the amide bands of PNIPAAm. The amide II band, which is stated to be the out-of-phase resonance between in-plane N−H-bending and C−N-stretching [204, 205], is completely absent. Also amide A and B as well as other combination bands that involve N−H-bending or -stretching vibrations are no longer present.

Four distinct regions of new vibrational bands are observed in the measured spectra after deuteration. One band at 1163 cm^{-1} replaces the band at 1174 cm^{-1}, which is of unknown origin. A second broad contribution at 1367 cm^{-1} is located at exactly the same position as the symmetric CH_2-bending vibration, thereby altering the apparent amplitude ratio between $\delta_s(CH_3)$ at 1387 cm^{-1} and $\delta_s(CH_2)$. Both new bands at 1163 cm^{-1} and 1367 cm^{-1} are almost unaffected by humidity. The intense amide II' band at about 1450 cm^{-1} is overlapping with the asymmetric CH_x-bending vibrations at 1467 cm^{-1} and 1459 cm^{-1}. Four additional components are observed within the amide II' envelope at wavenumbers 1470 cm^{-1}, 1449 cm^{-1}, 1427 cm^{-1}, and 1406 cm^{-1}. These components partly show a strong dependence on humidity, as will be discussed in a moment. Bands in the amide A region of the undeuterated film are replaced by their deuterated counterparts that appear between 2120 cm^{-1} and 2720 cm^{-1}. This ν(ND) or amide A' region [207] is strongly overlapped by the stretching region $\nu(D_2O)$ of heavy water, which occurs within the same spectral window. The D_2O-stretching region

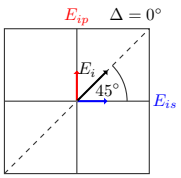

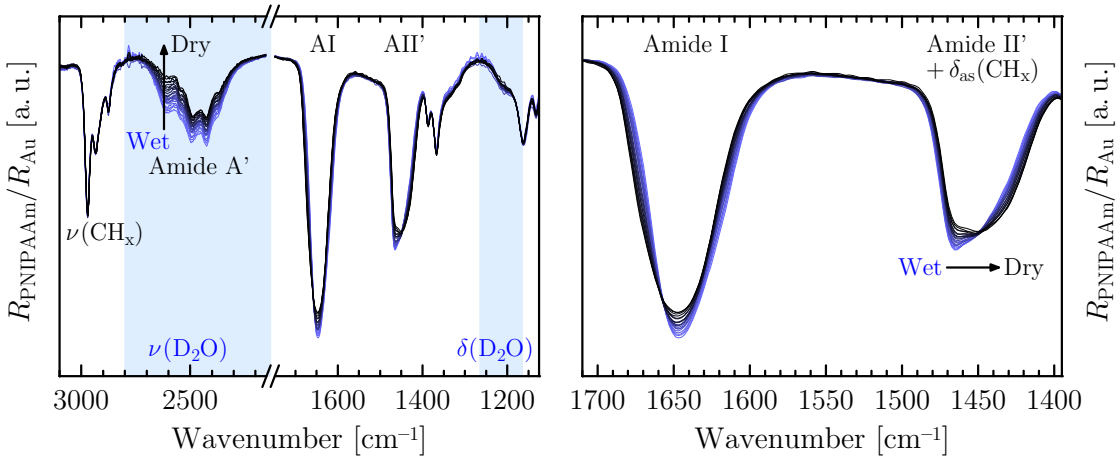

Figure 3.13: Effects of changing D_2O humidity on a deuterated PNIPAAm film on Au measured with infrared microscopy. Regions of prominent liquid-water absorption are marked in light blue. The right plot shows a zoom of the amide I (AI) and amide II' (AII') bands. All reflectivity spectra were baseline-corrected and corrected for atmospheric CO_2 absorption between 2300–2385 cm^{-1}.

itself exhibits several major vibrational components [228] that make it difficult to analyze the polymer vibrational bands. The amide A' region comprises at least five components observed in dry state at 2611 cm^{-1}, 2547 cm^{-1}, 2491 cm^{-1}, 2424 cm^{-1}, and 2366 cm^{-1}, where the first component at 2611 cm^{-1} appears to consist of two closely located subcomponents. The band at 2366 cm^{-1} might be overlapped by slight residues from asymmetric CO_2-stretching between 2300–2385 cm^{-1}. The origin of the amide A' components is not yet fully understood.

Band assignments for the deuterated film are, in general, rather intricate. However, some similarities to the undeuterated film are expected and also observed. Since the amide I band arises mainly from C=O-stretching, it should exhibit an almost identical spectral composition in both the deuterated and the undeuterated case. Indeed, the amide I band still consists of three (slightly shifted) major components at 1673 cm^{-1}, 1658 cm^{-1}, and 1632 cm^{-1} in dry state and two major components at 1655 cm^{-1} and 1617 cm^{-1} in humid state. Their intensities also scale similarly with humidity. It is therefore reasonable to assign the first three bands to free, single-bonded, and double-bonded C=O groups, that is, to intra- or interchain >C=O···D−N-bonded carbonyl groups. The last two bands are assigned to monohydrogen- and dihydrogen-bonded C=O groups with D_2O, i. e., >C=O···D_2O. Upon deuteration, N−D-bending is shifting to lower wavenumbers compared to N−H-bending. Small contributions of in-plane N−H-bending to the amide I band [215], then, explain the sensitivity of this band towards *N*-deuteration and why the observed band components show downshifts of about 6–13 cm^{-1}. At 1638 cm^{-1}, a minor contribution is visible at low humidity that might correspond to the small component at 1654 cm^{-1} in H_2O-atmospheric measurements, possibly indicating monohydrogen-bonded C=O groups with one free lone pair of electrons.

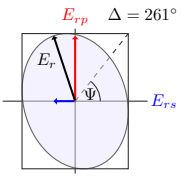

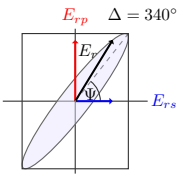

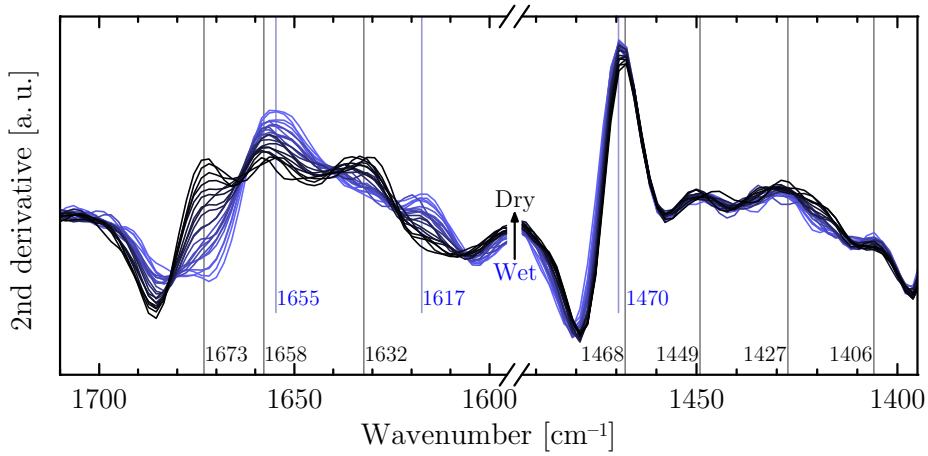

Figure 3.14: Second-derivative spectra corresponding to the deuterated PNIPAAm film on Au in Fig. 3.13 showing band-component changes in the amide I and II' region during changing D_2O humidity.

Contradictory assignments, if any, are discussed in the literature concerning vibrational bands that arise from major contributions of N−D modes. Based on theoretical calculations on NMA (*N*-methylacetamide), some authors state that N−D-bending—due to its shifted frequency—no longer couples to C−N-stretching (or couples less) [208, 215, 231], whereby the amide II band is instead replaced by the unperturbed ν(CN) vibration at about 1470 cm^{-1} (amide II') and the δ(ND) vibration at about 970 cm^{-1} (amide III') [204, 208], the latter of which mixes with other bands in the 1070–900 cm^{-1} region [215]. Completely opposite reasoning assigns the amide II' band to the coupling of N−D-bending and C−N-stretching [232]. Other authors assign the band solely to N−D-bending [225], to C−N−D-bending [233], or to N−D-bending coupled via Fermi resonance with other unspecified vibrations [234].

Amide II' shows certain similarities compared to the undeuterated amide II band. While the component at 1449 cm^{-1} is only slightly affected by humidity, a strong correlation is observed between the dry-state component at 1427 cm^{-1} and the humid-state component at 1470 cm^{-1}. The effects of humidity on amide II' resemble the previously discussed behavior of the amide II band. This suggests that amide II' contains non-negligible contributions from N−D-bending. The 1427 cm^{-1} component might be assigned to free N−D groups, whereas the components at 1449 cm^{-1} and 1470 cm^{-1} might be assigned to amide–amide- and amide–D_2O-bonded N−D groups, respectively. In order to better distinguish the latter two components, additional measurements with higher water content within the film were performed, as will be discussed later. Unambiguous assignments in the amide II' region are also complicated owing to the spectral overlap with $\delta_{as}(CH_x)$. This requires optical simulations, which are not straightforward, though, due to film inhomogeneities. It is noteworthy that the non-overlapped CH_x-bending region of the undeuterated film also contains three minor components at about 1442 cm^{-1}, 1425 cm^{-1}, and 1407 cm^{-1}. Their origin, however, is

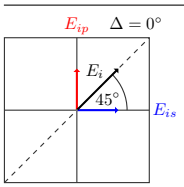

yet unclear. Theoretical considerations like density-functional-theory calculations might aid reliable band assignments in this region.

Discussions of band components in the amide A' region are usually avoided in the literature, which is partly due to the overlapping water-stretching vibrations. Deuteration studies on nylon-66 [229] and other polyamide films [208, 235] show that the two major components of this region arise from Fermi resonance between N−D-stretching and a combination mode of amide II' + amide III' ($1470\,\mathrm{cm}^{-1} + 970\,\mathrm{cm}^{-1}$). For the measured deuterated PNIPAAm films, however, no unequivocal band is visible in a wide range around $970\,\mathrm{cm}^{-1}$, and band assignments in the amide II' and III' regions are generally not certain at the moment. It is therefore difficult to identify the true origin of the coupling or resonance concerning the corresponding components at $2491\,\mathrm{cm}^{-1}$ and $2424\,\mathrm{cm}^{-1}$. In order to verify if these two bands are really connected via Fermi resonance, one needs to perform temperature-dependent measurements in dry state over a large temperature range, which will be the aim of future studies. The wavenumber position of N−D-stretching is expected to increase with temperature due to weakening of the hydrogen bonds [208, 214, 229]. Therefore, the resonance with the combination band should be disrupted and the doublet be replaced by a single band.

Despite the aforementioned uncertainties, one nevertheless expects at least two contributions within amide A' that correspond to the stretching vibrations of free and hydrogen-bonded N−D. The observed bands at $2547\,\mathrm{cm}^{-1}$ and $2424\,\mathrm{cm}^{-1}$ might be assigned to these vibrations with the following reasoning: Observed absorption frequencies of single bonds are, to first-order approximation, proportional to the square root of force constant divided by reduced mass μ [156, 203], with $\mu = m_1 m_2/(m_1 + m_2)$. Provided that the force constants of N−H- and N−D-stretching are approximately equal, one therefore expects $\nu(\mathrm{ND})_\mathrm{f}$ and $\nu(\mathrm{ND})_\mathrm{b}$ to be located at about $2510\,\mathrm{cm}^{-1}$ and $2420\,\mathrm{cm}^{-1}$, respectively.

In summary, the measurements under D_2O atmosphere substantiate the band assignments for the amide I and II regions of the undeuterated film. Assuming similar interactions between the two water species and the polymer, the observations on the spectral composition of amide I and II/II' allow one to assign distinct bands that correspond to amide–amide- as well as amide–water-interacted C=O and N−H/N−D groups. How these bands change in amplitude depending on humidity has been sufficiently demonstrated. Nevertheless, measurements at yet higher water content of the polymer film should further clarify polymer–water interactions. For this reason, the evaporation of water (heavy water) films from an undeuterated (deuterated) PNIPAAm layer is examined next.

Evaporating water films:
Measurements of aqueous PNIPAAm solutions [50] show that the amide I and II bands each consist essentially of one vibration located at about $1620\,\mathrm{cm}^{-1}$ and $1555\,\mathrm{cm}^{-1}$, respectively. Compared to the results discussed above, these vibrations correspond to dihydrogen-bonded C=O groups and monohydrogen-bonded N−H groups with water. This is expected from

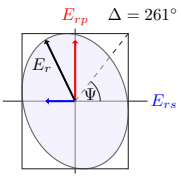

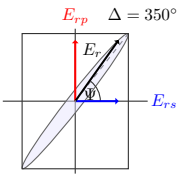

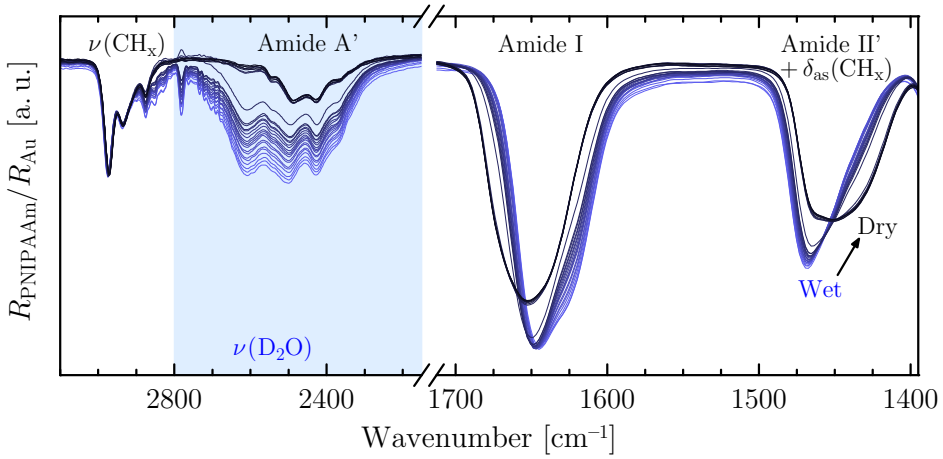

Figure 3.15: Evaporating D_2O drop from a deuterated, ≈ 200 nm thick, PNIPAAm film on Au substrate measured over a period of 80 min. A quick release of water is indicated by the sudden jump in $\nu(D_2O)$ amplitude and amide I/II' positions and shapes. Artifacts from D_2O vapor caused by evaporation are visible between 2700–2900 cm^{-1}. All spectra were corrected for atmospheric CO_2 absorption between 2300–2385 cm^{-1}.

investigations on NMA solutions, which establish that the carbonyl oxygen atoms are normally solvated by two water molecules [236], although the interaction potential of a single H_2O molecule favors a linear hydrogen bond [221].

Evaporating water films from PNIPAAm layers were investigated in order to verify whether dihydrogen-bonded C=O groups are also favored for PNIPAAm films at higher water contents. In-situ spectra of an evaporating D_2O drop are displayed in Fig. 3.15 and reveal drastic changes in the amide regions of PNIPAAm. Initially, the prominent stretching region $\nu(D_2O)$ clearly indicates the presence of large amounts of water, either within the film, on top of it, or both. Larger band shifts of amide I and II compared to measurements in humid air, though, show that significantly more water molecules are interacting with the polymer. Moreover, the amide I component at 1620 cm^{-1} (dihydrogen-bonded C=O) is gaining intensity at higher water content, while the component at about 1650 cm^{-1} (mixed hydrogen-bonded C=O) stays almost constant. Second-derivative analysis even shows that the 1650 cm^{-1} component starts to decrease in amplitude, which suggests a conversion from mixed- to dihydrogen-bonded C=O groups. This substantiates that the amide carbonyl groups of PNIPAAm are preferably solvated by two water molecules if the water content is sufficiently high. Concomitantly, the components at 2547 cm^{-1} in the amide A' band and 1427 cm^{-1} in the amide II' band further decrease in amplitude. Their previous assignments to free N−D-stretching and a free-N−D-bending contribution to amide II' therefore seem justified.

At a certain point during water evaporation, a sharp transition between hydrated and *almost-dry* state occurs within less than 2 min, as is evident from Fig. 3.15. This can be explained by the following proposed model for the several stages of the evaporation process,

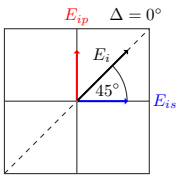

represented schematically in Fig 3.16. After pipetting a drop of water onto the polymer layer, the polymer film becomes strongly hydrated by water molecules and is covered with a bulk-water film. Diffusion of PNIPAAm chains into that film is expected to be slow. The topmost water layer is therefore considered to be almost free of polymer. Importantly, diffusion of water is in equilibrium between polymer–water layer and bulk water. In contrast, there is a high concentration gradient of water between water top-layer and dry air of the microscope chamber, leading to evaporation of the water drop. As the drop size decreases, the location of the highest concentration gradient moves towards the polymer–water interface, resulting in diffusion of water molecules out of the polymer film into the water top-layer. This is in agreement with a decreasing amount of dihydrogen-bonded C=O groups (1620 cm^{-1}), which indicates a slow dehydration of the film. A sudden jump in amplitude and frequency of amide bands and $\nu(D_2O)$ then correlates with a quick release of water from the polymer layer due to the steep increase in concentration gradient of water, once the bulk-water film is gone. Only small amounts of water molecules remain bound within the polymer film. Complete drying is observed after additional purging for 40 min. This relatively long time period is related to the fact that the atmosphere inside the microscope was not completely dry during water evaporation (estimated 3–5% D_2O humidity from single-channel spectra).

The measurements show that the PNIPAAm film reacts very quickly upon changes in humidity or aqueous environment, which is of interest for possible applications.

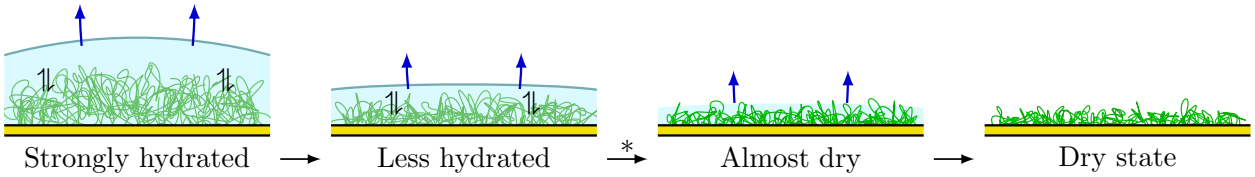

Figure 3.16: Proposed model of an evaporating water drop from a PNIPAAm layer, showing a sharp transition (∗) between hydrated (swollen, amide–water interacted) and dry (collapsed, amide–amide interacted) state. The thick blue arrows indicate diffusion of water molecules into the dry air, whereas the black double arrows represent the equilibrium of water diffusion between polymer–water film and bulk water.

A final analysis concerns the CH_x-stretching and -bending vibrations during D_2O evaporation. Their frequencies are highly indicative for the current solvation state of PNIPAAm. Maeda et al. [50, 237] observed band shifts to lower wavenumbers occurring above the LCST of PNIPAAm in aqueous solution. They correlated these shifts to a dehydration of the isopropyl groups, which is supported by ab-initio calculations [238]. Upon evaporation of the D_2O film, similar downshifts are detected. Corresponding in-situ second-derivative spectra are displayed in Fig. 3.17. Most prominent red shifts occur for $\nu_{as}(CH_3)$ [4 cm^{-1}] and $\nu_{as}(CH_2)$ [3 cm^{-1}] as well as for $\delta_s(CH_3)$ and $\delta_s(CH_2)$ [2 cm^{-1}]. These shifts further demonstrate the water-binding capabilities of PNIPAAm films.

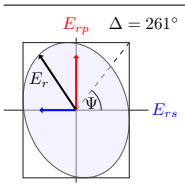

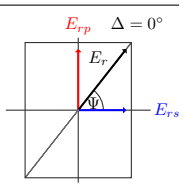

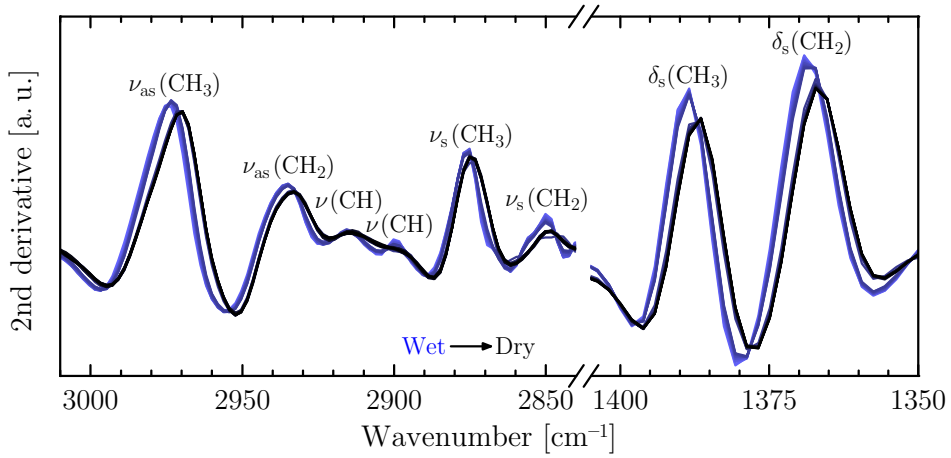

Figure 3.17: 2nd-derivative spectra of the CH_x-stretching and -bending regions during evaporation of a D_2O film from a deuterated, ≈ 500 nm thick, PNIPAAm film on Au. Small artifacts of D_2O vapor overlap from 2800-2900 cm^{-1}.

Spectra of evaporating H_2O films from undeuterated PNIPAAm layers (see Appendix F.) show essentially the same characteristics as discussed for the D_2O case. Notably, the almost complete conversion from free N−H groups (1509 cm^{-1}) in dry state to hydrogen-bonded N−H (1554 cm^{-1}) in wet state supports the band assignments in the amide A and II regions.

b) Quantitative band analysis

Swelling in H_2O atmosphere:

Compared to gold substrates, film-interference effects [129] for polymer films below ≈ 200 nm thickness are more obvious when using silicon instead. Changes in the onset of the interference pattern allow one to sensitively monitor swelling and deswelling. To verify humidity-dependent swelling, the 117 nm thick PNIPAAm film on silicon was measured between 35% and < 2% humidity, as shown in Fig. 3.18. In humid state, the presence of water within the film is again evident from the broad $\nu(H_2O)$ band around 3500 cm^{-1}. Thickness interference is clearly visible as a slope in the baselines. Between 35% humidity (light blue line) and dry state (black line), this slope is decreasing distinctly, proving the deswelling of the film.

From reflectivity spectra referenced to the initial humid state (lower part of Fig. 3.18), the changes in baseline slope are even more evident. Downward- and upward-pointing bands respectively amount to decreasing and increasing contributions of a spectral component with respect to the humid starting conditions, whereas sigmoidal shapes indicate band shifts or overlapping amplitude changes. Band shifts are observed in the amide as well as the CH_x-stretching and -bending regions of PNIPAAm. To be specific, the largest CH_x vibrational shifts occur for bands associated with the isopropyl groups. $\nu_{as}(CH_3)$, for instance, shifts

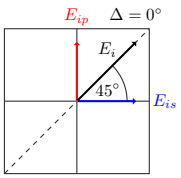

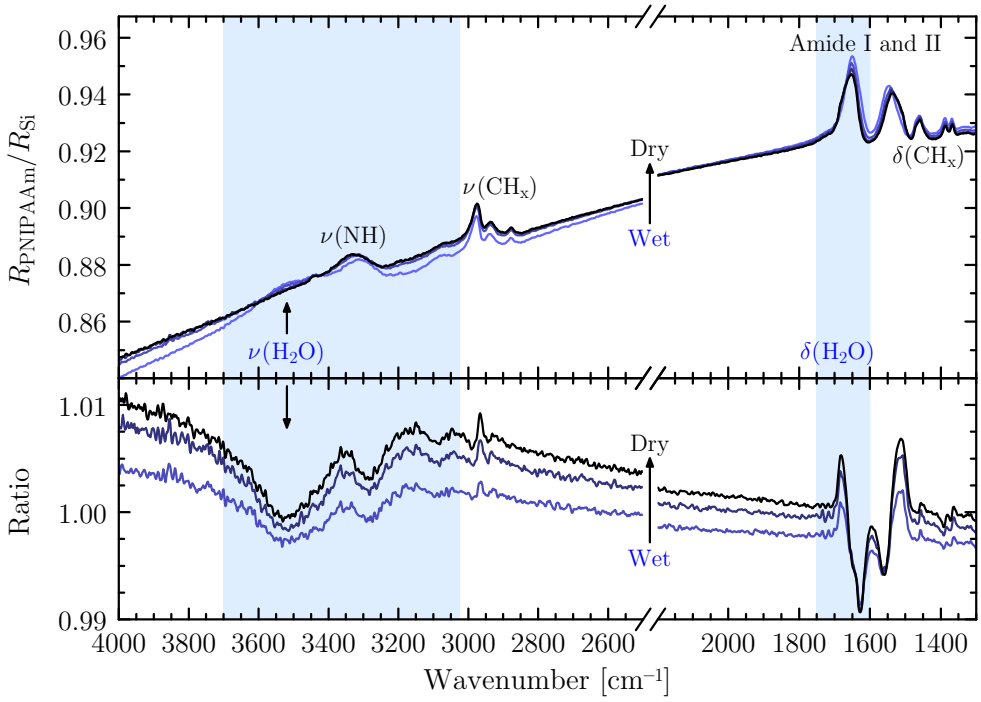

Figure 3.18: Effects of changing humidity on the 117 nm thick PNIPAAm film on Si. The top part shows four reflectivity spectra ranging from 35% humidity (light blue line) to dry-air conditions (black line, baseline-corrected). Referenced spectra with respect to the humid starting conditions are plotted in the lower part and clearly demonstrate the release of bound water (changing $\nu(H_2O)$ intensity) and deswelling of the film (changing baseline slope) accompanied by shifts in the amide, $\nu(CH_x)$, and $\delta(CH_x)$ vibrational bands of PNIPAAm.

from 2973 cm^{-1} down to 2971 cm^{-1}, showing once more its sensitivity towards various hydration states, in accordance to measurements of PNIPAAm solutions below and above the LCST [50, 53, 237]. The amide I/II region exhibits an expected W shape that originates, on the one hand, from an overlap with the decreasing $\delta(H_2O)$ contribution and, on the other hand, from an upward shift of amide I (mostly due to free C=O groups) as well as a downward shift of amide II (more free N−H groups) upon the release of water from the film. The amide III band at 1260 cm^{-1} (not shown) is also affected in humid state, since it contains contributions from N−H-bending vibrations that shift to higher wavenumbers.

Optical simulations:
A quantitative analysis of the swelling behavior requires optical simulations that are based on an appropriate optical model. Usually in the literature, band fits are performed directly onto the reflectivity spectra using Gaussian band shapes. While this is to some extent justified as a first-order approximation for isotropic films of thicknesses below ≈ 100 nm, this method also has several drawbacks. First, optical effects like thickness-induced band shifts play an important role for thicker or inhomogeneous films and may lead to misinterpretations of

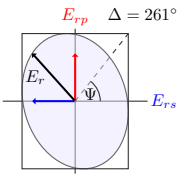

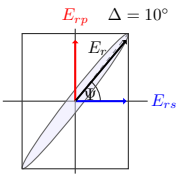

actual band positions and shapes. Second, out-of-plane anisotropy is normally neglected, but it becomes apparent that *p*-polarized reflectivity has potentially strong effects at non-normal incidence [134]. And finally, film thickness and quantitative material composition are not accessible directly. For these reasons, reflectivity spectra were simulated or fitted within an optical layer model that is based on the optical properties of the sample under investigation.

The modeling process of humidity-dependent reflectivity spectra consists of five parts. First, choosing a realistic optical model. Second, verifying that the *dry-state* spectrum can be simulated within that model using the optical constants n and k of PNIPAAm as previously determined by infrared ellipsometry (Section 3.1.4.). Third, estimating water content and thickness of the polymer film. Fourth, finding oscillator parameters for the additional amide components in humid state. And fifth, fitting the oscillator strengths of the amide I and II subcomponents to extract their relative contributions to the respective band envelopes.

The polymer–water film was modeled with a Bruggeman effective-medium approximation, which assumes a random mixture of polymer and water with variable volume fractions. Literature data were used for n and k of water at room temperature [166]. The observed strong band shifts of amide I and II indicate that hydration of the film affects not only the topmost layer, but indeed the whole film. Therefore, the film was modeled as a single layer without any gradient in volume fractions. The optical constants of the gold substrate were determined ellipsometrically. In the case of silicon substrate with native oxide layer, $n = 3.42$ and $k = 0$ were assumed for silicon [154], while literature data were used for the oxide [18].

Comparison of dry-state simulated spectra and measured spectra in Figs. 3.9 and 3.18 reveals a small downward shift of amide I and a small upward shift of amide II. At the same time, a slight deviation is observed around $3500\,\mathrm{cm}^{-1}$, which coincides with the $\nu(\mathrm{H_2O})$ region. This indicates that the purging of the microscope chamber was not sufficient to achieve a true dry state. A small amount of water still remained within the polymer film even after 24 h of purging. Hence, the final spectrum cannot be described solely by the dry-state optical constants. Additional humid-state oscillators are necessary.

Water content $f_{\mathrm{H_2O}}$ and swollen-film thickness $\tilde{d}$ in the simulated spectra were estimated by using the observed $\nu(\mathrm{H_2O})$ amplitude as a marker. Simultaneously, the baseline slopes in the referenced spectra were analyzed. It turns out that the PNIPAAm film on gold contains approximately $f_{\mathrm{H_2O}} = (1.0 \pm 0.5)$ vol% water in dry state and $f_{\mathrm{H_2O}} = (9.5 \pm 1.0)$ vol% in humid state with corresponding film thicknesses of $\tilde{d} = (119.0 \pm 0.5)$ nm and $\tilde{d} = (127.0 \pm 1.0)$ nm, respectively. Water contents and film thicknesses of the PNIPAAm film on silicon substrate are $f_{\mathrm{H_2O}} = (0.5 \pm 0.5)$ vol% and $f_{\mathrm{H_2O}} = (7.5 \pm 1.2)$ vol% as well as $\tilde{d} = (117.0 \pm 0.5)$ nm and $\tilde{d} = (125.0 \pm 1.5)$ nm. The smaller uptake of water and the smaller swelling degree might be explained by the film inhomogeneities shown in Appendix E.

In order to extract the oscillator parameters of the several amide components in humid state, the first measured spectrum of PNIPAAm on gold at approximately 35% humidity

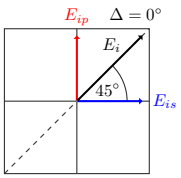

was evaluated. Two additional oscillators were used for the amide I band corresponding to stretching vibrations of C=O groups that form two hydrogen bonds with water and those that form mixed hydrogen bonds (amide–amide and amide–water). One additional oscillator was placed within the amide II band corresponding to N−H groups hydrogen-bonded to water. Positions, oscillator strengths, and band widths of the additional oscillators as well as oscillator strengths of the dry-state components were set as free fit parameters.

Table 3.4 gives an overview of the fitted oscillator parameters of dry-state and humid-state components obtained from infrared ellipsometry and microscopy, respectively. As expected, components that involve one or more hydrogen bond with water molecules exhibit broader band widths compared to free components. Fit errors in the amide II region are much smaller than in the amide I region, since amide I comprises three closely situated components in the center of its band envelope.

Band	Component	$\tilde{\nu}_0$ [cm^{-1}]	$\tilde{\sigma}$ [cm^{-1}]
Amide I	ν(C=O), free (no hydrogen bonds)	1678.2 ± 0.8	19.7 ± 0.9
	ν(C=O), single (bonded with H−N group)	1663.2 ± 0.5	18.6 ± 1.3
	ν(C=O), mixed (bonded with one H−N and one H_2O)	1657.0 ± 2.5	29.9 ± 1.9
	ν(C=O), double (bonded with two H−N groups)	1643.8 ± 0.4	30.6 ± 0.9
	ν(C=O), di-H_2O (bonded with two H_2O molecules)	1628.0 ± 0.6	35.6 ± 1.0
Amide II	δ(N−H), free (no hydrogen bonds)	1507.7 ± 0.2	25.5 ± 0.5
	δ(N−H), single (bonded with O=C group)	1532.9 ± 0.2	42.5 ± 0.4
	δ(N−H), mono (bonded with OH_2)	1542.9 ± 2.0	46.1 ± 1.3

Table 3.4: Oscillator parameters $\tilde{\nu}_0$ (center frequency) and $\tilde{\sigma}$ (band width) of amide I and II subcomponents obtained from fits on ellipsometric measurements in dry state (Section 3.1.4.) and microscopy measurements in humid state.

In the next step, reflectivity spectra of PNIPAAm on gold—including the final spectrum in the *almost-dry* state—were fitted using the amplitudes $\tilde{F}$ of the eight oscillators in Tab. 3.4 as free fit parameters, whereas oscillator positions and widths were being fixed. Furthermore, the amide A/B as well as the $\nu(CH_x)$ and $\delta(CH_x)$ regions were modeled by adjusting the corresponding oscillator positions and strengths.

Results of fitted and simulated spectra are displayed in Fig. 3.19. The left panel shows referenced spectra between the final dry state and the initial humid state for both the PNIPAAm film on gold and on silicon substrate. The change in baseline slope corresponding to changes in swollen-film thickness was successfully modeled, and generally good agreement between measured and simulated band shapes is found. Four results obtained from the simulations will now be discussed in detail.

First, the measured band shape of $\nu(H_2O)$ deviates slightly from the simulated one, which is based on the optical properties of bulk water [228]. This deviation can be explained by the

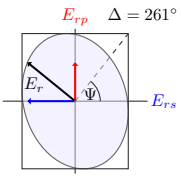

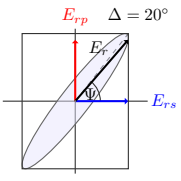

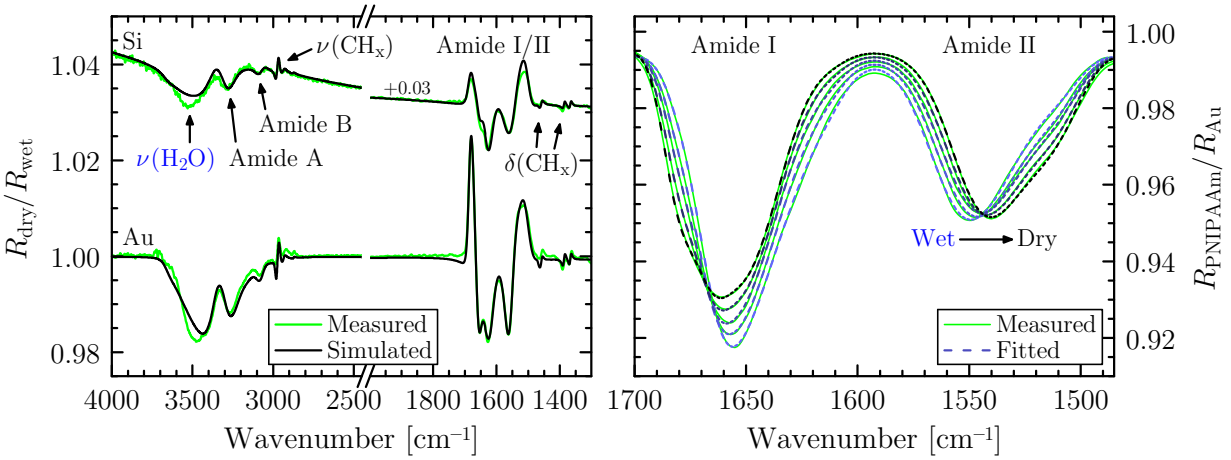

Figure 3.19: Measured and simulated/fitted reflectivity spectra of spin-coated PNIPAAm films in dependence of humidity. Left: Referenced spectra between final dry states and initial humid states corresponding to the 117 nm and 116 nm thick PNIPAAm films on Si (upper spectra, Cassegrain objective) and on Au (lower spectra, grazing-incidence objective), respectively. Right: Fitted amide I and II bands of the 116 nm thick PNIPAAm film on Au between 35% and < 2% humidity. Measured grazing-incidence spectra were scaled by a factor of 0.5 to account for the double reflection caused by the optical path within the objective (see Section 2.2.1.).

fact that the properties of bound water within the polymer film are dominated by polymer–water interactions. These interactions strongly influence the water-stretching vibrations, but also the bending and combination bands at respectively 1650 cm^{-1} and 2115 cm^{-1} [228]. Compared to the simulations, the measured combination band (not shown) exhibits a narrower band width, whereas ν(H$_2$O) seems to be shifted to higher wavenumbers with a simultaneous increase in amplitude. Similar effects were observed by Max and Chapados [239] who compared the spectral compositions of pure water and KCl-solvated water using factor analysis of ATR absorbance spectra. As an outlook, a combined set-up of infrared microscopy and visible ellipsometry would allow the determination of water content and swollen-film thickness with more accuracy. It would then be feasible to fit on the sub-vibrational bands of ν(H$_2$O) to characterize the effects of polymer–water interactions on water.

The second point concerns the CH$_x$-stretching and -bending regions. The sigmoidal band shapes in the referenced spectra correspond to band shifts of up to 2 cm^{-1} between humid and dry state. Table 3.5 lists the CH$_x$-oscillator positions before and after hydration of the film at 35% humidity. As discussed before, these shifts are a direct measure of the hydration state of PNIPAAm.

Third, due to the upward-shifting amide II band and the downward-shifting amide A band (N−H-stretching) with increasing humidity, the Fermi resonance between amide A and amide B—the first overtone of amide II—is enhanced. This causes an increase in oscillator strength by a factor of ≈ 1.6 for amide B and a decrease by a factor of ≈ 0.8 for amide A.

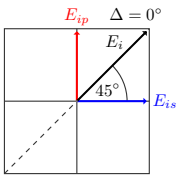

Band	Dry-state, $\tilde{\nu}_0$ [cm^{-1}]	Humid-state, $\tilde{\nu}_0$ [cm^{-1}]	Band shift [cm^{-1}]
$\nu_{as}(CH_3)$	2970.1	2972.1	+2.0
$\nu_{as}(CH_2)$	2934.6	2936.1	+1.5
$\nu_{s}(CH_3)$	2872.7	2873.2	+0.5
$\delta_{as}(CH_3)$	1468.3	1467.8	−0.5
$\delta_{as}(CH_2)$	1457.9	1458.9	+1.0
$\delta_{s}(CH_3)$	1386.0	1387.0	+1.0
$\delta_{s}(CH_2)$	1366.1	1366.9	+0.8

Table 3.5: Oscillator center frequencies $\tilde{\nu}_0$ of PNIPAAm's CH_x-stretching and -bending vibrations in dry and humid state obtained from optical simulations. The overall errors are estimated to be $\pm 0.6\,\mathrm{cm}^{-1}$.

Amide B is shifting from 3066 cm^{-1} in dry state to 3074 cm^{-1} in humid state, while amide A is shifting from 3313 cm^{-1} to 3296 cm^{-1}, showing its strong dependence on film hydration.

The final and essential point addresses the band composition of amide I and II. The right panel of Fig. 3.19 clearly shows that the measured band shapes can be described quantitatively using the eight oscillators of free, amide–amide, and amide–water interacted C=O and N−H groups. Figure 3.20 shows the progression of fitted oscillator strengths with increasing humidity, i. e., with increasing water content and swollen-film thickness. Comparing the relative changes in oscillator strengths, hydration of the film equally affects free and single-bonded C=O groups, whereas double-bonded C=O groups become hydrated much slower. Hydration of the latter seems to be faster, though, at higher water contents. Hydration of N−H groups mainly affects previously single-bonded groups. Even at 9.5 vol% water content, a significant amount of free N−H groups persists, which is in agreement with the small influence of hydration on $\nu(NH)_f$ at 3437 cm^{-1} in Fig. 3.9. Compared to free carbonyl groups, 50% of free N−H groups in dry state remain free at 35% humidity, whereas only 20% of free C=O stay non-hydrated. This might be explained by the fact that water offers twice as many hydrogen atoms for possible hydrogen bonding with C=O than oxygen atoms for N−H. Similarly, 15% of single-bonded N−H, 11% of single-bonded C=O, and 55% of the originally double-bonded C=O groups remain non-hydrated. Because single-bonded C=O groups have a free lone pair of electrons, hydrogen bonding between water and these groups is favored energetically over breaking the double-hydrogen bond between C=O and two H−N groups. Lastly, the amount of water-bonded N−H groups increases almost linearly with increasing humidity, as expected. The same is true for mixed-bonded C=O groups at low humidity. At a water content of about 6 vol%, however, this increase is slowing down. Simultaneously, the amount of dihydrogen-bonded C=O groups continuously increases at a faster rate. Extrapolating these findings, dihydrogen bonding seems to be favored at higher water contents such that the majority of C=O groups will be hydrated by two water molecules. Preliminary simulations of evaporating water films from PNIPAAm films support this hypothesis.

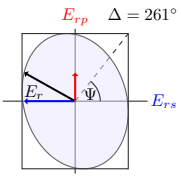

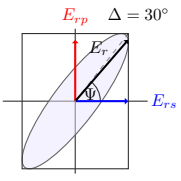

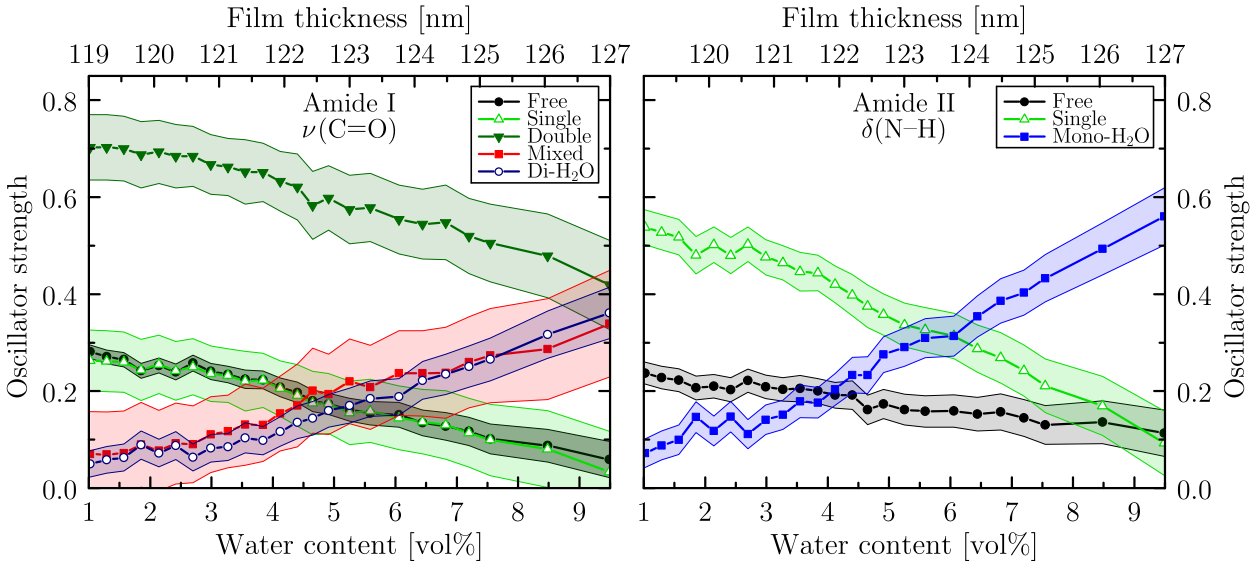

Figure 3.20: Fitted oscillator strengths of the amide I and II subcomponents in dependence of water content and thickness of the swollen $d_{\mathrm{dry}} = 116\,\mathrm{nm}$ thick PNIPAAm film on Au. Largest and smallest water content correlate with humidities of respectively 35% and $< 2\%$. Stretching vibrations of carbonyl components in amide I refer to C=O groups that are either free, single- or double-hydrogen-bonded to H−N groups, dihydrogen-bonded to H_2O, or mixed-bonded to both N−H and H_2O. Similarly, components of N−H-bending in amide II refer to N−H groups that are free, single-bonded to O=C groups, or monohydrogen-bonded to H_2O. Fit errors are marked as error bands. Estimated errors of water content and film thickness did not exceed ±1 vol% and ±1 nm. Data points are connected to guide the eye.

Summary:

In the first part, PNIPAAm films were measured with infrared microscopy in H_2O atmosphere and also in D_2O atmosphere after *N*-deuteration of the films. By means of second-derivative analysis, this allowed the identification of several subcomponents that make up the amide I and amide II/II' band envelopes in dry as well as in humid or wet state. These subcomponents correspond to amide–amide and amide–water interacted C=O and N−H groups, the relative amplitudes of which reflect the current hydration state of the PNIPAAm films. Measurements of evaporating D_2O and H_2O drops from PNIPAAm films substantiated the band assignments and gave insights into the diffusion equilibrium between polymer–water layer and water top-layer. In the second part, reflectivity spectra of PNIPAAm films were successfully modeled in dependence of humidity. Quantitative interpretation concerning water content, swollen-film thickness, and the complex composition of PNIPAAm's amide I and II bands was possible within the Bruggeman effective-medium approximation. Measured band shifts of CH_x-stretching and -bending vibrations that correlate with the hydration state could be reproduced. Finally, the various amide-oscillator contributions were analyzed, which yielded quantitative insights into changing polymer–polymer and polymer–water interactions.

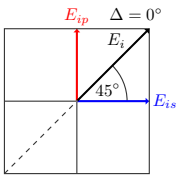

3.1.6. Temperature-induced structural changes

Temperature is known to have strong effects on the structural properties of PNIPAAm in aqueous solution [26, 50, 60]. A coil-to-globule transition is observed above the LCST, which manifests itself in changing polymer–water and polymer–polymer interactions. Hysteresis effects depending on temperature are also well established [50, 240]. Whether or not temperature induces similar effects in a PNIPAAm film of very low water content is investigated in this section.

Infrared microscopy combined with a temperature-controlled in-situ stage was used to record reflectivity spectra of the 132 nm thick spin-coated PNIPAAm film on flat silicon (100) substrate. Before the measurements, the film was exposed to humid air and therefore swollen to a certain extent. The cell was then purged with nitrogen gas for several minutes to remove residual water vapor. Using the optical layer model introduced in the previous section, the water content of the film was estimated to be approximately 1.5% in the initial state at 20 °C. Measurements were performed while heating the sample from 20 °C to 50 °C, then cooling it down to 5 °C, and finally heating it up to 20 °C again. Referenced reflectivities with respect to the initial state are depicted in Fig. 3.21.

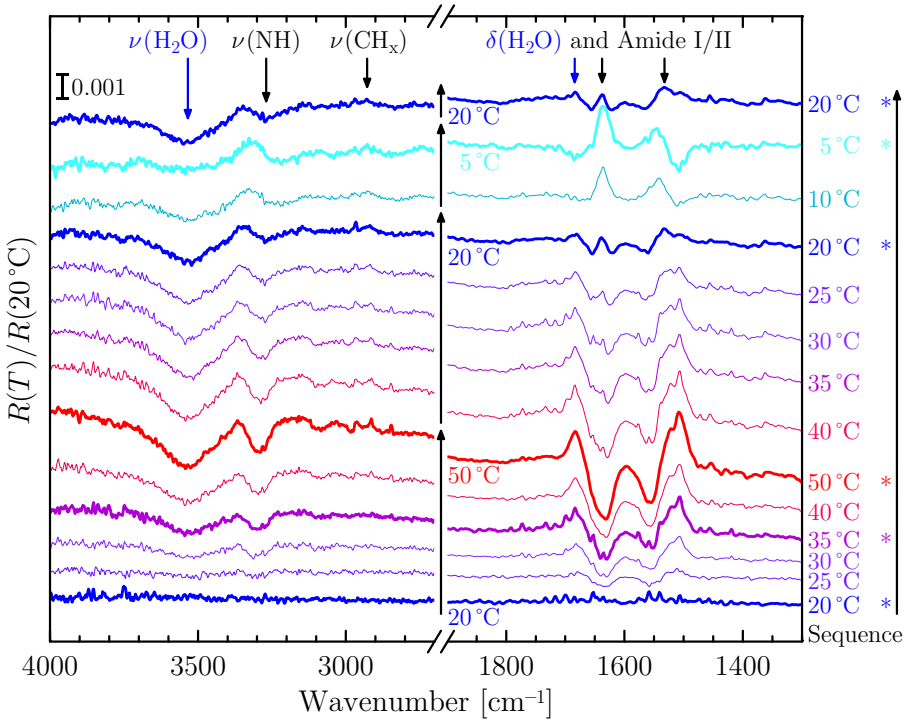

Figure 3.21: Temperature-dependent reflectivity of the 132 nm thick PNIPAAm film on Si (100) substrate. Spectra were referenced to the 2.2 nm thin PGMA film measured at the same temperatures and then also referenced to the initial state at 20 °C, thereby revealing changes with respect to that state. Spectra discussed in the text are marked (∗) and displayed as thicker lines.

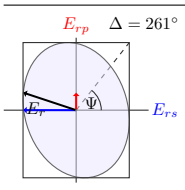

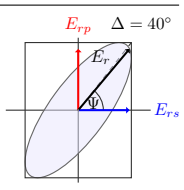

In the heating cycle to 50 °C, the overall spectral features resemble those observed in humidity-dependent measurements, as was shown in Fig. 3.18. Downward- and upward-pointing bands respectively refer to decreasing and increasing contributions of the corresponding spectral component, while sigmoidal shapes suggest band shifts. The release of water from the film is indicated by a decrease in $\nu(H_2O)$ amplitude, an upward-shift of $\nu(NH)$, downward-shifts of $\nu(CH_x)$, as well as a W shape of the amide I/II region caused by overlapping band shifts. Furthermore, the increasing baseline slope at higher wavenumbers correlates with a slight deswelling of the film. However, when cooling the film down to 20 °C again, the observed band changes and baseline slope are not reversed entirely.

At 5 °C, the water-stretching band $\nu(H_2O)$ reaches its initial amplitude, whereas the W shape of amide I/II is flipped. The strongly upward-pointing bands around 1636 cm^{-1} and 1547 cm^{-1}, which respectively correspond to hydrogen-bonded C=O and N−H groups, as well as the downward-pointing bands at 1678 cm^{-1} and 1509 cm^{-1} of free C=O and N−H show that more amide groups are hydrogen-bonded, both to other amide groups and to water. This is especially evident from the $\nu(NH)$ band of bonded N−H groups that is downward-shifted by $\approx$ 3 cm^{-1} compared to the initial state with the same water content. Closer inspection reveals that the contributions of amide–amide and amide–water interacted N−H groups are approximately equally strong. The main spectral contributions in the amide I band stem from double-bonded or dihydrogen-bonded C=O groups, while the same amount of single- or mixed-bonded groups is present as in the initial state. Two hydrogen bonds with H−N groups or water molecules therefore seem favored.

Finally, heating of the film to 20 °C results again in a small release of water, coinciding with more free C=O and N−H groups. Nevertheless, structural changes of the film are apparent comparing the amide regions to the fifth measured spectrum at 35 °C with similar water content. Such non-reversible changes were not observed in humidity-dependent measurements at constant temperature, discussed in the previous section. Amide I and II obviously exhibit hysteresis effects induced by temperature. If these effects are in some way connected with a coil-to-globule transition is still an open question. Wang et al. [240] suggest that intrachain hydrogen bonding may play an important role after the coil-to-globule transition for PNIPAAm in aqueous solutions, but also that these intrachain bonds are dissolved again below 25 °C due to the good-solvent qualities of water. This, however, is not observed in the present case, probably due to the low water content of the film. Future investigations could aim at measurements during repeated heating and cooling cycles as well as different initial water contents to gain a deeper understanding of the polymer–water and polymer–polymer interactions.

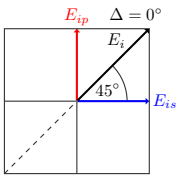

3.2. Optical properties of 4–15 nm thin PNIPAAm brushes in dry and humid state

This section aims at first at the pre-characterization of polymer brushes by VIS ellipsometry. Brush criteria are applied in order to determine whether the prepared films exhibit brush or mushroom conformation. Layer homogeneity is then tested with atomic force microscopy and infrared microscopy. Interactions at the PGMA/PNIPAAm interface are analyzed by considering the various grafting-density effects. The brush profile as well as the strengths of hydrogen bonds between amide groups are investigated with time-resolved N-deuteration experiments. Polymer–polymer interactions within the brushes are then quantified by describing the measured spectra using the optical constants of spin-coated PGMA and PNIPAAm films. Finally, the swelling behavior of brushes and spin-coated films in humid air is compared.

3.2.1. Overview, pre-characterization, and homogeneity tests

a) Brush conformation

PNIPAAm brushes with different molecular weights and grafting densities were prepared on silicon (111) wedges. Criteria are presented in the literature [68, 70] that allow one to estimate whether the polymer films really exist in the brush regime or rather in a mushroom or an intermediate regime. In the brush regime,

$$d_\mathrm{g} \,/\, (2R_\mathrm{g}) \ll 1\,, \tag{3.3}$$

where d_g is the distance between grafting sites, and R_g is the radius of gyration. For good and bad solvents, R_g can respectively be approximated by the Flory Radius R_F and the radius R_C of a collapsed chain [26, 70]:

$$\begin{aligned} \text{Good solvent:} \quad & R_\mathrm{g} \to R_\mathrm{F} = l_\mathrm{mono} \cdot N_\mathrm{mono}^{3/5} \\ \text{Bad solvent:} \quad & R_\mathrm{g} \to R_\mathrm{C} = l_\mathrm{mono} \cdot N_\mathrm{mono}^{1/3} \end{aligned} \tag{3.4}$$

Here, the monomer length is given by $l_\mathrm{mono} = d_\mathrm{chain}/N_\mathrm{mono}$ after Eq. (2.84). Assuming that water is a good solvent for PNIPAAm below the LCST [50], then the first criterion should apply. The second criterion, however, is a much tighter one for the film being in the brush regime [26]. The above criteria were, for instance, applied in Refs. [26, 47]. Further considerations concerning the correct estimation of R_g can also be found in Ref. [26].

Table 3.6 gives an overview on characteristic sample parameters, including layer thicknesses and the brush-criteria ratios $d_\mathrm{g}/(2R_\mathrm{F})$ and $d_\mathrm{g}/(2R_\mathrm{C})$. PGMA and PNIPAAm layer thicknesses were determined with VIS ellipsometry employing optical modeling in analogy to

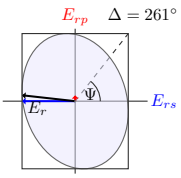

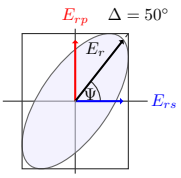

Section 3.1.2. Thicknesses were fitted using Cauchy layers for which the corresponding Cauchy parameters were fixed to the values determined from the spin-coated PGMA and PNIPAAm films. The densities $\varrho_{\mathrm{PNIPAAm}} = 1.07\,\mathrm{g/cm^3}$ [241, 242] and $\varrho_{\mathrm{PGMA}} = 1.08\,\mathrm{g/cm^3}$ [243] were used to calculate the grafting densities σ after Eq. (1.3).

No.	Top-layer	d [nm]	Γ [mg/m^2]	σ [nm^{-2}]	d_g [nm]	R_F [nm]	$d_\mathrm{g}/(2R_\mathrm{F})$	R_C [nm]	$d_\mathrm{g}/(2R_\mathrm{C})$	t [hh:min]
1	SiO_2	1.5								
2	PGMA	2.4	2.6	0.089						0:20
3	PN56k	10.8	11.6	0.124	2.84	10.4	0.14	1.99	0.71	3:40
4	PN56k	11.5	12.3	0.132	2.75	10.4	0.13	1.99	0.69	15:24
5	PN132k	4.0	4.3	0.020	7.16	17.4	0.21	2.65	1.35	0:29
6	PN132k	8.0	8.6	0.039	5.06	17.4	0.15	2.65	0.96	1:15
7	PN132k	12.5	13.4	0.061	4.05	17.4	0.12	2.65	0.76	15:24
8	PN132k	14.5	15.5	0.071	3.76	17.4	0.11	2.65	0.71	19:07
9	PN94k	12.6	13.5	0.086	3.40	14.2	0.10	2.36	0.72	16:00

Table 3.6: Overview of PNIPAAm-brush thicknesses d (as determined by VIS ellipsometry) as well as surface concentrations Γ, grafting densities σ, distances d_g between grafting sites, Flory radii R_F, collapsed-chain radii R_C, brush-criteria ratios $d_\mathrm{g}/(2R_\mathrm{F})$ for good solvents and $d_\mathrm{g}/(2R_\mathrm{C})$ for bad solvents, as well as annealing times t. Parameters were calculated after Eqs. (1.1)–(1.3) and (3.4). Thicknesses were fitted using Cauchy layers for PGMA and PNIPAAm with fixed parameters as determined from spin-coated films according to Section 3.1.2. Errors of thicknesses and grafting densities did not exceed 0.3 nm and 0.005 nm^{-2}. Brushes 3–8 had the same oxide thickness of 1.5 nm and PGMA thickness of 2.4 nm, whereas brush 9 exhibited 0.9 nm SiO_2 and 2.7 nm PGMA thickness. Samples 1 and 2 serve as reference samples for relative tan Ψ and reflectivity measurements.

With respect to the brush criteria in Eq. (3.4), all PNIPAAm films fulfill $d_\mathrm{g}/(2R_\mathrm{F}) \ll 1$ and therefore exist in the brush regime below the LCST at good-solvent conditions. At bad-solvent conditions—above the LCST, for example—the brushes are probably in a transition or mushroom regime, which has potential influence on the deswelling behavior [26].

b) Homogeneity tests with atomic force microscopy

Average layer thicknesses and grafting densities of the prepared brushes range between 4.0–14.5 nm and 0.02–0.13 nm^{-2}, respectively. How annealing time ($\Leftrightarrow$ grafting density) is affecting surface homogeneity was tested with atomic force microscopy. Figure 3.22 exemplarily shows the surface topographies of the PGMA anchoring layer as well as of three different PNIPAAm brushes with thicknesses of 4.0 nm, 8.0 nm, and 10.8 nm. For grafting densities $\geq 0.04\,\mathrm{nm^{-2}}$, the brush layers form closed films and are generally very smooth with root-mean-square roughness values smaller than 0.8 nm. The PGMA layer as well as the smoothest PNIPAAm brushes typically show values around $R_\mathrm{rms} = 0.35$ nm. Only AFM measurements of brush 5 (top-right map in Fig. 3.22), which has the smallest grafting density of 0.02 nm^{-2},

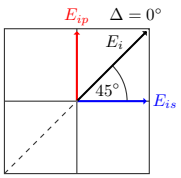

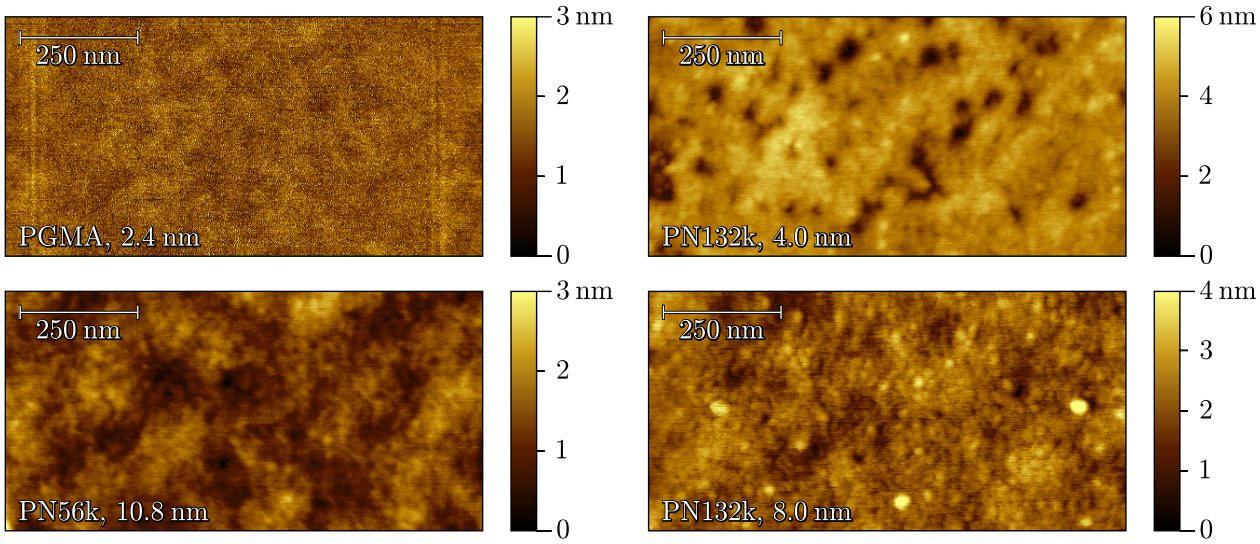

Figure 3.22: AFM surface topography measurements ($1000 \times 500\,\mathrm{nm}^2$) of a PGMA anchoring layer (top-left, $R_{\mathrm{rms}} = 0.37\,\mathrm{nm}$), a 56 kDa PNIPAAm brush (bottom-left, $R_{\mathrm{rms}} = 0.36\,\mathrm{nm}$), as well as two 132 kDa PNIPAAm brushes (top-right, $R_{\mathrm{rms}} = 0.67\,\mathrm{nm}$; bottom-right, $R_{\mathrm{rms}} = 0.46\,\mathrm{nm}$). Root-mean-squared roughness values R_{rms} were calculated according to $R_{\mathrm{rms}} = [\frac{1}{n}\sum_{i=1}^{n} z_i^2]^{0.5}$, with the sum running over the measured height positions z_i of all n pixels of the image. From separate left- and right-scans, the errors of R_{rms} were estimated to be 0.05 nm.

indicate that the film is not closed completely. Small holes with diameters between 10 nm and 50 nm suggest that the annealing time was not long enough for the PNIPAAm chains to covalently bond with the PGMA sublayer in an even distribution.

c) Pushing the sensitivity limits of infrared microscopy

Next to atomic force microscopy, infrared microscopy was employed to test the brushes for sample homogeneity on a larger scale. Reflectivity measurements of three different PN132k brushes with thicknesses of 4.0 nm, 8.0 nm, and 14.5 nm are displayed in Fig. 3.23. Linescans were performed with a standard Cassegrain objective on three consecutive spots separated by 200 µm, with the microscope's knife-edge apertures set to $160 \times 160\,\mu\mathrm{m}^2$. The 2.4 nm thin PGMA anchoring-layer sample served as the reference surface. Owing to the low signal-to-noise ratio caused by the small spot size and the small thickness of the polymer films, each spot was measured for 128 min in order to spectrally resolve even low-intensity vibrational bands. This could only be achieved by precisely controlling the atmospheric conditions inside the microscope chamber using dry-air purging with adjustable purge rate.

Measured reflectivities $R_{\mathrm{Brush}}/R_{\mathrm{PGMA}}$ of the three spots prove the lateral homogeneity of the brushes within the given spot size at the current signal-to-noise ratio. Band shapes, amplitudes, and positions do not change from spot to spot. Notably, infrared microscopy is capable of resolving even the small amide and $\nu(\mathrm{CH_x})$ bands of the 4.0 nm ultra-thin brush.

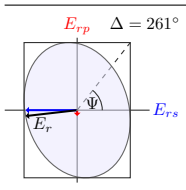

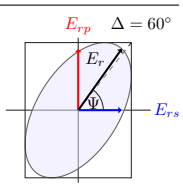

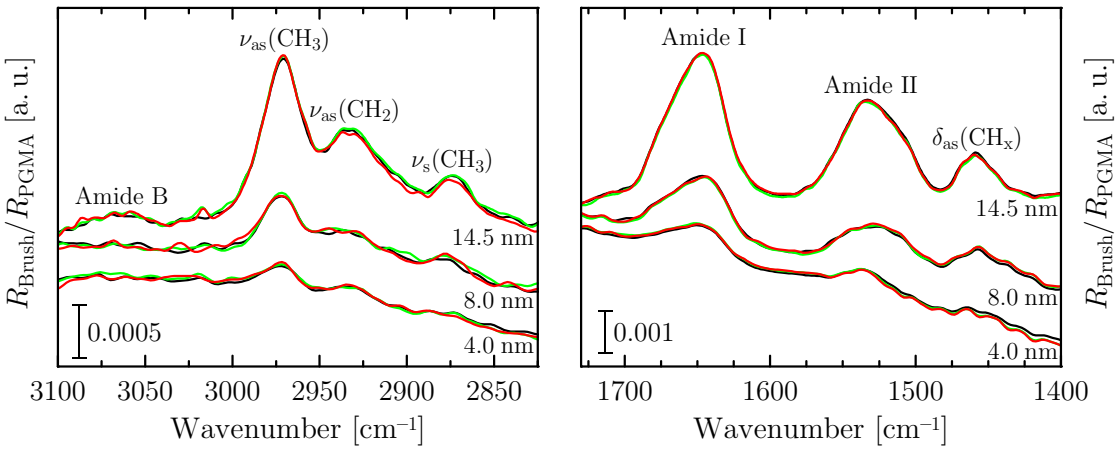

Figure 3.23: Homogeneity tests with infrared microscopy on PNIPAAm brushes 5, 6, and 8 with thicknesses of 4.0 nm, 8.0 nm, and 14.5 nm. With a standard Cassegrain objective, three spots separated by 200 µm were measured on each brush (black, green, and red lines). The $\nu(CH_x)$ and amide I/II regions of PNIPAAm are respectively shown in the left and right panel.

3.2.2. Properties of the PGMA/PNIPAAm interface

The characteristic carbonyl and epoxy bands of PGMA as well as the ester bands that originate from the PGMA/PNIPAAm bond can, in principle, be used to study grafting-density effects of the functional PNIPAAm top-layer as well as interactions at the PGMA/PNIPAAm interface. Figure 3.24 depicts the mechanism by which PNIPAAm covalently bonds to the PGMA anchoring layer. The carboxy-terminated chain ends react with epoxy groups of PGMA, resulting mainly in ester bondings that give rise to characteristic C=O- and C−O−C-stretching vibrations in the infrared. With increasing grafting density (annealing time), one therefore expects an increase in amplitudes of these ester-specific bands with a simultaneous decrease of epoxy-specific bands.

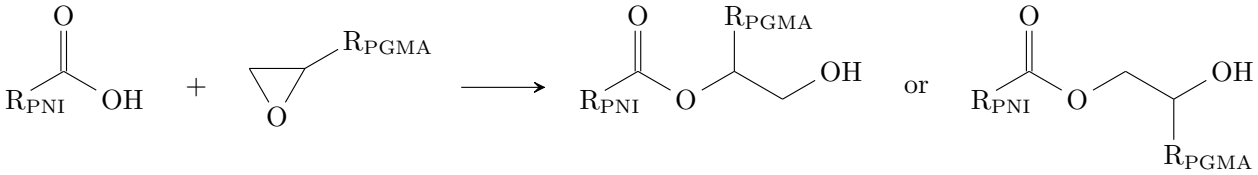

Figure 3.24: Principal grafting reactions between PNIPAAm's carboxylic groups and PGMA's epoxy groups resulting in ester bonds [76].

Figure 3.25 shows measured $\tan\Psi$ spectra in the ν(C=O) and amide I/II regions for the PGMA anchoring layer and the brushes 3–8 with layer thicknesses between 4.0 nm and 14.5 nm. The band composition of amide I and II is identical to the one of spin-coated PNIPAAm films discussed in Section 3.1.5.a). Amide I consists of three components situated at 1680 cm^{-1}, 1664 cm^{-1}, and 1645 cm^{-1}, corresponding to stretching vibrations of

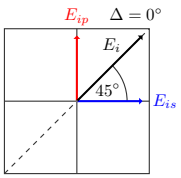

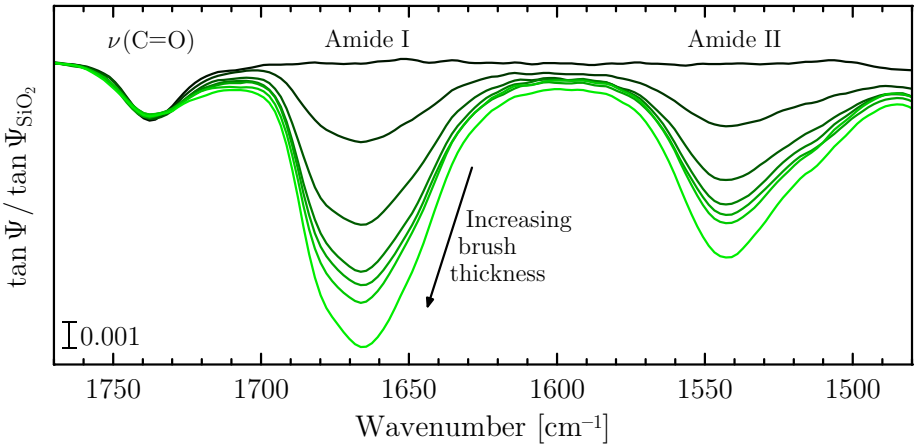

Figure 3.25: Referenced tan Ψ spectra of the PGMA anchoring layer (upmost line) and PNIPAAm brushes 3–8 in order of increasing layer thickness (black to gray lines, 4.0 nm to 14.5 nm). Spectra were baseline-shifted to coincide at 1770 cm^{-1} for better comparability.

C=O groups that are free, single-bonded, and double-bonded with H−N groups, respectively. Amide II, on the other hand, consists of two components at 1544 cm^{-1} and 1509 cm^{-1}, corresponding to bending-vibration contributions of single-bonded and free N−H groups.

With increasing grafting densities, amide I and II scale accordingly. No relative amplitude changes are observed between the different components. In contrast, a slight decrease of free PGMA C=O-stretching is found at 1735 cm^{-1} accompanied by band broadening as well as an increase at 1730 cm^{-1} and a broad feature at 1710 cm^{-1}. The latter is pure film effect originating from an increase in film thickness. The former three observations might be explained by hydrogen bonding of PGMA's C=O groups with H−N groups of PNIPAAm, which causes the downward-shift and band broadening of ν(C=O). Hydrogen bonding is possible due to the anticipated interpenetration of PNIPAAm chains into the PGMA layer [243, 244]. With regard to in-situ experiments in aqueous environment, band broadening is also expected due to hydrogen-bond interactions between C=O groups and water.

Since the PGMA layers of the prepared brushes are only 2.4 nm thin, it is difficult to monitor changes in the other vibrational bands of PGMA, which are all less prominent than ν(C=O). Small band changes are observed between 1100–1300 cm^{-1} (not shown), possibly correlating with C−O−C-stretching of ester groups and other PGMA-specific vibrations. However, these vibrational bands are strongly overlapped by the broad amide III band of PNIPAAm, which prohibits unambiguous interpretations. CH-stretching of the epoxy-methyne group at 3001 cm^{-1} is observable as a small shoulder in the $\nu_{as}(CH_3)$ band of PNIPAAm, but no changes with grafting density can be discussed at the current signal-to-noise ratio.

Similarly, no significant changes are found for the deformation vibrations of the epoxy rings at 909 cm^{-1} and 850 cm^{-1}. This is not totally unexpected since the maximum grafting

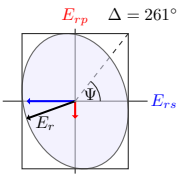

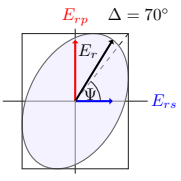

density of $\sigma_{\mathrm{PNIPAAm}} = 0.136\,\mathrm{nm}^{-2}$ (see Tab. 3.6), which also coincides with the number of COOH end groups/nm^2, is still very small compared to the surface concentration of epoxy groups [243], given by $\sigma_{\mathrm{PGMA}} \cdot N_{\mathrm{mono}} \approx 11.0$ epoxy groups/nm^2 (see Tabs. 2.1 and 3.6). This also holds when considering that the number of available epoxy groups for grafting reactions reduces by about 70% [244] to 3.3 groups/nm^2 due to self-crosslinking and interactions of parts of the PGMA chains with the substrate (the so-called train fraction).

Systematic studies of PNIPAAm brushes with constant layer thickness but varying chain lengths might shed more light on the vibrational properties of the PGMA/PNIPAAm interface.

3.2.3. Polymer–polymer interactions in PNIPAAm brushes

Time-dependent N-deuteration experiments are a useful tool in order to learn more about polymer–polymer interactions within a PNIPAAm film, including the strength of hydrogen bonds between amide groups. Unlike the spin-coated PNIPAAm films discussed earlier, PNIPAAm brushes allow one to study the effects of N-deuteration on the whole film more easily, since all polymer chains are covalently bonded to the PGMA anchoring sublayer. Treatment of the brushes with liquid D_2O followed by drying therefore has less impact on film thickness and homogeneity. This makes it possible to investigate deuterated brushes quantitatively in dry state, which is the foundation for a detailed analysis of polymer–water interactions during temperature-dependent swelling experiments in D_2O.

For measurements of undeuterated and deuterated PNIPAAm brushes, the polymer-brush samples were mounted onto a movable sample holder, installed, and aligned within the purged ellipsometer chamber. After $\tan\Psi$ measurements in undeuterated state, the brushes were submerged into D_2O and then dried under water-vapor-free conditions inside the ellipsometer. The drying process, as monitored via repeated $\tan\Psi$ measurements of the $\nu(D_2O)$ band amplitude, was completed after only a few minutes.

a) Time-dependent N-deuteration (H↔D exchange)

The upper panel of Fig. 3.26 shows referenced $\tan\Psi$ spectra of the $d_{\mathrm{dry}} = 14.5\,\mathrm{nm}$ thin PN132k brush at several intermediate stages of the N−H → N−D exchange process between undeuterated and fully deuterated state. Band-amplitude changes of amide A, I, and II upon deuteration are observed as expected from the previous deuteration studies of spin-coated PNIPAAm films in Section 3.1.5.a). Due to the changing N−H/N−D composition, amide A and II decrease in amplitude, while amide A' and II' bands of increasing amplitudes arise at correspondingly lower frequencies. The amide I band is slightly shifting to lower wavenumbers and increasing in amplitude. This is related to small contributions of N−H-bending to amide I in the undeuterated case that occur at higher wavenumbers compared to N−D-bending.

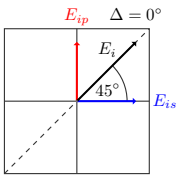

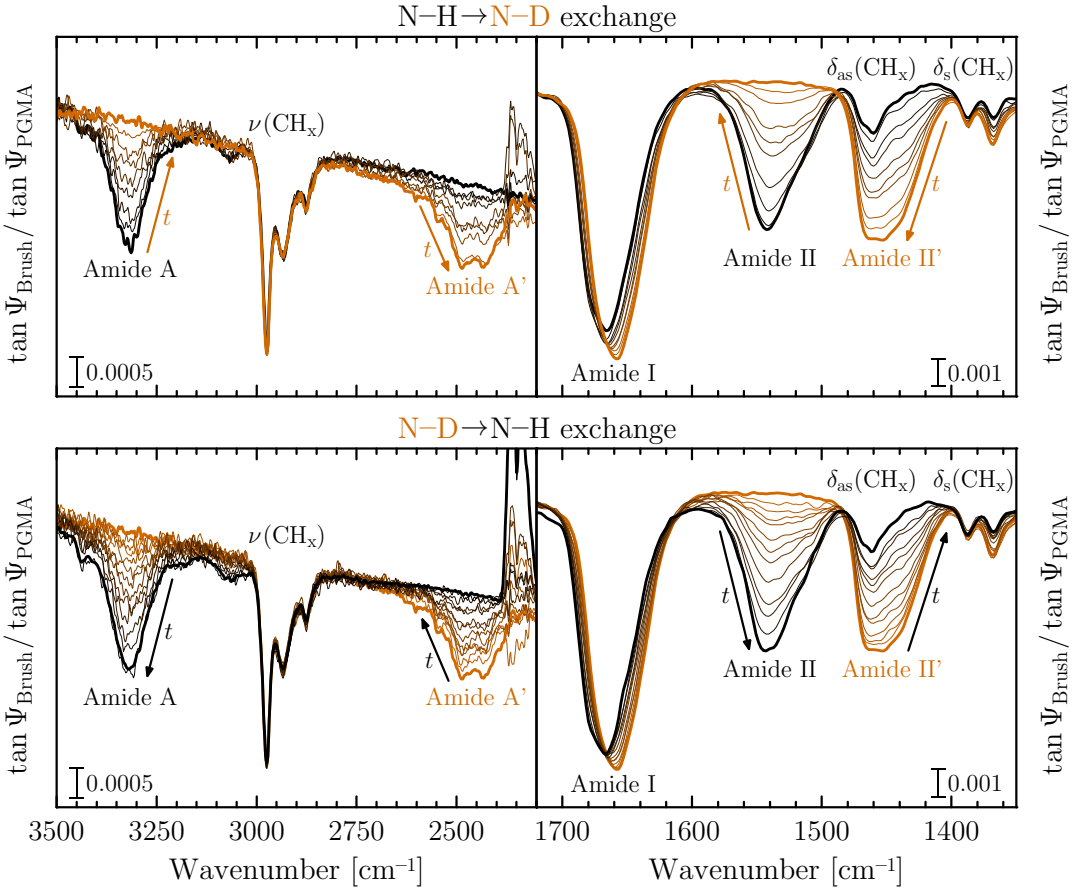

Figure 3.26: Effects of *N*-deuteration (N−H → N−D, upper spectra) and de-deuteration (lower spectra) on the d_{dry} = 14.5 nm thin 132 kDa PNIPAAm brush measured ellipsometrically at $\varphi_0 = 65°$. Measurements were performed at intermediate stages between undeuterated (black lines) and deuterated (brown lines) state after repeatedly immersing the sample in liquid D_2O (H_2O) with subsequent drying. Immersion times were t = [10, 20, 25, 30, 60, 190, 620, 1500, 58000] s in the N−H → N−D cycle and t = [10, 20, 30, 60, 110, 200, 400, 800, 1400, 2400, 4800, 120000] s in the N−D → N−H cycle. Cumulative immersion times up to the second last spectra were 2455 s and 10230 s, respectively. Spectra were PGMA-referenced and baseline-corrected. Artifacts from atmospheric CO_2 absorption are overlapping the amide A' band around 2350 cm^{-1}. The first spectrum in the upper panel (black line) contains minute residues of N−D vibrations originating from previous deuteration experiments on that sample.

Besides the amplitude changes of amide II upon deuteration, its band envelope is undergoing alterations as well. In dry state, the band consists of two contributions stemming from free N−H-bending at about 1509 cm^{-1} and C=O-interacted N−H-bending at about 1544 cm^{-1}, as was shown in Section 3.1.5.a). At first, contributions from interacted N−H groups decrease in amplitude, whereas the free contributions are almost unaffected. With progressing deuteration, the amplitude ratio between interacted and free contribution decreases further. Similar effects are observed in the amide II' band envelope between 1470–1420 cm^{-1}.

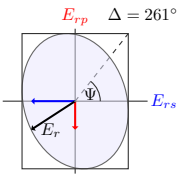

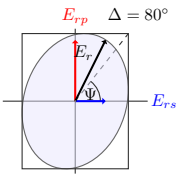

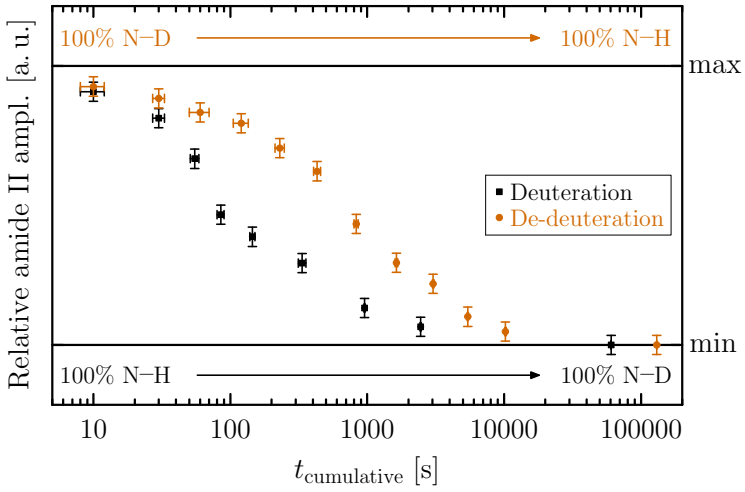

Figure 3.27: Time-dependent amide II band amplitude during N−H → N−D and N−D → N−H exchange within the $d_{\mathrm{dry}} = 14.5\,\mathrm{nm}$ thin PNIPAAm brush, corresponding to the measured spectra in Fig. 3.26. The time coordinate reflects cumulative immersion times of the brush in liquid D_2O (black squares) and liquid H_2O (brown circles). The brush was dried for 20 min prior to each measurement. For better comparison, the relative amplitudes $\tan\Psi(t_{\mathrm{cumulative}})/\tan\Psi_{\mathrm{max}}$ are plotted for the H→D cycle, whereas $1-\tan\Psi(t_{\mathrm{cumulative}})/\tan\Psi_{\mathrm{max}}$ is shown for the D→H cycle. $\tan\Psi_{\mathrm{max}}$ is the maximum band amplitude in the fully undeuterated state at $t_{\mathrm{cumulative}} = 0\,\mathrm{s}$.

The lower panel of Fig. 3.26 shows the reverse N−D → N−H exchange process. Although the spectra are qualitatively similar, it is noteworthy that free and interacted N−H groups form to an approximately equal amount at the beginning. Only at longer immersion times, more interacted groups are affected by D→H exchange. This might be explained by the brush's depth profile, that is, the relative amounts of polymer and water at a given distance from the substrate. Neutron reflectometry on PNIPAAm brushes below the LCST [245, 246] reveals a gradient-like profile, meaning that the topmost parts of the brush are substantially more hydrated than the deeper parts closer to the substrate. The exchange process therefore primarily affects the topmost parts of the polymer chains at first. Since these—after drying of the brush—are less likely to be involved in interchain amide–amide interactions, one observes a larger amplitude ratio between free and interacted N−H groups compared to the final undeuterated state.

The main difference between the N−H → N−D process and the N−D → N−H process lies in the exchange rate, which differs considerably by a factor of about 4–8. This is illustrated in Fig. 3.27, which shows the time-dependent amide II band amplitude for both processes. In detail, the kinetics of the exchange processes are governed by the accessibility of water molecules at the amide groups' nitrogen atoms as well as the strength of N−H and N−D hydrogen bonding and the strength of amide-hydrogen bonding to neighboring carbonyl groups within the polymer chains.

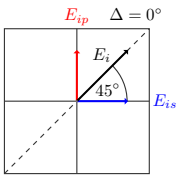

Figure 3.27 substantiates the hypothesis that the brush profile is playing an important role during the exchange process. Approximately half of the amide groups are deuterated very quickly after only about $t_{\text{cumulative}} = 100\,\text{s}$, which might be due to the high water content in the topmost portion of the brush. The exchange then slows down significantly and approaches an exponential rate. After about $t_{\text{cumulative}} = 1000\,\text{s}$, the rate slows down even more. This might be related to the lower water content of the brush near the substrate, but also to the inaccessibility of free N−H groups to D_2O molecules. Eventually, these groups become deuterated after longer immersion times in D_2O. This could be explained by the good-solvent qualities of water below the LCST and the high mobility of the polymer chains.

De-deuteration occurs much slower than deuteration, with the onset of the exponential exchange rate at $t_{\text{cumulative}} \approx 500\,\text{s}$ and the less-than-exponential rate at $t_{\text{cumulative}} \approx 6000\,\text{s}$. This verifies that N−D···O=C hydrogen bonds are much stronger than N−H···O=C bonds within the brush. The strength of amide–amide hydrogen bonding not only determines the exchange rate, but it also has significant influence on the temperature-dependent switching behavior of PNIPAAm brushes in H_2O and D_2O, as will be shown in Section 3.3. In this respect, the temperature dependence of the brush profile might be of importance, too. To gain more insights, the measurements should therefore also be repeated at elevated temperatures of the D_2O and H_2O solutions above the LCST of PNIPAAm, which is the aim of future work. Since the profile is then expected to exhibit a very sharp transition between low and high water content [245, 246], one would anticipate a more exponential exchange rate right from the beginning of the exchange experiment.

H↔D exchange was proven to be a reversible process by repeating the measurements several times.

b) Quantitative band analysis

Figure 3.28 compares the effects of full *N*-deuteration on the $d_{\text{dry}} = 10.8\,\text{nm}$ thin 56 kDa PNIPAAm brush and the $d_{\text{dry}} = 14.5\,\text{nm}$ thin 132 kDa brush. No significant differences are found in the composition of the amide bands, which might be explained by the very similar values of $d_g/(2R_F) = 0.14$ and 0.11, respectively (see Tab. 3.6). These values state that the two brushes exhibit a similar brush conformation and therefore almost identical amide–amide interactions, despite their different grafting densities of respectively $0.124\,\text{nm}^{-2}$ and $0.071\,\text{nm}^{-2}$.

Some differences are found when comparing the dry-state measurements of brushes after brush preparation (Fig. 3.25) and after in-situ experiments in H_2O and D_2O (Fig. 3.28). A small decrease in film thickness of about 10–20% is found, accompanied by an amplitude decrease of vibrational bands corresponding to free C=O and N−H groups at $1680\,\text{cm}^{-1}$ and $1509\,\text{cm}^{-1}$, respectively. This indicates that a small fraction of non-covalently bonded PNIPAAm chains remained present after brush preparation—either within the brush or

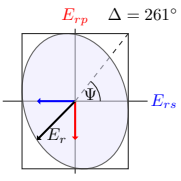

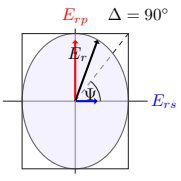

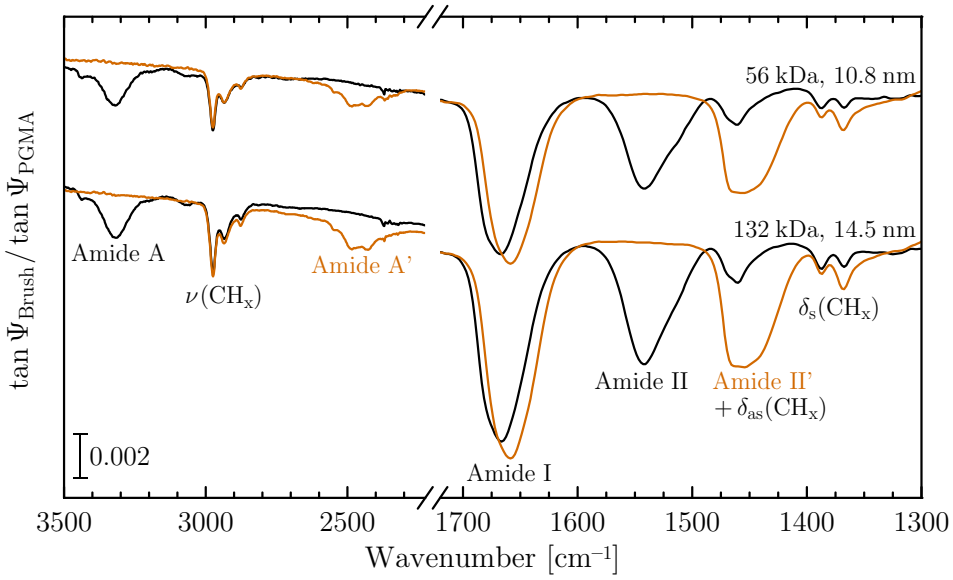

Figure 3.28: Referenced dry-state tan Ψ spectra of undeuterated (black lines) and deuterated (brown lines) PNIPAAm brushes. The upper and lower spectra respectively correspond to the 10.8 nm thin 56 kDa brush and the 14.5 nm thin 132 kDa brush. Spectra were baseline-shifted for better comparability. Small baseline changes occur owing to slight sample misalignments upon immersion of the brushes in liquid D_2O.

probably on top of it—and is being washed out during the experiments in liquid water. Directly after preparation, the top part of the polymer film is therefore unlikely to exist in brush conformation. Thus, amide–amide interactions reduce, leading to higher relative amounts of free amide groups.

The amide I and II/II' bands of the PN132k brush in Fig. 3.28 are now analyzed quantitatively by simulating the corresponding tan Ψ spectra using an optical layer model of Si/SiO_2/PGMA/PNIPAAm. $n = 3.42$ and $k = 0$ were assumed for the silicon substrate [154], while literature data were used for the oxide layer [18]. The optical properties of brush and anchoring layer were described by the dry-state optical constants of spin-coated PNIPAAm and PGMA films, as determined in Section 3.1.4.

The left panel of Fig. 3.29 shows measured and simulated spectra in the ν(C=O) region of PGMA as well as the amide I/II and $\delta(CH_x)$ regions of PNIPAAm. Overall, good agreement is found for amide I and II. Small deviations, however, are observed in the CH_x-bending vibrational bands. Also the PGMA-related C=O-stretching band around 1735 cm^{-1} differs markedly, which is related to PNIPAAm–PGMA interactions and self-crosslinking of PGMA chains during the grafting process of the PNIPAAm top-layer, as discussed in Section 3.2.2. These differences can be accounted for by adjusting the corresponding oscillator parameters in the simulation. With regard to in-situ measurements in liquid water, further changes are expected in the C=O-stretching region due to additional PGMA–water interactions.

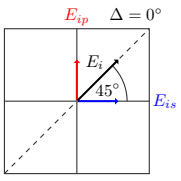

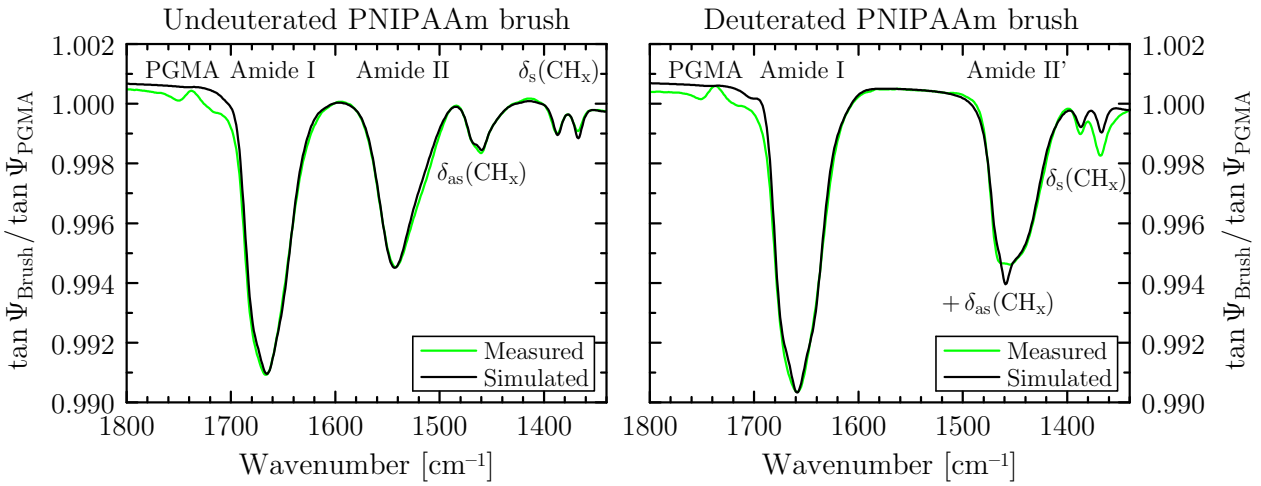

Figure 3.29: Measured and simulated PGMA-referenced $\tan\Psi$ spectra at $\varphi_0 = 65°$ of the fully undeuterated (left) and fully deuterated (right) PN132k brush from Fig. 3.28 in the amide I/II and $\delta(CH_x)$ regions of PNIPAAm and the $\nu(C{=}O)$ region of PGMA. Simulations were carried out with $d_{Brush} = 10.5$ nm using the optical constants of PNIPAAm and PGMA as determined from spin-coated polymer films in Section 3.1.4. Oscillator frequencies and amplitudes of amide I and II subcomponents were adjusted in the deuterated case, while maintaining constant band widths.

Corresponding changes in oscillator frequency, amplitude, and band width of $\nu_{PGMA}(C{=}O)$ could then be used to analyze the PGMA/water and PGMA/PNIPAAm interaction strengths as well as the amount of water- and PNIPAAm-interacted carbonyl groups.

In the following discussions, the focus lies on PNIPAAm-specific vibrational bands. Less free C=O and N−H groups of PNIPAAm are found in the simulated brush spectra compared to the measured ones, which can be seen in the band composition of amide I and II. The corresponding *free* subcomponents at respectively 1680 cm^{-1} and 1509 cm^{-1} show lower amplitudes at the expense of larger amounts of double-bonded C=O groups (1645 cm^{-1}) and single-bonded N−H groups (1544 cm^{-1}). This is explained by the fact that a smaller portion of PNIPAAm chains is exposed to the surface in the much thicker spin-coated films. Thus, the optical constants of these films, which were used for the simulations, are more dominated by amide–amide-interacted C=O and N−H groups.

The right panel of Fig. 3.29 shows measured and simulated spectra of the same brush, but in fully deuterated state. In order to simulate $\tan\Psi$, the corresponding C=O and N−H oscillators within amide I and II were shifted according to positions obtained from second-derivative analysis, while keeping the band widths of the oscillators constant. Since transition dipole moments of N−H-related vibrational modes as well as the strength of C=O···H−N hydrogen bonds are changing upon deuteration, the oscillator strengths of single- and double-bonded $\nu(C{=}O)$ had to be increased, whereas the amplitude of the single-bonded $\delta(N{-}D)$ contributions to amide II' had to be reduced.

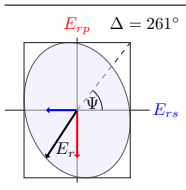

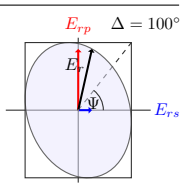

As before, similarly good agreement is found for the amide I band, with the same small difference in the free ν(C=O) contribution, observed at 1673 cm^{-1} in the deuterated state. In contrast, the simulated amide II' band clearly deviates in form of a distinct band at 1459 cm^{-1}, which is associated with asymmetric bending vibrations of CH_2 groups in the PNIPAAm main chain. Differences are also observed in the $\delta_s(CH_3)$ and $\delta_s(CH_2)$ bands at respectively 1387 cm^{-1} and 1367 cm^{-1}. Again, the measured band shapes can be reproduced by adjusting the corresponding oscillator strengths and positions. Theoretical input from DFT calculations or other methods is needed, however, to discuss the nature of these band changes. Whether deuteration is also affecting the CH_x groups of PNIPAAm is not clear at this moment. If so, the strongest effect seems to occur for the CH_2-associated bands, which stands in stark contrast to the fact that CH_3 groups of PNIPAAm are more hydrated in aqueous solutions than CH_2 groups (see Fig. 3.17 and Ref. [50]).

It is clear from the above simulations that PNIPAAm brushes, including polymer–polymer interactions, can be described quantitatively using optical layer models. Despite the deviations in the CH_x-specific bands, the simulated (un)deuterated PNIPAAm parameters can be used as a starting point for modeling in-situ spectra of brushes in liquid H_2O and D_2O.

3.2.4. Humidity effects on PNIPAAm brushes

PNIPAAm brushes show similar swelling effects in humid air as the spin-coated PNIPAAm films discussed in Section 3.1.5. Reflectivity spectra of the thickest brush, plotted in the left panel of Fig. 3.30, were measured with infrared microscopy in four humidity steps between 35% and $< 2\%$. The broad $\nu(H_2O)$ band of water and the changing baseline slope are clearly visible in the first two spectra, indicating the presence of water and the swelling/deswelling of the brush. Band shifts in the amide regions are observed as expected. Subcomponents of amide I and II corresponding to free, amide–amide-, and amide–water-interacted C=O and N−H groups increase and decrease according to humidity. Amide A is shifting by approximately 10 cm^{-1} between dry and humid state due to changing polymer–water interactions, which also enhances the Fermi resonance between amide A and B at higher water contents of the brush. In contrast to spin-coated films, PNIPAAm brushes seem to bind more water in humid state, which is indicated by the larger $\nu(H_2O)$ band amplitude. Moreover, the release of bound water occurs much more quickly upon decreasing humidity.

A quantitative analysis of the measured spectra is difficult due to the baseline drift at low wavenumbers, which is probably caused by backside reflections of the transparent silicon wedges. For this reason, the brush was also measured ellipsometrically, as shown in the right panel of Fig. 3.30. The larger angle of incidence of $\varphi_0 = 65°$ compared to $\bar{\varphi}_0 \approx 16°$ of the Cassegrain objective makes for a higher sensitivity towards changes in band amplitudes and positions.

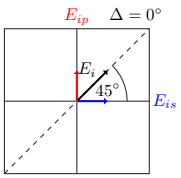

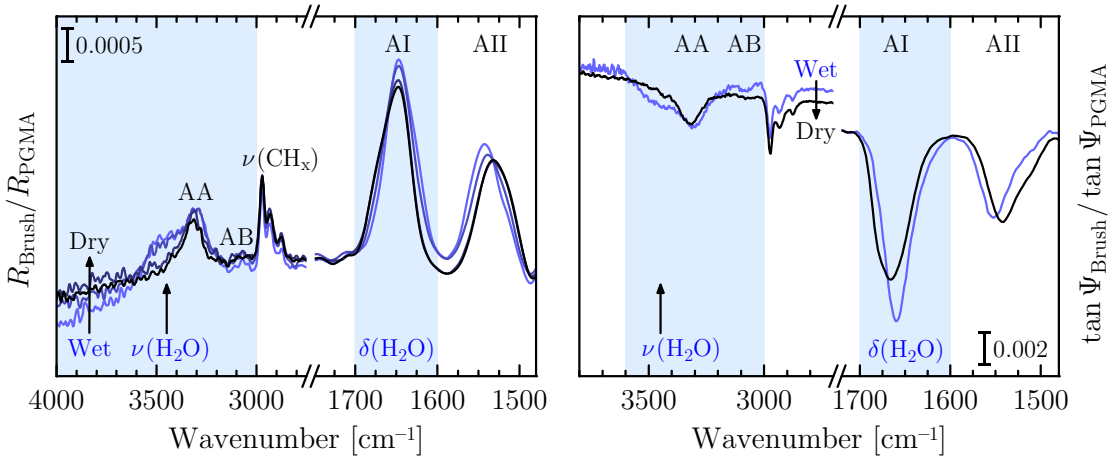

Figure 3.30: Effects of changing humidity on the $d_{\mathrm{dry}} = 14.5\,\mathrm{nm}$ thin PNIPAAm brush. Reflectivity was measured with infrared microscopy (left, Cassegrain objective) at humidities between 35% (light blue line) and $< 2\%$ (black line). tan Ψ measurements with infrared ellipsometry (right, $\varphi_0 = 65°$) were performed at $(20 \pm 8)\%$ and $< 0.5\%$ humidity. Amide A, B, I, and II bands are marked as AA, AB, AI, and AII, respectively. Reflectivity spectra were baseline-corrected and also corrected for water-vapor absorption.

Spectra were simulated using the same optical model with oscillator parameters of amide I and II as introduced in Section 3.1.5. At the highest achievable humidity of $(20 \pm 8)\%$, the brush exhibits a water content of $f_{\mathrm{H_2O}} = (7.5 \pm 1.5)$ vol%, which is much higher compared to the 5.5 vol% observed at 20% humidity for spin-coated films. Oscillator strengths of the amide I and II subcomponents, however, are almost the same as for the film at $f_{\mathrm{H_2O}} = 7.5$ vol%. This suggests that polymer–water interactions are comparable despite the slightly different water-binding qualities. Further investigations are necessary in order to understand these differences. Also, the atmospheric conditions have to be controlled more precisely to exclude systematic errors in humidity.

Additional measurements were also performed at humidities higher than 35%. For this, a polymer-brush sample was mounted inside the in-situ flow cell. The cell was filled with water, and subsequently emptied and slowly dried. This allowed the monitoring of the transition from mainly dihydrogen-bonded C=O groups in wet state, over mainly monohydrogen- or mixed-bonded C=O groups in humid state, to amide-interacted and free groups in dry state. The corresponding analysis can be found in Appendix G.

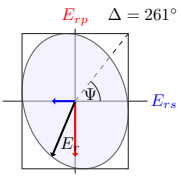

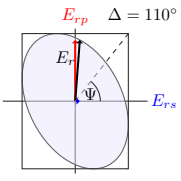

3.3. Temperature-sensitive swelling of PNIPAAm brushes in H_2O and D_2O

Various research groups focused on investigations on hydration states and swelling behavior of PNIPAAm in solution [45, 50–54] as well as of PNIPAAm hydrogels [55–60] and microgels [61–63]. The swelling behavior of PNIPAAm brushes, though, is still not fully understood. Investigations with visible ellipsometry [26, 47] and infrared ATR spectroscopy [26] show that the overall swelling properties appear to be similar compared to these of PNIPAAm in solution, but brush parameters like grafting density and chain length seem to have potentially strong effects on swelling degree and conformational changes [26, 47, 65]. To elucidate these effects, PNIPAAm brushes with different grafting densities and chain lengths are investigated qualitatively in this section for their swelling behavior around the lower critical solution temperature of about 32 °C [43–45, 72].

In-situ infrared-spectroscopic ellipsometry was employed to measure PNIPAAm brushes in aqueous environments at different temperatures. Two different solvents—normal water (H_2O) and heavy water (D_2O)—were used, the reasons for which are manyfold, as will become clear in a moment. The course of the measurements was as follows: First, the brushes were installed into the in-situ cell and measured in dry state through the wedge-shaped silicon substrate in order to correct for variations in the optical paths that occur for different samples; see Section 2.1.4.c). Afterwards, the cell was filled with D_2O at 25 °C and cooled down to 20 °C. Ellipsometric measurements were then performed at 25 °C and 45 °C with subsequent substitution of D_2O for H_2O and measuring at the same temperatures. In the end, thicker PNIPAAm brushes were also measured again in finer temperature steps as well as in separate heating and cooling cycles to monitor potential hysteresis effects.

Figure 3.31 shows in-situ $\tan\Psi$ spectra of the $d_{\mathrm{dry}} = 12.5$ nm thin PNIPAAm brush in the heating cycle between 25 °C and 45 °C. Most prominent features are the bulk contributions of water, namely the stretching regions $\nu(H_2O)$ and $\nu(D_2O)$ around respectively 3470 cm^{-1} and 2580 cm^{-1}, the bending regions $\delta(H_2O)$ and $\delta(D_2O)$ around respectively 1650 cm^{-1} and 1215 cm^{-1}, as well as the libration region $\nu_{\mathrm{L1}}(H_2O)$ around 730 cm^{-1} in the case of normal water. Clearly, the water signature is dominating the spectra. Depending on thickness and water content of the swollen brush, these bulk-water contributions are up to ≈ 1.5 magnitudes larger than the vibrational bands of the polymer brush. Moreover, the optical properties of water itself are strongly dependent on temperature, which makes it almost impossible to deduce any useful information from the raw $\tan\Psi$ spectra alone. For this reason, temperature-dependent $\tan\Psi$ spectra were also measured under the same conditions using the silicon wedge no. 1 (see Tab. 3.6), which has neither a linker nor a brush top-layer. Referencing brush spectra with these measurements then eliminates the bulk signal of water.

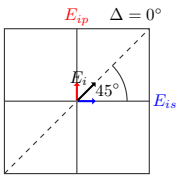

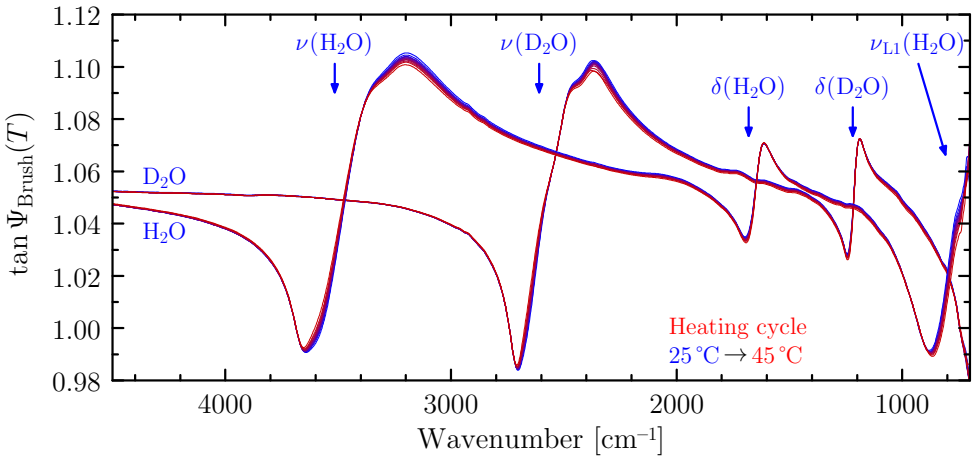

Figure 3.31: Temperature-dependent in-situ tan Ψ spectra of the $d_{\mathrm{dry}} = 12.5$ nm thin PNIPAAm brush measured in H_2O and D_2O between 25 °C and 45 °C.

Referenced tan Ψ spectra are shown in Fig. 3.32, and an enlarged view of the amide region of PNIPAAm is presented in Fig. 3.33. The vibrational bands of the brush—predominantly the amide bands and the $\nu(CH_x)$ vibrations—are now clearly visible, as are influences of the two different solvents. The optical contrast between reference and brush measurements manifests itself in downward-pointing polymer bands and upward-pointing water bands at the corresponding positions of $\nu(H_2O)$, $\nu(D_2O)$, $\delta(H_2O)$, $\delta(D_2O)$, and $\nu_{L1}(H_2O)$. A quantitative analysis of these bands and their temperature-dependent variations gives valuable information about thickness and water content of the brush around the phase transition [25]. Details will be presented in Section 3.5.4.

There are various reasons why D_2O was used as a second solvent. For one thing, the bending vibration of normal water at 1650 cm^{-1} is substantially masking the amide I band of PNIPAAm at about 1630 cm^{-1}, making a quantitative analysis of the brush structure rather difficult. Figure 3.33 illustrates this effect. In H_2O, the amide I band appears smaller in amplitude compared to measurements in heavy water. When using D_2O, the bending vibration of water is shifting to about 1215 cm^{-1}, thereby exposing the true nature of the amide I band. For another thing, PNIPAAm brushes below the LCST are strongly hydrated in aqueous solutions [26], which leads to large contributions of the free-water signature that in turn overlaps with the amide I band. Furthermore, interactions between PNIPAAm and water are expected to be different, because D_2O can form stronger hydrogen bonds than H_2O, despite its similar bond length [45, 50, 247, 248]. The phase transition is also likely to be affected [50], which in turn yields deeper insights into polymer–water and polymer–polymer interactions. Also, information about the brush's depth profile can, in principle, be extracted from the exchange rate between heavy and normal water when substituting one solvent for another.

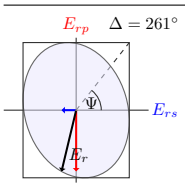

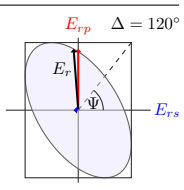

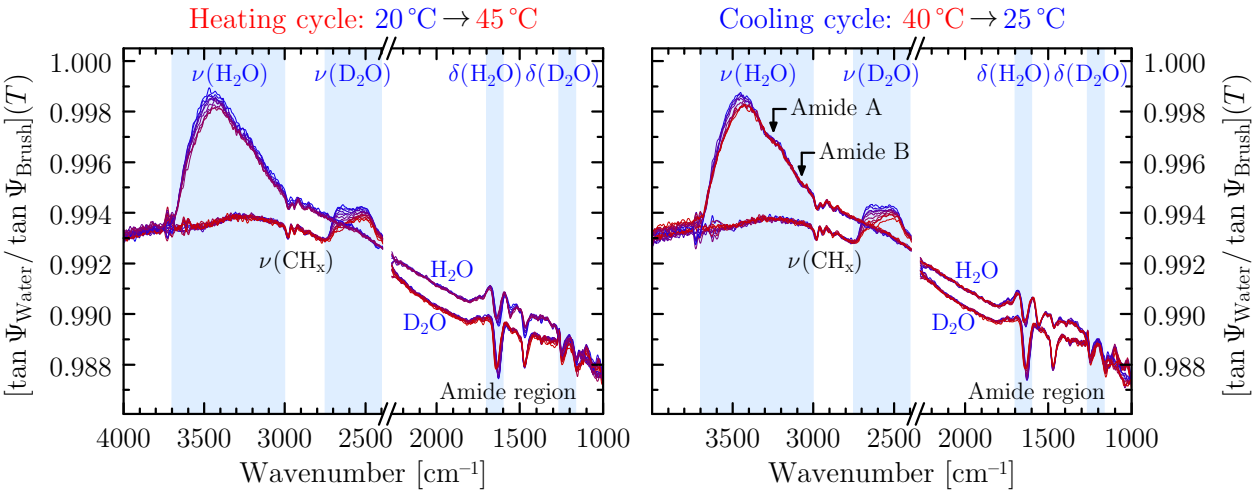

Figure 3.32: Referenced $\tan\Psi$ spectra of the $d_{\mathrm{dry}} = 12.5\,\mathrm{nm}$ thin PN132k brush during temperature-dependent switching in H_2O and D_2O between 20 °C and 45 °C. Note that the strong double band around $3700\,\mathrm{cm}^{-1}$ is an artifact corresponding to combination vibrations of atmospheric CO_2 [249].

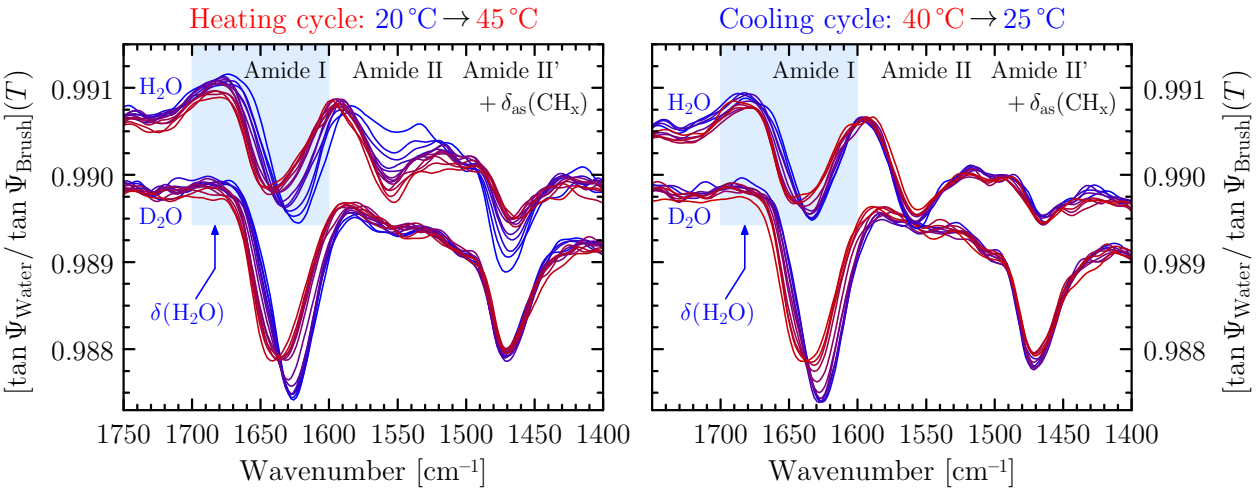

Figure 3.33: Amide region of the $d_{\mathrm{dry}} = 12.5\,\mathrm{nm}$ thin PN132k brush during temperature-dependent switching in H_2O and D_2O between $T = 20\,°\mathrm{C}$ and $T = 45\,°\mathrm{C}$.

3.3.1. Analysis of vibrational bands

From Figs. 3.32 and 3.33, it is already obvious that the amide bands are strongly affected in shape and position when the PNIPAAm brush is heated above its lower critical solution temperature. Furthermore, changes in optical contrast in the $\nu(H_2O)$ and $\nu(D_2O)$ regions indicate temperature-dependent changes of the amount of bound water inside the brush. Owing to the referencing, thickness and absolute water content of the brush cannot be estimated directly, but can only be accessed by quantitative optical simulations. Nonetheless,

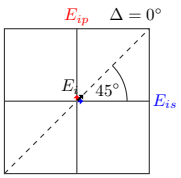

qualitative spectra evaluation with respect to changes in composition and position of the vibrational bands is still possible and already yields useful information about the brush structure below and above the LCST.

The initial measurements were performed in D_2O, which causes N-deuteration of the amide groups, as was thoroughly discussed in Sections 3.1.5.a) and 3.2.3. Instead of an amide II band around 1550 cm^{-1}, which involves several δ(NH) contributions, an amide II' band is observed at about 1470 cm^{-1}, which consists of δ(ND) contributions and is partly overlapped by the asymmetric CH_x-bending vibrations. During the first measurements in H_2O, the brush still contained deuterated amide groups. Full de-deuteration took place during the heating cycle, which can be seen from the increasing amide II and the decreasing amide II' amplitude. Furthermore, amide A and B bands at about 3300 cm^{-1} and 3070 cm^{-1}, respectively, become visible, which are associated with ν(NH) and the first overtone of amide II. Note that the very small amide II band in the D_2O spectra also hints at minute residues of N−H groups within the brush in deuterated state.

The signal-to-noise ratio is not sufficient for making any definite statements about possible compositional changes of amide II and II'. Both bands seem to shift towards lower wavenumbers at increasing temperatures. Following the band assignments in Section 3.1.5., these shifts might be associated with increasing amounts of amide-interacted N−H and N−D groups at the expense of water-interacted groups, which indicates a dehydration of the brush above the LCST. Optical simulations, however, are needed to verify this hypothesis.

Band changes of amide I around 1630 cm^{-1} are much more pronounced and can therefore be discussed with more certainty. In heavy water, the band is shifting from 1626 cm^{-1} at 20 °C to 1641 cm^{-1} at 45 °C, with a sharp transition in amplitude and frequency occurring between 33 °C and 34 °C. Similar shifts are observed in normal water where the transition occurs between 32 °C and 33 °C. In the latter case, however, amide I is overlapped by the upward-pointing $\delta(H_2O)$ band, and it is also influenced by the simultaneous D→H exchange.

As discussed in Section 3.1.5., the amide I band composition characteristically depends on changes in the different kinds of polymer–water and polymer–polymer hydrogen bonding. In both D_2O and H_2O, amide I seems to comprise two or more subcomponents. Second-derivative analysis shown in Fig. 3.34 is helpful in order to identify them. In D_2O, two major amide I subcomponents are found at about 1626 cm^{-1} and 1647 cm^{-1}. In H_2O, two equivalent components are observed at 1635 cm^{-1} and 1650 cm^{-1}. The exact oscillator positions can only be derived from optical simulations owing to film effects and possible band shifts due to the measurement geometry. In comparison with the band assignments in Section 3.1.5. (see Figs. 3.11 and 3.14), the subcomponents correlate mainly with dihydrogen-bonded water-interacted C=O groups below the LCST (lower-wavenumber subcomponents; C=O···D_2O and C=O···H_2O) as well as double-bonded amide-interacted C=O groups above the LCST (higher-wavenumber subcomponents; C=O···D−N and C=O···H−N).

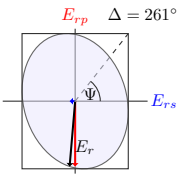

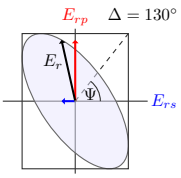

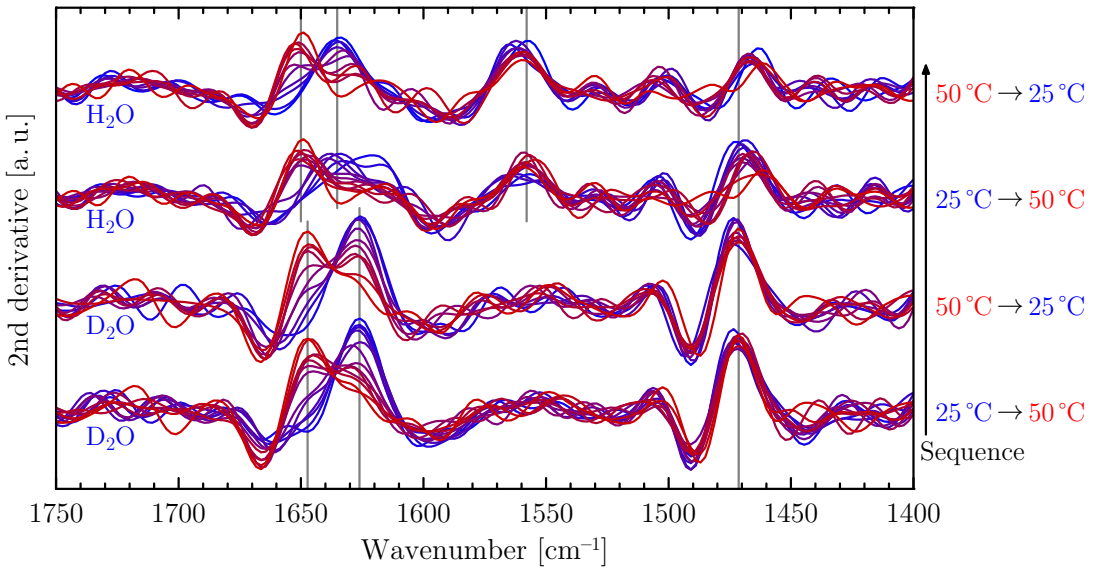

Figure 3.34: Second-derivative spectra corresponding to the $d_{\mathrm{dry}} = 12.5\,\mathrm{nm}$ thin PNIPAAm brush in Fig. 3.32, showing band-component changes in the amide I and II/II' region during deswelling and reswelling of the brush in H_2O and D_2O between 25 °C and 50 °C.

These assignments are in agreement with transmission measurements of PNIPAAm solutions [45, 50] and ATR FT-IR measurements on PNIPAAm brushes [26].

It can be concluded that polymer–water interactions dominate within the brush below the LCST. This is probably related to the good-solvent qualities of water and the expected strong hydration of the brush, as discussed in Section 3.2.1.a). Bittrich et al. [26] report typical water contents of 80–90 vol%. Above the LCST, at presumably bad-solvent qualities and much lower water content [26], the brush deswells while polymer–polymer interactions become more relevant.

A detailed quantitative band analysis of amide I will be given in Section 3.5.4. It then turns out that amide I contains mainly dihydrogen-bonded C=O groups below the LCST, but also a small contribution from mixed hydrogen-bonded groups that form one hydrogen bond with water and one with H−N groups. Above the LCST, the amount of mixed- and dihydrogen-bonded groups decreases, while double-bonded C=O groups become favored.

3.3.2. Testing for hysteresis effects

VIS ellipsometry [26] and QCM measurements [64] on PNIPAAm brushes reveal that the LCST behavior is governed by certain hysteresis effects—similar to PNIPAAm in solution [45, 50]—that predominantly affect the thickness of the swollen brush. Furthermore, the phase transition with temperature seems to be rather pronounced at higher grafting densities, whereas a more gradual transition is observed at lower grafting densities [26, 75].

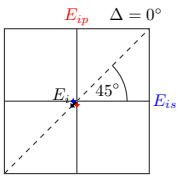

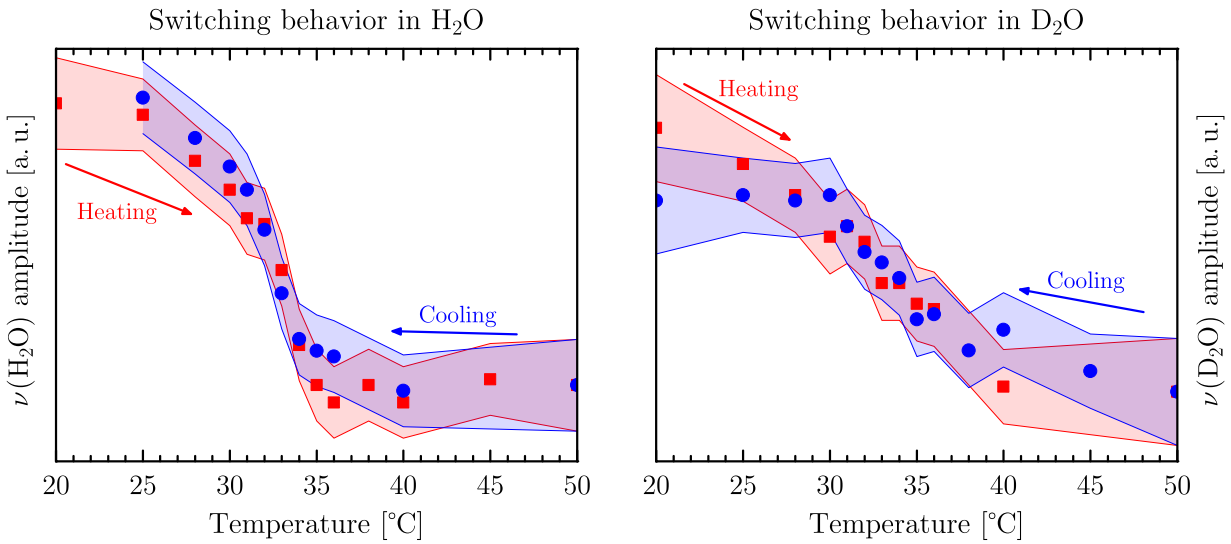

Figure 3.35: $\nu(H_2O)$ and $\nu(D_2O)$ amplitude progressions of the $d_{dry} = 12.5$ nm thin PN132k brush of Fig. 3.32 during temperature-dependent swelling in H_2O and D_2O. Amplitudes of $\nu(H_2O)$ and $\nu(D_2O)$ were measured around 3450 cm^{-1} and 2510 cm^{-1}, respectively. Experimental errors are marked as error bands to guide the eye.

Information about the switching behavior of PNIPAAm brushes can also be obtained from infrared-ellipsometric spectra, even without optical simulations. This is owing to the nature of the $\nu(H_2O)$ and $\nu(D_2O)$ stretching bands of water. The optical contrast associated with these bands changes if either thickness or water content of the swollen brush varies. Figure 3.35 shows the temperature dependence of the $\nu(H_2O)$ and $\nu(D_2O)$ amplitudes during heating and cooling of the $d_{dry} = 12.5$ nm thin PN132k brush in H_2O and D_2O between 20 °C and 50 °C. Starting at maximum amplitudes at low temperatures, the water-band amplitudes undergo a transition of sigmoidal shape towards smaller amplitudes at higher temperatures. These amplitude changes can be connected with a decrease in brush thickness, that is, with deswelling or collapsing of the polymer chains towards the substrate, but they are also associated with a changing water content and with the temperature-dependence of the bulk-water optical properties themselves (see Section 3.4.). For H_2O, a distinct transition occurs with an inflection point at about (32.2 ± 0.3) °C, close to the LCST of PNIPAAm in solution [43–45]. For D_2O, the transition is less pronounced, and its inflection point lies at about (33.0 ± 1.0) °C. Similar to PNIPAAm solutions, this delayed transition might be associated with stronger hydrogen bonds between amide groups and water within the deuterated swollen brush [50].

For both H_2O and D_2O, no obvious hysteresis effects are observed during deswelling and reswelling. Band amplitudes upon heating and cooling overlap within the experimental errors. These findings agree with the results by Bittrich et al. [26] who investigated brushes with $\overline{M}_n = 47\,000$ g/mol and found distinct hysteresis effects only at grafting densities larger

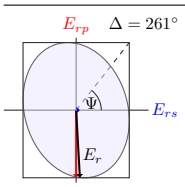

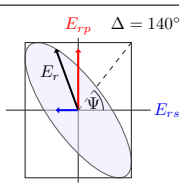

than $\sigma = 0.07\,\mathrm{nm}^{-2}$. The brush analyzed with infrared ellipsometry exhibits $\sigma = 0.06\,\mathrm{nm}^{-2}$, which is probably why a hysteresis is not present or not that pronounced. Further measurements of brushes with different grafting densities and molecular weights are necessary, though, to validate whether or not grafting density is the only influential parameter. Note, however, that considering only the water-band amplitudes is just a rough estimation of possible swelling and hysteresis effects. A more complete picture can only be obtained from optical simulations (discussed in Section 3.5.4.) that factor in changes in baseline slope due to thin-film interference effects. Together with the water-band amplitudes and shapes, this slope is directly related to the thickness and water content of the swollen brush.

The peak positions of amide I as well as of the CH_x-stretching and -bending vibrations also show similar temperature-dependent progressions as the $\nu(H_2O)$ and $\nu(D_2O)$ amplitudes. Since the shifts in amide I are related to amplitude changes of different subcomponents, the spectra must be evaluated quantitatively within a proper optical model to gain conclusive results about hysteresis effects, which is the aim of future work.

3.3.3. Dependence on grafting density and molecular weight

As previously discussed, the actual switching behavior of PNIPAAm brushes is more complex than just a temperature-dependent deswelling and reswelling. Changing polymer–water and polymer–polymer interactions are intrinsically important during the LCST transition. For better understanding the dependencies of this transition, five brushes with different grafting densities between $\sigma = 0.020\,\mathrm{nm}^{-2}$ and $0.124\,\mathrm{nm}^{-2}$ as well as molecular weights of $\overline{M}_n = 132\,000\,\mathrm{g/mol}$ and $56\,000\,\mathrm{g/mol}$ were measured in-situ in D_2O and H_2O at 25 °C and 45 °C. Corresponding spectra are compared in Fig. 3.36, ordered by increasing dry-state brush thickness from bottom to top.

Except for the $d_{\mathrm{dry}} = 14.5\,\mathrm{nm}$ thick brush, neither brush was measured in fully deuterated or de-deuterated state, which is why different amplitude ratios are found between amide II and II'. The same is true for amide A/B and amide A'. Nevertheless, an analysis of the amide I composition in both D_2O and H_2O—following the band analysis in Section 3.3.1.—shows that all brushes undergo a similar transition from mainly polymer–water-interacted amide groups below the LCST to polymer–polymer-interacted amide groups above the LCST. Simultaneously, a deswelling and/or reduction of water content inside the brushes is correlated, again, with the decreasing $\nu(H_2O)$ and $\nu(D_2O)$ band amplitudes.

Notably, all brush spectra obtained in D_2O show a lower baseline compared to H_2O. At the same time, the $\nu(D_2O)$ band amplitudes are much smaller than the corresponding $\nu(H_2O)$ amplitudes. The PN132k brush with $d_{\mathrm{dry}} = 4.0\,\mathrm{nm}$ even shows negative $\nu(D_2O)$ bands. This is also found for the 2.4 nm thin PGMA anchoring layer, which was measured in D_2O and H_2O, too. Brush spectra in D_2O also exhibit small contributions from upward-pointing

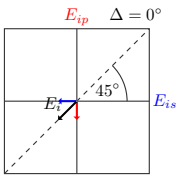

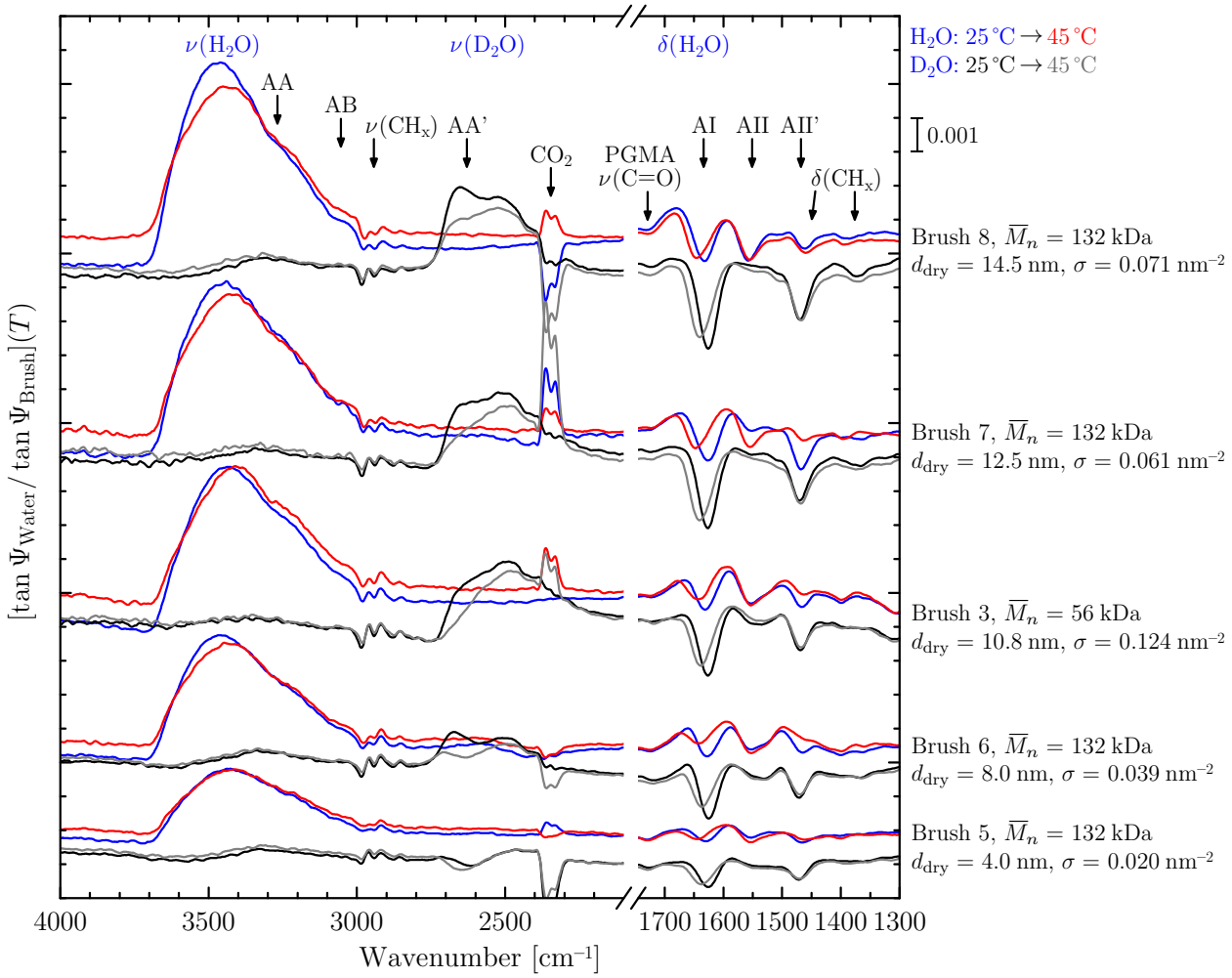

Figure 3.36: Referenced $\tan\Psi$ spectra of PNIPAAm brushes no. 3, 5, 6, 7, and 8—see Tab. 3.6 in Section 3.2.1.a)—during temperature-dependent switching in D_2O (black and gray lines) and H_2O (blue and red lines) from 25 °C to 45 °C. Spectra were baseline-corrected according to Section 2.1.4.c) and Savitzky–Golay-smoothed (31 points, polynomial order 5). Spectra of different brushes are baseline-shifted for better comparability, whereas the baseline relations in each set of four brush spectra (blue, red, black, gray) are kept true. Amide A, B, A', I, II, and II' bands are marked as AA, AB, AA', AI, AII, and AII', respectively.

$\nu(H_2O)$ bands. This hints at minute residues of H_2O in the D_2O reference measurements. No $\nu(H_2O)$ peaks are observed in the raw D_2O $\tan\Psi$ spectra, though. The causes of the aforementioned effects are not fully understood yet and thus still under investigation.

For the four PN132k brushes, the relative $\nu(H_2O)$ bands at 25 °C and 45 °C as well as the relative baseline slopes scale according to changes in grafting density and dry-state brush thickness. Larger amplitude changes are observed for higher grafting densities. This suggests that all brushes exhibit the same brush and mushroom (or intermediate) conformations below

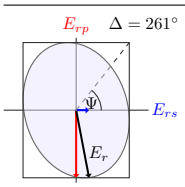

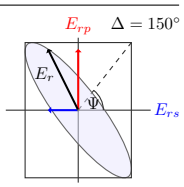

and above the LCST, respectively, as proposed in Section 3.2.1.a). The $\nu(H_2O)$ bands and baseline slopes of the PN56k brush scale a little bit differently with dry-state brush thickness compared to the PN132k brushes. Absolute values of swollen-brush thickness and water content are therefore expected to show a different dependence on grafting density, which is in accordance with VIS-ellipsometry measurements [26].

The main goal in the next sections is to understand the swelling behavior of PNIPAAm brushes quantitatively on the basis of optical layer models. Swollen-brush thickness and water content in dependence of temperature have to be determined and should match with corresponding values from in-situ visible ellipsometry. Quantifying the amide-band composition, then, will reveal absolute amounts of water- and amide-interacted amide groups below and above the LCST.

In-situ brush spectra can only be modeled successfully if high-quality optical constants $n(T)$ and $k(T)$ are used for H_2O and D_2O. These must therefore be determined first. In principle, the same in-situ infrared-ellipsometry set-up as used for measuring the brushes is suitable for this task. If the substrate geometry is properly accounted for [20] and the substrate's optical constants are known, then measured $\tan\Psi$ and Δ spectra can be inverted directly to obtain n and k. Indeed, this strategy proved successful for modeling the temperature-dependent swelling behavior of the $d_{dry} = 12.6$ nm thick PN94k brush [25]. However, the results are affected by several systematic errors. These originate, for example, from lateral variations in substrate properties, time-dependent changes of the native oxide layer, non-linearity of the MCT detector, as well as variations in the optical path due to the opening angle of the beam and the wedged-shaped substrate. For these reasons, additional transmission measurements were performed that allow one to calculate the extinction coefficient $k(T)$ and, consequently, the refractive index $n(T)$ by Kramers–Kronig integral relations.

Details about transmission measurements of water are given in Section 3.4. PNIPAAm brushes are then modeled quantitatively in Section 3.5.

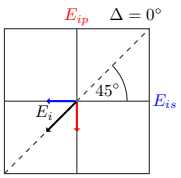

3.4. Temperature-dependent optical constants of H_2O and D_2O

The optical properties of water vary strongly in dependence of temperature [110, 250–253]. In order to successfully model ellipsometric in-situ spectra of brushes in aqueous solutions, it is therefore imperative to determine $n(T)$ and $k(T)$ of H_2O and D_2O as the first step. The optical constants of liquids are usually obtained from measurements in ATR configuration [151, 166]. In the current work, however, special transmission cells were used to perform transmission measurements on normal and heavy water between 8000–700 cm^{-1} in a temperature range from 20–45 °C. By means of optical modeling, these measurements allow one to calculate the extinction coefficients $k(T)$ and, consequently, the refractive indices $n(T)$ by Kramers–Kronig integral relations.

Two transmission cells with path lengths of $d_{Cell} = 6.60\,\mu m$ and $3.26\,\mu m$ were available. H_2O and D_2O were measured in both cells between 20 °C and 45 °C, as shown in Fig. 3.37. Since absorbance is scaling proportionally with wavenumber, transmittance in the D_2O-stretching region around 2500 cm^{-1} is considerably larger compared to the H_2O-stretching region at 3400 cm^{-1}, despite the similar absolute k values. The H_2O-stretching bands measured with the 6.60 µm cell are too strong to be detectable without band distortions. The minimum transmittance in this case is about 0.03%, which is too small even for the very linearly responding DTGS detector [136]. The minimum transmittances in the other spectra are larger than 0.20%. Since the photometric accuracy of the utilized Vertex 70 spectrometer is better than 0.10% transmission, these spectra should be suitable for a quantitative evaluation. This was confirmed for the D_2O measurements by rescaling the corresponding absorbance spectra of the short and long cells to match in band amplitudes (remember that absorbance is proportional to path length). Except for differences in the interference fringes above 4000 cm^{-1}, the measured band shapes coincide, suggesting that the stretching bands can be considered distortion-free.

Some artifact bands are observed at 2512 cm^{-1} and 1456 cm^{-1} in the H_2O spectra and at 3418 cm^{-1} and 1461 cm^{-1} in the D_2O spectra. These bands can be assigned to HOD vibrations due to minute residues of D_2O or H_2O that are bound by the epoxy spacer separating the windows. These residues are difficult to remove when changing the liquid, even if the cell is purged multiple times. Slowly over time during the measurements, $H_2O \leftrightarrow D_2O$ exchange occurs within the epoxy, giving rise to the aforementioned vibrational bands. Their positions coincide with two different HOD species, as demonstrated by Max and Chapados who investigated H_2O/D_2O mixtures using factor analysis [228]. These species—denoted as OH_3D and OD_3H—respectively correspond to small amounts of D−O−H molecules hydrogen-bonded to H−O−H without the presence of D_2O molecules, on the one hand, as well as small amounts

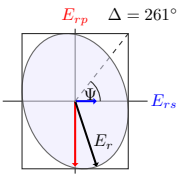

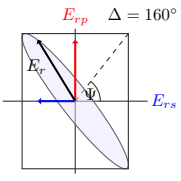

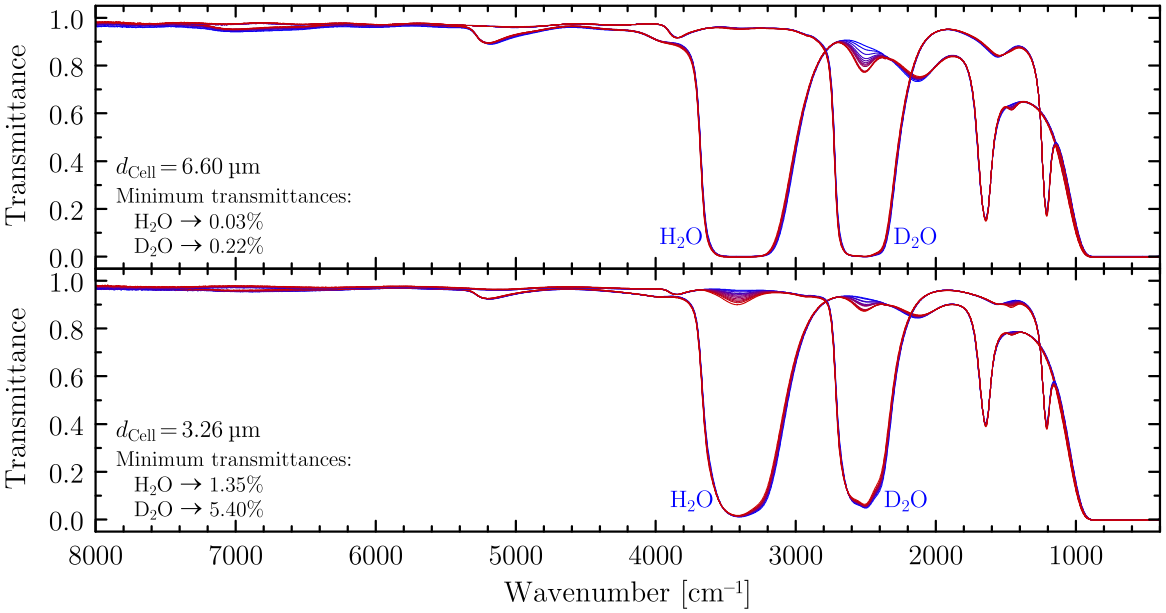

Figure 3.37: Transmittance spectra (4 cm^{-1} resolution) of liquid H_2O and D_2O measured between 20 °C and 45 °C using transmission cells with path lengths of 6.60 µm (top) and 3.26 µm (bottom). Minimum transmittances in the stretching regions of H_2O and D_2O are denoted at the left. The photometric accuracy of the spectrometer was 0.10% transmission.

of D−O−H hydrogen-bonded to D−O−D without the presence of H_2O on the other hand. Either specie absorbs in both the stretching and the bending regions of H_2O and D_2O. To minimize their effect on the true n and k values of pure H_2O and D_2O, only the 6.60 µm spectra were used for D_2O, since these are almost free of HOD bands. The situation for H_2O spectra is more difficult and will be discussed in a moment.

The transmission cells used in this work consist of CaF_2 windows that are transparent down to ≈ 900 cm^{-1}. Since water absorbs significantly between 900–0 cm^{-1}, it is necessary to extrapolate the accessible wavenumber region in order for the Kramers–Kronig transform to yield reliable results. Starting point for the investigations, therefore, was the meticulous study by Max and Chapados [166] who provide reference data for n and k of H_2O and D_2O at room temperature from 6000 cm^{-1} to 0 cm^{-1}. To avoid artificial concatenation of measured data above and reference data below 900 cm^{-1}, the optical constants were first fitted over the whole range of 6000–0 cm^{-1} after Eq. (2.75) using Gaussian oscillators that correspond to the various vibrational modes of (heavy) water. Initial values for oscillator positions, amplitudes, and band widths were taken from Refs. [166, 228]. The resulting set of oscillators served as input parameters for the following fitting process of measured transmission spectra. During the fits, parameters of oscillators situated below ≈ 1200 cm^{-1} were held constant. Nevertheless, since these are also expected to be affected by temperature [110, 250, 254], their potential effect on the refractive index n via Kramers–Kronig transform must be evaluated

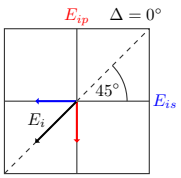

in the end. H_2O spectra were fitted with two additional oscillators placed at 2512 cm^{-1} and 1456 cm^{-1} that correspond vibrations of small HOD residues. After the fit, n and k were recalculated at each temperature without these two oscillators.

The modeling process is now described in more detail. A five-layer optical model consisting of Air/CaF_2/Water/CaF_2/Air was assumed after Fig. 2.12 with literature data for the CaF_2 windows [142, 255]. This model produces fast oscillations within the 4 mm thick windows. Since these oscillations are well below the spectral resolution of the measurement (4 cm^{-1}), they were damped by emulating the apodization process during spectra acquisition of the Fourier spectrometer. For this, the computed transmittances were transformed into Fourier space by Fast-Fourier transform (FFT) [101], multiplied with the Blackman–Harris four-term apodization function [256], and then transformed back into wavenumber space by inverse FFT.

The path lengths of the cells were, at first, estimated from empty-cell measurements in dry state using the fringe method [138]. Max and Chapados also derived analytical equations for calculating the transmittance of a cell with non-parallel windows that has a varying path length of $d_{Cell} \pm \delta_{Cell}$ [140]. By applying these equations, the path lengths were determined accurately, and plane-parallelism of the windows was verified up to $\delta_{Cell} = \pm 10$ nm.

Thermal expansion of the cells was then measured in dry and wet state. Between 20 °C and 45 °C, an increase in path length of 50 nm was found for the empty 6.60 µm cell, whereas the 3.26 µm cell expanded by 35 nm. In wet state, obvious interference fringes are only visible between approximately 4000–8000 cm^{-1}. This region was used to determine $d_{Cell}(T)$, which resulted in the same increases in path lengths as obtained in dry state. Temperature-dependent changes in refractive index of the CaF_2 windows are expected to be smaller than 0.0004 in the probed temperature range [257] and are therefore negligible.

Transmittance (absorbance) spectra were now fitted by varying the parameters of oscillators situated between 4200–1150 cm^{-1} for D_2O and between 5200–1200 cm^{-1} for H_2O. After each iteration during the fits, current n and k values were recalculated from 6000–0 cm^{-1} with the high-frequency dielectric constant being fixed to $\varepsilon_\infty = (1.333)^2$ [166]. The resulting temperature-dependent optical constants $n(T)$ and $k(T)$ are plotted in Fig. 3.38.

With minor restrictions, $n(T)$ and $k(T)$ can be considered accurate enough for simulating polymer-brush spectra between 4000–1100 cm^{-1} for D_2O and between 4000–1300 cm^{-1} for H_2O. Below 1100 cm^{-1}, the absorption properties of the CaF_2 windows dominate the transmittance spectra and hinder a reliable fit on parameters of oscillators situated in this region. This also affects the very broad $\nu_2 - \nu_{L2}$ combination band of H_2O around 1190 cm^{-1} [228]. The associated oscillator had to be fixed, which causes slight deviations in k between 1400–1100 cm^{-1} compared to ATR absorbance measurements in the literature [110]. Furthermore, in the case of H_2O, some artifacts from HOD vibrations remain around 2500 cm^{-1} and 1450 cm^{-1}, even after recalculation of n and k without the corresponding oscillators. The

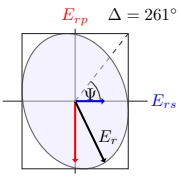

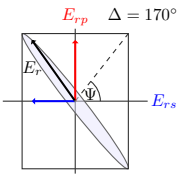

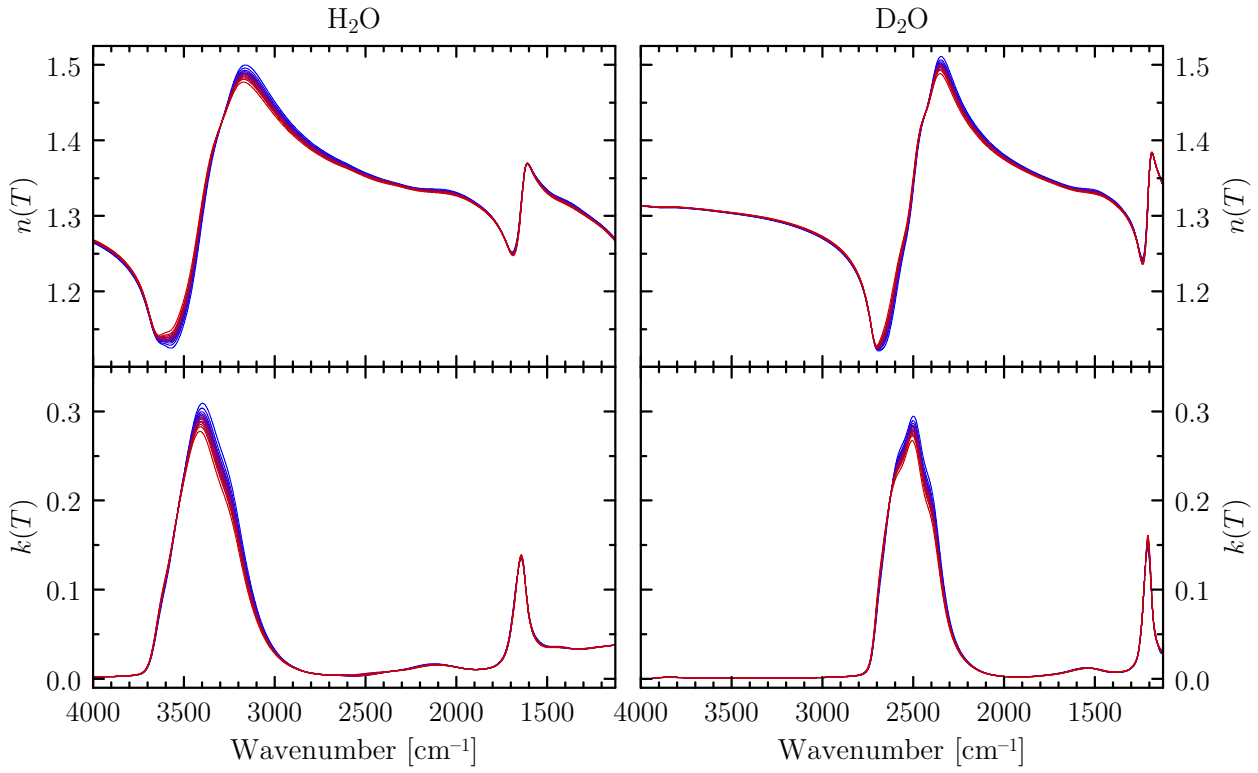

Figure 3.38: Temperature-dependent optical constants of H_2O and D_2O as determined from infrared transmission measurements. Temperatures were $T = [20, 25, 28, 30, 31, 32, 33, 34, 35, 36, 38, 40, 45]$ °C.

absolute k values in these two regions, however, are small compared to the stretching and bending vibrations and also to polymer bands that occur there. Importantly, HOD bands also overlap with both the stretching and the bending vibrations of H_2O and D_2O. This causes an overestimation of the respective band amplitudes by about 1–3% in the k spectra.

The temperature-dependent influence of ε_∞ on n and k has yet to be determined. ε_∞ was varied by ±5%, but its effect on transmittance spectra could not be distinguished from changes in path lengths of the cells. Lastly, the libration regions below 1000 cm^{-1} also undergo changes with increasing temperature [110, 250, 254] and therefore yield T-dependent contributions to n and k via the Kramers–Kronig transform. To estimate this effect, the amplitudes of oscillators situated in these regions were varied up to ±10% with increasing temperature, as shown in Fig. 3.39 for the refractive index at 45 °C. At 1100 cm^{-1}, the absolute values of $n(45\,°C)$ change by ±0.014 for H_2O and by ±0.004 for D_2O. Deviations from the fitted results quickly diminish at higher wavenumbers in the case of D_2O. For H_2O, the influence of bands involving libration modes is stronger since these are located at higher wavenumbers. Complementary transmission measurements using, for example, cells with ZnSe or Si windows, which exhibit transmission cut-offs at lower wavenumbers compared to CaF_2, might aid in determining physically correct libration oscillator parameters.

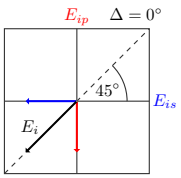

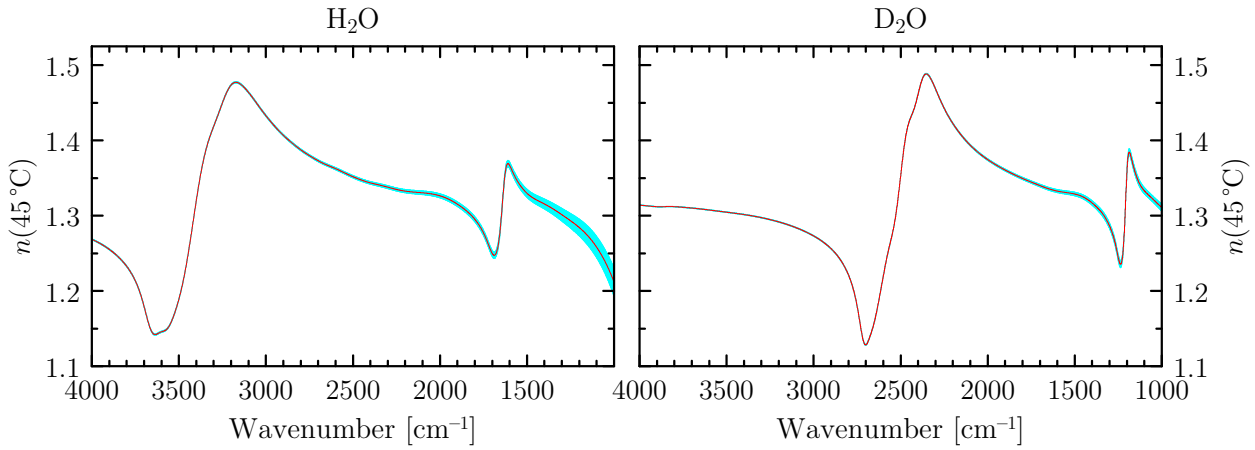

Figure 3.39: Effect of the Kramers–Kronig transform on $n(45\,°C)$ of H_2O and D_2O (red lines) when varying the amplitudes of oscillators associated with librations below 1000 cm^{-1} by ±10% (light bands).

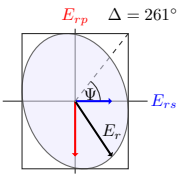

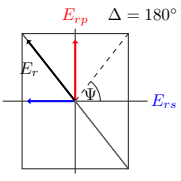

3.5. Systematic investigations of PNIPAAm brushes in aqueous solutions

3.5.1. Motivation

Quantitative interpretation of infrared spectra of functional polymer films or proteins in aqueous environment is always complicated by the overlapping vibrational bands of water. Experiments are therefore often performed in heavy water to separate water and polymer contributions, as was discussed in Section 3.3. In particular, the amide I and II bands are strongly altered in amplitude, position, and shape by the bending vibration of normal water, which is of the same order of magnitude. This can pose severe problems that are, however, easily overlooked when just regarding the amide region of the spectrum. As a result, quantitative conclusions about amide-band composition, for example, are drawn from basically uninterpretable spectra. Often it is attempted to subtract the water contributions in order to reveal a "more true" band composition [258–260]. While this might work in some cases for transmission spectra, it does not necessarily work for reflection spectra, mainly because of film effects. Even for transmission measurements, the subtraction approach is rather questionable, since the strong oscillators associated with the molecular vibrations of water can cause strong band shifts of the measured water bands, depending on the water content of the film. In reflection, these shifts can be of the order of some $10\,\mathrm{cm}^{-1}$, rendering impossible a quantitative evaluation that is based on band analysis at the level of the measured spectra.

This is the main reason why simulating the spectra within a physical model is not only beneficial, but essential for gaining physically meaningful results. Because the model is based on the actual sample properties, it is possible to separate the different spectral contributions that originate from water, polymer brush, or anchoring layer. Also film effects, which often cause inconceivable effects on the spectra, are taken care of within the model. Most importantly, overlapping water bands do *not* pose an intrinsic problem any longer. On the contrary, they are automatically accounted for, since the water content is a physical parameter of the model.

3.5.2. Strategy for the quantitative modeling of in-situ spectra

a) In-situ brush model

The aim of the modeling process in the long run is to extract quantitative information about brush structure and interactions between polymer and water in dependence of temperature as well as brush parameters like grafting density. For this purpose, a box model is assumed with constant water content inside the brush and an instantaneous transition to 100 vol% water at

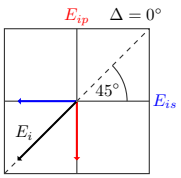

the brush–water/water interface (see Fig. 2.21). This brush profile should be accurate enough to correctly describe the polymer brush above its LCST [245, 246]. Below the LCST, where the profile is expected to show a gradual decrease from low to high water content towards the brush surface [245, 246], this model can be thought of as a description to obtain average values for brush thicknesses and water contents. Regardless of the profile, polymer–polymer and polymer–water interactions are always accessible, because the infrared light is probing the complete brush depth.

The optical layer model of the brushes consists of Water/Brush/PGMA/SiO_2/Si, with water being the substrate material of the model and silicon being the ambient, according to Figs. 2.7 and 2.21. Water is modeled using the temperature-dependent optical constants of H_2O and D_2O determined in Section 3.4., whereas literature data are used for the oxide layer [18], and $n = 3.42$ and $k = 0$ are assumed for the silicon substrate [154]. The brush and PGMA layers are modeled with a modified Bruggeman effective-medium approximation between water and polymer constituents. In principle, the brush profile can be implemented into the model, too. With measurements at only one incidence angle, though, there are not enough independent experimental quantities to extract an unambiguously correct profile. As for the previously discussed modeling of polymer films and brushes—see Sections 3.1.5.b) and 3.2.3.b)—changing polymer–polymer and polymer–water interactions are quantified within the mEMA layer by adjusting the corresponding oscillator parameters of the polymer. Reference spectra of a silicon wedge in contact with water are simulated within the same model, but without PGMA and brush top-layers.

In the first step of the modeling process, the thickness $\tilde{d}$ and the water content f_{Water} of the swollen or collapsed brush have to be determined. In the second step, spectral changes of PNIPAAm's amide and CH_x vibrational bands with respect to the dry state are analyzed, which yields insights into the various interactions that occur at the solid–liquid interface. Since water-specific and polymer-specific bands are overlapping one another, the first and second step of the modeling process have to be repeated in an iterative manner.

b) Incidence angle and baseline-correction

During the measurements, the external angle of incidence was set to $\varphi_0 = 45°$ with respect to the outer reflex at the silicon wedge. With a wedge angle of 1.5° and a rotation of the sample holder of 7.4° to detect the inner reflex, the internal angle of incidence is given by $\tilde{\varphi}_0 = 11.8°$ according to Snell's law. In order to account for the opening angle of the set-up, spectra are simulated at $\tilde{\varphi}_0 = [10.8°, 11.8°, 12.8°]$ and then averaged. This is imperative because strong vibrational bands like $\nu(H_2O)$ are very sensitive to smallest changes in $\tilde{\varphi}_0$.

It is clear from the wedge geometry in Fig. 2.7 that measured spectra contain contributions from the incident air/wedge interface as well as the wedge/air interface at the reflection side. The corresponding transmission coefficients after the Fresnel equations, however, cancel to

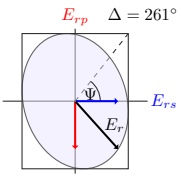

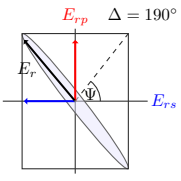

first-order approximation in referenced $\tan\Psi$ spectra if brush and reference measurements are performed under the same angle of incidence [20].

Measured spectra are baseline-corrected as described in Section 2.1.4.c). The additional dry-state correction factor $\tan\Psi^{\text{simul}}_{\text{dry}} / \tan\Psi^{\text{simul}}_{\text{ref, dry}}$ and the correction difference $\Delta^{\text{simul}}_{\text{dry}} - \Delta^{\text{simul}}_{\text{ref, dry}}$ that are used to compensate for thin-film-interference effects are simulated within the above model by replacing water with air and the polymer oscillator layers by constant values $n = n_\infty = 1.5007$ and $k = 0$ for PGMA as well as $n = n_\infty = 1.4832$ and $k = 0$ for PNIPAAm, as determined in Section 3.1.4.

c) Swollen-brush thickness and water content

Within the brush model, the parameters $\tilde{d}$ and f_{Water} for thickness and water content of the swollen brush are strongly correlated. Changing either one of them produces very similar effects in the band amplitudes of both polymer and water. In order to decorrelate the two parameters, additional phase measurements Δ at (multiple) large angles of incidence seem necessary. With the flow cell for in-situ infrared ellipsometry, however, the internal incidence angle at the substrate/brush interface is smaller than 16°. At this angle, $\tan\Psi$ and Δ are two almost redundant parameters. Furthermore, Δ measurements are not feasible for ultra-thin brushes at a sufficiently high signal-to-noise ratio. Due to the strong absorbing qualities of water in the mid-infrared, there is also no absorption-free region that would allow for the separation of thickness and refractive index by using, for example, Cauchy dispersions. A different strategy must therefore be pursued.

The overall thickness of the polymer–water layer is of the order of several 10 nm and, thus, induces thin-film interference, which causes a distinct baseline drift at higher wavenumbers. This spectral characteristic is used to fix the thickness of the swollen-brush layer. Simultaneously, the large vibrational bands of water—especially the $\nu(H_2O)$ band—are analyzed to fix the water content of the brush. With increasing swollen-brush thickness, the $\nu(H_2O)$ amplitude becomes more sensitive to f_{Water}. Most importantly, the frequency of $\nu(H_2O)$ is shifting to higher wavenumbers with increasing water content, because $\nu(H_2O)$ comprises five very strong oscillators [228]. Also the band shape is changing markedly. Both effects allow one to decorrelate $\tilde{d}$ and f_{Water} sufficiently.

As a boundary condition, measured amplitudes of polymer-specific bands that are *not* expected to change with varying water content have to be reproduced correctly. This concerns, for example, the asymmetric CH_x-bending vibrations of PNIPAAm, the frequencies of which are sensitive to hydration, but the amplitudes of which remain almost constant. This can be seen, for example, in humidity-dependent measurements of PNIPAAm films (see Fig. 3.8 in Section 3.1.5.). The amplitudes of symmetric CH_x-bending as well as CH_x-stretching vibrations show small correlations with hydration. The former increase slightly, whereas the latter decrease at higher humidities.

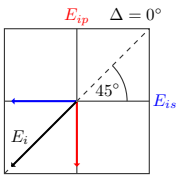

d) Modeling the amide I and II bands

Amide I and II respectively consist of five and three subcomponents that are associated with free, amide-interacted, and water-interacted C=O and N−H groups, as discussed in Section 3.1.5.a). The number of free fit parameters of the corresponding oscillators is large enough to reproduce virtually any observed band shape and amplitude. It is therefore imperative to enforce a physical constraint onto the simulated spectra. This constraint is given by the total number of C=O and N−H groups and the associated average number N_p of dipole moments probed by the infrared light.

For a layer with a single Lorentzian oscillator after Eqs. (2.72) and (2.74), the oscillator strength F is proportional to N_p,

$$F \sim N_p \,, \tag{3.5}$$

with $\tilde{\nu}_0$ being the center frequency of the oscillator. From Eq. (2.75) and the imaginary part of Eq. (2.73), one obtains an analogous expression for a single Gaussian oscillator,

$$N_p \sim \tilde{F}\,\tilde{\sigma}\,\tilde{\nu}_0, \tag{3.6}$$

where $\tilde{F}$ and $\tilde{\sigma}$ are its strength and band width. For the five Gaussian amide I oscillators and the three Gaussian amide II oscillators, this yields the constraints

$$\sum_j \tilde{F}^{(j)}\,\tilde{\sigma}^{(j)}\,\tilde{\nu}_0^{(j)} \stackrel{!}{=} \text{const.} \tag{3.7}$$

Equation (3.7) is expected to be successfully applicable for amide I, which consists mainly of C=O-stretching contributions. Since amide II is a coupled mode of N−H-bending and C−N-stretching, hydrogen bonding might affect the corresponding transition dipole moments in unexpected ways and thereby alter the above constraint.

The different contributions of amide I and II subcomponents to the overall band envelopes are modeled by varying the oscillator strengths $\tilde{F}$ only. Except for the di-H_2O- and H_2O-interacted ν(C=O) and δ(N−H) components at respectively 1625 cm^{-1} and 1554 cm^{-1}, all band widths $\tilde{\sigma}$ are held constant. It is assumed that band shifts due to weakening of hydrogen bonds at elevated temperatures are negligibly small compared to amplitude changes.

3.5.3. Hydration of PGMA films

Before investigating the actual swelling behavior of PNIPAAm brushes, hydration effects of the PGMA anchoring layer must be understood, since these have a potentially strong influence on the quantitative modeling of the brushes. Fukuda et al. [261] showed with optical micrography that PGMA gels swell in many solvents, but do *not* swell at all in water, despite the presence of hydroxy groups on the polymer chains. In order to verify this non-swelling

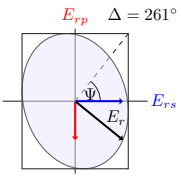

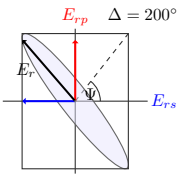

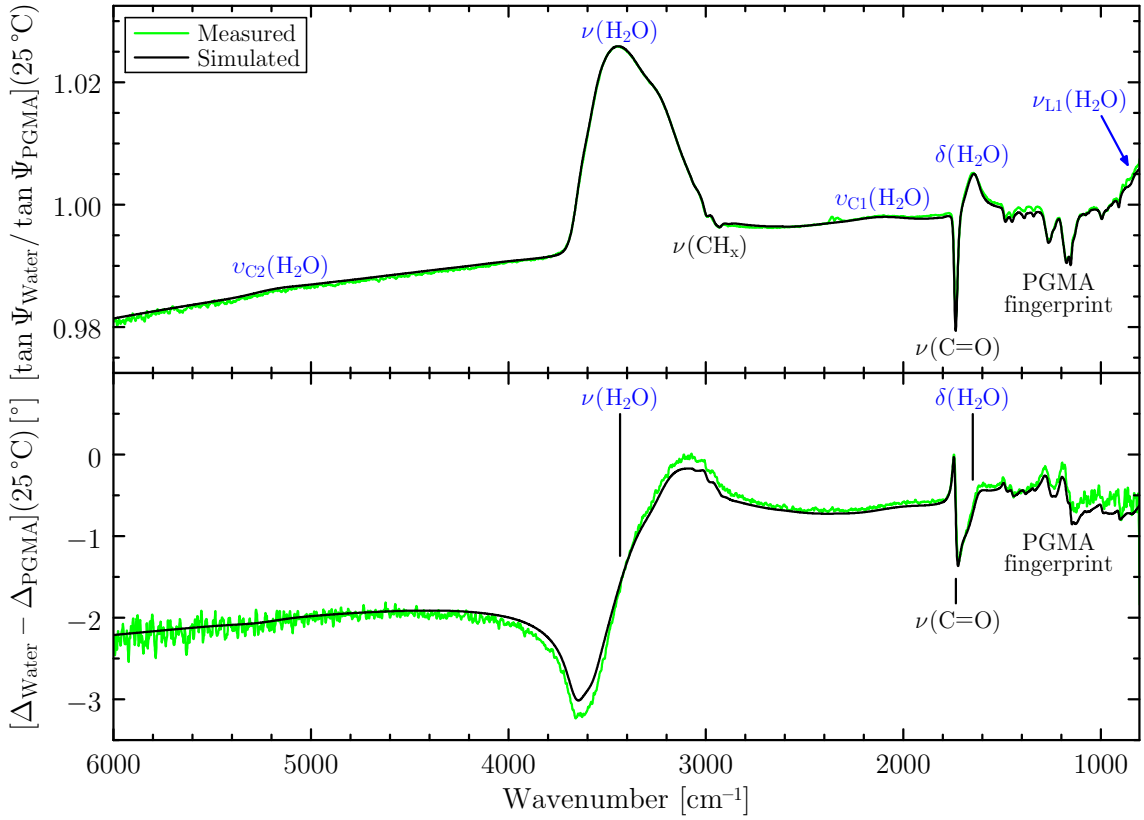

Figure 3.40: Measured and simulated referenced and baseline-corrected ellipsometric in-situ spectra of the 119 nm thick PGMA film in H_2O at 25 °C. The baseline slope in $\tan\Psi$ as well as band shapes and amplitudes of the water vibrational bands and PGMA-specific bands are modeled correctly. Deviations in Δ and in $\tan\Psi$ below 2000 cm^{-1} are likely to be related to film inhomogeneities.

in the infrared, the 119 nm thick spin-coated PGMA film was measured in-situ in H_2O and D_2O at 25 °C and 45 °C. These measurements were also performed for two other reasons. First, the film is thick enough to yield prominent film-interference effects. This allows one to confirm whether the baseline-correction procedure for ellipsometric in-situ spectra proposed in Section 2.1.4.c) works properly. Second, PGMA does not exhibit any vibrational bands in the $\nu(D_2O)$ region between 2800–2000 cm^{-1}. Therefore, general aspects of using aqueous D_2O solutions can be addressed quantitatively, and the validity of the model in which H_2O is replaced by D_2O can be tested.

Figure 3.40 compares measured and simulated referenced and baseline-corrected $\tan\Psi$ and Δ spectra of the 119 nm thick PGMA film in H_2O at 25 °C. The optical contrast between film and reference sample is reproduced correctly, which can be seen from the matching amplitudes and shapes of the water-specific vibrational bands. These are the large $\nu(H_2O)$ band around 3480 cm^{-1}, the $\delta(H_2O)$ and $\nu_{L1}(H_2O)$ bands around respectively 1650 cm^{-1} and 730 cm^{-1}, and even the two small but broad combination bands around 5150 cm^{-1} and

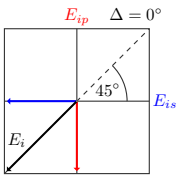

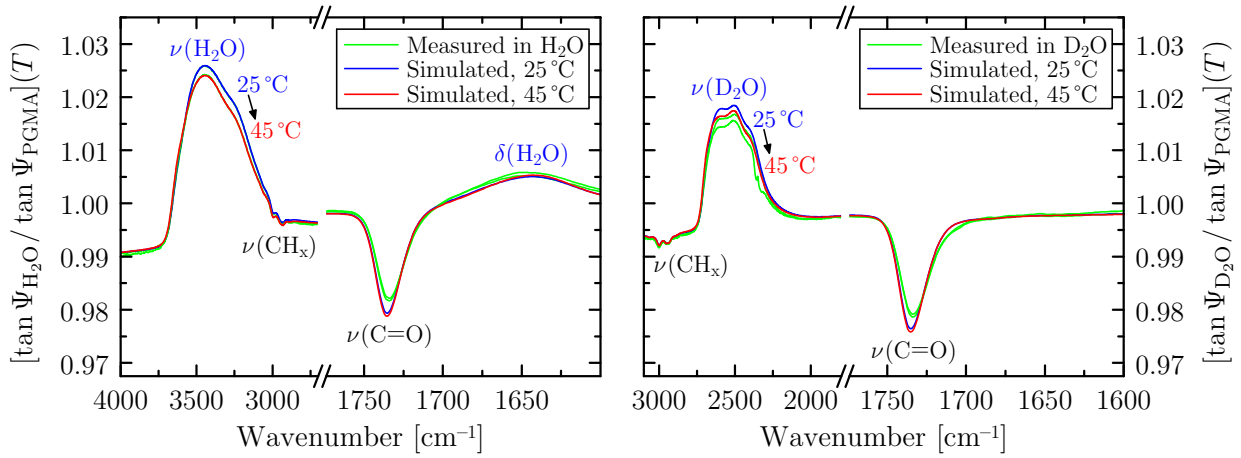

Figure 3.41: Measured and simulated in-situ tan Ψ spectra of the 119 nm thick PGMA film in H_2O (left) and D_2O (right) at 25 °C and 45 °C in the water-stretching and PGMA-carbonyl-stretching regions. $\nu(D_2O)$ is overlapped by atmospheric CO_2 absorption around 2350 cm^{-1}.

2100 cm^{-1} [228]. The simulated baseline slope in tan Ψ at higher wavenumbers agrees with the measurement. Small baseline deviations observed between 2000–1300 cm^{-1} are probably related to film inhomogeneities, as discussed in Section 3.1.3. and in Appendix E.

Simulation parameters for thickness $\tilde{d}$ and water content f_{H_2O} of the PGMA layer were $\tilde{d}(25\,°C) = (122 \pm 2)$ nm and $f_{H_2O}(25\,°C) = (4 \pm 2)$ vol%. These values substantiate Fukuda's results that PGMA does not swell in water. The strong self-crosslinking between the PGMA chains might explain why the polymer is unsolvable in water. The latter was confirmed by repeating the in-situ measurements several times and afterwards measuring a non-changing dry-state thickness with VIS ellipsometry. The very small hydration of the PGMA layer, if any, also manifests itself in the fact that the vibrational bands of PGMA can be described by the pure dry-state optical constants, that is, the PGMA bands do not undergo amplitude changes or frequency shifts. This is true for all $\nu(CH_x)$ and fingerprint bands. The only exception is the carbonyl-stretching band $\nu(C{=}O)$ at 1735 cm^{-1}, details of which will be given in a moment.

Figure 3.41 shows measured and simulated tan Ψ spectra of the PGMA layer in H_2O and D_2O at 25 °C and 45 °C. Thickness and water content are found to be $\tilde{d}(45\,°C) = (122 \pm 2)$ nm and $f_{H_2O}(45\,°C) = (1 \pm 1)$ vol% in H_2O. For simulations in heavy water, the same parameters for $\tilde{d}$ and f_{D_2O} were used as for normal water. The simulated $\nu(C{=}O)$ peak position occurs at 1735.5 cm^{-1} in H_2O and at 1735.0 cm^{-1} in D_2O. This difference is due to the overlapping upward-pointing $\delta(H_2O)$ band in the case of normal water. The measured $\nu(C{=}O)$ band is shifted to 1734.0 cm^{-1} and 1733.5 cm^{-1}, respectively, and it also exhibits a smaller amplitude. Both effects indicate hydrogen bonding $C{=}O \cdots H_2O$ of carbonyl groups to surrounding water molecules. Whether hydrogen bonding takes place only in the topmost part of the PGMA layer or whether the very small hydration does affect the whole layer, cannot be deduced

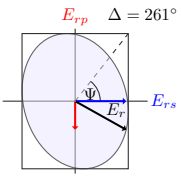

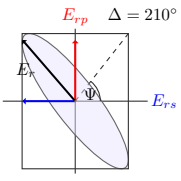

from the simulations. With regard to measurements of PNIPAAm brushes, it can be expected, though, that the ν(C=O) band will show similar or even stronger changes, because additional hydrogen bonding is possible with PNIPAAm's N−H groups.

The final point concerns the water-specific bands, in particular the $\nu(D_2O)$ band around 2500 cm^{-1}. Although PGMA bands as well as the baseline slope at higher wavenumbers do not differ significantly in D_2O compared with PGMA in H_2O, relatively strong amplitude deviations are observed between measured and simulated water bands, as shown in the right panel of Fig. 3.41. The measured $\nu(D_2O)$ bands are much smaller in amplitude. At first glance, this decrease in optical contrast seems to suggest a fundamentally stronger hydration of the PGMA film. However, with $\tilde{d}$ and f_{D_2O} as the only free parameters of the model, the measured band amplitudes cannot be reproduced while maintaining correct band shapes of $\nu(D_2O)$. A control measurement of the 2.4 nm thin PGMA anchoring layer even shows downward-pointing D_2O bands, which means that the effective refractive index of the PGMA–D_2O layer should be smaller than the refractive index of pure D_2O. The nature of these effects is still under investigation. In the following, the focus will therefore lie on the quantitative evaluation of PNIPAAm swelling experiments in H_2O only.

Nevertheless, the above findings for PGMA in contact with H_2O confirm that quantitative modeling of in-situ infrared-ellipsometric spectra is possible and that layer thicknesses and water contents can be extracted correctly.

3.5.4. Structural properties of the brush–water interface

In-situ measurements were performed on the d_{dry} = 14.5 nm thin PN132k brush in H_2O and D_2O at 25 °C and 45 °C. The sequence of measurements was H_2O→D_2O→H_2O at 25 °C followed by H_2O→D_2O→H_2O at 45 °C after heating the in-situ cell at a rate of about 1 °C/min. As expected from the *N*-deuteration experiments in Section 3.2.3., H→D exchange occurs much faster than D→H exchange. Further details about deuteration and de-deuteration effects are still being analyzed. The main interest now lies in swelling effects of the brush in H_2O as well as variations in polymer–water interactions induced by temperature changes. In the following, the initial H_2O brush spectra at each of the two temperatures are therefore evaluated quantitatively.

a) Simulating in-situ swollen-brush spectra below the LCST

Figure 3.42 compares measured and simulated brush spectra in H_2O at 25 °C—below the lower critical solution temperature of PNIPAAm. The band amplitude and shape of $\nu(H_2O)$ around 3460 cm^{-1} as well as the baseline slope above 3700 cm^{-1} allowed for the determination of both thickness, $\tilde{d}(25\,°C) = (57 \pm 3)$ nm, and water content, $f_{H_2O}(25\,°C) = (79.5 \pm 2.0)$ vol%, of the swollen brush. These values amount to a swelling degree of about $\tilde{d}/d_{dry} = 4$ and are

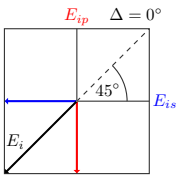

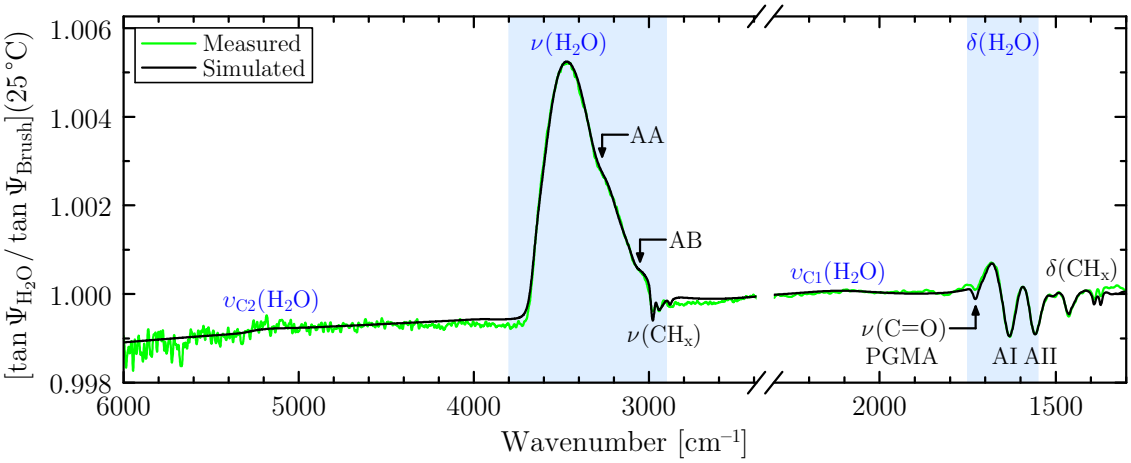

Figure 3.42: Measured and simulated referenced and baseline-corrected ellipsometric $\tan\Psi$ spectra of the $d_{dry} = 14.5$ nm thin PN132k brush in H_2O at 25 °C. The baseline slope in $\tan\Psi$ as well as band shapes and amplitudes of the water vibrational bands and PNIPAAm-specific bands were modeled successfully.

in accordance with VIS-ellipsometric measurements by Burkert et al. [46] on a PN132k brush with very similar dry-state thickness and grafting density [46].

The left panel of Fig. 3.43 shows the same spectra in comparison with a simulation in which all brush oscillators are set to zero amplitudes. With the water-stretching band being reproduced in the simulated $\tan\Psi$ spectrum, the $\delta(H_2O)$ band at 1650 cm^{-1} is intrinsically fixed in amplitude, position, and shape. This, then, enables one to determine the composition of the overlapping amide I and II bands. Moreover, band shapes and positions of most of the remaining PNIPAAm-specific bands as well as the $\nu(C{=}O)$ band of the PGMA anchoring layer could be modeled successfully. The obtained band changes with respect to the dry-state—shown in the right panel of Fig. 3.43—yield valuable information about hydration properties of the brush as well as polymer–polymer and polymer–water interactions.

Several spectral features reflect the strong hydration of the brush. First, the oscillator frequencies of the CH_x-bending vibrations between 1480–1320 cm^{-1} are shifted by up to +6 cm^{-1} compared to the dry state. Similar shifts are observed in the CH_x-stretching region between 3020–2800 cm^{-1}. The measured $\nu_{as}(CH_3)$ band in particular also shows a smaller amplitude compared to the simulation. This suggests that the band is indeed involved in a Fermi resonance, possibly with CH_x-bending vibrations [217], which changes upon hydration of the brush. Second, amide I and II are shifted to lower and higher wavenumbers, respectively. These shifts are induced by changes in band composition that reflect the different types of interactions within the brush. Details will be discussed in a moment. Third, as a consequence of the amide I and II shifts, the three bands in the amide A/B region are shifted and also undergo amplitude changes. The amide I/II-overtone band at 3194.7 cm^{-1} in dry

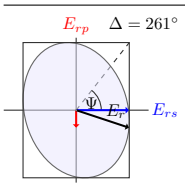

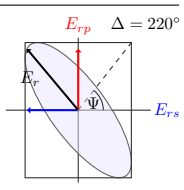

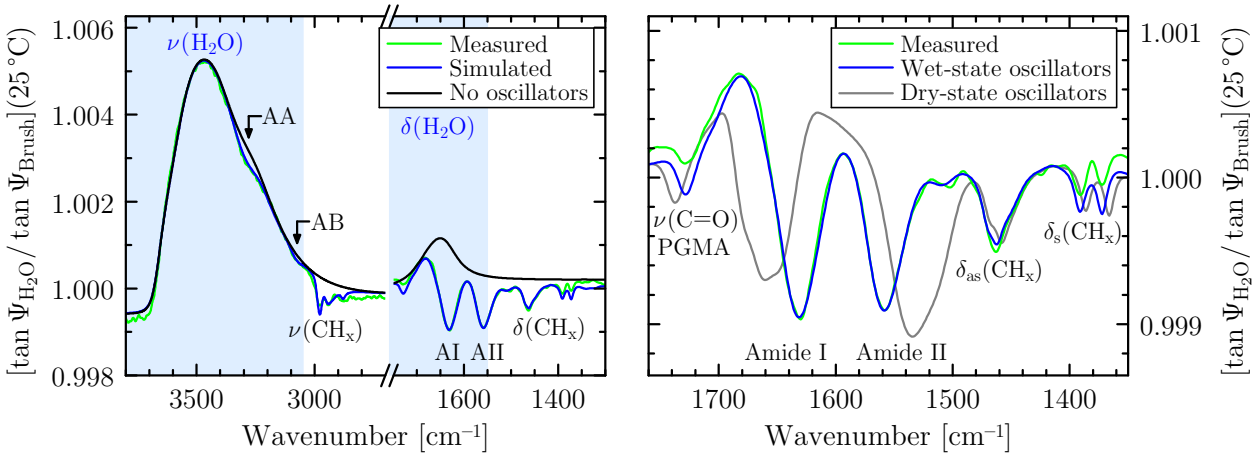

Figure 3.43: Measured tan Ψ spectra of the $d_{dry} = 14.5$ nm thin PN132k brush in H_2O at 25 °C in comparison with simulated spectra with and without oscillators in the polymer layers (left) as well as a comparison between using wet-state and dry-state oscillators (right).

state is shifted to $(3186.7 \pm 6.0)\,cm^{-1}$. The Fermi resonance between ν(NH) [amide A] and the first overtone of amide II [amide B] is strongly enhanced, whereby amide A is shifting from $3312.6\,cm^{-1}$ down to $(3290.6 \pm 5.0)\,cm^{-1}$, while amide B is shifting from $3066.1\,cm^{-1}$ up to $(3079.1 \pm 5.0)\,cm^{-1}$. Lastly, the PGMA anchoring layer is also affected by hydration. The center frequency of ν(C=O) is shifted from $1729.1\,cm^{-1}$ to $(1720.1 \pm 2.0)\,cm^{-1}$, with the observed tan Ψ peak position being shifted from $1737.4\,cm^{-1}$ to $1728.4\,cm^{-1}$.

Most prominent band changes occur in the amide I and II bands. Recalling the band composition from humidity-dependent measurements of PNIPAAm films (Section 3.1.5.), amide I consists of stretching contributions of di-H_2O-interacted C=O groups ($1625\,cm^{-1}$), amide- and mixed-interacted C=O groups (1645–$1664\,cm^{-1}$), as well as free C=O groups ($1680\,cm^{-1}$). Amide II comprises bending contributions of H_2O-interacted N−H groups ($1554\,cm^{-1}$), amide-interacted N−H groups ($1544\,cm^{-1}$), and free N−H groups ($1509\,cm^{-1}$).

Compared to the dry state where C=O and N−H groups are obviously either free or amide-interacted, the main contributions in water now stem from di-H_2O- and H_2O-interacted C=O and N−H groups, respectively. Nevertheless, amide I and II can only be modeled correctly if amide-interacted contributions are taken into account. For amide II, this concerns the shoulder at $1544\,cm^{-1}$. Maybe surprisingly, also a small dip is observed at about $1507\,cm^{-1}$, which seems to be related to free N−H groups, despite the large water content of the brush. The small shoulder of amide I at $1660\,cm^{-1}$, which is barely visible in the measured spectra, is yet revealed by the simulation. This contribution is related to mixed-interacted C=O groups that form one hydrogen bond with H_2O and one with a neighboring H−N group. It amounts to about 20% of the total number of C=O groups inside the brush. This means that even in a swollen and strongly hydrated state of about 80 vol% water content, polymer–polymer

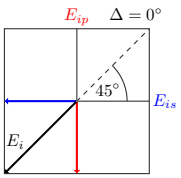

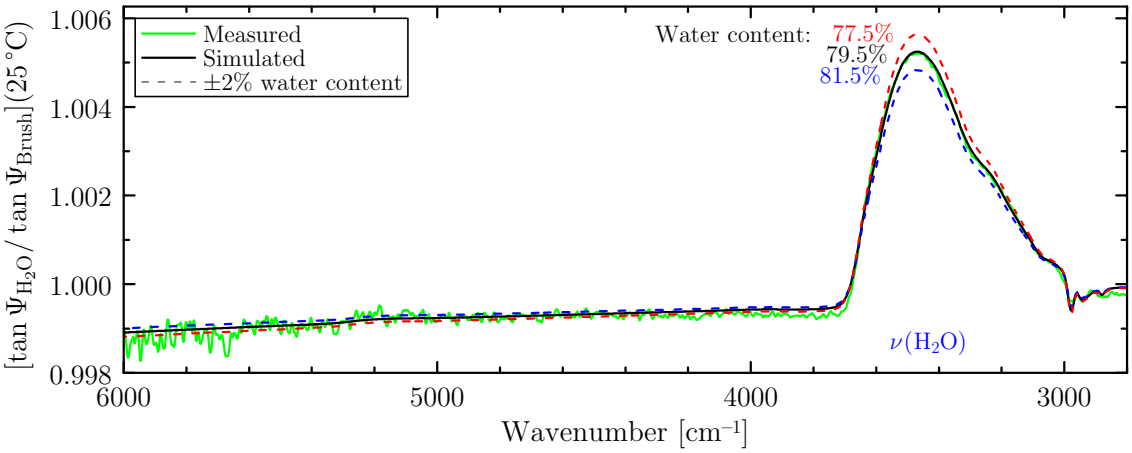

Figure 3.44: Sensitivity of the $\nu(H_2O)$ band and the baseline in $\tan\Psi$ towards changes of ± 2 vol% in water content of the $d_{dry} = 14.5$ nm thin PN132k brush in H_2O at 25 °C. The thickness of the swollen brush is $\tilde{d}(25\,°C) = (57 \pm 3)$ nm.

interactions (C=O $\cdots$ H−N) play an important role in the swelling behavior of the brush.

During the simulation, the constraint of Eq. (3.7) for the conserved number of dipole moments could be maintained for amide I. For amide II, on the other hand, it did not hold. The measured amide II band is much smaller than expected. This can be seen in the right panel of Fig. 3.43 by comparing simulated spectra based on dry- and wet-state oscillators. Possible reasons for this deviation are still being investigated to exclude, for example, systematic errors from the baseline-correction procedure.

Before moving on to measurements of the brush at 45 °C, it has to be mentioned that the above simulations rest solely upon the high optical contrast in the infrared. Decorrelating swollen-brush thickness $\tilde{d}$ and water content f_{H_2O}, for instance, is only possible because $\nu(H_2O)$ scales highly non-linear with f_{H_2O} and is extremely sensitive to absolute changes in water content if the polymer brush is strongly hydrated. This is illustrated in Fig. 3.44, which shows the impact of a varying water content of ± 2 vol% on the simulated spectra. With increasing f_{H_2O}, the optical contrast between brush and water-reference spectra reduces, leading to a strongly decreasing $\nu(H_2O)$ band amplitude. Simultaneously, the baseline slope at higher wavenumbers decreases as well. With these dependencies in mind, the possible precision of determining $\tilde{d}$ and f_{H_2O} can, in principle, be vastly improved by recording $\tan\Psi$ spectra at several angles of incidence.

b) Changing interactions within the collapsed brush above the LCST

From several studies on comparable PNIPAAm brushes [26, 46], it is expected that the measured PN132k brush deswells above its LCST, similar to a coil-to-globule transition. Interactions within the brush are expected to change from mainly polymer–water-dominated to

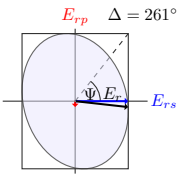

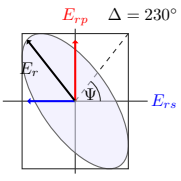

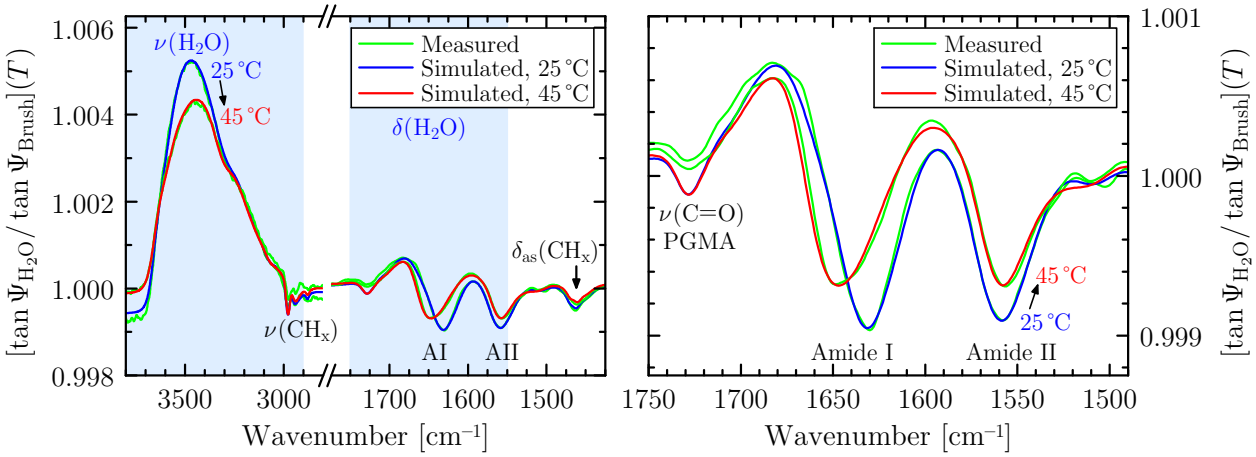

Figure 3.45: Measured and simulated tan Ψ spectra of the $d_{dry} = 14.5$ nm thin PN132k brush in H_2O at 25 °C and 45 °C, with a zoom of the amide I/II region shown in the right panel. Swollen-brush thicknesses and water contents are $\tilde{d}(25\,°C) = (57 \pm 3)$ nm and $f_{H_2O}(25\,°C) = (79.5 \pm 2.0)$ vol% as well as $\tilde{d}(45\,°C) = (17 \pm 5)$ nm and $f_{H_2O}(45\,°C) = (28.0 \pm 12.0)$ vol%.

polymer–polymer-dominated [26, 262]. Figure 3.45 compares measured and simulated spectra at both 25 °C and 45 °C. The spectrum above the LCST was modeled successfully with a brush thickness of $\tilde{d}(45\,°C) = (17 \pm 5)$ nm and a water content of $f_{H_2O}(45\,°C) = (28.0 \pm 12.0)$ vol%. These values are smaller than the ones obtained by Burkert et al. [46] from VIS ellipsometry on a similar $d_{dry} = 12.5$ nm thick brush. The two brushes differ only slightly in grafting density, with $\sigma = 0.07\,\text{nm}^{-2}$ and $\sigma_{Burkert} = 0.06\,\text{nm}^{-2}$. Whether or not this small difference in σ can cause such changes in the swelling behavior has yet to be investigated with systematic grafting-density-dependent measurements.

Nevertheless, the simulations reveal drastic changes in polymer–polymer and polymer–water interactions. The amide bands—especially the amide I band—undergo substantial alterations. This is illustrated in Fig. 3.46, which shows the number of dipoles associated with the five ν(C=O) amide I subcomponents in wet state at 25 °C and 45 °C as well as in humid state (35% humidity) and in dry state. No free or single-bonded C=O groups are present if the brush is in contact with liquid water. This agrees with humidity-dependent measurements on spin-coated PNIPAAm films discussed in Section 3.1.5.b). There, Fig. 3.20 shows the ν(C=O) oscillator strengths for water contents between 1–9 vol%. Extrapolating the results indicates that all previously free or single-bonded C=O groups become mixed- or dihydrogen-bonded if the water content of the film reaches approximately 14 vol%. As discussed before, the brush contains about 20% mixed-bonded and 80% di-H_2O-bonded C=O groups at 25 °C without the presence of double-bonded groups, meaning that there are no pure polymer–polymer interactions below the LCST. Water therefore dictates the interactions within the brush. At 45 °C, less di-H_2O-bonded C=O groups are found. Simultaneously, mixed-bonded groups

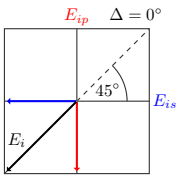

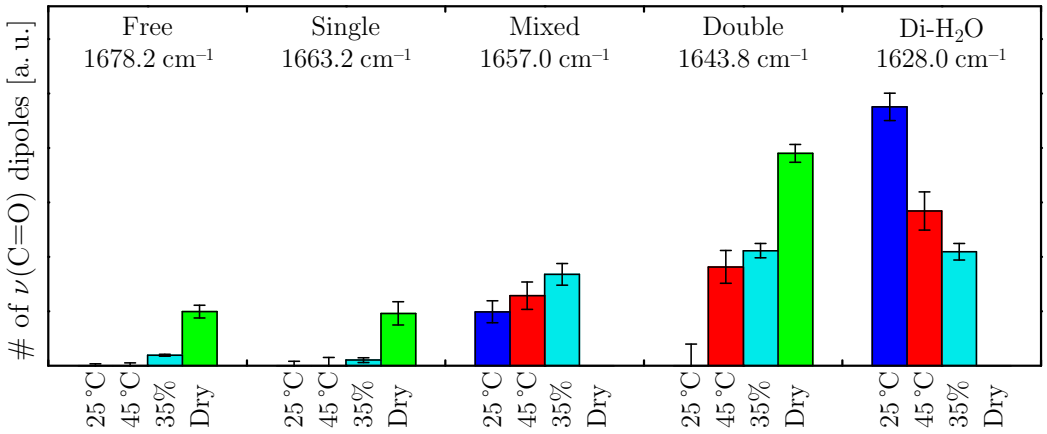

Figure 3.46: Hydration-dependent number of ν(C=O) dipoles of the five amide I subcomponents shown for the PNIPAAm brush in H_2O at 25 °C and 45 °C, determined with in-situ infrared ellipsometry, in comparison with the ones of spin-coated PNIPAAm films in humid state (35% humidity) and dry state, determined infrared-microscopically and -ellipsometrically, respectively; see Sections 3.1.4. and 3.1.5.b).

increase in number, but most importantly, double-bonded C=O groups are highly favored. Remember that these are C=O groups that form hydrogen bonds with two neighboring H−N groups. Polymer–polymer interactions therefore heavily influence the swelling behavior of the brush.

c) Further band changes due to hydration

The final point concerns temperature-dependent band shifts of PNIPAAm's amide A and B as well as CH_x-stretching and -bending bands. Table 3.7 compares obtained values for oscillator frequencies $\tilde{\nu}_0$ in water at 25 °C and 45 °C as well as in dry state. All observed band shifts are in accordance with the strength of hydration at the corresponding state. Strongest shifts of $-22\,\mathrm{cm}^{-1}$ and $+13\,\mathrm{cm}^{-1}$ are respectively found for amide A and B at 25 °C. The $\delta(CH_x)$ bands are shifted by up to $+6\,\mathrm{cm}^{-1}$ with respect to the dry state. With decreasing water content of the brush, the bands tend to shift towards their dry-state values. Interestingly, the $\nu(CH_x)$ bands are shifted by up to $+9\,\mathrm{cm}^{-1}$ at 25 °C, but also remain shifted by about $+6\,\mathrm{cm}^{-1}$ at 45 °C. This confirms, on the one hand, that these bands are highly indicative for the current hydration state of the brush, as was suggested by Maeda et al. [50] for aqueous PNIPAAm solutions. On the other hand, it might indicate that the hydration of isopropyl groups and the main chain of the polymer differs from the hydration of amide groups. This suggests that the CH_3 groups are intrinsically involved in the actual deswelling behavior. The experimental errors in the $\nu(CH_x)$ region, however, are too large to obtain conclusive evidence for this hypothesis. Similarly strong $\nu(CH_x)$ band shifts were also reported by Bittrich et al. [26] who performed ATR-infrared measurements on a PN132k brush.

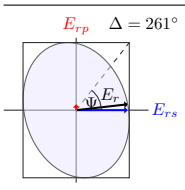

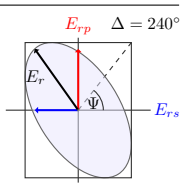

Band	Swollen state at 25 °C		Collapsed state at 45 °C		Dry state
$[\mathrm{cm}^{-1}] \rightarrow$	$\tilde{\nu}_0$	Shift	$\tilde{\nu}_0$	Shift	$\tilde{\nu}_0$
Amide A	3290.6	−22.0	3308.6	−4.0	3312.6
Amide B	3079.1	+13.0	3072.1	+6.0	3066.1
$\nu_{as}(CH_3)$	2978.1	+8.0	2976.1	+6.0	2970.1
$\nu_{as}(CH_2)$	2943.6	+9.0	2940.6	+6.0	2934.6
$\nu_{s}(CH_3)$	2879.7	+7.0	2877.7	+5.0	2872.7
$\delta_{as}(CH_3)$	1470.3	+2.0	1469.3	+1.0	1468.3
$\delta_{as}(CH_2)$	1461.9	+4.0	1459.9	+2.0	1457.9
$\delta_{s}(CH_3)$	1391.0	+5.0	1389.0	+3.0	1386.0
$\delta_{s}(CH_2)$	1372.1	+6.0	1369.1	+3.0	1366.1

Table 3.7: Oscillator center frequencies $\tilde{\nu}_0$ of PNIPAAm's amide A/B, CH_x-stretching, and CH_x-bending vibrations in wet state at 25 °C and 45 °C as well as in dry state, obtained from optical simulations. The overall errors are estimated to be $\pm 5.0\,\mathrm{cm}^{-1}$ for amide A/B, $\pm 1.5\,\mathrm{cm}^{-1}$ for $\nu(CH_x)$, and $\pm 0.5\,\mathrm{cm}^{-1}$ for $\delta(CH_x)$. Band shifts are given with respect to the dry-state values.

d) Comparison with in-situ VIS ellipsometry

In order to assess the reliability of the infrared-ellipsometric simulations, the results for the $d_{dry} = 14.5\,\mathrm{nm}$ thick PN132k brush discussed above and for the $d_{dry} = 12.6\,\mathrm{nm}$ thick PN94k brush (see Tab. 3.6) published in Ref. [25] are compared with VIS-ellipsometric results from the literature [25, 46]. Table 3.8 shows the corresponding values for swollen-brush thicknesses $\tilde{d}$ and water contents f_{H_2O}.

Overall good agreement is found for the thicknesses of the swollen or collapsed brushes, keeping in mind the slight temperature differences between VIS and infrared measurements. The water content matches below the LCST for the PN132k brush. Above the LCST, the infrared results indicate a stronger deswelling with correspondingly much less water bound within the brush. Note, however, that the VIS measurements were performed in phosphate buffer solutions at pH 7.4, whereas unbuffered purified water was used for all infrared measurements. The use of a buffer might significantly influence the LCST behavior of PNIPAAm brushes [263].

Despite these differences, the trends in both thickness and water content as well as the correlation between these two parameters are reasonably similar for infrared and visible ellipsometry. This substantiates the trustworthiness of the in-situ infrared approach and the subsequent quantitative analysis of the amide band composition.

Accuracy and precision for the infrared PN132k results are much better compared to the PN94k results due to several improvements of the optical set-up and the procedure of spectra evaluation, including the baseline-correction and the use of higher-quality optical constants of water (see Section 3.4.) in the simulation.

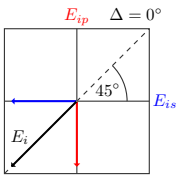

Method	PN132k			PN94k		
	T [°C]	$\tilde{d}$ [nm]	f_{H_2O} [vol%]	T [°C]	$\tilde{d}$ [nm]	f_{H_2O} [vol%]
IR	25.00 ± 0.05	57 ± 3	79.5 ± 2.0	24.7 ± 0.2	43 ± 8	86 ± 13
	45.00 ± 0.05	17 ± 5	28.0 ± 12.0	38.6 ± 0.2	20 ± 9	68 ± 15
VIS	23.0 ± 0.1	46.3 ± 0.3	74.8 ± 0.3	24.6 ± 0.1	45.6 ± 0.5	—
	40.0 ± 0.1	26.7 ± 0.6	58.2 ± 0.3	38.6 ± 0.1	19.5 ± 0.5	—

Table 3.8: Comparison between IR- and VIS-ellipsometric results for T-dependent swollen-brush thicknesses $\tilde{d}$ and water contents f_{H_2O} of PNIPAAm brushes with different molecular weights. IR results for the $d_{dry} = 14.5$ nm thick PN132k brush are compared with VIS results from Ref. [46] for a 12.5 nm thick brush. The $d_{dry} = 12.6$ nm thick PN94k brush (IR) is compared with an 11.0 nm thick brush (VIS), details of which were already published in Ref. [25]. Note that VIS measurements were performed in 10 mM PBS buffer at pH 7.4, whereas purified water from a Millipore system was used for IR measurements. VIS data for water contents f_{H_2O} were not available in the case of the PN94k brush.

e) Conclusions and outlook

In-situ measurements of PGMA films and PNIPAAm brushes with corresponding optical simulations show the high potential of in-situ infrared ellipsometry for gaining quantitative insights into the structural properties of thin organic films in contact with aqueous solutions. With careful optical modeling, it was possible to obtain thicknesses and water contents of the $d_{dry} = 14.5$ nm thin PN132k brush in swollen and collapsed state. Using the dry- and wet-state oscillators as determined by ex-situ infrared ellipsometry and humidity-dependent infrared microscopy on spin-coated PNIPAAm films, the band compostion of amide I was successfully analyzed. Changing polymer–polymer and polymer–water interactions were identified below and above the LCST. Also band shifts of CH_x-bending and -stretching vibrations could be connected with the current hydration state.

The obtained results already reveal many details about the brush properties. Further improvements of both the optical set-up and the spectra-evaluation process are yet feasible to gain even deeper insights and increase the accuracy. As mentioned before, measurements at multiple angles of incidence would allow one to decorrelate film thickness and water content more easily. Also anisotropy could be probed this way. Moreover, rigorously derived equations for $\tan\Psi$ and Δ that included the geometry and tension of the wedge-shaped substrate would eliminate some of the possible issues due to the baseline-correction procedure. With these improvements, the brush profile should be determinable, because every band in $\tan\Psi$—and especially the water-stretching band—is highly sensitive to incidence angle, thickness, water content, and distribution of water throughout the depth profile.

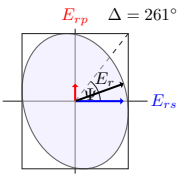

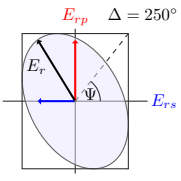

3.6. Protein adsorption

3.6.1. Motivation

Controlling adsorption and desorption of proteins or cells at biocompatible surfaces is of high potential for biomedical and biotechnological applications. In this respect, various polymer and polymer-brush systems have been investigated in the literature using visible ellipsometry, infrared spectroscopy, quartz crystal microbalance, zeta-potential analysis, X-ray microscopy, fluorescence microscopy, and other techniques. These polymer systems include, for instance, fluorohydrocarbon polymers [99], PAA mono brushes [39, 82], PNIPAAm brushes [46–49] and PNIPAAm-modified surfaces [264, 265], PEG [46] and PEG-based brushes [40, 266], PHEMA brushes [267–269], PS- and PMMA-based surfaces [270–273], hyperbranched polyesters [274], binary P2VP/PAA brushes [38], as well as binary P2VP/PNIPAAm brushes [46, 66] and PNIPAAm/PAA brushes [67].

The basic idea behind controlling the protein-binding properties of polymer surfaces is to use external stimuli like pH or temperature to switch the surface between an adsorbing and a repelling state. Regarding polymer brushes, this can be achieved with either mono brushes or mixed brushes. PAA brushes, for example, can be switched between the two states by changing the pH value of the aqueous environment [39, 82]. Mixed brushes, on the other hand, may contain a passive component and at least one active component that is sensitive to stimuli and might react, e. g., by swelling, thereby determining the surface properties of the brush. Examples are P2VP/PAA [20, 21, 27, 38] and PAA-*b*-PS/PEG brushes [22] where P2VP and PAA are pH-sensitive, or PNIPAAm/P2VP [46, 66] and PNIPAAm/PAA brushes [67] in which PNIPAAm is the active component reacting upon temperature changes.

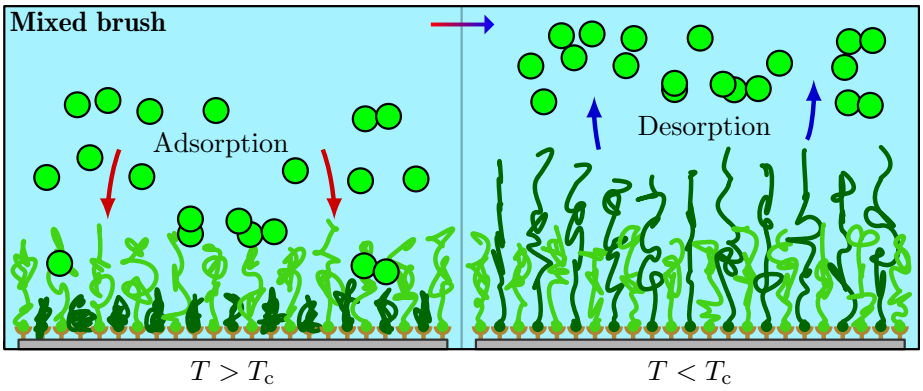

Figure 3.47: Sketch of proteins adsorbing and desorbing at a mixed binary brush upon changes in temperature. The passive light green polymer is protein-adsorbing, whereas the active (swellable) dark green polymer is protein-repelling. Around a critical temperature T_c, the brush switches between a protein-adsorbing and a protein-repelling state.

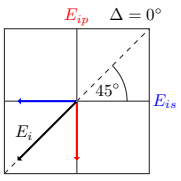

The principle of a temperature-sensitive binary brush is depicted in Fig. 3.47. The passive light green polymer is the protein-adsorbing component of the brush, e. g., PAA or P2VP, whereas the active dark green polymer constitutes the protein-repelling component, e. g., PNIPAAm. Temperature changes then induce deswelling or swelling of the PNIPAAm chains, leading to controlled protein adsorption or desorption around a critical temperature T_c. For PNIPAAm, this temperature is expected to be tunable around the LCST of about 32 °C, which is favorable for bioapplications.

In order to compose, for instance, binary PNIPAAm/PAA brushes that are in principle tunable by temperature as well as pH [67], the protein-adsorbing and -repelling properties of the corresponding mono brushes must be understood first. In-situ infrared ellipsometry is again a useful complementary method for this purpose, since it reveals the vibrational bands of the involved materials. This allows one to identify composition and interactions of the different polymers, the protein, and the solvent. Building on the existing literature, protein adsorption on PNIPAAm mono brushes is investigated in the upcoming sections in dependence of temperature, while PAA Guiselin brushes are analyzed with respect to pH.

Examplarily, Fig. 3.48 shows referenced $\tan\Psi$ spectra of PNIPAAm and PAA brushes in protein-free buffer after exposure to buffer solutions containing 0.25 mg/ml human serum albumin (HSA). In contrast to the protein-repelling PNIPAAm brush, large amounts of HSA adsorb at the PAA brush. This is indicated by the upward-pointing protein-specific amide bands as well as the huge downward-pointing water bands. The latter originate from the optical contrast between protein and protein-free measurement, and their absolute values correlate with amount and refractive index of the adsorbed protein as well as the amount of bound water. Amide I is notably overlapped by the downward-pointing $\delta(H_2O)$ band. The

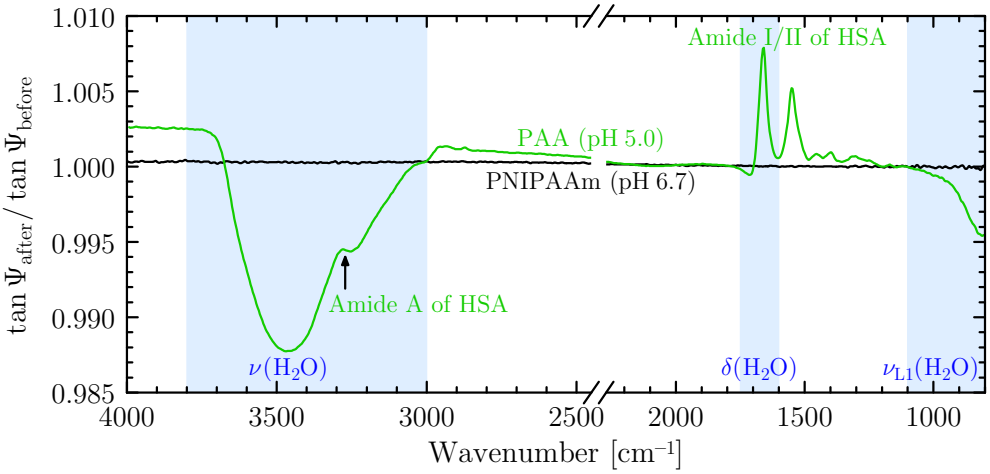

Figure 3.48: HSA adsorption at PNIPAAm and PAA mono brushes at 25 °C. $\tan\Psi$ spectra were measured in protein-free buffer solutions before and after exposing the brushes to protein solutions with concentrations of $c = 0.25$ mg/ml for 70 min. The PNIPAAm brush is clearly protein-repelling.

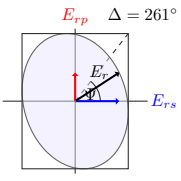

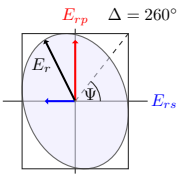

band amplitudes of amide I and II also reflect the amount of adsorbed protein. The band shapes, on the other hand, give valuable information on the protein conformation [215, 275].

Protein structure, brush chemistry, water content, and interactions are accessible in the infrared, but yield overlapping spectral information. Before investigating HSA adsorption at PNIPAAm and PAA brushes in more detail, it is thus necessary to identify the characteristic vibrational bands of HSA and test if they are affected, for example, by changes in pH.

3.6.2. pH-dependent properties of human serum albumin

In order to determine the effects of pH on the structural properties of adsorbed and solvated human serum albumin, in-situ measurements were performed on differently concentrated HSA solutions using ATR infrared ellipsometry and infrared transmission spectroscopy. These techniques are sensitive enough to resolve the amide bands of the protein, the band composition of which allows one to assess the protein secondary structure [215, 275]. In the first step, HSA (mono)layers on silicon and CaF_2 substrates are investigated at pH 5 and 7. The results are then used in the second step to interpret spectra of different protein solutions.

a) HSA monolayers

The kinetics of protein adsorption are governed by various parameters, such as flow conditions of proteins towards the adsorbing surface, pH and temperature of the solution, difference in protein concentration between solution and surface, as well as protein–water, water–surface,

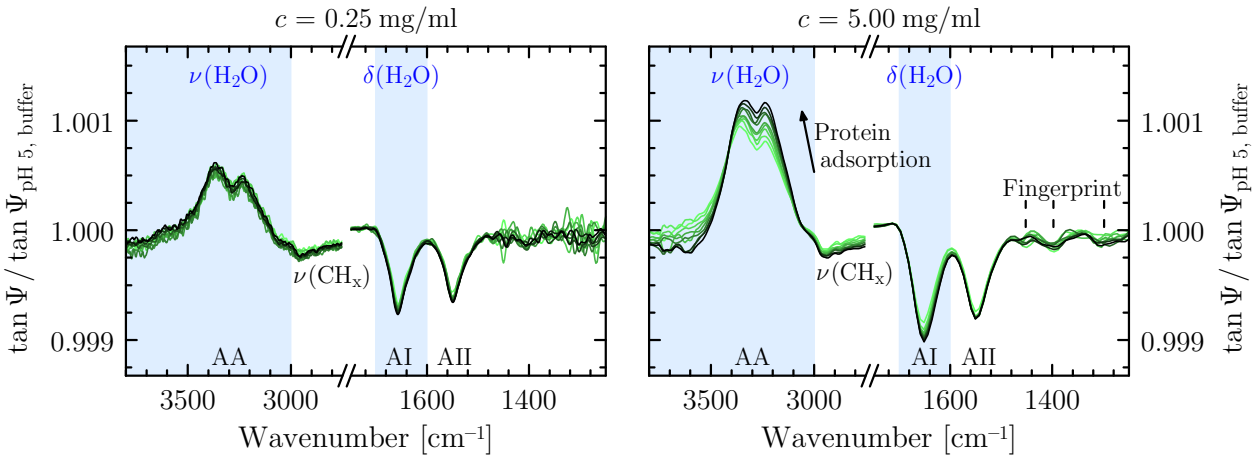

Figure 3.49: HSA-(mono)layer formation on a silicon ATR crystal from two differently concentrated HSA solutions at pH 5 measured with ATR ellipsometry at 25 °C. Left: $c = 0.25$ mg/ml, 4 cm^{-1} resolution, monitored over 100 min. Right: $c = 5.00$ mg/ml, 16 cm^{-1} resolution, recorded over 70 min. Spectra were referenced to protein-free buffer solutions at pH 5 measured before the adsorption process. Amide A, I, and II bands are labeled with AA, AI, and AII, respectively. For better amplitude comparability, all spectra were baseline-corrected to coincide at 1710 cm^{-1}.

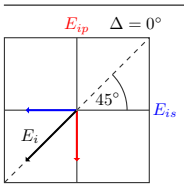

and protein–surface interactions [276–278]. The protein concentration in solution, for instance, correlates with the initial adsorption rate, the amount of adsorbed proteins, but also with conformational changes of the proteins during the adsorption process [276–279]. The latter can involve structural rearrangements of the proteins due to spreading at the surface [276–278] as well as changing protein–water interactions and changes in the hydration state [215, 278, 280, 281]. Water in particular plays an important role during the adsorption process [278, 280].

Both the protein- and the water-specific vibrational bands are readily accessible by means of infrared spectroscopy. Figure 3.49 shows the time-dependent formation of HSA layers on silicon ATR crystals from two different HSA solutions at pH 5 with concentrations of $c = 0.25\,\mathrm{mg/ml}$ and $c = 5.00\,\mathrm{mg/ml}$. The adsorption processes were measured with ATR ellipsometry over periods of 100 min and 70 min, respectively. Most prominent features in the spectra are the downward-pointing protein-specific amide A, I, and II bands as well as the upward-pointing $\nu(H_2O)$ band due to the optical contrast between protein spectra and protein-free reference spectra. Further small HSA bands are also observable in the CH_x-stretching and fingerprint regions.

Most of the protein is already adsorbed after the first few minutes, as is evident from the time-dependent amide II amplitude progression, shown in Fig. 3.50. In detail, the HSA adsorption kinetics depend on the protein concentration within the buffer solution. At the smaller concentration of $c = 0.25\,\mathrm{mg/ml}$, the amide band amplitudes increase by about 20% with respect to the initial spectrum, while the $\nu(H_2O)$ band amplitude remains almost constant. In contrast, at the higher concentration of $c = 5.00\,\mathrm{mg/ml}$, the $\nu(H_2O)$ amplitude increases continuously. This suggests either a dehydration of adsorbed proteins due to spreading and conformational changes, or the accumulation of more than just a protein monolayer on

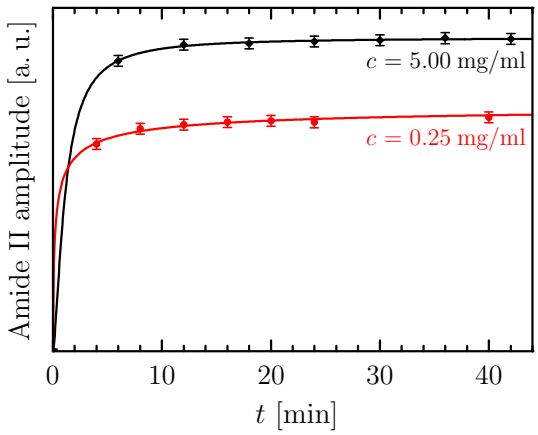

Figure 3.50: Amide II $\tan\Psi$ band amplitude during HSA adsorption, corresponding to the spectra in Fig. 3.49. To guide the eye, points were connected by fitting a function "Ampl. $\propto t^a/(t^a + b^a)$" with free parameters a and b.

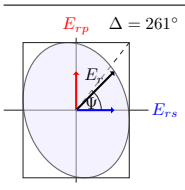

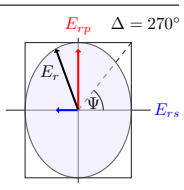

the silicon substrate. Furthermore, the amide II amplitude increases by about 9%, whereas amide I increases by 20%. This change in amplitude ratio of amide I/II is also indicative of structural changes of the proteins during adsorption. The effect is even stronger when considering that amide I is also overlapped by the upward-pointing water-bending vibration $\delta(H_2O)$, which is likely to evolve similarly with $\nu(H_2O)$.

Since the measured spectra also contain contributions from the protein/buffer interface as well as the protein solution itself, it is difficult to study the effects of pH on the adsorbed layer alone. The ATR flow cell was therefore purged with protein-free buffer to remove these spectral contributions. Note that this rinsing process might also partly remove non-strongly bound proteins, which causes potential problems for a quantitative analysis concerning the amount of adsorbed protein [278]. Subsequent purging of the cell with buffer at pH 5, 7, and again 5 resulted in the spectra displayed in Fig. 3.51. A certain amount of proteins is desorbing from the substrate or the protein layer when changing the pH from 5 to 7. Lowering the buffer's pH back to 5 also causes some desorption or rearranging at the substrate, which is probably due to the flow conditions within the cell. Nevertheless, differences in composition of the protein-specific vibrational bands can be discussed.

Analysis of the amide I and II band compositions can yield valuable information about the secondary structure of the protein [215, 275], that is, the contributions of α-helix, β-sheets, β-turns, and random-coil conformations to the overall protein structure. In agreement with

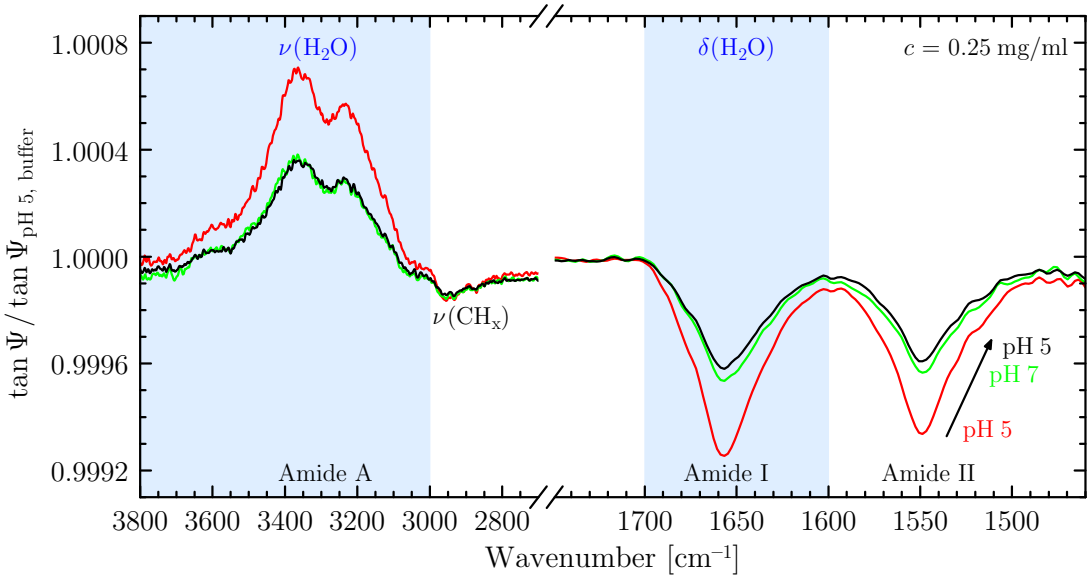

Figure 3.51: HSA layer—adsorbed from a protein solution with $c = 0.25$ mg/ml—in subsequent contact with buffer solutions at pH 5 (red line), 7 (green line), and 5 (black line). The baseline-corrected tan Ψ spectra were referenced to protein-free buffer before the adsorption process. Small residues of water-vapor absorption are overlapping the amide I/II region.

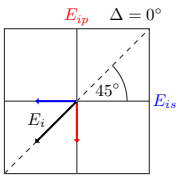

ATR FT-IR measurements on HSA solutions at pH 7.4 by Barbucci and Magnani [183], the main contribution to amide I is situated at about 1656 cm^{-1} and is assignable to α-helix as well as random-coil conformation [275]. Smaller band components are observed at 1675 cm^{-1} and 1631 cm^{-1}, corresponding to β-sheet conformation [275]. Importantly for the upcoming HSA adsorption experiments on PAA brushes, the relative α-helix and β-sheets contributions to the amide band envelopes do not change between pH 5 and 7.

HSA (mono)layers were also measured with infrared transmission microscopy. Protein was adsorbed to the CaF_2 windows of the transmission cell from HSA solutions at pH 5 with $c = 0.25$ mg/ml and $c = 1.00$ mg/ml. Afterwards, transmission spectra were collected while purging the cell with protein-free buffer at pH 5 and 7. Within the given signal-to-noise ratio, no significant pH-dependent changes were found in the amide I and II band compositions.

b) HSA solutions

After the adsorption of HSA layers from low-concentrated HSA solutions as described above, higher-concentrated protein solutions were investigated in transmission as well as with ATR ellipsometry. For this, the monolayer measurements in protein-free buffer served as a reference to subtract the spectral contributions stemming from the adsorbed layers. Figure 3.52 shows referenced absorbance spectra of HSA solutions at pH 5 and 7 with concentrations of $c = (10.0 \pm 0.2)$ mg/ml. Similar to the protein layers discussed in the previous section, solvated HSA does not undergo conformational changes between pH 5–7 (within the error of c), in agreement with Ref. [282]. ATR measurements confirm this result.

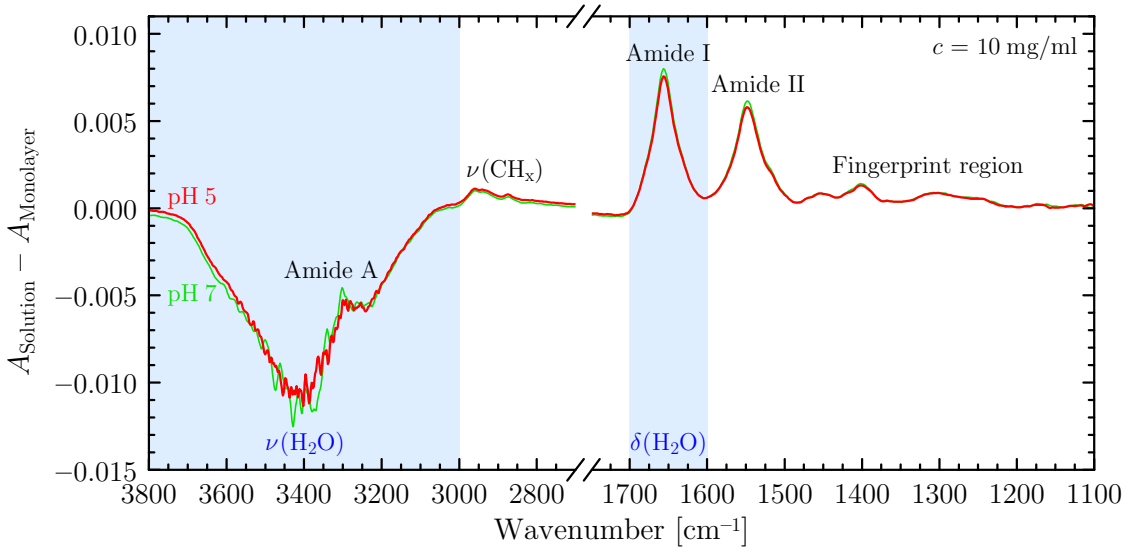

Figure 3.52: Absorbances of HSA solutions with concentrations of $c = (10.0 \pm 0.2)$ mg/ml at pH 5 (red line) and 7 (green line) measured with a $d_{Cell} = 3.26$ µm transmission cell at 25 °C. Spectra were referenced to absorbances of HSA (mono)layers in contact with protein-free buffer.

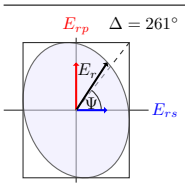

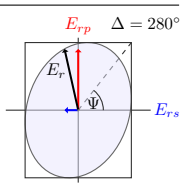

3.6.3. Temperature-dependent protein resistance of PNIPPAm brushes

PNIPAAm brushes were investigated in the literature for temperature- and pH-dependent HSA adsorption using visible ellipsometry [46, 47]. Burkert et al. [46] showed that HSA adsorbs on PN132k brushes below pH < 4 and attributed this to the denaturation of the protein and its molten globule-like state [184]. Above pH 4, however, no adsorption was found. Within the sensitivity of their ellipsometry set-up, Xue et al. [47] verified the HSA repellency of PNIPAAm brushes at pH 7 for various grafting densities between $\sigma = 0.08$–$0.21\ \mathrm{nm}^{-2}$ and molecular weights ranging from $\overline{M}_n = 44\,000$ g/mol to 202 000 g/mol. They also analyzed BSA (bovine serum albumin) adsorption on PNIPAAm brushes. No adsorption was found with visible ellipsometry, but small amounts of adsorbed BSA could be verified using radioisotope assays.

In-situ infrared ellipsometry might shed more light on the subject. The $d_{\mathrm{dry}} = 14.5$ nm thin PN132k brush was measured for HSA adsorption at 25 °C and 40 °C using a protein concentration of $c = 0.25$ mg/ml at pH 6.7. At each temperature, a measurement sequence of protein-free buffer, HSA in buffer, and protein-free buffer was conducted. At the end, the brush was measured again at 25 °C in protein-free buffer. Corresponding referenced tan Ψ spectra at the three temperatures are displayed in Fig. 3.53.

Deviations from unity in the form of upward- or downward-pointing bands are an indicator of structural or chemical changes of the brush. The first spectrum at 25 °C exhibits a

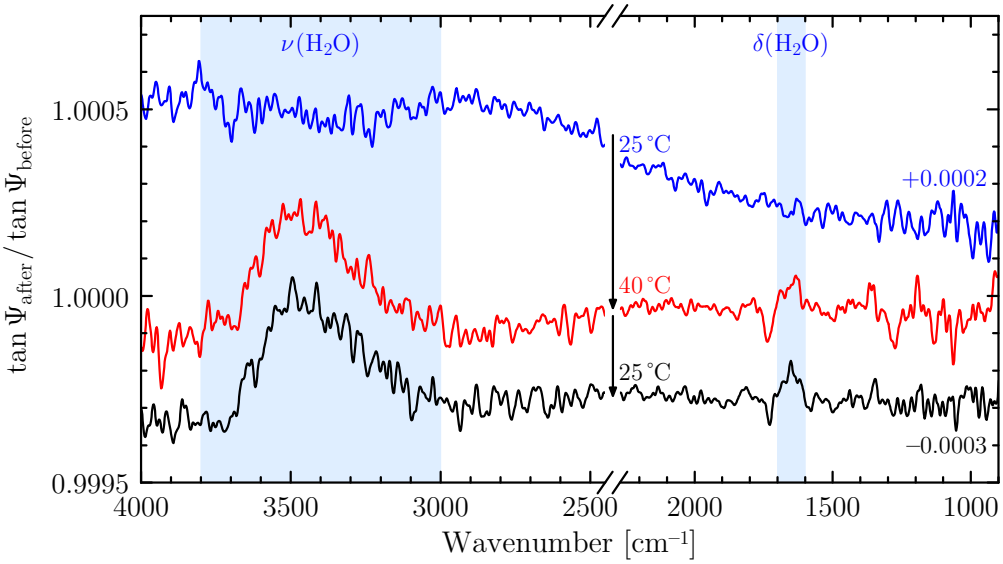

Figure 3.53: Temperature-dependent HSA resistance of a PNIPAAm and PAA mono brush. Referenced tan Ψ spectra with respect to protein-free buffer were measured at 25 °C, 40 °C, and again 25 °C after exposing the brush to protein solution with concentration of $c = 0.25$ mg/ml for several minutes.

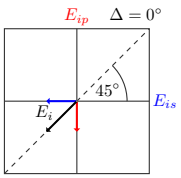

slight baseline drift at higher wavenumbers—which is due to effects of the PID-temperature stabilization of the in-situ cell—but most importantly, no HSA-specific bands are observable. That is, the brush can be considered HSA-repelling at 25 °C.

In the second spectrum at 40 °C, however, various vibrational bands emerge. Most prominent ones are the water bands, marked in light blue in the figure. The absence of an amide II band around 1550 cm^{-1} suggests that no protein has adsorbed to the brush. A simultaneously occurring stronger amide I band around 1650 cm^{-1} would be overlapped by $\delta(H_2O)$, but the amplitude ratio of $\nu(H_2O)$ to $\delta(H_2O)$ indicates that there are no changes in the amide I region. Smaller bands also appear at 1730 cm^{-1} and between 1375–1000 cm^{-1}. The former is only attributable to the C=O-stretching vibration of the brush's PGMA anchoring layer, whereas the band at about 1270 cm^{-1} is too strong to be associated with either PGMA, PNIPAAm, or HSA. It might be assignable to the sodium-phosphate buffer ions [283], which is substantiated by comparing measurements of buffer and salt-free water.

Since buffer ions are naturally surrounded by a hydration shell and can interact with brush and protein, they have a significant influence on the hydration state and swelling behavior of the brush [263, 284, 285]. Compared to salt-free water conditions, the PNIPAAm brush is less swollen below the LCST. Above, the brush collapses, but after exposure to HSA, an increase in water content is indicated by the upward-pointing water bands. A possible explanation is that the presence of proteins and their hydration shell [278, 286, 287] induces a redistribution of the buffer ions. Changes in the C=O-stretching band at 1730 cm^{-1} might then be caused by changes in PGMA–buffer-ion interactions. Further systematic studies are necessary, though, to clarify this hypothesis. The aforementioned effects are illustrated in Fig. 3.54.

In the final spectrum at 25 °C, the brush reswells, but the water and C=O bands do not revert to their initial values. If buffer and/or protein are the cause of this hysteresis-like effect has yet to be determined.

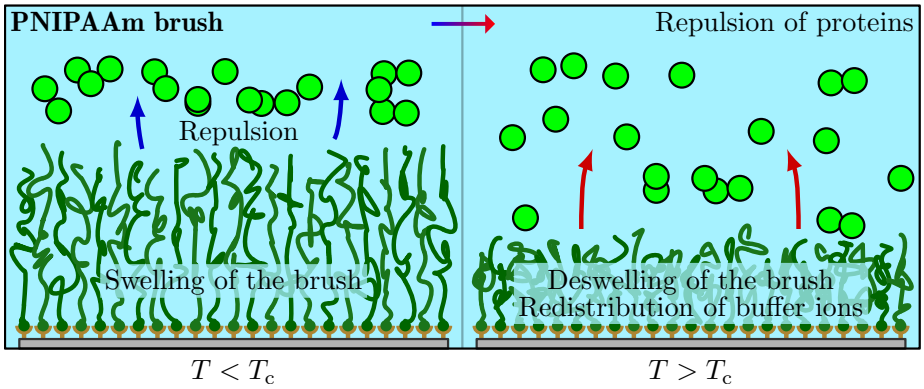

Figure 3.54: Sketch of a protein-repelling PNIPAAm brush in dependence of temperature, illustrating the possibly occurring overlapping effects at the solid–liquid interface, namely swelling/deswelling of the brush, protein repulsion, and changing brush–buffer interactions.

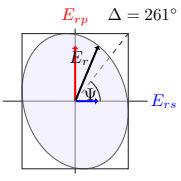

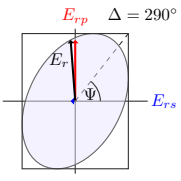

3.6.4. pH-dependent protein adsorption on PAA brushes

Several research groups investigated BSA adsorption on PAA brushes [39, 82, 195–198, 288]. De Vos et al. [39], for instance, used optical reflectometry to study the influence of polymer length, grafting density, and salt concentration on the pH-dependent adsorption behavior. They found adsorption maxima around pH 5.0–5.4 at a salt concentration of 10 mM. The amount of adsorbed BSA highly increased with both increasing polymer length and grafting density as well as with decreasing salt concentration. Bittrich et al. [82] combined visible ellipsometry with quartz crystal microbalance to gain information about the amount of water and buffer ions coupled to the brush during pH-dependent swelling and protein adsorption processes. After BSA adsorption at pH 5.2 (6.0), they monitored protein desorption in-situ at pH 7.6 and gave quantitative evidence for the swelling of the brush–protein layer as well as the incorporation of buffer molecules into it.

In-situ infrared ellipsometry is, in principle, capable of monitoring the various pH-dependent effects that occur at the brush–water interface, as is depicted in Fig. 3.55. With increasing pH of the solution, PAA brushes undergo swelling and dissociation effects [23, 289–291]

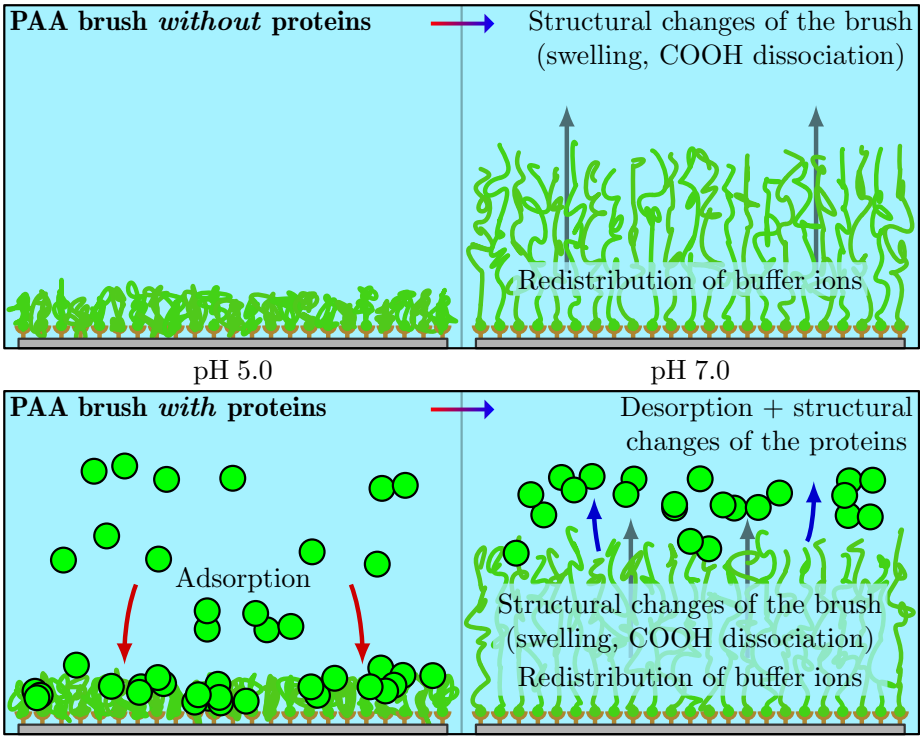

Figure 3.55: Sketch of protein adsorption and desorption at a PAA brush, illustrating the possibly occurring effects at the solid–liquid interface when raising the pH of the solution, namely protein desorption, structural and chemical changes of the brush, changes in the properties of bound water, redistribution of buffer ions, and conformational changes of adsorbed and solvated proteins.

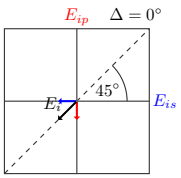

with a simultaneous ion redistribution inside the brush [23, 28, 290, 292, 293]. If proteins adsorb, then structural changes of both brush and protein as well as desorption of proteins can take place upon changing the pH. The challenge is to unequivocally assign the corresponding spectral signatures in the infrared, since these all overlap to some degree.

The present work focuses on the investigation of HSA adsorption on PAA Guiselin brushes at pH 5 with subsequent partial protein desorption between pH 6–7. Infrared ellipsometry is employed to gain insights into brush/protein structure and chemistry during protein adsorption and desorption. Data from additional swelling/dissociation experiments [23] are used to interpret the measured infrared spectra. In-situ visible ellipsometry is utilized to obtain quantitative information about brush thickness and amount of adsorbed protein.

For the VIS protein, IR protein, and IR PAA swelling/dissociation experiments, the PAA-brush samples S1, S2/S3, and S4 were used, respectively—see Section 2.4.2.b). Samples S2 and S3 showed similar trends, and therefore only spectra of sample S2 are presented here. Infrared measurements were done by Dennis Aulich, while VIS-ellipsometric measurements including quantitative evaluation were performed by Eva Bittrich at the IPF Dresden.

a) Protein adsorption process

The in-situ cell was filled with a 10 mM buffer solution at pH 5.0. The brush was kept in contact with the solution for 30 min in order to stabilize the temperature of the in-situ system as well as to reach an equilibrium state between solution and brush. A tan Ψ spectrum recorded at that sample state served as the reference spectrum for all subsequent measurements.

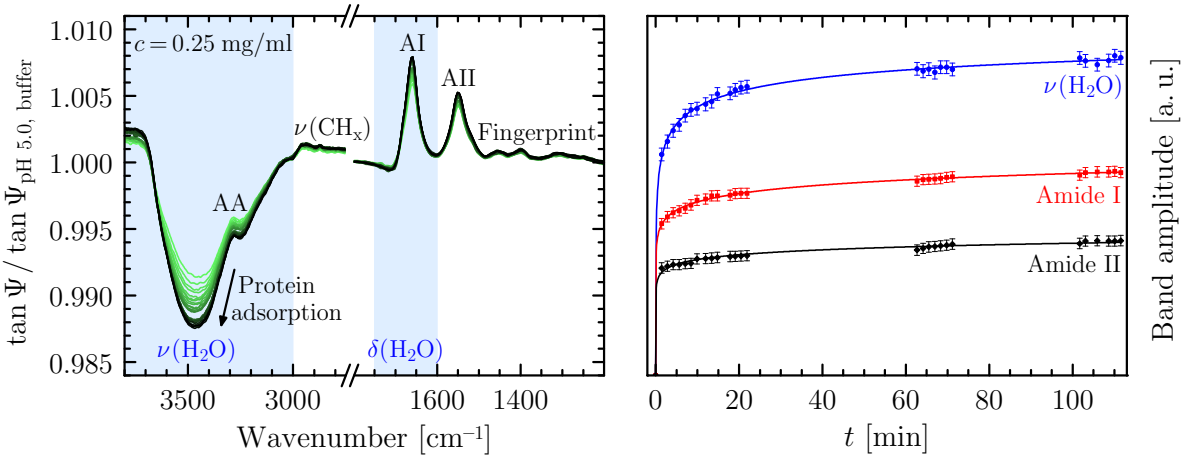

Figure 3.56: HSA adsorption at 25 °C on the $d_{\mathrm{dry}} = 7.4$ nm thin PAA brush from a $c = 0.25$ mg/ml protein solution at pH 5.0. Left: Measured tan Ψ spectra referenced to initial protein-free buffer. Amide A, I, II, and the fingerprint region of HSA are marked as AA, AI, AII, and FP, respectively. Raw data measured by Dennis Aulich. Right: Time-dependent (85 s resolution) tan Ψ band amplitudes (|"Peak height" − 1.000|) of $\nu(H_2O)$, amide I, and amide II. To guide the eye, points were connected by fitting functions "Ampl. $\propto t^a/(t^a + b^a)$" with free parameters a and b.

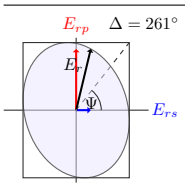

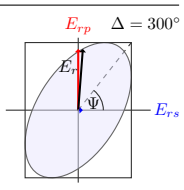

Human serum albumin was added to the buffer solution such that a concentration of $c = 0.25\,\mathrm{mg/ml}$ was obtained. The adsorption process was then monitored over a period of about 120 min by repeated $\tan\Psi$ measurements, as displayed in the left panel of Fig. 3.56. The right panel shows the corresponding time-dependent amplitude progressions of the characteristic protein-amide bands between 1700–1500 cm^{-1} as well as the broad water-stretching band around 3500 cm^{-1}. After about 110 min, these bands showed no further variations, which indicates maximum adsorption. Besides the major contributions due to adsorbed protein, the amide and water bands also contain minor contributions from the interface between brush and protein buffer solution. This influence on the overall $\tan\Psi$ amplitudes can be estimated from $\tan\Psi$ measurements of the previously discussed experiments on protein-repelling PNIPAAm brushes. There, one finds $\tan\Psi$ amplitudes of about 0.00025 for $\nu(H_2O)$ and of less than 0.00005 for amide I/II. If proteins adsorb to the PAA brush, the optical contrast in the amide I/II region decreases even further. The influence of the protein solution is therefore negligibly small compared to the measured band amplitudes in Fig. 3.56, which are larger than 0.008 and 0.004, respectively. In other words, the observed water and amide bands are only associated with the structural and chemical properties of the brush–protein layer.

The large amplitudes of the amide and water bands indicate ternary protein adsorption [294], that is, adsorption within the brush. The amount of adsorbed HSA correlates directly with the amide II band amplitude, which scales almost linearly. $\nu(H_2O)$ reflects both the amount of adsorbed protein and the amount of additional water bound to the brush, but also the thickness of the swollen brush. The water bands scale highly non-linear as was shown in Section 3.5.4.a). Amide I at about 1659 cm^{-1} correlates with the amount of adsorbed protein, too, but it is overlapped by the downward-pointing $\delta(H_2O)$ band around 1650 cm^{-1}. The exact position of $\delta(H_2O)$ also depends on the water and protein content of the brush. Figure 3.57 shows a zoom of the amide I and II bands during protein adsorption.

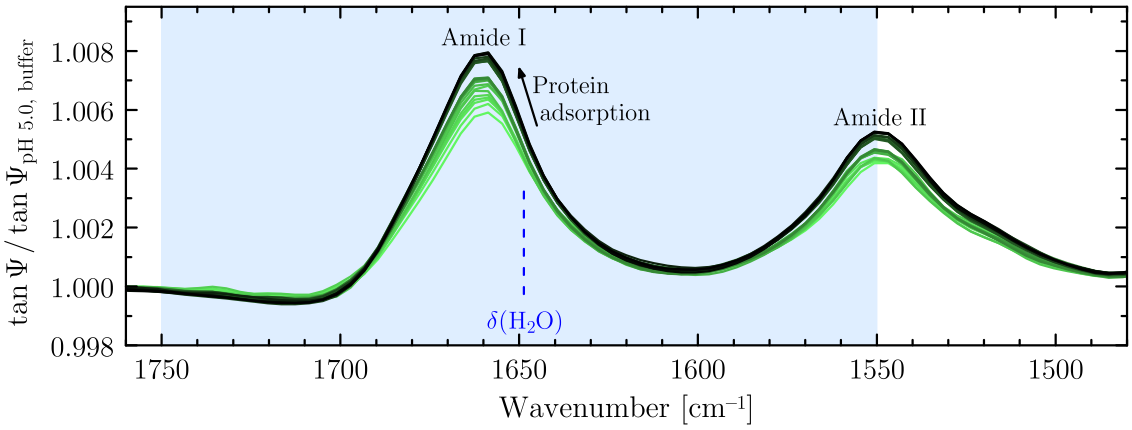

Figure 3.57: Amide I/II region during the HSA adsorption process on the PAA brush shown in Fig. 3.56. The downward-pointing $\delta(H_2O)$ band is overlapping the amide I (and II) band at about 1650 cm^{-1}.

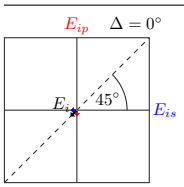

As more and more protein is penetrating the brush, both amide I and $\delta(H_2O)$ are increasing in amplitude, leading to a shift of amide I from 1659.5 cm^{-1} to 1660.8 cm^{-1} between initial and final adsorption spectrum. Also the apparent band shape is changing slightly. Note that both effects are pure optical effects and do *not* indicate any conformational changes of the protein upon adsorption. This is also evident from the amide II band shape, which is not changing at all. Furthermore, both amide bands resemble the band shapes obtained from transmission measurements of HSA solutions (Fig. 3.52). This means that the protein secondary structure remains almost undisturbed after protein adsorption onto the brush, which is important for possible applications.

A more detailed analysis of the protein conformation should build on optical simulations that factor in film effects as well as the influence of water on the amide bands. Otherwise, wrong conclusions might be drawn from the measured band shapes and amplitudes alone.

b) Controlled protein desorption

After maximum adsorption of HSA, the in-situ cell was consecutively purged with protein-free buffer solutions of increasing pH in order for the protein to desorb. The whole desorption process was monitored by repetitive tan Ψ measurements over a period of 240 min, as shown in Fig. 3.58. Corresponding time-resolved amplitudes of the characteristic $\nu(H_2O)$, amide I, and amide II bands are plotted in Fig. 3.59.

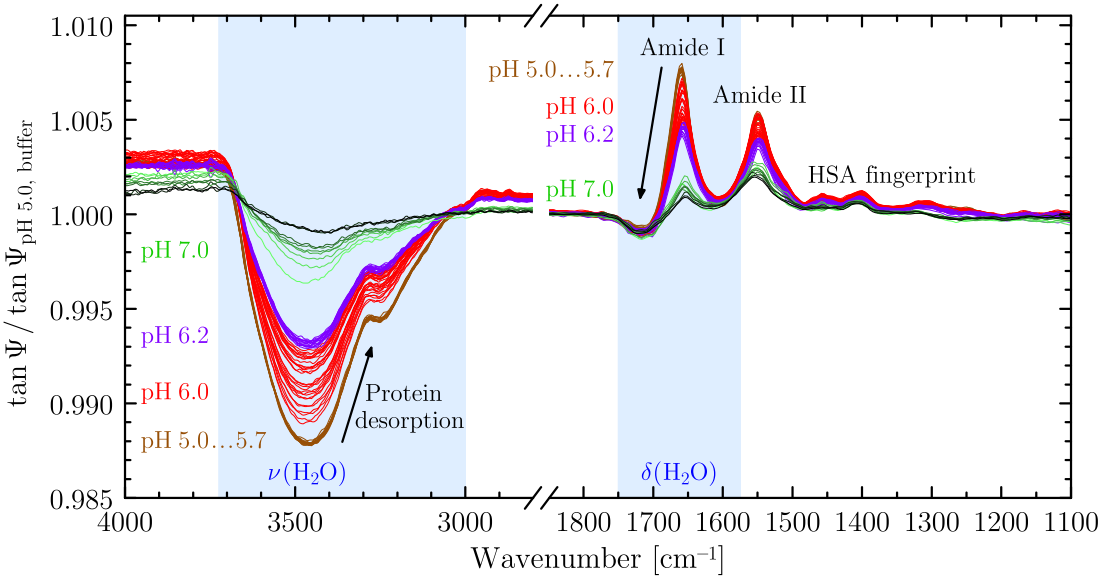

Figure 3.58: HSA desorption from the $d_{dry} = 7.4$ nm thin PAA brush in protein-free buffer solutions between pH 5.4–7.0. Measured tan Ψ spectra were referenced to the initial protein-free buffer spectrum at pH 5.0 before exposing the brush to proteins. Raw data measured by Dennis Aulich. Note that the amide I band is strongly overlapped by the downward-pointing $\delta(H_2O)$ band.

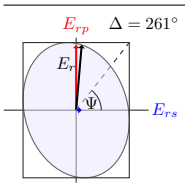

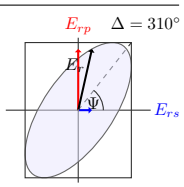

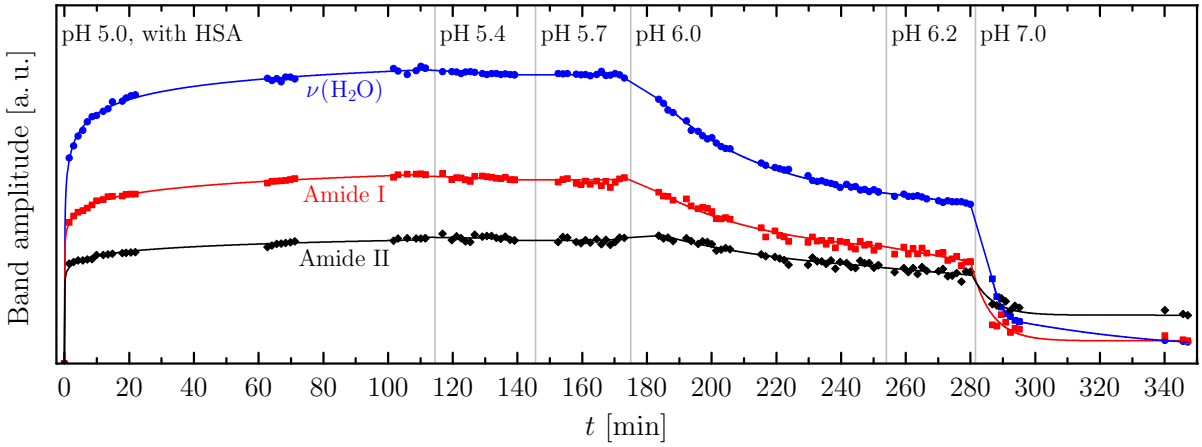

Figure 3.59: Time-dependent (85 s resolution) tan Ψ band amplitudes (|"Peak height" − 1.000|) of $\nu(H_2O)$, amide I, and amide II during HSA adsorption at pH 5.0 and controlled HSA desorption with increasing pH, corresponding to the PAA-brush spectra in Figs. 3.56 and 3.58. To guide the eye, points during desorption were connected by fitting exponential-decay functions.

At pH 5.4, the relative amplitude changes of $\nu(H_2O)$ and amide I are smaller than 2% compared to the last adsorption spectrum at pH 5.0. This suggests that adsorbed proteins stayed attached to the brush and that only loosely bound proteins or proteins in solution were removed from the cell. Amide II, in fact, is almost unaltered, which rather indicates a slight deswelling of the brush. At pH 5.7—at the isoelectric point (IEP) of defatted HSA—the infrared signature still presents no notable changes. This is explained by the intrinsic pH value inside the brush, which generally differs from the one in solution [23, 290, 291].

The desorption process of HSA is initiated at pH 6.0. tan Ψ spectra recorded over a period of 68 min (red lines) show exponentially decreasing H_2O and HSA band amplitudes towards a stable point at which desorption and re-adsorption are in equilibrium. The $\nu(H_2O)$ and amide I peaks diminish to about 60% of their initial values, while amide II reduces to 76%. HSA seems to desorb due to its negative net charge above the IEP, resulting in electrostatic repulsion from the likewise negatively charged brush. Over the next 92 min, the pH value of the buffer was increased stepwise to 6.2 (purple lines) and 7.0 (green to black lines). This lead to further desorption indicated by a continuing decrease of the $\nu(H_2O)$, amide I, and amide II amplitudes, the absolute values of which dropped down to 8%, 12%, and 37%, respectively.

During the desorption process, the amplitude ratio between amide I and II decreases continuously until amide II even exceeds amide I at pH 7.0. This would suggest substantial structural changes of the adsorbed protein. However, the pH-dependent HSA measurements in Section 3.6.2. showed that HSA does *not* undergo significant conformational changes between pH 5.0 and 7.0. The observed changes in the amide I/II ratio could therefore be originating from either the buffer solution, from the brush structure and chemistry itself, and/or from changing brush–protein interactions. This will now be discussed in more detail.

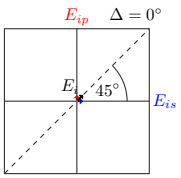

First, amide I is overlapped by the downward-pointing $\delta(H_2O)$ band around 1650 cm^{-1}. Moreover, the spectral signature of water is depending on the local salt concentration as well as the local pH [290], which might lead to further changes in the amide I region.

Second, PAA brushes are exhibiting a characteristic switching behavior when raising the pH from 5.0 to 7.0 [23, 289–291]. The carboxylic groups of PAA undergo dissociation from COOH to COO^-, as illustrated in Fig. 3.60. This manifests itself in a downward-pointing ν(C=O) peak at 1726 cm^{-1} and two upward-pointing $\nu_{as}(COO^-)$ and $\nu_{ss}(COO^-)$ peaks at 1562 cm^{-1} and 1414 cm^{-1}, respectively, which is shown in a switching spectrum in Fig. 3.61.

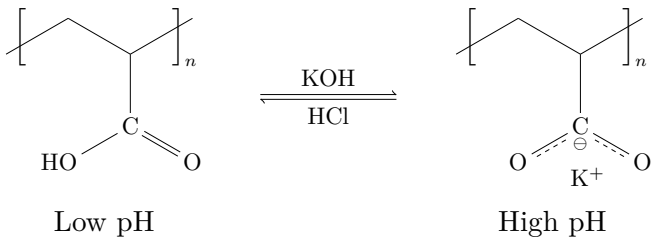

Figure 3.60: Dissociation and reprotonation of PAA's carboxylic groups in dependence of pH by adding, for example, KOH or HCl to the solution.

Clearly, the PAA bands are contributing a non-negligible part to the amide II and fingerprint band envelopes. Also $\nu(H_2O)$ is affected in position and shape due to overlapping features in that region. Amide I, on the contrary, is hardly affected at all.

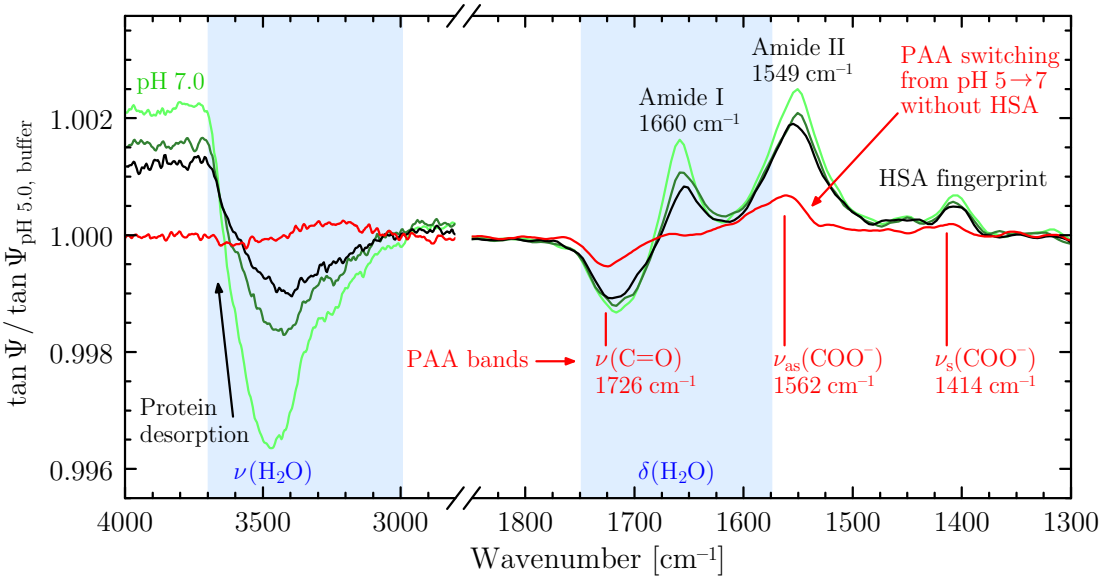

Figure 3.61: Selected HSA desorption spectra (green to black lines) from the PAA-brush measurements at pH 7.0 (see Fig. 3.58) in comparison with a switching spectrum of the $d_{dry} = 5.1$ nm thin PAA brush from pH 5 to 7 (red line). The latter reveals vibrations of PAA's carboxylic groups that overlap with the amide region of HSA as well as the water-bending vibration $\delta(H_2O)$.

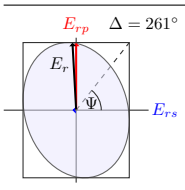

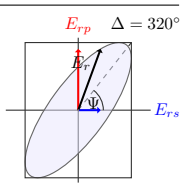

PAA brushes also swell in the order of some 10% between pH 5.0–7.0 owing to electrostatic repulsion between the negatively charged COO^- groups [289, 291]. It is rather unlikely that the swelling behavior and the simultaneous incorporation of buffer ions into the brush [82] are not influenced by the presence of bound proteins. Changes in swelling would result in different amounts and distributions of water and buffer ions inside the brush, thereby modifying amplitude and shape of the water vibrational bands around 3460 cm^{-1} and 1650 cm^{-1}.

Third, the considerable amount of free charges in the brush–protein system might induce an enhanced switching amplitude of the PAA brush, resulting in much more pronounced carboxylic bands, which would in turn affect the apparent amide II band shape and amplitude.

All of the aforementioned effects give rise to potentially ambiguous changes or distortions of the vibrational bands in the desorption spectra and cannot be verified or falsified by pure analysis of these spectra alone. Additional measurements as well as optical-model calculations become necessary.

c) Swelling behavior and protein content

In order to quantitatively assess the thickness $d_{combined}$ of the swollen brush–protein layer as well as its PAA, water, and HSA contents (% PAA, % H_2O, and % HSA), the experiment was repeated at the IPF Dresden using in-situ VIS ellipsometry. Measured tan Ψ and Δ spectra

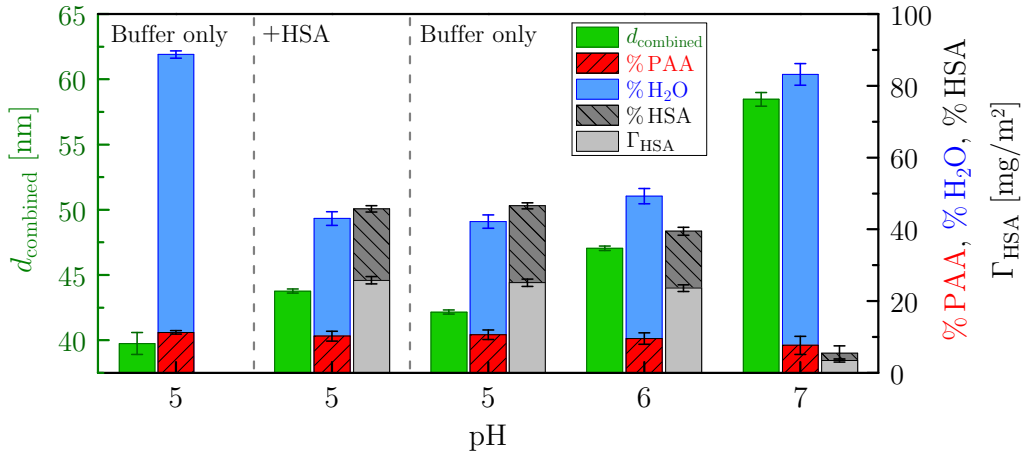

Figure 3.62: pH-dependent thickness $d_{combined}$ of the combined brush–protein layer, volume percentage of PAA (% PAA), water (% H_2O) and protein (% HSA) within the brush, as well as the absolute amount of adsorbed protein Γ_{HSA} as determined by in-situ VIS ellipsometry on the $d_{dry} = 4.7$ nm thin PAA brush. Starting condition was the PAA brush swollen in a 10 mM buffer solution at pH 5. After several minutes, the solution was exchanged for pH 5 buffer containing 0.25 mg/ml HSA. After 85 min, the solution was consecutively replaced for protein-free buffer solutions at pH 5, 6, and 7, and these were kept inside the cell for 60, 100, and 60 min, respectively. tan Ψ and Δ spectra were recorded at the end of each equilibration period. Measurements and quantitative evaluation were performed by Eva Bittrich.

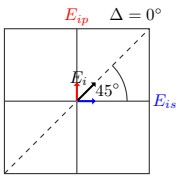

were evaluated with a three-component EMA layer of brush/buffer/protein. The absolute amount of adsorbed protein Γ_{HSA} was derived using a modified *de Feijter* approach [82, 295].

Figure 3.62 shows pH-dependent results for d_{combined}, % PAA, % H_2O, % HSA, and Γ_{HSA}. At pH 5 without protein, the brush is swollen by a factor of 8.5 compared to the dry state. With 89 vol%, its water content is accordingly high. After exchanging the solution for a HSA solution with $c = 0.25$ mg/ml, the swollen-brush thickness increased from 39.7 nm to 43.8 nm and decreased again to 42.1 nm after replacing the solution for protein-free buffer. Within the experimental errors, however, Γ_{HSA} decreased only marginally. This deswelling of the brush confirms the previous observations of an almost constant amide II band and slightly diminishing amide I and $\nu(H_2O)$ bands when exchanging the HSA solution for protein-free buffer.

At pH 6, partial protein desorption takes place. Simultaneously, the brush begins to swell while binding additional buffer solution. At pH 7, the majority of proteins desorbs, with 14% remaining adsorbed to the brush compared to the pH 5 state. This is a surprisingly similar value compared to the amide I amplitude ratio of 12% between final desorption state at pH 7.0 and initial state at pH 5.4 in the in-situ infrared-ellipsometry measurements. This also suggests that the main contribution in the final amide II band envelope must have non-protein origins.

Lastly, the brush is swollen to almost 60 nm at pH 7 with a correspondingly high buffer content. This swelling behavior of PAA brushes—and polyelectrolyte brushes in general—is not yet fully understood by means of infrared spectroscopy. The VIS-ellipsometric results, however, allow one to estimate the effects of COOH dissociation on the HSA–PAA spectra, as will be discussed in the next section.

d) Analyzing the spectrally overlapping effects

In order to understand the final desorption spectrum in Figs. 3.58 and 3.61, a detailed look at the PAA-specific bands is necessary. The top panel of Fig. 3.63 shows measured infrared-ellipsometric $\tan\Psi$ spectra [23] of a PAA brush switched between pH 2 and 10. $\mathrm{COOH} \rightarrow \mathrm{COO^-}$ dissociation at increasing pH is revealed by corresponding changes in the $\nu(\mathrm{C{=}O})$ and $\nu(\mathrm{COO^-})$ bands, as discussed before. Another band at 1250 $\mathrm{cm^{-1}}$ is attributed to $\nu(\mathrm{CO})$ of the non-ionized COOH groups. The broad band around 2050 $\mathrm{cm^{-1}}$ can be assigned to a combination of far-infrared PAA bands with $\delta(H_2O)$ [296]. A second broad feature observed at about 2580 $\mathrm{cm^{-1}}$ is associated with vibrations of $\mathrm{COOH{-}H_2O}$-interacted carboxylic groups [296]. Upward- and downward-pointing bands respectively correlate with increasing and decreasing amounts of corresponding vibrations with respect to the reference spectrum at pH 2.

Similar to the swelling behavior of PNIPAAm brushes discussed in Section 3.5., one would expect distinct $\nu(H_2O)$ and $\delta(H_2O)$ bands of large amplitude, knowing that the brush is

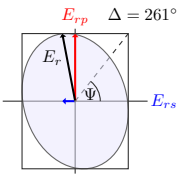

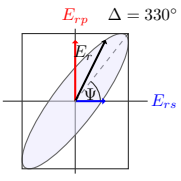

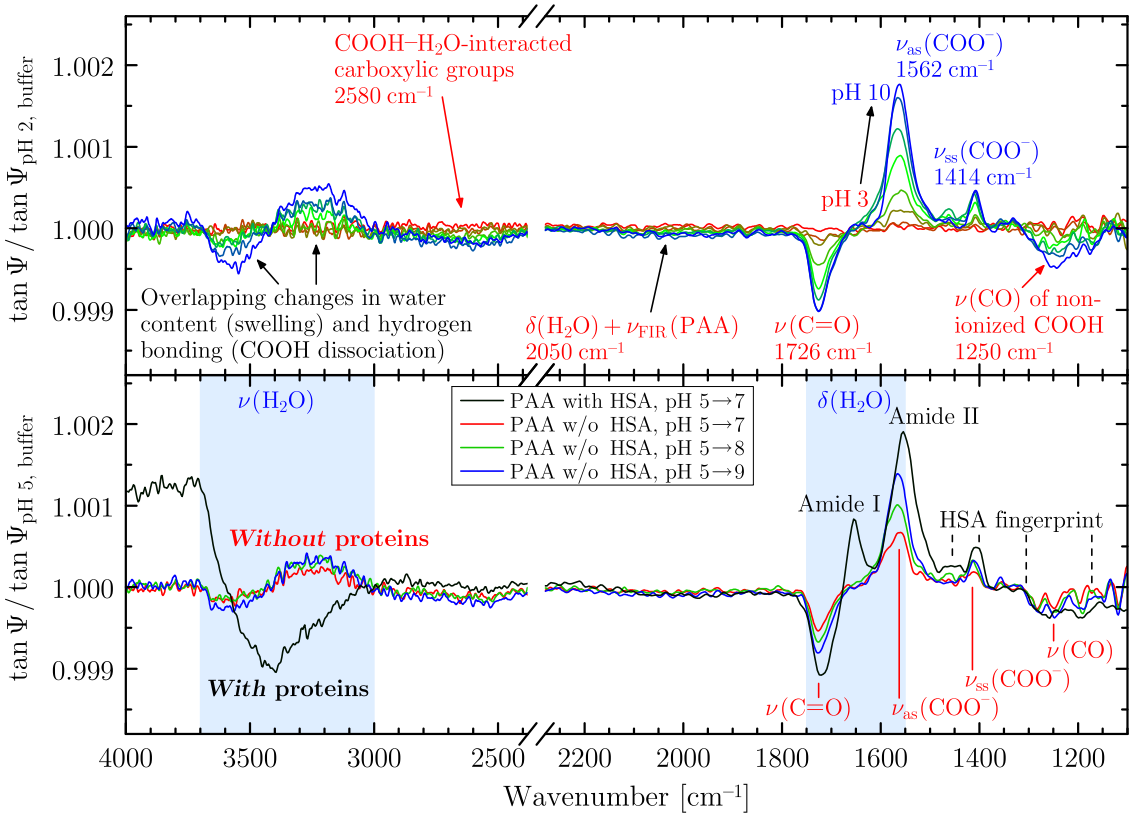

Figure 3.63: Top: In-situ tan Ψ measurements from Ref. [23] showing the switching of the $d_{dry} = 5.1$ nm thin PAA brush from pH 2 to 10 in steps of pH 1 by adding KOH to the solution. Spectra are referenced to the initial state at pH 2. Upward- and downward-pointing bands therefore respectively correlate with increasing and decreasing amounts of the corresponding molecular vibrations with respect to that state. Bottom: PAA switching spectra from pH 5 to 7 (red line), 8 (green line), and 9 (blue line) in comparison with the final HSA desorption spectrum (black line) from the PAA-brush measurements at pH 7.0 (see Fig. 3.58).

swelling by several 10 nm with increasing pH. On the contrary, no unambiguous water band is visible in the $\delta(H_2O)$ region between 1700–1600 cm^{-1}, whereas a sigmoidal band shape is found between 3700–3000 cm^{-1} in the $\nu(H_2O)$ region. This shape is probably related to the fact that the local pH inside the brush is influenced by the local salt concentration depending on the distance from the substrate. Theoretical investigations by Gong et al. [290] show that for a PAA brush with a grafting density of $\sigma = 0.30\,nm^{-2}$, the local pH varies between 4.2 and 5.8 if the buffer solution has a pH of 5.8. With this difference, the vibrational bands of water, which overlap with the PAA bands, change accordingly [239, 297], and so do PAA–buffer interactions.

The lower panel of Fig. 3.63 shows a comparison between the final HSA–PAA desorption spectrum and three PAA switching spectra from pH 5 → 7, pH 5 → 8, and pH 5 → 9 without protein. Striking similarities are found in the 1800–1100 cm^{-1} region, whereas the

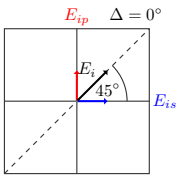

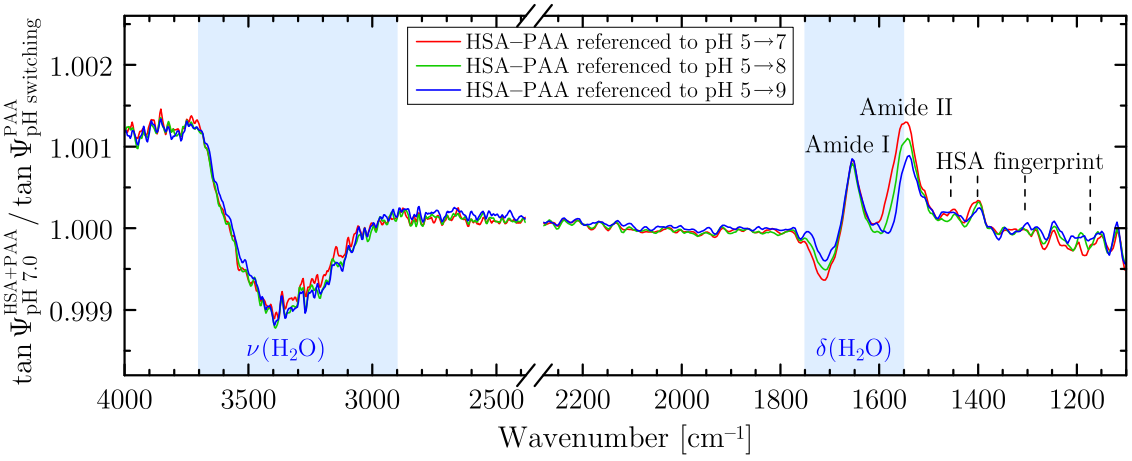

Figure 3.64: Ratios between final referenced HSA–PAA desorption tan Ψ spectrum at pH 7.0 (see Fig. 3.58) and referenced PAA switching spectra from pH 5 to 7 (red line), 8 (green line), and 9 (blue line). Taking the ratio should remove PAA-specific bands and leave only bands that are due to remaining adsorbed HSA.

water-stretching region between 3700–3000 cm^{-1} differs notably. This is, in part, explained by the small absolute amount of still-adsorbed protein, but the similar relative amounts of $\%\,\mathrm{PAA} = 7.7\%$ and $\%\,\mathrm{HSA} = 5.5\%$, which both are very small compared to $\%\,\mathrm{H_2O} = 83.2\%$. Bulk-like water contributions therefore still dominate the $\nu(\mathrm{H_2O})$ region of the HSA–PAA spectrum. The PAA and HSA bands, however, are of the same order of magnitude. Furthermore, amide I is almost unaffected by overlapping PAA bands, while amide II is enhanced by $\nu_{\mathrm{as}}(\mathrm{COO^-})$. The amplitude ratios between the amide bands and the other characteristic HSA bands can therefore be used to compare the relative band amplitudes with the ones obtained from HSA transmission measurements in order to determine the contributions of the PAA bands to the spectral composition. With these considerations in mind, the influence of the COOH and $\mathrm{COO^-}$ bands on the HSA–PAA spectrum is now estimated based on the assumption that the different samples from the HSA and PAA swelling experiments yield comparable switching amplitudes.

Figure 3.64 displays the ratio between the final HSA–PAA spectrum and the three PAA switching spectra from pH 5 to 7, 8, and 9. The bands at 2580 cm^{-1} and 2050 cm^{-1} are no longer present due to the referencing, hence indicating the applicability of the method. The upward-pointing amide I band is still overlapped by the downward-pointing $\delta(\mathrm{H_2O})$ band. From optical simulations, the ratio between $\delta(\mathrm{H_2O})$ and $\nu(\mathrm{H_2O})$ band amplitude is known to be approximately 0.5. With this knowledge, the $\delta(\mathrm{H_2O})$ band can then be subtracted from amide I. This finally allows one to compare the amide I/II and amide/fingerprint ratios for the different PAA switching spectra. Best agreement is found if the brush is switching from pH 5.0 to 8.5.

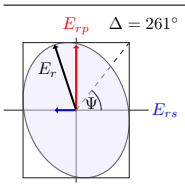

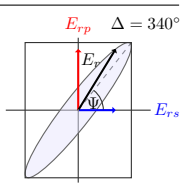

The above result does not imply a pH of 8.5 within the PAA brush, because the spectra only reflect relative pH-induced changes. It rather suggests a larger local pH difference inside the brush due to differently distributed ions and counterions if protein is adsorbed and then partly desorbed again. The large amount of free charges within the brush–protein system therefore seems to cause an enhanced switching amplitude of the PAA brush, which is equivalently induced if the buffer solution shows a pH difference of $(8.5 - 5.0) = 3.5$. These findings are in agreement with several investigations that demonstrate a counterion redistribution in the presence of proteins [82, 298] as well as charge-regulation processes of brush and proteins upon protein adsorption and desorption [39, 82, 288, 299].

e) Future studies using optical simulations

In-situ infrared ellipsometry turned out to be a very useful method for investigating protein adsorption on polymer brushes. By analyzing the protein-specific amide bands, it was shown that HSA adsorption and desorption at PAA brushes can be monitored in-situ with a time resolution of at least 85 s. Next to protein desorption, chemical changes of the brush could be observed upon increasing pH. Interpreting in-situ IR-SE spectra quantitatively, however, is a difficult task, because the various different effects at the solid–liquid interface yield overlapping spectral information. Nevertheless, a semi-quantitative evaluation was possible with the help of additional input from in-situ VIS ellipsometry measurements. It could then be demonstrated that the presence of proteins leads to changes in the pH-dependent switching behavior of the brush.

In the end, full optical simulations are imperative for a deeper quantitative understanding of structure and chemistry of brush and protein. Systematic studies are needed that allow one to distinguish the several overlapping effects that make for the effective refractive index of the brush–protein system. In the first step, the swelling and dissociation behavior of PAA brushes has to be described in dependence of salt concentration and distribution by an appropriate effective-medium model. This model must include the buffer solution as well as the polymer in the form of separate low-pH and high-pH carboxyl oscillators in order to quantify brush–buffer interactions correctly. The brush profile might be considered, too. In the second step, the optical constants of the protein, as determined, e. g., from ATR ellipsometry or transmission measurements, are used to model protein adsorption and desorption at the brush in a three-component brush/buffer/protein mEMA model, similar to the spectra evaluation of VIS-ellipsometry data. This should reveal the interactions among the three components at a quantitative level. Preliminary results as well as the successful quantitative modeling of PNIPAAm brushes in Section 3.5. already indicate that this modeling process is indeed feasible.

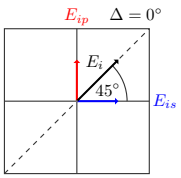

4. Summary and outlook

Functional polymer films have great potential for possible biochemical and biomedical applications. In particular, surfaces that are tunable in dependence of external stimuli like temperature are of special interest. Infrared ellipsometry and microscopy are two techniques that allow one to probe the structural and chemical properties of such organic surfaces. Moreover, these techniques are applicable for in-situ purposes. Up until now, the biggest obstacle was to quantitatively separate the different effects that occur at the solid–liquid interface when a sample is in contact with aqueous environment. This problem was successfully tackled in this thesis. New experimental as well as optical-modeling strategies were developed that enable one to access various sample properties, such as layer thicknesses, water content, and—most importantly—changing interactions among and between the sample constituents and solvent.

Infrared ellipsometry was used to determine the optical constants of spin-coated 55–135 nm thick PNIPAAm and PGMA films in dry state, which served as the foundation for subsequent quantitative spectra evaluation of stimuli-dependent experiments. The optical constants were built from sums of oscillator contributions corresponding to the molecular vibrations of the polymers. The amide I and II bands of PNIPAAm were found to consist of respectively three and two subcomponents that are related to different polymer–polymer hydrogen-bond interactions between C=O and N−H groups of the polymer.

A variety of humidity-dependent infrared-microscopic measurements on PNIPAAm films in H_2O and D_2O vapor were conducted in order to identify different polymer–water hydrogen-bond interactions. The set of dry-state PNIPAAm oscillators was consequently extended for several new wet-state oscillators. With this extended set at hand, it was possible to model PNIPAAm films at different humidities. A modified EMA approach allowed one to quantify thickness and water content of the swollen polymer layers, as well as to track changing polymer–polymer and polymer–water interactions throughout the drying process of the films. This yielded deeper insights into the different hydration states of PNIPAAm.

Next, 4.0–14.5 nm thin PNIPAAm brushes were characterized in dry state in dependence of grafting density and molecular weight. Ellipsometric spectra could be described with the optical constants of the spin-coated films. Small changes in the band composition of amide I and II compared to the thicker films were assigned to larger relative amounts of surface-exposed non-interacted amide groups. Time-dependent *N*-deuteration experiments revealed the relative strengths of hydrogen bonding inside the brushes. Deuterated-brush spectra were modeled by redshifting the corresponding amide oscillators. PNIPAAm brushes in humid air showed similar swelling effects and polymer–water interactions as the thicker films.

The temperature-dependent swelling behavior of PNIPAAm brushes in aqueous environment was successfully monitored with in-situ infrared ellipsometry. To achieve this, an existing in-situ cell was mounted to a redesigned sample holder with a PID-controlled Peltier

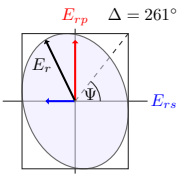

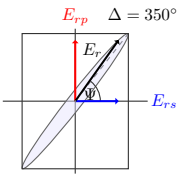

heating-and-cooling system that features a stability of ±0.05 °C. This made it possible to separate the spectral information of brush and overlapping bulk-water signature. Measurements in H_2O and D_2O, then, gave insights into changing interactions during (de)swelling.

The main goal was to describe ellipsometric in-situ spectra at a quantitative level. Since the optical properties of water vary strongly in the probed temperature range of 20–50 °C, the optical constants of H_2O and D_2O had to be determined first. Transmission measurements were performed using special cells with micrometer-short path lengths in order to resolve the strong vibrational bands of water. A careful optical-modeling strategy was pursued to fit on the optical constants with a high enough accuracy for the following brush evaluation.

After introducing a baseline-correction procedure for in-situ infrared-ellipsometric spectra, a spin-coated thick PGMA film served as the first test sample. As expected, the film showed almost no swelling. The layer thickness, as previously determined from ex-situ measurements, could be reproduced correctly. Afterwards, a PNIPAAm brush of 14.5 nm dry-state thickness was measured below and above its lower critical solution temperature (LCST), the temperature around which the brush undergoes a phase transition from an extended to a collapsed state. Again, spectra were modeled successfully. Swollen-brush thicknesses and water contents showed similar tendencies as determined by VIS ellipsometry on comparable brushes. The swelling and deswelling behavior was confirmed, and most importantly, changing polymer–polymer and polymer–water interactions were identified based on the set of dry- and wet-state oscillators. Below the LCST, the brush is strongly hydrated, such that polymer–water interactions dominate. Nevertheless, about a fifth of PNIPAAm's C=O groups form mixed hydrogen bonds with water and neighboring H−N groups. Above the LCST, the brush collapses and releases a significant amount of water. Polymer–water interactions are still present, but C=O groups tend to form hydrogen bonds with two H−N groups.

A semi-quantitative analysis was performed concerning protein monolayers and solutions of human serum albumin (HSA), as well as HSA-repelling and -adsorbing PNIPAAm and PAA brushes, respectively. Time-resolved infrared ellipsometry allowed the monitoring of protein-adsorption processes on PAA brushes at pH 5 with subsequent controlled protein-desorption at increasing pH. Simultaneously, an enhanced switching amplitude of the PAA brushes was found. Complementary in-situ VIS-ellipsometric measurements gave quantitative information about PAA, water, and HSA contents as well as the amount of still-adsorbed protein.

All in all, in-situ infrared ellipsometry and microscopy on organic films in contact with water or water vapor as well as protein solutions have proven to be valuable tools for gaining a deeper understanding of film properties and interactions. For the first time, spectra were evaluated quantitatively on the basis of physical models. The successful modeling of PNIPAAm brushes, which proved it possible to separate film effects and interactions, is the cornerstone for future investigations on more complicated material systems like mixed brushes, and for studying, for example, structural changes of proteins during adsorption to thin films.

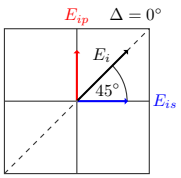

Appendices

A. Details on Fourier-transform spectrometers

Fourier-transform spectrometers offer several advantages compared to dispersive spectrometers. All spectral components emitted by the globar are measured simultaneously, limited only by the absorption properties of the used optical elements in the set-up like beamsplitter and transmission windows. A consequence of this so-called multiplex or *Fellgett* advantage [300] is an increased signal-to-noise ratio because no monochromator is needed to scan the whole spectrum. The *Jacquinot* advantage [301] refers to the fact that monochromators also require entrance and exit slits, which in turn decrease the throughput. In Fourier-transform spectrometers, however, the throughput is determined only by a single circular Jacquinot aperture that limits the diameter of the collimated globar beam.

Globars are silicon carbide rods heated to elevated temperatures between about 1000 °C and 1600 °C. Their spectral behavior is comparable to that of a black-body radiator, which allows one to measure a wide spectral range at once. Close to the path of the actual globar radiation, light from a HeNe laser is being sent through the interferometer. Its purpose is twofold. Via an appropriate internal detector, on the one hand, it enables the measuring of the mirror position by evaluating the corresponding sinusoidal laser interferogram [105]. Zero-crossings in this interferogram then trigger the sampling of the globar interferogram at equidistant positions, which is necessary for standard Fourier-transform algorithms [101]. The accuracy and stability of the laser wavelength at 632.8 nm ($1/15802\,\mathrm{cm}^{-1}$) directly correlate with an accurate determination of the mirror position—usually better than 0.005 µm [105]—and consequently, they make for a very high wavenumber accuracy $< 0.01\,\mathrm{cm}^{-1}$. This automatic internal wavenumber calibration [105] is known in the literature as *Connes'* advantage [302]. On the other hand, the HeNe laser ensures a coherent superposition of interferograms from consecutive scans [303], which is of special importance for in-situ measurements that can last several minutes or even hours.

Two important points concern the actual Fourier transform of the interferogram: apodization and zero-filling. Defining the optical path length L as twice the mirror displacement, $L = 2z$, the interferogram in an ideal spectrometer measured with an ideal detector is given by [1]

$$\mathcal{I}(L) = \int_{-\infty}^{+\infty} \mathcal{I}(\tilde{\nu}) \cos(2\pi\,\tilde{\nu} L)\,\mathrm{d}\tilde{\nu} \qquad \Leftrightarrow \qquad \mathcal{I}(\tilde{\nu}) = \int_{-\infty}^{+\infty} \mathcal{I}(L) \cos(2\pi\,\tilde{\nu} L)\,\mathrm{d}L\,, \tag{A.1}$$

where integration over L from $-\infty$ to $+\infty$ results in a spectrum $\mathcal{I}(\tilde{\nu})$ over the whole wavenumber range. In practice, however, the mirror displacement is limited, meaning that

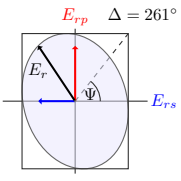

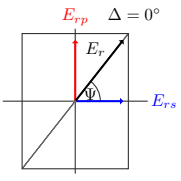

the maximum optical path length is a finite value $L_{\max}$. In a computational implementation of the Fourier transform, e. g., the Fast-Fourier transform (FFT) algorithm [101], the integral therefore has to be replaced by a finite sum with limits $\pm L_{\max}$. This causes artifacts in the transformed spectra [304] which have to be accounted for appropriately: A naïve boxcar truncation introduces sidelobes to the true instrument line shape. In order to remove these, an apodization function $D(L)$ that smoothly decays to zero at $\pm L_{\max}$ is inserted as a convolution function into the Fourier transform in Eq. (A.1) [1, 104, 105]. While different functions (triangular, bell-shaped, etc.) with different effects on sidelobes and maximum resolution are discussed in the literature [104, 303, 305], the Blackman–Harris three-term apodization function [256] is solely used in the present work.

The Fast-Fourier transform requires that the number of data points in the interferogram is a power of 2. To fulfill this requirement, the appropriate number of zeros is added to the ends of the interferogram. This so-called zero-filling is also applied for other reasons: First, if desired, to maintain the number of data points for spectra recorded at different resolutions [305]. And second, it is used to reduce the picket-fence effect [306, 307] that arises when the spectrum contains sharp features that do not coincide with the sampling points of the FFT [308]. A zero-filling factor of 2 (recommended standard) or even 4 or 8, then, proves sufficient in order to interpolate the spectrum and increase its quality [105, 308]. Zero-filling is important, for example, for measurements on polymers with very sharp vibrational bands.

For further details on Fourier-transform spectrometers, the interested reader is referred to Refs. [1, 105, 199, 306, 307].

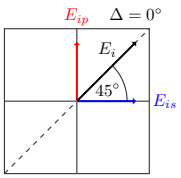

B. Details on measurements with imperfect optical components

This appendix provides additional information about the Müller matrix formalism introduced in Section 2.1.4.b). Müller matrices $\mathcal{M}_n$ are usually derived in the eigensystems of the optical elements. When calculating the matrix of the whole system, they therefore have to be transformed into the system of the incident Stokes vector. This is accomplished by rotator matrices $\mathcal{R}(\alpha)$:

$$\mathcal{R}(\alpha) \equiv \mathcal{M}_{\mathrm{Rot}}(\alpha) = \begin{bmatrix} 1 & 0 & 0 & 0 \\ 0 & \cos 2\alpha & \sin 2\alpha & 0 \\ 0 & -\sin 2\alpha & \cos 2\alpha & 0 \\ 0 & 0 & 0 & 1 \end{bmatrix} \tag{B.1}$$

In the cartesian coordinate system defined with the z axis parallel to the propagation direction of the light, rotation about an angle α transforms a Stokes vector according to

$$S'(\alpha) = \mathcal{R}(\alpha)\, S\,. \tag{B.2}$$

In order to transfrom Müller matrices from their eigensystem into the original coordinate system, incident and resulting Stokes vectors are subject to inverse rotations,

$$\mathcal{M}_{\mathrm{new}}(\alpha) = \mathcal{R}(-\alpha) \cdot \mathcal{M}_{\mathrm{old}} \cdot \mathcal{R}(\alpha)\,. \tag{B.3}$$

Overview of Müller matrices:

Ideal polarizer with transmission axis in x direction with respect to the cartesian coordinate system (defined by the plane of incidence):

$$\mathcal{M}_{\mathrm{Pol}} = \frac{1}{2} \begin{bmatrix} 1 & 1 & 0 & 0 \\ 1 & 1 & 0 & 0 \\ 0 & 0 & 0 & 0 \\ 0 & 0 & 0 & 0 \end{bmatrix} \tag{B.4}$$

Non-ideal polarizer with degree of polarization smaller than 1, parameterized by the maximum and minimum transmittances τ_{M} and τ_{m}:

$$\mathcal{M}_{\mathrm{Pol}}(\vartheta) = K \times \begin{bmatrix} 1 & \cos 2\vartheta & 0 & 0 \\ \cos 2\vartheta & 1 & 0 & 0 \\ 0 & 0 & \sin 2\vartheta & 0 \\ 0 & 0 & 0 & \sin 2\vartheta \end{bmatrix} \tag{B.5}$$

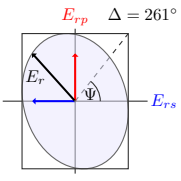

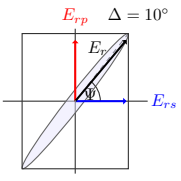

Here, $K = \frac{\tau_\mathrm{M} + \tau_\mathrm{m}}{2}$, $\cos 2\vartheta = \frac{\tau_\mathrm{M} - \tau_\mathrm{m}}{\tau_\mathrm{M} + \tau_\mathrm{m}} \equiv$ degree of polarization, $\sin 2\vartheta = \frac{2\sqrt{\tau_\mathrm{M}\tau_\mathrm{m}}}{\tau_\mathrm{M} + \tau_\mathrm{m}}$, and $\tan\vartheta = \sqrt{\tau_\mathrm{m}/\tau_\mathrm{M}} \equiv$ attenuation. For ideal polarizers, $\tau_\mathrm{m} = \sin 2\vartheta = \tan\vartheta = 0$ and $\cos 2\vartheta = 1$.

Ideal retarder with phase shift $\delta_\mathrm{Ret} = \delta_\mathrm{f} - \delta_\mathrm{s}$ between fast (f) and slow (s) axis:

$$\mathcal{M}_\mathrm{Ret}(\delta_\mathrm{Ret}) = \begin{bmatrix} 1 & 0 & 0 & 0 \\ 0 & 1 & 0 & 0 \\ 0 & 0 & \cos\delta_\mathrm{Ret} & \sin\delta_\mathrm{Ret} \\ 0 & 0 & -\sin\delta_\mathrm{Ret} & \cos\delta_\mathrm{Ret} \end{bmatrix} \tag{B.6}$$

Products of the matrices (B.5) and (B.6) now allow one to describe polarization effects of real retarders, isotropic samples, and non-ideal polarizers [89, 94, 309]:

Real retarder with phase shift $\delta_\mathrm{Ret} = \delta_\mathrm{f} - \delta_\mathrm{s}$ and $\tan\psi_\mathrm{Ret} = \sqrt{\tau_\mathrm{f}/\tau_\mathrm{s}} \neq 0$:

$$\mathcal{M}_\mathrm{Ret}(\psi_\mathrm{Ret}, \delta_\mathrm{Ret}) = K_\mathrm{R} \times \begin{bmatrix} 1 & -\cos 2\psi_\mathrm{Ret} & 0 & 0 \\ -\cos 2\psi_\mathrm{Ret} & 1 & 0 & 0 \\ 0 & 0 & \sin 2\psi_\mathrm{Ret}\cos\delta_\mathrm{Ret} & \sin 2\psi_\mathrm{Ret}\sin\delta_\mathrm{Ret} \\ 0 & 0 & -\sin 2\psi_\mathrm{Ret}\sin\delta_\mathrm{Ret} & \sin 2\psi_\mathrm{Ret}\cos\delta_\mathrm{Ret} \end{bmatrix}$$
$$K_\mathrm{R} = \frac{\tau_\mathrm{s} + \tau_\mathrm{f}}{2} \tag{B.7}$$

Note that the sign of ψ_Ret is mere definition.

Isotropic reflecting surface with ellipsometric parameters $\tan\Psi$ and Δ as well as reflection coefficients r_p and r_s:

$$\mathcal{M}_\mathrm{Sample}(\Psi, \Delta) = K_\mathrm{S} \times \begin{bmatrix} 1 & -\cos 2\Psi & 0 & 0 \\ -\cos 2\Psi & 1 & 0 & 0 \\ 0 & 0 & \sin 2\Psi\cos\Delta & \sin 2\Psi\sin\Delta \\ 0 & 0 & -\sin 2\Psi\sin\Delta & \sin 2\Psi\cos\Delta \end{bmatrix}$$
$$K_\mathrm{S} = \frac{|r_p|^2 + |r_s|^2}{2} \tag{B.8}$$

Anisotropic, depolarizing, or optically active samples exhibit non-zero block-off-diagonal matrix elements. Measuring their whole Müller matrix usually requires two retarders in the optical train, one before and one after the sample.

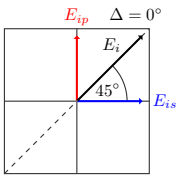

Wire-grid polarizer with additional phase shift $\delta = \delta_\mathrm{M} - \delta_\mathrm{m}$ between τ_M and τ_m component:

$$\mathcal{M}_\mathrm{Pol}(\vartheta,\delta) \equiv \mathcal{M}_\mathrm{Pol}(\vartheta)\cdot\mathcal{M}_\mathrm{Ret}(\delta) = K \times \begin{bmatrix} 1 & \cos 2\vartheta & 0 & 0 \\ \cos 2\vartheta & 1 & 0 & 0 \\ 0 & 0 & \sin 2\vartheta\cos\delta & \sin 2\vartheta\sin\delta \\ 0 & 0 & -\sin 2\vartheta\sin\delta & \sin 2\vartheta\cos\delta \end{bmatrix} \tag{B.9}$$

Wire-grid polarizer with arbitrary orientation α of the τ_M axis:

$$\begin{aligned} \mathcal{M}_\mathrm{Pol}(\vartheta,\delta,\alpha) &\equiv \mathcal{R}(-\alpha)\cdot\mathcal{M}_\mathrm{Pol}(\vartheta,\delta)\cdot\mathcal{R}(\alpha)\,, \\ &= K \times \begin{bmatrix} 1 & c\cdot\cos 2\alpha & c\cdot\sin 2\alpha & 0 \\ c\cdot\cos 2\alpha & \cos^2 2\alpha + s\cdot\sin^2 2\alpha\cos\delta & \sin 2\alpha\cos 2\alpha(1-s\cdot\cos\delta) & -s\cdot\sin 2\alpha\sin\delta \\ c\cdot\sin 2\alpha & \sin 2\alpha\cos 2\alpha(1-s\cdot\cos\delta) & \sin^2 2\alpha + s\cdot\cos^2 2\alpha\cos\delta & s\cdot\cos 2\alpha\sin\delta \\ 0 & s\cdot\sin 2\alpha\sin\delta & -s\cdot\cos 2\alpha\sin\delta & s\cdot\cos\delta \end{bmatrix} \end{aligned} \tag{B.10}$$

As before,

$$K = \frac{\tau_\mathrm{M}+\tau_\mathrm{m}}{2}\,, \quad c = \cos 2\vartheta = \frac{\tau_\mathrm{M}-\tau_\mathrm{m}}{\tau_\mathrm{M}+\tau_\mathrm{m}}\,, \quad s = \sin 2\vartheta = \frac{2\sqrt{\tau_\mathrm{M}\tau_\mathrm{m}}}{\tau_\mathrm{M}+\tau_\mathrm{m}}\,, \quad \delta = \delta_\mathrm{M} - \delta_\mathrm{m}\,. \tag{B.11}$$

The small intensity of infrared light sources limits the feasible number of measurements at different polarizer settings. Four azimuth combinations (α_1, α_2) with at least one non-parallel setting are sufficient to accurately determine both Ψ and Δ. With $\alpha_i = 0°$, 45°, 90°, and 135°, the trigonometric functions appearing in the polarizer Müller matrices simplify to 0 or ± 1:

$$\mathcal{M}_\mathrm{Pol}(\vartheta_i,\delta_i,\left[\!\!\left[\begin{smallmatrix}0°\\90°\\45°\\135°\end{smallmatrix}\right]\!\!\right]) = K_i \times \begin{bmatrix} 1 & \left[\!\!\left[\begin{smallmatrix}\pm c_i\\0\end{smallmatrix}\right]\!\!\right] & \left[\!\!\left[\begin{smallmatrix}0\\\pm c_i\end{smallmatrix}\right]\!\!\right] & 0 \\ \left[\!\!\left[\begin{smallmatrix}\pm c_i\\0\end{smallmatrix}\right]\!\!\right] & \left[\!\!\left[\begin{smallmatrix}1\\s_i\cos\delta_i\end{smallmatrix}\right]\!\!\right] & 0 & \left[\!\!\left[\begin{smallmatrix}0\\\mp s_i\sin\delta_i\end{smallmatrix}\right]\!\!\right] \\ \left[\!\!\left[\begin{smallmatrix}0\\\pm c_i\end{smallmatrix}\right]\!\!\right] & 0 & \left[\!\!\left[\begin{smallmatrix}s_i\cos\delta_i\\1\end{smallmatrix}\right]\!\!\right] & \left[\!\!\left[\begin{smallmatrix}\pm s_i\sin\delta_i\\0\end{smallmatrix}\right]\!\!\right] \\ 0 & \left[\!\!\left[\begin{smallmatrix}0\\\pm s_i\sin\delta_i\end{smallmatrix}\right]\!\!\right] & \left[\!\!\left[\begin{smallmatrix}\mp s_i\sin\delta_i\\0\end{smallmatrix}\right]\!\!\right] & s_i\cos\delta_i \end{bmatrix} \tag{B.12}$$

Here, $s_i = \sin 2\vartheta_i$ and $c_i = \cos 2\vartheta_i$, with $i = 1, 2$ for the first and second polarizer.

With Müller matrices for the several optical elements at hand, it is now possible to calculate the detector intensities for calibration and sample measurements:

$$\begin{aligned} \mathcal{E}(\alpha_1,\alpha_2) &\equiv \mathcal{M}_\mathrm{Pol}(\vartheta_2,\delta_2,\alpha_2)\cdot\mathcal{M}_\mathrm{Pol}(\vartheta_1,\delta_1,\alpha_1)\cdot\bar{S}\,, \\ \mathcal{R}(\alpha_1,\alpha_2) &\equiv \mathcal{M}_\mathrm{Pol}(\vartheta_2,\delta_2,\alpha_2)\cdot\mathcal{M}_\mathrm{Ret}(\psi_\mathrm{Ret},\delta_\mathrm{Ret})\cdot\mathcal{M}_\mathrm{Pol}(\vartheta_1,\delta_1,\alpha_1)\cdot\bar{S}\,, \\ \mathcal{I}(\alpha_1,\alpha_2) &\equiv \mathcal{M}_\mathrm{Pol}(\vartheta_2,\delta_2,\alpha_2)\cdot\mathcal{M}_\mathrm{Sample}(\Psi,\Delta)\cdot\mathcal{M}_\mathrm{Pol}(\vartheta_1,\delta_1,\alpha_1)\cdot\bar{S}\,, \\ \widetilde{\mathcal{I}}(\alpha_1,\alpha_2) &\equiv \mathcal{M}_\mathrm{Pol}(\vartheta_2,\delta_2,\alpha_2)\cdot\mathcal{M}_\mathrm{Ret}(\psi_\mathrm{Ret},\delta_\mathrm{Ret})\cdot\mathcal{M}_\mathrm{Sample}(\Psi,\Delta)\cdot\mathcal{M}_\mathrm{Pol}(\vartheta_1,\delta_1,\alpha_1)\cdot\bar{S} \end{aligned} \tag{B.13}$$

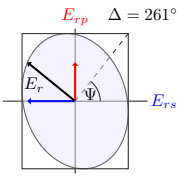

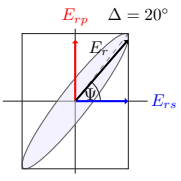

Equations (B.13) are now given explicitly for the azimuths $\alpha_i = 0°$, $90°$, $45°$, and $135°$ using symbolic notation $\left[\begin{smallmatrix}\vert\\ \_\end{smallmatrix}\right] \equiv \left[\begin{smallmatrix}0°\\ 90°\end{smallmatrix}\right]$ and $\left[\begin{smallmatrix}/\\ \backslash\end{smallmatrix}\right] \equiv \left[\begin{smallmatrix}45°\\ 135°\end{smallmatrix}\right]$.

Empty-channel detector intensities *without* retarder

$$\mathcal{E}\left(\left[\begin{smallmatrix}\vert\\ \_\end{smallmatrix}\right],\left[\begin{smallmatrix}\vert\\ \_\end{smallmatrix}\right]\right) = K_1K_2\Big\{\bar{\mathrm{s}}_0\Big(1+[\pm c_1][\pm c_2]\Big)+\bar{\mathrm{s}}_1\,[\pm c_1 \pm c_2]\Big\} \tag{B.14}$$

$$\mathcal{E}\left(\left[\begin{smallmatrix}/\\ \backslash\end{smallmatrix}\right],\left[\begin{smallmatrix}/\\ \backslash\end{smallmatrix}\right]\right) = K_1K_2\Big\{\bar{\mathrm{s}}_0\Big(1+[\pm c_1][\pm c_2]\Big)+\bar{\mathrm{s}}_2\,[\pm c_1 \pm c_2]\Big\} \tag{B.15}$$

$$\mathcal{E}\left(\left[\begin{smallmatrix}\vert\\ \_\end{smallmatrix}\right],\left[\begin{smallmatrix}/\\ \backslash\end{smallmatrix}\right]\right) = K_1K_2\Big\{\bar{\mathrm{s}}_0+\bar{\mathrm{s}}_1\,[\pm c_1]+\bar{\mathrm{s}}_2\,[s_1][\pm c_2]\cos\delta_1+\bar{\mathrm{s}}_3\,[\pm s_1][\pm c_2]\sin\delta_1\Big\} \tag{B.16}$$

$$\mathcal{E}\left(\left[\begin{smallmatrix}/\\ \backslash\end{smallmatrix}\right],\left[\begin{smallmatrix}\vert\\ \_\end{smallmatrix}\right]\right) = K_1K_2\Big\{\bar{\mathrm{s}}_0+\bar{\mathrm{s}}_2\,[\pm c_1]+\bar{\mathrm{s}}_1\,[s_1][\pm c_2]\cos\delta_1-\bar{\mathrm{s}}_3\,[\pm s_1][\pm c_2]\sin\delta_1\Big\} \tag{B.17}$$

Detector intensities of sample *without* retarder

$$\begin{aligned}\mathcal{I}\left(\left[\begin{smallmatrix}\vert\\ \_\end{smallmatrix}\right],\left[\begin{smallmatrix}\vert\\ \_\end{smallmatrix}\right]\right) = \mathcal{K}\Big\{&\bar{\mathrm{s}}_0\Big(1+[\pm c_1][\pm c_2]\Big)+\bar{\mathrm{s}}_1\,[\pm c_1 \pm c_2]\\ &-\cos 2\Psi\Big[\bar{\mathrm{s}}_0\,[\pm c_1 \pm c_2]+\bar{\mathrm{s}}_1\Big(1+[\pm c_1][\pm c_2]\Big)\Big]\Big\}\end{aligned} \tag{B.18}$$

$$\begin{aligned}\mathcal{I}\left(\left[\begin{smallmatrix}/\\ \backslash\end{smallmatrix}\right],\left[\begin{smallmatrix}/\\ \backslash\end{smallmatrix}\right]\right) = \mathcal{K}\Big\{&\bar{\mathrm{s}}_0+\bar{\mathrm{s}}_2\,[\pm c_1]-\cos 2\Psi\Big[\bar{\mathrm{s}}_1\,[s_1]\cos\delta_1-\bar{\mathrm{s}}_3\,[\pm s_1]\sin\delta_1\Big]\\ &+\sin 2\Psi\cos\Delta\Big[\bar{\mathrm{s}}_0\,[\pm c_1][\pm c_2]+\bar{\mathrm{s}}_2\,[\pm c_2]\Big]\\ &+\sin 2\Psi\,\sin\Delta\Big[\bar{\mathrm{s}}_1\,[\pm s_1][\pm c_2]\sin\delta_1+\bar{\mathrm{s}}_3\,[s_1][\pm c_2]\cos\delta_1\Big]\Big\}\end{aligned} \tag{B.19}$$

$$\begin{aligned}\mathcal{I}\left(\left[\begin{smallmatrix}\vert\\ \_\end{smallmatrix}\right],\left[\begin{smallmatrix}/\\ \backslash\end{smallmatrix}\right]\right) = \mathcal{K}\Big\{&\bar{\mathrm{s}}_0+\bar{\mathrm{s}}_1\,[\pm c_1]-\cos 2\Psi\Big[\bar{\mathrm{s}}_0\,[\pm c_1]+\bar{\mathrm{s}}_1\Big]\\ &+\sin 2\Psi\cos\Delta\Big[\bar{\mathrm{s}}_2\,[s_1][\pm c_2]\cos\delta_1+\bar{\mathrm{s}}_3\,[\pm s_1][\pm c_2]\sin\delta_1\Big]\\ &+\sin 2\Psi\,\sin\Delta\Big[\bar{\mathrm{s}}_3\,[s_1][\pm c_2]\cos\delta_1-\bar{\mathrm{s}}_2\,[\pm s_1][\pm c_2]\sin\delta_1\Big]\Big\}\end{aligned} \tag{B.20}$$

$$\begin{aligned}\mathcal{I}\left(\left[\begin{smallmatrix}/\\ \backslash\end{smallmatrix}\right],\left[\begin{smallmatrix}\vert\\ \_\end{smallmatrix}\right]\right) = \mathcal{K}\Big\{&\bar{\mathrm{s}}_0+\bar{\mathrm{s}}_1\,[s_1][\pm c_2]\cos\delta_1+\bar{\mathrm{s}}_2\,[\pm c_1]-\bar{\mathrm{s}}_3\,[\pm s_1][\pm c_2]\sin\delta_1\\ &-\cos 2\Psi\Big[\bar{\mathrm{s}}_0\,[\pm c_2]+\bar{\mathrm{s}}_1\,[s_1]\cos\delta_1+\bar{\mathrm{s}}_2\,[\pm c_1][\pm c_2]-\bar{\mathrm{s}}_3\,[\pm s_1]\sin\delta_1\Big]\Big\}\end{aligned} \tag{B.21}$$

$$\mathcal{K} \equiv K_1K_2K_\mathrm{S}$$

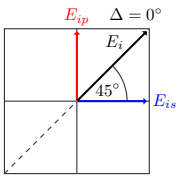

Empty-channel detector intensities *with* retarder

Retarder calibration measurements of ψ_{Ret} and δ_{Ret} correspond to a sample measurement in which the retarder acts as sample. Detector intensities $\mathcal{R}(\alpha_1, \alpha_2)$ can therefore be obtained from Eqs. (B.18)–(B.21) using the substitution

$$\mathcal{R}(\alpha_1, \alpha_2) = \mathcal{I}(\alpha_1, \alpha_2)\Big|_{\Psi\to\psi_{\mathrm{Ret}},\, \Delta\to\delta_{\mathrm{Ret}},\, K_{\mathrm{S}}\to K_{\mathrm{R}}}. \tag{B.22}$$

Detector intensities of sample *with* retarder

With the help of the addition theorems

$$\begin{aligned} \cos\Delta\cos\delta - \sin\Delta\sin\delta &= \cos(\Delta+\delta)\,, \\ \sin\Delta\cos\delta + \cos\Delta\sin\delta &= \sin(\Delta+\delta)\,, \end{aligned} \tag{B.23}$$

one finds that the phase shifts of sample and retarder add up.

$$\begin{aligned} \widetilde{\mathcal{I}}\big(\big[\begin{smallmatrix}\square\\ \text{—}\end{smallmatrix}\big],\big[\begin{smallmatrix}\square\\ \text{—}\end{smallmatrix}\big]\big) = \widetilde{\mathcal{K}}\Big\{ &\big(1+\cos 2\Psi\cos 2\psi_{\mathrm{Ret}}\big)\Big[\bar{\mathrm{s}}_0\big(1+[\pm c_1][\pm c_2]\big)+\bar{\mathrm{s}}_1\,[\pm c_1\pm c_2]\Big] \\ &-\big(\cos 2\Psi+\cos 2\psi_{\mathrm{Ret}}\big)\Big[\bar{\mathrm{s}}_0\,[\pm c_1\pm c_2]+\bar{\mathrm{s}}_1\big(1+[\pm c_1][\pm c_2]\big)\Big]\Big\} \end{aligned} \tag{B.24}$$

$$\begin{aligned} \widetilde{\mathcal{I}}\big(\big[\begin{smallmatrix}\diagup\\ \diagdown\end{smallmatrix}\big],\big[\begin{smallmatrix}\diagup\\ \diagdown\end{smallmatrix}\big]\big) = \widetilde{\mathcal{K}}\Big\{ &\big(1+\cos 2\Psi\cos 2\psi_{\mathrm{Ret}}\big)\Big[\bar{\mathrm{s}}_0+\bar{\mathrm{s}}_2\,[\pm c_1]\Big] \\ &-\big(\cos 2\Psi+\cos 2\psi_{\mathrm{Ret}}\big)\Big[\bar{\mathrm{s}}_1\,[s_1]\cos\delta_1-\bar{\mathrm{s}}_3\,[\pm s_1]\sin\delta_1\Big] \\ &+\sin 2\Psi\sin 2\psi_{\mathrm{Ret}}\cos(\Delta+\delta_{\mathrm{Ret}})\Big[\bar{\mathrm{s}}_0\,[\pm c_1][\pm c_2]+\bar{\mathrm{s}}_2\,[\pm c_2]\Big] \\ &+\sin 2\Psi\sin 2\psi_{\mathrm{Ret}}\sin(\Delta+\delta_{\mathrm{Ret}})\Big[\bar{\mathrm{s}}_1\,[\pm s_1][\pm c_2]\sin\delta_1+\bar{\mathrm{s}}_3\,[s_1][\pm c_2]\cos\delta_1\Big]\Big\} \end{aligned} \tag{B.25}$$

$$\begin{aligned} \widetilde{\mathcal{I}}\big(\big[\begin{smallmatrix}\square\\ \text{—}\end{smallmatrix}\big],\big[\begin{smallmatrix}\diagup\\ \diagdown\end{smallmatrix}\big]\big) = \widetilde{\mathcal{K}}\Big\{ &\big(1+\cos 2\Psi\cos 2\psi_{\mathrm{Ret}}\big)\Big[\bar{\mathrm{s}}_0+\bar{\mathrm{s}}_1\,[\pm c_1]\Big] \\ &-\big(\cos 2\Psi+\cos 2\psi_{\mathrm{Ret}}\big)\Big[\bar{\mathrm{s}}_0\,[\pm c_1]+\bar{\mathrm{s}}_1\Big] \\ &+\sin 2\Psi\sin 2\psi_{\mathrm{Ret}}\cos(\Delta+\delta_{\mathrm{Ret}})\Big[\bar{\mathrm{s}}_2\,[s_1][\pm c_2]\cos\delta_1+\bar{\mathrm{s}}_3\,[\pm s_1][\pm c_2]\sin\delta_1\Big] \\ &+\sin 2\Psi\sin 2\psi_{\mathrm{Ret}}\sin(\Delta+\delta_{\mathrm{Ret}})\Big[\bar{\mathrm{s}}_3\,[s_1][\pm c_2]\cos\delta_1-\bar{\mathrm{s}}_2\,[\pm s_1][\pm c_2]\sin\delta_1\Big]\Big\} \end{aligned} \tag{B.26}$$

$$\begin{aligned} \widetilde{\mathcal{I}}\big(\big[\begin{smallmatrix}\diagup\\ \diagdown\end{smallmatrix}\big],\big[\begin{smallmatrix}\square\\ \text{—}\end{smallmatrix}\big]\big) = \widetilde{\mathcal{K}}\Big\{ &\big(1+\cos 2\Psi\cos 2\psi_{\mathrm{Ret}}\big)\Big[\bar{\mathrm{s}}_0+\bar{\mathrm{s}}_1\,[s_1][\pm c_2]\cos\delta_1+\bar{\mathrm{s}}_2\,[\pm c_1]-\bar{\mathrm{s}}_3\,[\pm s_1][\pm c_2]\sin\delta_1\Big] \\ &-\big(\cos 2\Psi+\cos 2\psi_{\mathrm{Ret}}\big)\Big[\bar{\mathrm{s}}_0\,[\pm c_2]+\bar{\mathrm{s}}_1\,[s_1]\cos\delta_1+\bar{\mathrm{s}}_2\,[\pm c_1][\pm c_2]-\bar{\mathrm{s}}_3\,[\pm s_1]\sin\delta_1\Big]\Big\} \end{aligned} \tag{B.27}$$

$$\widetilde{\mathcal{K}} \equiv K_1 K_2 K_{\mathrm{S}} K_{\mathrm{R}}$$

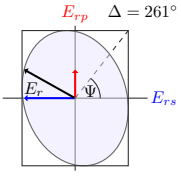

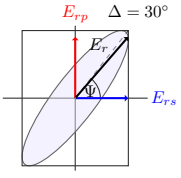

$\tan\Psi$ and Δ from rotating-polarizer or rotating-analyzer measurements:
In addition to $\tan\Psi$ measurements with parallel polarizers, equations for measurements with fixed analyzer or polarizer are now presented. If the detector exhibits polarization-dependent properties, it is preferable to measure $\tan\Psi$ with a fixed analyzer at different polarizer positions. The analyzer, then, is commonly set to 45° or 135°. For strong or varying source polarization and "benign detectors" on the other hand, the polarizer is held fixed at 45°, while the analyzer is being rotated. This measuring mode is important, for example, for measurements at a synchrotron (BESSY II) where the beam properties usually show strong time dependence.

The following equations show intensity combinations for the cases of rotating-polarizer and rotating-analyzer with 0°/90° and 45°/135° azimuths of the non-fixed polarizer.

Rotating polarizer:

$$\frac{\mathcal{I}(\,\mathbb{I}\,,\diagdown)-\mathcal{I}(=,\diagdown)}{\mathcal{I}(\,\mathbb{I}\,,\diagdown)+\mathcal{I}(=,\diagdown)}=\frac{c_1\left[\frac{\bar{\mathrm{s}}_1}{\bar{\mathrm{s}}_0}-\cos 2\Psi\right]+s_1c_2\sin\delta_1\left[-\frac{\bar{\mathrm{s}}_3}{\bar{\mathrm{s}}_0}\sin 2\Psi\cos\Delta+\frac{\bar{\mathrm{s}}_2}{\bar{\mathrm{s}}_0}\sin 2\Psi\sin\Delta\right]}{1-\frac{\bar{\mathrm{s}}_1}{\bar{\mathrm{s}}_0}\cos 2\Psi+s_1c_2\cos\delta_1\left[-\frac{\bar{\mathrm{s}}_2}{\bar{\mathrm{s}}_0}\sin 2\Psi\cos\Delta-\frac{\bar{\mathrm{s}}_3}{\bar{\mathrm{s}}_0}\sin 2\Psi\sin\Delta\right]} \tag{B.28}$$

$$\frac{\mathcal{I}(\diagdown,\diagdown)-\mathcal{I}(\diagup,\diagdown)}{\mathcal{I}(\diagdown,\diagdown)+\mathcal{I}(\diagup,\diagdown)}=\frac{c_1\left[\frac{\bar{\mathrm{s}}_2}{\bar{\mathrm{s}}_0}-\sin 2\Psi\cos\Delta\,c_2\right]+s_1\sin\delta_1\left[\frac{\bar{\mathrm{s}}_3}{\bar{\mathrm{s}}_0}\cos 2\Psi-\frac{\bar{\mathrm{s}}_1}{\bar{\mathrm{s}}_0}\sin 2\Psi\sin\Delta\,c_2\right]}{-1+\frac{\bar{\mathrm{s}}_2}{\bar{\mathrm{s}}_0}\sin 2\Psi\cos\Delta\,c_2+s_1\cos\delta_1\left[\frac{\bar{\mathrm{s}}_1}{\bar{\mathrm{s}}_0}\cos 2\Psi+\frac{\bar{\mathrm{s}}_3}{\bar{\mathrm{s}}_0}\sin 2\Psi\sin\Delta\,c_2\right]} \tag{B.29}$$

Rotating analyzer:

$$\frac{\mathcal{I}(\diagup,\,\mathbb{I}\,)-\mathcal{I}(\diagup,=)}{\mathcal{I}(\diagup,\,\mathbb{I}\,)+\mathcal{I}(\diagup,=)}=-\frac{c_2\left(\cos 2\Psi\left[1+\frac{\bar{\mathrm{s}}_2}{\bar{\mathrm{s}}_0}c_1\right]+s_1\left[-\frac{\bar{\mathrm{s}}_1}{\bar{\mathrm{s}}_0}\cos\delta_1+\frac{\bar{\mathrm{s}}_3}{\bar{\mathrm{s}}_0}\sin\delta_1\right]\right)}{1+\frac{\bar{\mathrm{s}}_2}{\bar{\mathrm{s}}_0}c_1-\cos 2\Psi\,s_1\left[\frac{\bar{\mathrm{s}}_1}{\bar{\mathrm{s}}_0}\cos\delta_1-\frac{\bar{\mathrm{s}}_3}{\bar{\mathrm{s}}_0}\sin\delta_1\right]} \tag{B.30}$$

$$\frac{\mathcal{I}(\diagup,\diagup)-\mathcal{I}(\diagup,\diagdown)}{\mathcal{I}(\diagup,\diagup)+\mathcal{I}(\diagup,\diagdown)}=\frac{c_2\left(\sin 2\Psi\cos\Delta\left[\frac{\bar{\mathrm{s}}_2}{\bar{\mathrm{s}}_0}+c_1\right]+\sin 2\Psi\sin\Delta\,s_1\left[\frac{\bar{\mathrm{s}}_3}{\bar{\mathrm{s}}_0}\cos\delta_1+\frac{\bar{\mathrm{s}}_1}{\bar{\mathrm{s}}_0}\sin\delta_1\right]\right)}{1+\frac{\bar{\mathrm{s}}_2}{\bar{\mathrm{s}}_0}c_1-\cos 2\Psi\left[\frac{\bar{\mathrm{s}}_1}{\bar{\mathrm{s}}_0}s_1\cos\delta_1-\frac{\bar{\mathrm{s}}_3}{\bar{\mathrm{s}}_0}s_1\sin\delta_1\right]} \tag{B.31}$$

Equations (B.28)–(B.31) can be solved for $\tan\Psi$ and $\cos\Delta$ with prior knowledge of the imperfection parameters c_i, s_i, and δ_i as well as the Stokes parameters $\bar{\mathrm{s}}_0$, $\bar{\mathrm{s}}_1$, $\bar{\mathrm{s}}_2$, and $\bar{\mathrm{s}}_3$; see Subsection 1. in Section 2.1.4.b). Similar equations are obtained for measurements with retarder, which are necessary for determinating Δ between 0° and 360°.

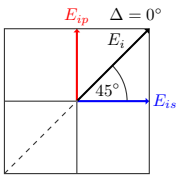

C. Abelès transfer-matrix method

The Abelès method allows one to calculate p- and s-polarized reflection and transmission coefficients of an isotropic multi-layer stack with isotropic ambient and substrate. Free parameters of the model are the layer thicknesses d_j and complex refractive indices $N_j = \sqrt{\varepsilon_j}$, together with the ambient and substrate parameters $N_a = \sqrt{\varepsilon_a}$ and $N_s = \sqrt{\varepsilon_s}$. The 2×2 transfer matrices of ambient, substrate, and layers read [1, 6, 310]

$$\mathcal{T}^{p,\,s}_{\mathrm{Amb}} = \begin{bmatrix} q_{p,s}(\varphi_a, N_a) & 1 \\ q_{p,s}(\varphi_a, N_a) & -1 \end{bmatrix}, \tag{C.1}$$

$$\mathcal{T}^{p,\,s}_{\mathrm{Sub}} = \begin{bmatrix} 1 & 0 \\ q_{p,s}(\varphi_s, N_s) & 0 \end{bmatrix}, \tag{C.2}$$

$$\mathcal{T}^{p,\,s}_{j} = \begin{bmatrix} \cos\beta_j & i\sin\beta_j \,/\, q_{p,s}(\varphi_j, N_j) \\ i\sin\beta_j \cdot q_{p,s}(\varphi_j, N_j) & \cos\beta_j \end{bmatrix}, \tag{C.3}$$

with the abbreviations

$$q_p(\varphi, N) \equiv \cos\varphi \,/\, N, \qquad q_s(\varphi, N) \equiv \cos\varphi \cdot N, \tag{C.4}$$

and the angular phase thickness β_j of the j-th layer,

$$\beta_j = 2\pi\,\tilde{\nu}\,\cos\varphi_j\,N_j\,d_j\,. \tag{C.5}$$

The product $N_j\,d_j$ is often referred to as the optical thickness of the layer. The transmission angles φ_j inside the j-th layer are calculated by Snell's law, $N_j \sin\varphi_j = N_{j+1}\sin\varphi_{j+1}$. Finally, reflection and transmission coefficients as well as reflectivity and transmittance in p and s direction are calculated from Eqs. (C.1)–(C.3) by [1, 6, 310]

$$r_p = \frac{\mathcal{T}^p_{21}}{\mathcal{T}^p_{11}}\,, \qquad R_p = |r_p|^2\,, \qquad t_p = \frac{2q_p(\varphi_a, N_a)}{\mathcal{T}^p_{11}}\,, \qquad T_p = \frac{\mathrm{Re}\big(q_p(\varphi_s, N_s)\big)}{\mathrm{Re}\big(q_p(\varphi_a, N_a)\big)}\,|t_p|^2\,, \tag{C.6}$$

$$r_s = \frac{\mathcal{T}^s_{21}}{\mathcal{T}^s_{11}}\,, \qquad R_s = |r_s|^2\,, \qquad t_s = \frac{2q_s(\varphi_a, N_a)}{\mathcal{T}^s_{11}}\,, \qquad T_s = \frac{\mathrm{Re}\big(q_s(\varphi_s, N_s)\big)}{\mathrm{Re}\big(q_s(\varphi_a, N_a)\big)}\,|t_s|^2\,. \tag{C.7}$$

The ellipsometric ratios $\rho = \tan\Psi \cdot \mathrm{e}^{i\Delta} = r_p/r_s$ and $\tilde{\rho} = \tan\tilde{\Psi} \cdot \mathrm{e}^{i\tilde{\Delta}} = t_p/t_s$ are readily computed using the above equations. Unpolarized reflectivity and transmittance are given

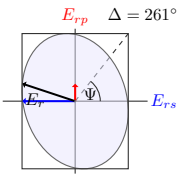

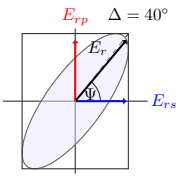

by

$$R = \frac{R_p + R_s}{2} \quad \text{and} \quad T = \frac{T_p + T_s}{2}\,. \tag{C.8}$$

If the substrate cannot be regarded as semi-infinite and reflections from its backside have to be considered, then—according to the sample geometry shown in Fig. 2.17—the substrate has to be treated as a regular layer with defined thickness d_s, and the ambient (usually air) is being promoted to the new substrate.

Taylor expansion of $\mathcal{T}_j^{p,\,s}$ reveals that transfer matrices of very thin layers commute to first order. Although ellipsometry is very sensitive to thin-film layer thicknesses, this shows that it is very difficult to determine the order of layers in unknown thin-film layer stacks. Systematic sample characterization after each preparation step is therefore preferred when dealing with complex-structured samples, if possible.

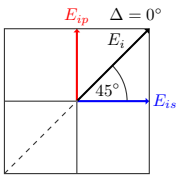

D. VIS-ellipsometric pre-characterization of spin-coated polymer films

Figure D.1 displays measured and joint-fitted Ψ and Δ spectra of the spin-coated PGMA and PNIPAAm films that were introduced in Section 3.1.2. Films were prepared on Si (111) and Au substrates and measured at three different angles of incidence.

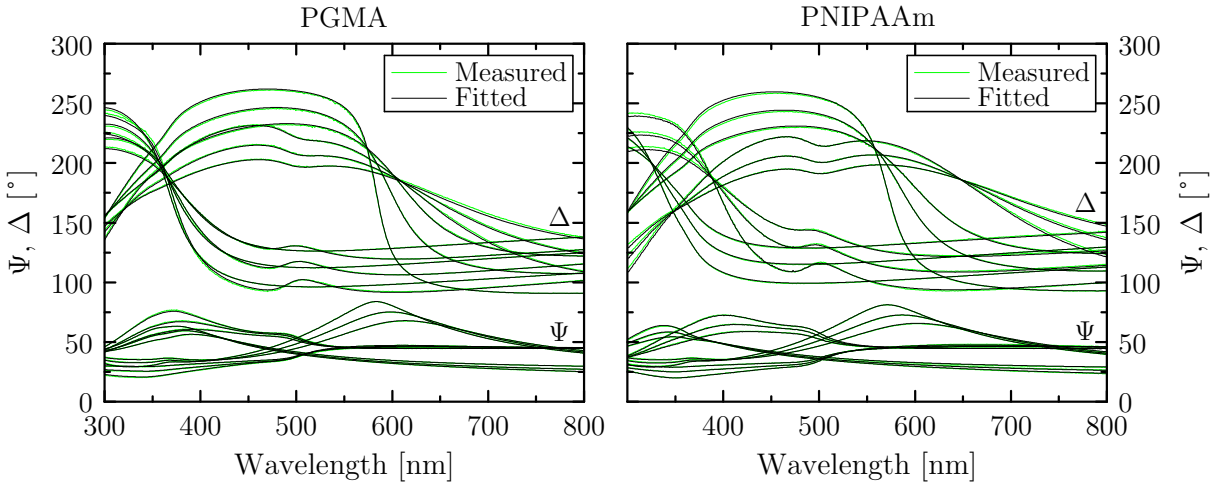

Figure D.1: Measured (black lines) and fitted (green lines) Ψ and Δ spectra of spin-coated PGMA (left) and PNIPAAm (right) films at 65°, 60°, and 55° angle of incidence. For both polymers, a joint fit on polymer thicknesses and Cauchy parameters was performed using measured spectra from two films on silicon (111) and two films on gold substrates (see Tab. 3.3).

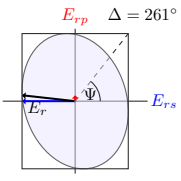

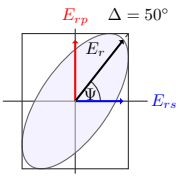

E. Additional homogeneity tests with infrared microscopy and AFM

Figure E.1 shows a reflectivity linescan of the 116 nm thick PNIPAAm film on gold substrate corresponding to the six left-most visually mapped fields in Fig. 3.2 (see Section 3.1.3.). Small band-amplitude changes confirm the slight decrease in film thickness towards the edges of the sample.

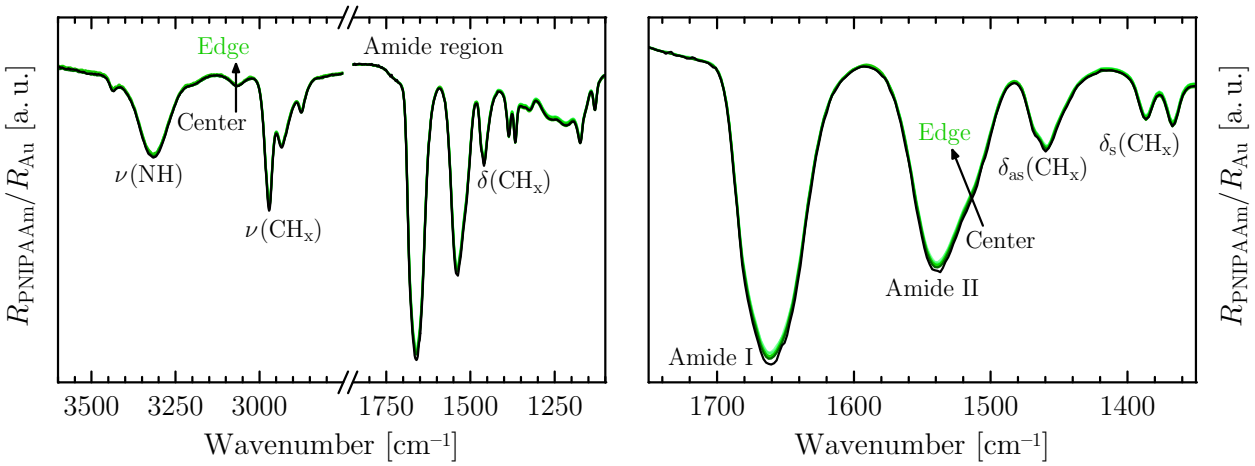

Figure E.1: Infrared-microscopy linescan of the 116 nm thick PNIPAAm film on Au corresponding to the centers of the first six fields in Fig. 3.2. Baselines were corrected to coincide between 1900–2250 cm^{-1}. Small amplitude changes in the vibrational bands of PNIPAAm amount to a decrease in mean film thickness of approximately 4 nm towards the edges of the sample.

Complementary to homogeneity tests on spin-coated PNIPAAm films on gold, linescans were also performed on PNIPAAm films on silicon (111) wedges using visible and infrared microscopy. Figure E.2 shows a visible-microscopy map of the 117 nm thick PNIPAAm film over an area of 6030 µm × 500 µm.

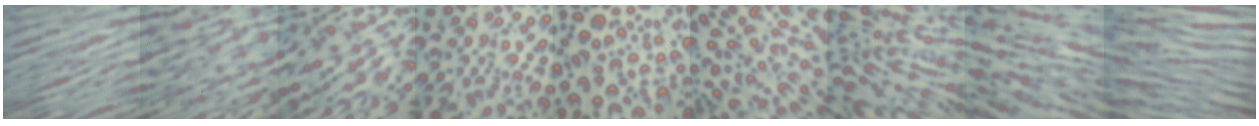

Figure E.2: Visible-microscopy map (9 · 670 µm × 500 µm) of the 117 nm thick PNIPAAm film on Si.

Similar artifacts from the spin-coating process are found as described for PNIPAAm films on gold. A homogeneity linescan with IR microscopy, as shown in Fig. E.3, confirms a small decrease in film thickness towards the edges of the sample. The characteristic baseline slope caused by thin-film interference [129] reduces. Concomitantly, slight decreases in amplitude of the δ(CH$_x$) and ν(CH$_x$) vibrational bands are monitored when comparing the peak heights

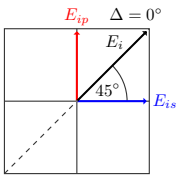

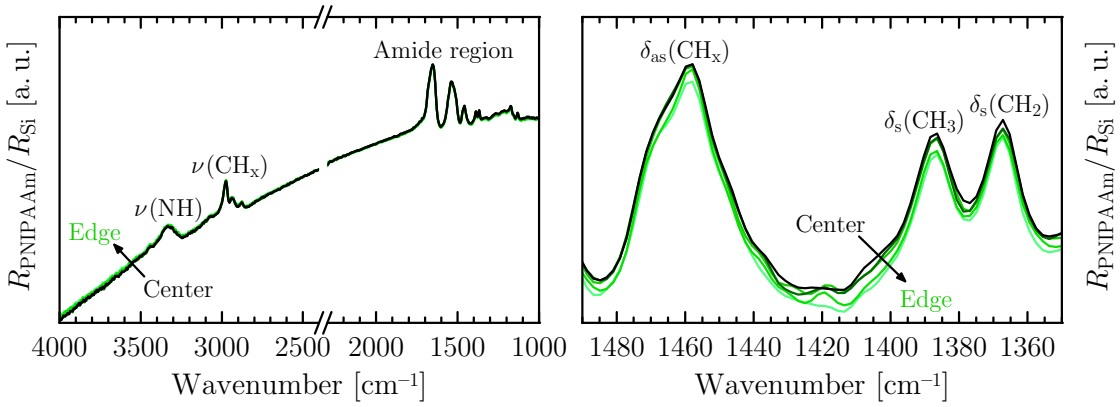

Figure E.3: Infrared-microscopy linescan of the 117 nm thick PNIPAAm film on Si corresponding to the centers of the first five fields in Fig. E.2. Baselines were corrected to coincide between 1900–2250 cm^{-1}. Small amplitude changes in the δ(CH$_x$) region as well as changes in baseline slope correlate with a decreasing film thickness of a few nanometers towards the edge of the sample.

using Lorentzian curve fits. Note that for this sample, the larger amide and ν(NH) bands proved to be unsuitable for analysis due to minute residues of water-vapor absorption.

AFM measurements (Fig. E.4) in the center of the sample as well as near the edges indicate that the film is less homogenous on a microscopic scale compared to PNIPAAm films on gold substrate. The center area of the sample exhibits thickness variations of about 35 nm, but the film still shows inhomogeneities of approximately ±5 nm with increasing radial distance from the center, which is problematic for accurate ellipsometric phase measurements Δ.

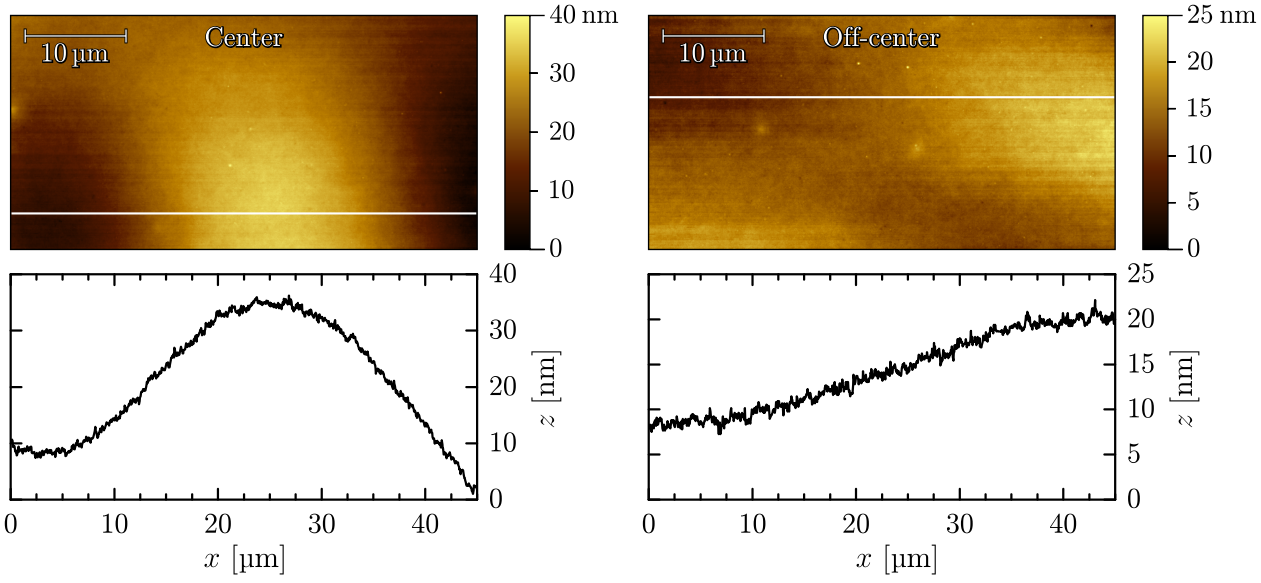

Figure E.4: AFM maps of thickness variations z of the 117 nm thick PNIPAAm film on Si(111). The left/right map correspond to spots within the 5th/9th visually mapped fields in Fig. E.2.

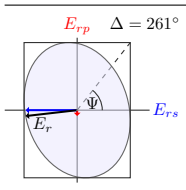

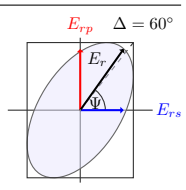

F. Evaporating films of normal water

Similar to in-situ infrared-microscopy measurements of evaporating D_2O films from spin-coated deuterated PNIPAAm layers in Section 3.1.5.a), evaporation of H_2O drops from undeuterated films was also monitored, as shown in Fig. F.1. Upon evaporation, a quick conversion from amide–water-interacted to amide–amide-interacted and free C=O and N−H groups is observed. This is indicated, on the one hand, by a decrease of the amide–water-hydrogen-bonded N−H-bending contribution at 1554 cm^{-1} with a simultaneous increase of the amide–amide-bonded and free contributions at 1544 cm^{-1} and 1509 cm^{-1}, respectively. In wet state, almost no free N−H groups are present, as can be seen from the small amplitudes of free N−H-bending and -stretching at respectively 1509 cm^{-1} and 3437 cm^{-1}. On the other hand, stretching vibrations of dihydrogen-bonded C=O at 1625 cm^{-1}, which are clearly visible in the presence of the water film, vanish in dry state, while contributions from free C=O groups at 1680 cm^{-1} increase in amplitude. Since amide I is strongly overlapped by the water-bending vibration $\delta(H_2O)$ at about 1650 cm^{-1}, it is difficult—without an appropriate optical model—to evaluate the relative contributions of single-bonded, mixed-bonded, and double-bonded C=O groups to the amide I band envelope (see Section 3.1.5.a), the corresponding stretching vibrations of which occur at 1664 cm^{-1}, 1660 cm^{-1}, and 1645 cm^{-1}.

Next to the changing band composition of amide I and II, the strong hydration of the film also manifests in shifts of $\nu(CH_x)$ and $\delta(CH_x)$ to higher wavenumbers compared to the dry state. Furthermore, the amide B resonance at about 3066 cm^{-1} between ν(NH) and the first overtone of amide II is strongly enhanced due to the downward-shifting ν(NH) band and the upward-shifting amide II band.

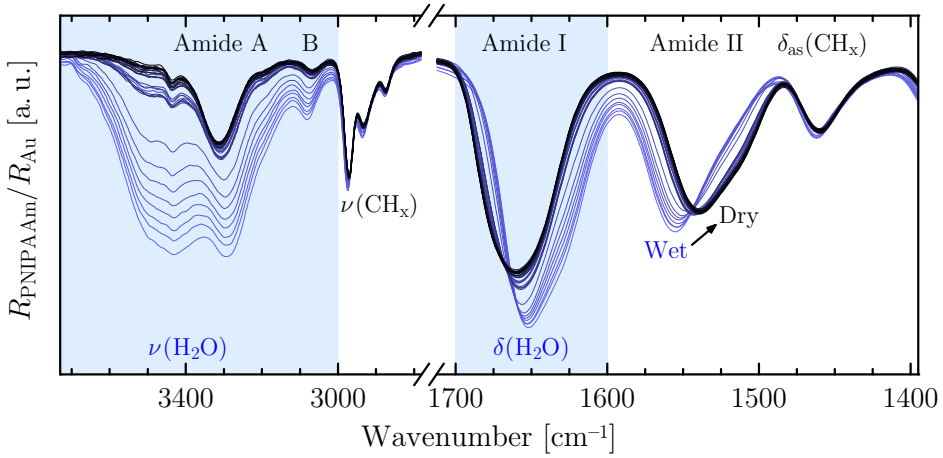

Figure F.1: Evaporating H_2O drop from an undeuterated, ≈ 160 nm thick, PNIPAAm film on Au substrate measured over a period of 75 min. A jump in $\nu(H_2O)$ and amide I/II amplitudes indicates a quick release of water. A second smaller jump coincides with a point where the dry-air purge rate of the microscope chamber was increased. All spectra were corrected for water-vapor absorption.

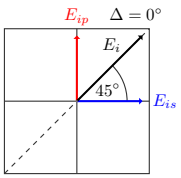

G. Hydration of amide groups at higher humidity

The band shapes of amide I and II that are measured for aqueous PNIPAAm solutions [50] suggest that the majority of PNIPAAm's carbonyl oxygen atoms is indeed solvated by two water molecules. In order to establish the transition from monohydrogen- or mixed-bonded C=O groups to dihydrogen-bonded groups, brush measurements at high water content are necessary. For this purpose, the drying process of the $d_{\mathrm{dry}} = 12.5\,\mathrm{nm}$ thick brush was monitored within the in-situ cell, which allowed for higher humidities than 35% and, thus, for a smooth transition between wet, humid, and dry state.

Ellipsometric measurements were performed at 25 °C, starting with an initial dry-state measurement for reference purposes, followed by a wet-state measurement for which the cell filled with liquid H_2O. The dry state was then achieved by emptying the cell and slowly purging it with dry air over a period of 732 min. Time-dependent $\tan\Psi$ spectra referenced to the initial dry-state spectrum are plotted in Fig. G.1.

At first, the vibrational spectrum is dominated by the stretching, bending, and libration vibrations of liquid water, marked in light blue in the left panel. Importantly for a quantitative as well as a qualitative band analysis, the water bands are of sigmoidal shape at high water concentrations and cannot be interpreted as simple absorption-like bands. This affirms the importance of optical simulations for a correct understanding of infrared spectra.

In the right panel, the water-content is sufficiently low, such that upward- and downward-pointing peaks respectively indicate increasing and decreasing band components with respect

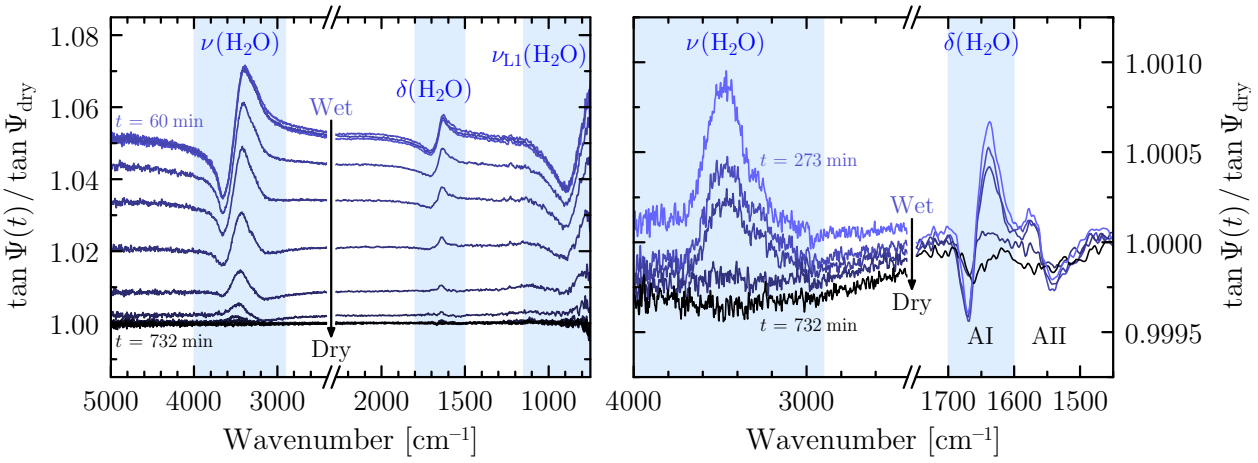

Figure G.1: Drying of the $d_{\mathrm{dry}} = 12.5\,\mathrm{nm}$ thin PNIPAAm brush within the in-situ cell. $\tan\Psi$ spectra are referenced to an initial dry-state spectrum obtained before filling the in-situ cell with water. Single-cycle spectra (left) were recorded over a period of 1 min each. Spectra at the end of the drying process (right) were averaged over 40 min. Strong sigmoidal shapes of the amide I (AI) and amide II (AII) bands indicate substantial changes in polymer–water and polymer–polymer interactions.

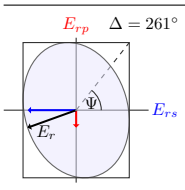

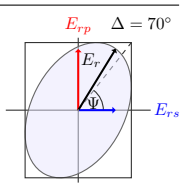

to the dry state. Downward-pointing peaks are observed at about 1670 cm^{-1} corresponding to free and single-bonded C=O groups as well as around 1542 cm^{-1} and 1509 cm^{-1} corresponding to single-bonded and free N−H groups, respectively. Water-bonded N−H groups correlate with the upward-pointing peak at about 1565 cm^{-1}. The strongly upward-pointing peak around 1635 cm^{-1} contains major contributions from dihydrogen-bonded C=O groups (1628 cm^{-1}), but still some small contributions from mixed-bonded groups (1657 cm^{-1}) and possibly double-bonded groups (1644 cm^{-1}). The peak also contains a non-negligible contribution from the water-bending vibration at about 1650 cm^{-1}. This amide I composition shows the tendency of the C=O groups to form hydrogen bonds with two water molecules, instead of one, at higher water contents.

The sigmoidal shape of amide II confirms the strong hydration of the brush. Accordingly, the two dips in the $\nu(H_2O)$ bands at approximately 3290 cm^{-1} and 3080 cm^{-1} show the strongly enhanced Fermi-resonance between N−H-stretching (amide A) and the first overtone of amide II (amide B).

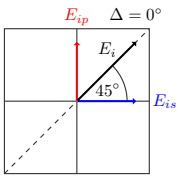

Bibliography

[1] **Röseler, A.**, *Infrared Spectroscopic Ellipsometry*. Akademie-Verlag Berlin, 1990, ISBN: 3-05-500623-2, http://d-nb.info/910758638. (Cited on pages 1, 11, 12, 16, 18, 19, 20, 28, 145, 146, and 153).

[2] **Röseler, A.**, "Spectroscopic ellipsometry in the infrared," *Infrared Physics* **1981**, 21 (6), 349–355, DOI: 10.1016/0020-0891(81)90042-7. (Cited on pages 1 and 11).

[3] **Röseler, A.**, *Spectroscopic Infrared Ellipsometry*, in *Handbook of Ellipsometry*, Tompkins, H. G.; Irene, E. A. (Editors). William Andrew, Inc., Norwich, 2005. ISBN: 978-0-8155-1499-2, http://www.sciencedirect.com/science/book/9780815514992. (Cited on pages 1, 12, 13, 19, and 26).

[4] **Röseler, A.; Korte, E.-H.**, *Infrared Spectroscopic Ellipsometry*, in *Handbook of Vibrational Spectroscopy*, Chalmers, J. M.; Griffiths, P. R. (Editors). John Wiley & Sons, Ltd, Chichester, 2006. ISBN: 978-0-471-98847-2, DOI: 10.1002/0470027320.s2208. (Cited on pages 1, 10, 13, and 19).

[5] **Azzam, R. M. A.; Bashara, N. M.**, *Ellipsometry and Polarized Light*. North-Holland Publ. Co., Amsterdam, 1977, ISBN: 0-7204-0694-3. (Cited on pages 1, 7, 8, 10, and 44).

[6] **Tompkins, H. G.; Irene, E. A.**, *Handbook of Ellipsometry*. William Andrew, Inc., Norwich, 2005, ISBN: 978-0-8155-1499-2, http://www.sciencedirect.com/science/book/9780815514992. (Cited on pages 1, 7, 8, 10, 20, 26, 37, 43, and 153).

[7] **Schubert, M.**, *Infrared Ellipsometry on Semiconductor Layer Structures*. Springer Berlin Heidelberg, 2005, ISBN: 978-3-540-23249-0, DOI: 10.1007/b11964. (Cited on pages 1, 7, and 44).

[8] **Fujiwara, H.**, *Spectroscopic Ellipsometry: Principles and Applications*. John Wiley & Sons, Ltd, Chichester, 2007, ISBN: 978-0-470-01608-4, DOI: 10.1002/9780470060193. (Cited on pages 1, 7, 8, 10, 37, 39, and 43).

[9] **Losurdo, M.; Hingerl, K.**, *Ellipsometry at the Nanoscale*. Springer Berlin Heidelberg, 2013, ISBN: 978-3-642-33955-4, DOI: 10.1007/978-3-642-33956-1. (Cited on pages 1 and 7).

[10] **Hinrichs, K.; Eichhorn, K.-J.**, *Ellipsometry of Functional Organic Surfaces and Films*. Springer Berlin, 2014, ISBN: 978-3-642-40127-5, DOI: 10.1007/978-3-642-40128-2. (Cited on pages 1 and 7).

[11] **Hinrichs, K.; Tsankov, D.; Korte, E.-H.; Röseler, A.; Sahre, K.; Eichhorn, K.-J.**, "Comparative Study of an Anisotropic Polymer Layer by Infrared Spectroscopic Techniques," *Applied Spectroscopy* **2002**, 56 (6), 737–743, DOI: 10.1366/000370202760077694. (Cited on page 1).

[12] **Garcia-Caurel, E.; Drévillon, B.; De Martino, A.; Schwartz, L.**, "Application of Fourier Transform Infrared Ellipsometry to Assess the Concentration of Biological Molecules," *Applied Optics* **2002**, 41 (34), 7339–7345, DOI: 10.1364/AO.41.007339. (Cited on pages 1 and 7).

[13] **Hinrichs, K.; Röseler, A.; Gensch, M.; Korte, E.-H.**, "Structure analysis of organic films by mid-infrared ellipsometry," *Thin Solid Films* **2004**, 455–456, 266–271, DOI: 10.1016/j.tsf.2004.01.011. (Cited on page 1).

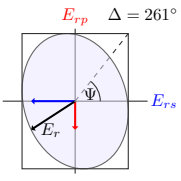

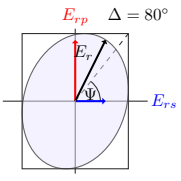

[14] **Hinrichs, K.; Gensch, M.; Nikonenko, N.; Pionteck, J.; Eichhorn, K.-J.**, "Spectroscopic Ellipsometry for Characterization of Thin Films of Polymer Blends," *Macromolecular Symposia* **2005**, 230 (1), 26–32, DOI: 10.1002/masy.200551138. (Cited on page 1).

[15] **Roodenko, K.; Mikhaylova, Y.; Ionov, L.; Gensch, M.; Stamm, M.; Minko, S.; Schade, U.; Eichhorn, K.-J.; Esser, N.; Hinrichs, K.**, "Ultrathin responsive polyelectrolyte brushes studied by infrared synchrotron mapping ellipsometry," *Applied Physics Letters* **2008**, 92 (10), 103102, DOI: 10.1063/1.2892132. (Cited on pages 1, 12, and 21).

[16] **Zhang, X.; Tretjakov, A.; Hovestädt, M.; Sun, G.; Syritski, V.; Reut, J.; Volkmer, R.; Hinrichs, K.; Rappich, J.**, "Electrochemical functionalization of gold and silicon surfaces by a maleimide group as a biosensor for immunological application," *Acta Biomaterialia* **2013**, 9 (3), 5838–5844, DOI: 10.1016/j.actbio.2012.10.022. (Cited on pages 1 and 7).

[17] **Hinrichs, K.; Gensch, M.; Röseler, A.; Esser, N.**, "Infrared ellipsometric study on the initial stages of oxide growth on Si(001)," *Journal of Physics: Condensed Matter* **2004**, 16 (39), S4335–S4343, DOI: 10.1088/0953-8984/16/39/008. (Cited on page 1).

[18] **Hinrichs, K.; Roodenko, K.; Rappich, J.**, "In situ monitoring of the etching of thin silicon oxide films in diluted NH_4F by IR ellipsometry," *Electrochemistry Communications* **2008**, 10 (2), 315–318, DOI: 10.1016/j.elecom.2007.12.014. (Cited on pages 1, 44, 76, 92, and 111).

[19] **Intelmann, C. M.; Hinrichs, K.; Syritski, V.; Yang, F.; Rappich, J.**, "Recombination Behaviour at the Ultrathin Polypyrrole Film/Silicon Interface Investigated by *In-situ* Pulsed Photoluminescence," *Japanese Journal of Applied Physics* **2008**, 47 (1), 554–557, DOI: 10.1143/JJAP.47.554. (Cited on pages 1 and 7).

[20] **Mikhaylova, Y.; Ionov, L.; Rappich, J.; Gensch, M.; Esser, N.; Minko, S.; Eichhorn, K.-J.; Stamm, M.; Hinrichs, K.**, "In Situ Infrared Ellipsometric Study of Stimuli-Responsive Mixed Polyelectrolyte Brushes," *Analytical Chemistry* **2007**, 79 (20), 7676–7682, DOI: 10.1021/ac070853a. (Cited on pages 1, 2, 7, 10, 14, 104, 112, and 124).

[21] **Hinrichs, K.; Aulich, D.; Ionov, L.; Esser, N.; Eichhorn, K.-J.; Motornov, M.; Stamm, M.; Minko, S.**, "Chemical and Structural Changes in a pH-Responsive Mixed Polyelectrolyte Brush Studied by Infrared Ellipsometry," *Langmuir* **2009**, 25 (18), 10987–10991, DOI: 10.1021/la901219f. (Cited on pages 1, 2, 7, and 124).

[22] **Aulich, D.; Hoy, O.; Luzinov, I.; Eichhorn, K.-J.; Stamm, M.; Gensch, M.; Schade, U.; Esser, N.; Hinrichs, K.**, "In-situ IR synchrotron mapping ellipsometry on stimuli-responsive PAA-b-PS/PEG mixed polymer brushes," *physica status solidi (c)* **2010**, 7 (2), 197–199, DOI: 10.1002/pssc.200982492. (Cited on pages 1, 7, 21, and 124).

[23] **Aulich, D.; Hoy, O.; Luzinov, I.; Brücher, M.; Hergenröder, R.; Bittrich, E.; Eichhorn, K.-J.; Uhlmann, P.; Stamm, M.; Esser, N.; Hinrichs, K.**, "In Situ Studies on the Switching Behavior of Ultrathin Poly(acrylic acid) Polyelectrolyte Brushes in Different Aqueous Environments," *Langmuir* **2010**, 26 (15), 12926–12932, DOI: 10.1021/la101762f. (Cited on pages 1, 3, 7, 51, 132, 133, 136, 137, 139, and 140).

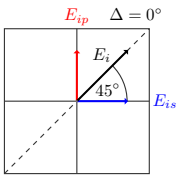

[24] **Hoy, O.; Zdyrko, B.; Lupitskyy, R.; Sheparovych, R.; Aulich, D.; Wang, J.; Bittrich, E.; Eichhorn, K.-J.; Uhlmann, P.; Hinrichs, K.; Müller, M.; Stamm, M.; Minko, S.; Luzinov, I.**, "Synthetic Hydrophilic Materials with Tunable Strength and a Range of Hydrophobic Interactions," *Advanced Functional Materials* **2010**, 20 (14), 2240–2247, DOI: 10.1002/adfm.201000170. (Cited on pages 1 and 7).

[25] **Furchner, A.; Bittrich, E.; Uhlmann, P.; Eichhorn, K.-J.; Hinrichs, K.**, "In-situ characterization of the temperature-sensitive swelling behavior of poly(*N*-isopropylacrylamide) brushes by infrared and visible ellipsometry," *Thin Solid Films* **2013**, 541, 41–45, DOI: 10.1016/j.tsf.2012.10.135. (Cited on pages 1, 7, 15, 29, 97, 104, 122, and 123).

[26] **Bittrich, E.; Burkert, S.; Müller, M.; Eichhorn, K.-J.; Stamm, M.; Uhlmann, P.**, "Temperature-Sensitive Swelling of Poly(*N*-isopropylacrylamide) Brushes with Low Molecular Weight and Grafting Density," *Langmuir* **2012**, 28 (7), 3439–3448, DOI: 10.1021/la204230a. (Cited on pages 1, 2, 4, 6, 7, 10, 11, 56, 81, 83, 84, 96, 97, 100, 101, 104, 119, 120, and 121).

[27] **Ionov, L.; Houbenov, N.; Sidorenko, A.; Stamm, M.; Luzinov, I.; Minko, S.**, "Inverse and Reversible Switching Gradient Surfaces from Mixed Polyelectrolyte Brushes," *Langmuir* **2004**, 20 (23), 9916–9919, DOI: 10.1021/la048158a. (Cited on pages 1, 2, and 124).

[28] **Currie, E. P. K.; Sieval, A. B.; Fleer, G. J.; Cohen Stuart, M. A.**, "Polyacrylic Acid Brushes: Surface Pressure and Salt-Induced Swelling," *Langmuir* **2000**, 16 (22), 8324–8333, DOI: 10.1021/la991528o. (Cited on pages 1 and 133).

[29] **Lahann, J.; Mitragotri, S.; Tran, T.-N.; Kaido, H.; Sundaram, J.; Choi, I. S.; Hoffer, S.; Somorjai, G. A.; Langer, R.**, "A Reversibly Switching Surface," *Science* **2003**, 299 (5605), 371–374, DOI: 10.1126/science.1078933. (Cited on page 1).

[30] **Gupta, S.; Agrawal, M.; Uhlmann, P.; Simon, F.; Oertel, U.; Stamm, M.**, "Gold Nanoparticles Immobilized on Stimuli Responsive Polymer Brushes as Nanosensors," *Macromolecules* **2008**, 41 (21), 8152–8158, DOI: 10.1021/ma801557u. (Cited on page 1).

[31] **Tokarev, I.; Tokareva, I.; Minko, S.**, "Optical Nanosensor Platform Operating in Near-Physiological pH Range via Polymer-Brush-Mediated Plasmon Coupling," *ACS Applied Materials & Interfaces* **2011**, 3 (2), 143–146, DOI: 10.1021/am101250x. (Cited on page 1).

[32] **Akkahat, P.; Mekboonsonglarp, W.; Kiatkamjornwong, S.; Hoven, V. P.**, "Surface-Grafted Poly(acrylic acid) Brushes as a Precursor Layer for Biosensing Applications: Effect of Graft Density and Swellability on the Detection Efficiency," *Langmuir* **2012**, 28 (11), 5302–5311, DOI: 10.1021/la204542e. (Cited on page 1).

[33] **Motornov, M.; Sheparovych, R.; Tokarev, I.; Roiter, Y.; Minko, S.**, "Nonwettable Thin Films from Hybrid Polymer Brushes Can Be Hydrophilic," *Langmuir* **2007**, 23 (1), 13–19, DOI: 10.1021/la061737q. (Cited on page 1).

[34] **Roosjen, A.; Kaper, H. J.; van der Mei, H. C.; Norde, W.; Busscher, H. J.**, "Inhibition of adhesion of yeasts and bacteria by poly(ethylene oxide)-brushes on glass in a parallel plate flow chamber," *Microbiology* **2003**, 149 (11), 3239–3246, DOI: 10.1099/mic.0.26519-0. (Cited on page 1).

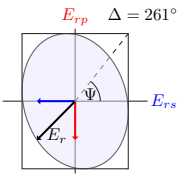

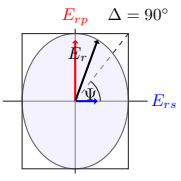

[35] **Cringus-Fundeanu, I.; Luijten, J.; van der Mei, H. C.; Busscher, H. J.; Schouten, A. J.**, "Synthesis and Characterization of Surface-Grafted Polyacrylamide Brushes and Their Inhibition of Microbial Adhesion," *Langmuir* **2007**, 23 (9), 5120–5126, DOI: 10.1021/la063531v. (Cited on page 1).

[36] **Nejadnik, M. R.; van der Mei, H. C.; Norde, W.; Busscher, H. J.**, "Bacterial adhesion and growth on a polymer brush-coating," *Biomaterials* **2008**, 29 (30), 4117–4121, DOI: 10.1016/j.biomaterials.2008.07.014. (Cited on page 1).

[37] **Zdyrko, B.; Klep, V.; Li, X.; Kang, Q.; Minko, S.; Wen, X.; Luzinov, I.**, "Polymer brushes as active nanolayers for tunable bacteria adhesion," *Materials Science and Engineering: C* **2009**, 29 (3), 680–684, DOI: 10.1016/j.msec.2008.12.017. (Cited on page 1).

[38] **Uhlmann, P.; Houbenov, N.; Brenner, N.; Grundke, K.; Burkert, S.; Stamm, M.**, "In-Situ Investigation of the Adsorption of Globular Model Proteins on Stimuli-Responsive Binary Polyelectrolyte Brushes," *Langmuir* **2007**, 23 (1), 57–64, DOI: 10.1021/la061557g. (Cited on pages 1, 2, and 124).

[39] **de Vos, W. M.; Biesheuvel, P. M.; de Keizer, A.; Kleijn, J. M.; Cohen Stuart, M. A.**, "Adsorption of the Protein Bovine Serum Albumin in a Planar Poly(acrylic acid) Brush Layer As Measured by Optical Reflectometry," *Langmuir* **2008**, 24 (13), 6575–6584, DOI: 10.1021/la8006469. (Cited on pages 1, 51, 124, 132, and 142).

[40] **Kizhakkedathu, J. N.; Janzen, J.; Le, Y.; Kainthan, R. K.; Brooks, D. E.**, "Poly(oligo(ethylene glycol)acrylamide) Brushes by Surface Initiated Polymerization: Effect of Macromonomer Chain Length on Brush Growth and Protein Adsorption from Blood Plasma," *Langmuir* **2009**, 25 (6), 3794–3801, DOI: 10.1021/la803690q. (Cited on pages 1 and 124).

[41] **Motornov, M.; Tam, T. K.; Pita, M.; Tokarev, I.; Katz, E.; Minko, S.**, "Switchable selectivity for gating ion transport with mixed polyelectrolyte brushes: approaching 'smart' drug delivery systems," *Nanotechnology* **2009**, 20 (43), 434006, DOI: 10.1088/0957-4484/20/43/434006. (Cited on page 1).

[42] **Luo, Y.-L.; Zhang, L.-L.; Xu, F.**, "Synthesis, thermo-responsive micellization and caffeine drug release of novel PBMA-b-PNIPAAm block polymer brushes," *Polymer Science Series A* **2012**, 54 (4), 270–281, DOI: 10.1134/S0965545X12040049. (Cited on page 1).

[43] **Heskins, M.; Guillet, J. E.**, "Solution Properties of Poly(N-isopropylacrylamide)," *Journal of Macromolecular Science: Part A – Chemistry* **1968**, A2 (8), 1441–1455, DOI: 10.1080/10601326808051910. (Cited on pages 1, 4, 96, and 101).

[44] **Kubota, K.; Fujishige, S.; Ando, I.**, "Solution Properties of Poly(*N*-isopropylacrylamide) in Water," *Polymer Journal* **1990**, 22 (1), 15–20, DOI: 10.1295/polymj.22.15. (Cited on pages 1, 4, 96, and 101).

[45] **Cheng, H.; Shen, L.; Wu, C.**, "LLS and FTIR Studies on the Hysteresis in Association and Dissociation of Poly(*N*-isopropylacrylamide) Chains in Water," *Macromolecules* **2006**, 39 (6), 2325–2329, DOI: 10.1021/ma052561m. (Cited on pages 1, 4, 63, 64, 96, 97, 100, and 101).

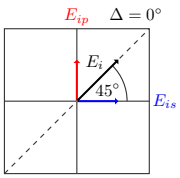

[46] **Burkert, S.; Bittrich, E.; Kuntzsch, M.; Müller, M.; Eichhorn, K.-J.; Bellmann, C.; Uhlmann, P.; Stamm, M.**, "Protein Resistance of PNIPAAm Brushes: Application to Switchable Protein Adsorption," *Langmuir* **2010**, 26 (3), 1786–1795, DOI: 10.1021/la902505q. (Cited on pages 1, 2, 7, 117, 119, 120, 122, 123, 124, and 130).

[47] **Xue, C.; Yonet-Tanyeri, N.; Brouette, N.; Sferrazza, M.; Braun, P. V.; Leckband, D. E.**, "Protein Adsorption on Poly(*N*-isopropylacrylamide) Brushes: Dependence on Grafting Density and Chain Collapse," *Langmuir* **2011**, 27 (14), 8810–8818, DOI: 10.1021/la2001909. (Cited on pages 1, 2, 83, 96, 124, and 130).

[48] **Xue, C.; Choi, B.-C.; Choi, S.; Braun, P. V.; Leckband, D. E.**, "Protein Adsorption Modes Determine Reversible Cell Attachment on Poly(*N*-isopropyl acrylamide) Brushes," *Advanced Functional Materials* **2012**, 22 (11), 2394–2401, DOI: 10.1002/adfm.201103056. (Cited on pages 1 and 124).

[49] **Halperin, A.; Kröger, M.**, "Thermoresponsive Cell Culture Substrates Based on PNIPAM Brushes Functionalized with Adhesion Peptides: Theoretical Considerations of Mechanism and Design," *Langmuir* **2012**, 28 (48), 16623–16637, DOI: 10.1021/la303443t. (Cited on pages 1 and 124).

[50] **Maeda, Y.; Higuchi, T.; Ikeda, I.**, "Change in Hydration State during the Coil–Globule Transition of Aqueous Solutions of Poly(*N*-isopropylacrylamide) as Evidenced by FTIR Spectroscopy," *Langmuir* **2000**, 16 (19), 7503–7509, DOI: 10.1021/la0001575. (Cited on pages 1, 4, 55, 56, 57, 63, 64, 65, 71, 73, 75, 81, 83, 94, 96, 97, 100, 101, 121, and 159).

[51] **Meersman, F.; Wang, J.; Wu, Y.; Heremans, K.**, "Pressure Effect on the Hydration Properties of Poly(*N*-isopropylacrylamide) in Aqueous Solution Studied by FTIR Spectroscopy," *Macromolecules* **2005**, 38 (21), 8923–8928, DOI: 10.1021/ma051582d. (Cited on pages 1, 55, 57, and 96).

[52] **Sun, B.; Lin, Y.; Wu, P.; Siesler, H. W.**, "A FTIR and 2D-IR Spectroscopic Study on the Microdynamics Phase Separation Mechanism of the Poly(*N*-isopropylacrylamide) Aqueous Solution," *Macromolecules* **2008**, 41 (4), 1512–1520, DOI: 10.1021/ma702062h. (Cited on pages 1 and 96).

[53] **Lai, H.; Wu, P.**, "A infrared spectroscopic study on the mechanism of temperature-induced phase transition of concentrated aqueous solutions of poly(N-isopropylacrylamide) and N-isopropylpropionamide," *Polymer* **2010**, 51 (6), 1404–1412, DOI: 10.1016/j.polymer.2010.01.036. (Cited on pages 1, 75, and 96).

[54] **Zhang, L. P.; Noda, I.; Wu, Y.**, "An application of concatenated 2D correlation spectroscopy: Exploration of the reversibility of the temperature-induced hydration variation of poly(*N*-isopropylmethacrylamide) in aqueous solution," *Journal of Molecular Structure* **2010**, 974 (1–3), 80–87, DOI: 10.1016/j.molstruc.2009.11.045. (Cited on pages 1, 63, and 96).

[55] **Ito, K.; Ujihira, Y.; Yamashita, T.; Horie, K.**, "Change in free volume during volume phase transition of poly(*N*-isopropylacrylamide) gel as studied by positron annihilation lifetimes: temperature dependence," *Polymer* **1999**, 40 (15), 4315–4323, DOI: 10.1016/S0032-3861(98)00657-0. (Cited on pages 1 and 96).

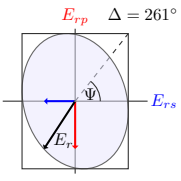

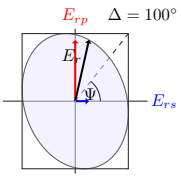

[56] **Okajima, T.; Harada, I.; Nishio, K.; Hirotsu, S.**, "Kinetics of volume phase transition in poly(N-isopropylacrylamide) gels," *The Journal of Chemical Physics* **2002**, 116 (20), 9068–9077, DOI: 10.1063/1.1473655. (Cited on pages 1, 63, and 96).

[57] **Wang, W.; Troll, K.; Kaune, G.; Metwalli, E.; Ruderer, M.; Skrabania, K.; Laschewsky, A.; Roth, S. V.; Papadakis, C. M.; Müller-Buschbaum, P.**, "Thin Films of Poly(*N*-isopropylacrylamide) End-Capped with *n*-Butyltrithiocarbonate," *Macromolecules* **2008**, 41 (9), 3209–3218, DOI: 10.1021/ma7027775. (Cited on pages 1, 63, and 96).

[58] **Harms, S.; Rätzke, K.; Faupel, F.; Egger, W.; Ravello, L.; Laschewsky, A.; Wang, W.; Müller-Buschbaum, P.**, "Free Volume and Swelling in Thin Films of Poly(*N*-isopropylacrylamide) End-Capped with *n*-Butyltrithiocarbonate," *Macromolecular Rapid Communications* **2010**, 31 (15), 1364–1367, DOI: 10.1002/marc.201000067. (Cited on pages 1, 63, and 96).

[59] **Sun, S.; Hu, J.; Tang, H.; Wu, P.**, "Chain Collapse and Revival Thermodynamics of Poly(*N*-isopropylacrylamide) Hydrogel," *The Journal of Physical Chemistry B* **2010**, 114 (30), 9761–9770, DOI: 10.1021/jp103818c. (Cited on pages 1, 63, and 96).

[60] **Hashimoto, C.; Nagamoto, A.; Maruyama, T.; Kariyama, N.; Irisa, Y.; Ikehata, A.; Ozaki, Y.**, "Hydration States of Poly(*N*-isopropylacrylamide) and Poly(*N*,*N*-diethylacrylamide) and Their Monomer Units in Aqueous Solutions with Lower Critical Solution Temperatures Studied by Infrared Spectroscopy," *Macromolecules* **2013**, 46 (3), 1041–1053, DOI: 10.1021/ma302317m. (Cited on pages 1, 4, 63, 64, 65, 66, 67, 81, and 96).

[61] **Daly, E.; Saunders, B. R.**, "A Study of the Effect of Electrolyte on the Swelling and Stability of Poly(*N*-isopropylacrylamide) Microgel Dispersions," *Langmuir* **2000**, 16 (13), 5546–5552, DOI: 10.1021/la991292o. (Cited on pages 1, 63, and 96).

[62] **Al-Manasir, N.; Zhu, K.; Kjøniksen, A.-L.; Knudsen, K. D.; Karlsson, G.; Nyström, B.**, "Effects of Temperature and pH on the Contraction and Aggregation of Microgels in Aqueous Suspensions," *The Journal of Physical Chemistry B* **2009**, 113 (32), 11115–11123, DOI: 10.1021/jp901121g. (Cited on pages 1 and 96).

[63] **Clarke, K. C.; Lyon, L. A.**, "Modulation of the Deswelling Temperature of Thermoresponsive Microgel Films," *Langmuir* **2013**, 29 (41), 12852–12857, DOI: 10.1021/la403280s. (Cited on pages 1, 63, and 96).

[64] **Liu, G.; Zhang, G.**, "Collapse and Swelling of Thermally Sensitive Poly(*N*-isopropylacrylamide) Brushes Monitored with a Quartz Crystal Microbalance," *The Journal of Physical Chemistry B* **2005**, 109 (2), 743–747, DOI: 10.1021/jp046903m. (Cited on pages 1 and 100).

[65] **Yim, H.; Kent, M. S.; Mendez, S.; Lopez, G. P.; Satija, S.; Seo, Y.**, "Effects of Grafting Density and Molecular Weight on the Temperature-Dependent Conformational Change of Poly(*N*-isopropylacrylamide) Grafted Chains in Water," *Macromolecules* **2006**, 39 (9), 3420–3426, DOI: 10.1021/ma0520949. (Cited on pages 2, 4, and 96).

[66] **Bittrich, E.; Burkert, S.; Eichhorn, K.-J.; Stamm, M.; Uhlmann, P.**, *Control of Protein Adsorption and Cell Adhesion by Mixed Polymer Brushes Made by the "Grafting-To" Approach*, in *Proteins at Interfaces III State of the Art*, Horbett, T.; Brash, J. L.; Norde, W. (Editors). American Chemical Society, Washington, DC, 2012. ISBN: 978-0-841-22796-5, DOI: 10.1021/bk-2012-1120.ch008. (Cited on pages 2, 7, and 124).

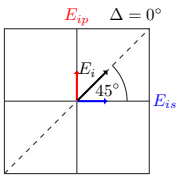

[67] **Bittrich, E.; Kuntzsch, M.; Eichhorn, K.-J.; Uhlmann, P.**, "Complex pH- and temperature-sensitive swelling behavior of mixed polymer brushes," *Journal of Polymer Science Part B: Polymer Physics* **2010**, 48 (14), 1606–1615, DOI: 10.1002/polb.22021. (Cited on pages 2, 7, 11, 124, and 125).

[68] **Brittain, W. J.; Minko, S.**, "A structural definition of polymer brushes," *Journal of Polymer Science Part A: Polymer Chemistry* **2007**, 45 (16), 3505–3512, DOI: 10.1002/pola.22180. (Cited on pages 4, 6, and 83).

[69] **Toomey, R.; Tirrell, M.**, "Functional Polymer Brushes in Aqueous Media from Self-Assembled and Surface-Initiated Polymers," *Annual Review of Physical Chemistry* **2008**, 59 (1), 493–517, DOI: 10.1146/annurev.physchem.59.032607.093623. (Cited on page 4).

[70] **Israelachvili, J. N.**, *Intermolecular and Surface Forces, Third Edition*. Academic Press Inc, San Diego, 2011, ISBN: 978-0-12-391927-4. (Cited on pages 4, 6, and 83).

[71] **Azzaroni, O.**, "Polymer brushes here, there, and everywhere: Recent advances in their practical applications and emerging opportunities in multiple research fields," *Journal of Polymer Science Part A: Polymer Chemistry* **2012**, 50 (16), 3225–3258, DOI: 10.1002/pola.26119. (Cited on page 4).

[72] **Taylor, L. D.; Cerankowski, L. D.**, "Preparation of films exhibiting a balanced temperature dependence to permeation by aqueous solutions—a study of lower consolute behavior," *Journal of Polymer Science: Polymer Chemistry Edition* **1975**, 13 (11), 2551–2570, DOI: 10.1002/pol.1975.170131113. (Cited on pages 4 and 96).

[73] **Zhulina, E. B.; Borisov, O. V.**, "Structure and interaction of weakly charged polyelectrolyte brushes: Self-consistent field theory," *The Journal of Chemical Physics* **1997**, 107 (15), 5952–5967, DOI: 10.1063/1.474320. (Cited on page 4).

[74] **Zdyrko, B.; Iyer, K. S.; Luzinov, I.**, "Macromolecular anchoring layers for polymer grafting: comparative study," *Polymer* **2006**, 47 (1), 272–279, DOI: 10.1016/j.polymer.2005.11.029. (Cited on pages 4 and 50).

[75] **Bittrich, E.**, *Design of new responsive materials based on functional polymer brushes*. PhD thesis, Technische Universität Dresden, Dresden, Germany, 2010. http://nbn-resolving.de/urn:nbn:de:bsz:14-qucosa-62669. (Cited on pages 5, 10, 48, 50, 51, and 100).

[76] **Blank, W. J.; He, Z. A.; Picci, M.**, "Catalysis of the epoxy-carboxyl reaction," *Journal of Coatings Technology* **2002**, 74 (926), 33–41, DOI: 10.1007/BF02720158. (Cited on pages 5 and 86).

[77] **Bittrich, E.; Uhlmann, P.; Eichhorn, K.-J.; Aulich, D.; Furchner, A.**, *Smart polymer surfaces and films*, in *Ellipsometry of Functional Organic Surfaces and Films*, Eichhorn, K.-J.; Hinrichs, K. (Editors). Springer Berlin, 2014. ISBN: 978-3-642-40127-5, DOI: 10.1007/978-3-642-40128-2_5. (Cited on page 7).

[78] **Habicht, J.; Schmidt, M.; Rühe, J.; Johannsmann, D.**, "Swelling of Thick Polymer Brushes Investigated with Ellipsometry," *Langmuir* **1999**, 15 (7), 2460–2465, DOI: 10.1021/la980573d. (Cited on page 7).

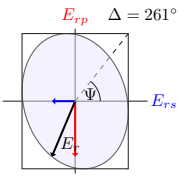

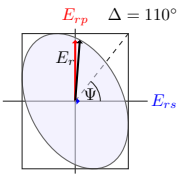

[79] **Biesalski, M.; Johannsmann, D.; Rühe, J.**, "Synthesis and swelling behavior of a weak polyacid brush," *The Journal of Chemical Physics* **2002**, 117 (10), 4988–4994, DOI: 10.1063/1.1490924. (Cited on page 7).

[80] **Biesalski, M.; Johannsmann, D.; Rühe, J.**, "Electrolyte-induced collapse of a polyelectrolyte brush," *The Journal of Chemical Physics* **2004**, 120 (18), 8807–8814, DOI: 10.1063/1.1690242. (Cited on page 7).

[81] **Schmaljohann, D.; Beyerlein, D.; Nitschke, M.; Werner, C.**, "Thermo-Reversible Swelling of Thin Hydrogel Films Immobilized by Low-Pressure Plasma," *Langmuir* **2004**, 20 (23), 10107–10114, DOI: 10.1021/la034653f. (Cited on page 7).

[82] **Bittrich, E.; Rodenhausen, K. B.; Eichhorn, K.-J.; Hofmann, T.; Schubert, M.; Stamm, M.; Uhlmann, P.**, "Protein adsorption on and swelling of polyelectrolyte brushes: A simultaneous ellipsometry-quartz crystal microbalance study," *Biointerphases* **2010**, 5 (4), 159–167, DOI: 10.1116/1.3530841. (Cited on pages 7, 51, 124, 132, 138, 139, and 142).

[83] **Hahn Berg, I. C.; Muller, D.; Arnebrant, T.; Malmsten, M.**, "Ellipsometry and TIRF Studies of Enzymatic Degradation of Interfacial Proteinaceous Layers," *Langmuir* **2001**, 17 (5), 1641–1652, DOI: 10.1021/la0008683. (Cited on page 7).

[84] **Garcia-Caurel, E.; Nguyen, J.; Schwartz, L.; Drevillon, B.**, "Application of FTIR ellipsometry to detect and classify micro-organisms," in *Society of Photo-Optical Instrumentation Engineers (SPIE) Conference Series, Proceedings SPIE 5141, Diagnostic Optical Spectroscopy in Biomedicine II*, Vol. 5141, pp. 249–259. 2003. DOI: 10.1117/12.500939. (Cited on page 7).

[85] **Wang, Z. H.; Jin, G.**, "A Label-Free Multisensing Immunosensor Based on Imaging Ellipsometry," *Analytical Chemistry* **2003**, 75 (22), 6119–6123, DOI: 10.1021/ac0347258. (Cited on page 7).

[86] **Fang, S.; Qing, H.**, "Application of ellipsometry in researches of biomedicine," *Journal of Clinical Rehabilitative Tissue Engineering Research* **2004**, 8 (14), 2796–2798. (Cited on page 7).

[87] **Nikonenko, N. A.; Bushnak, I. A.; Keddie, J. L.**, "Spectroscopic Ellipsometry of Mucin Layers on an Amphiphilic Diblock Copolymer Surface," *Applied Spectroscopy* **2009**, 63 (8), 889–898, DOI: 10.1366/000370209788964449. (Cited on page 7).

[88] **Almodóvar, J.; Place, L. W.; Gogolski, J.; Erickson, K.; Kipper, M. J.**, "Layer-by-Layer Assembly of Polysaccharide-Based Polyelectrolyte Multilayers: A Spectroscopic Study of Hydrophilicity, Composition, and Ion Pairing," *Biomacromolecules* **2011**, 12 (7), 2755–2765. (Cited on page 7).

[89] **Garcia-Caurel, E.; Ossikovski, R.; Foldyna, M.; Pierangelo, A.; Drévillon, B.; De Martino, A.**, *Advanced Mueller Ellipsometry Instrumentation and Data Analysis*, in *Ellipsometry at the Nanoscale*, Losurdo, M.; Hingerl, K. (Editors). Springer Berlin Heidelberg, 2013. ISBN: 978-3-642-33955-4, DOI: 10.1007/978-3-642-33956-1_2. (Cited on pages 7, 20, 26, and 148).

[90] **Aulich, D. M.**, *Spektroskopische In-situ-Infrarotellipsometrie an stimuli-reaktiven Polymerbürsten*. PhD thesis, Technische Universität Berlin, Berlin, Germany, 2010. Mensch und Buch Verlag, ISBN: 978-3-86664-818-0, http://d-nb.info/1006152482. (Cited on page 7).

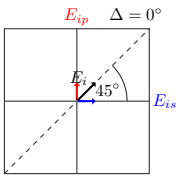

[91] **Rothen, A.**, "The Ellipsometer, an Apparatus to Measure Thicknesses of Thin Surface Films," *Review of Scientific Instruments* **1945**, 16 (26), 26–30, DOI: 10.1063/1.1770315. (Cited on page 8).

[92] **Rothen, A.**, "Measurements of the thickness of thin films by optical means, from Rayleigh and Drude to Langmuir, and the development of the present ellipsometer," in *Symposium Proceedings on Ellipsometry in the measurement of surfaces and thin films*, Passaglia, E.; Stromberg, R. R.; Kruger, J. (Editors), Vol. *National Bureau of Standards Miscellaneous Publication* 256, pp. 7–21. 1964. (Cited on page 8).

[93] **Drude, P.**, "Ueber die Gesetze der Reflexion und Brechung des Lichtes an der Grenze absorbirender Krystalle," *Annalen der Physik* **1887**, 268 (12), 584–625, DOI: 10.1002/andp.18872681205. (Cited on page 8).

[94] **Collins, R. W.; An, I.; Chen, C.**, *Rotating Polarizer and Analyzer Ellipsometry*, in *Handbook of Ellipsometry*, Tompkins, H. G.; Irene, E. A. (Editors). William Andrew, Inc., Norwich, 2005. ISBN: 978-0-8155-1499-2, http://www.sciencedirect.com/science/book/9780815514992. (Cited on pages 8, 10, and 148).

[95] **Schubert, M.**, *Theory and Application of Generalized Ellipsometry*, in *Handbook of Ellipsometry*, Tompkins, H. G.; Irene, E. A. (Editors). William Andrew, Inc., Norwich, 2005. ISBN: 978-0-8155-1499-2, http://www.sciencedirect.com/science/book/9780815514992. (Cited on page 10).

[96] **Azzam, R. M. A.**, "Photopolarimetric measurement of the Mueller matrix by Fourier analysis of a single detected signal," *Optics Letters* **1978**, 2 (6), 148–150, DOI: 10.1364/OL.2.000148. (Cited on page 10).

[97] **Aspnes, D. E.**, *The Accurate Determination of Optical Properties by Ellipsometry*, in *Handbook of Optical Constants of Solids*, Palik, E. D. (Editor). Academic Press, San Diego, 1985. ISBN: 0-12-544420-6. (Cited on pages 10 and 42).

[98] **Rauch, S.; Eichhorn, K.-J.; Kuckling, D.; Stamm, M.; Uhlmann, P.**, "Chain Extension of Stimuli-Responsive Polymer Brushes: A General Strategy to Overcome the Drawbacks of the "Grafting-To" Approach," *Advanced Functional Materials* **2013**, 23 (45), 5675–5681, DOI: 10.1002/adfm.201300849. (Cited on pages 10 and 50).

[99] **Werner, C.; Eichhorn, K.-J.; Grundke, K.; Simon, F.; Grählert, W.; Jacobasch, H.-J.**, "Insights on structural variations of protein adsorption layers on hydrophobic fluorohydrocarbon polymers gained by spectroscopic ellipsometry (part I)," *Colloids and Surfaces A: Physicochemical and Engineering Aspects* **1999**, 156 (1–3), 3–17, DOI: 10.1016/S0927-7757(99)00007-2. (Cited on pages 10, 51, and 124).

[100] **Michelson, A. A.; Morley, E.**, "On the Relative Motion of the Earth and the Luminiferous Æther," *Philosophical Magazine* **1887**, 24 (151), 449–463. (Cited on page 11).

[101] **Cooley, J. W.; Tukey, J. W.**, "An algorithm for the machine calculation of complex Fourier series," *Mathematics of Computation* **1965**, 19, 297–301, DOI: 10.2307/2003354. (Cited on pages 11, 107, 145, and 146).

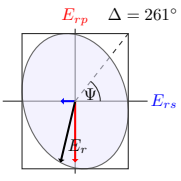

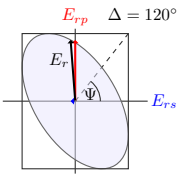

[102] **Röseler, A.; Molgedey, W.**, "Improvement in accuracy of spectroscopic IR ellipsometry by the use of IR retarders," *Infrared Physics* **1984**, 24 (1), 1–5, DOI: 10.1016/0020-0891(84)90039-3. (Cited on page 12).

[103] **den Boer, J. H. W. G.; Kroesen, G. M. W.; de Hoog, F. J.**, "Spectroscopic rotating compensator ellipsometry in the infrared: retarder design and measurement," *Measurement Science and Technology* **1997**, 8 (5), 484–492, DOI: 10.1088/0957-0233/8/5/004. (Cited on page 12).

[104] **Griffiths, P. R.**, *Resolution and Instrument Line Shape Function*, in *Handbook of Vibrational Spectroscopy*, Chalmers, J. M.; Griffiths, P. R. (Editors). John Wiley & Sons, Ltd, Chichester, 2006. ISBN: 978-0-471-98847-2, DOI: 10.1002/0470027320.s0111. (Cited on pages 12 and 146).

[105] **Günzler, H.; Gremlich, H.-U.**, *IR-Spektroskopie*. Wiley-VCH, Weinheim, 2003, ISBN: 978-3-527-30801-9. (Cited on pages 13, 14, 30, 145, and 146).

[106] **Theocharous, E.; Birch, J. R.**, *Detectors for Mid- and Far-Infrared Spectrometry: Selection and Use*, in *Handbook of Vibrational Spectroscopy*, Chalmers, J. M.; Griffiths, P. R. (Editors). John Wiley & Sons, Ltd, Chichester, 2006. ISBN: 978-0-471-98847-2, DOI: 10.1002/0470027320.s0213. (Cited on page 13).

[107] "Characteristics and use of infrared detectors: Technical information SD-12," Solid State Division, Hamamatsu Photonics K. K., Hamamatsu City, Japan, 2004. (Cited on page 13).

[108] **Palik, E. D.**, *Handbook of Optical Constants of Solids I and II*. Academic Press, San Diego, 1985 and 1991, ISBN: 0-12-544420-6 and 0-12-544422-2. (Cited on pages 14 and 39).

[109] **Sun, G.; Zhang, X.; Kaspari, C.; Haberland, K.; Rappich, J.; Hinrichs, K.**, "In-Situ Monitoring the Growth of Polypyrrole Films at Liquid/Solid Interface Using a Combination of Polarized Infrared Spectroscopy and Reflectance Anisotropy Spectroscopy," *Journal of The Electrochemical Society* **2012**, 159 (10), H811–H815, DOI: 10.1149/2.044210jes. (Cited on page 15).

[110] **Larouche, P.; Max, J.-J.; Chapados, C.**, "Isotope effects in liquid water by infrared spectroscopy. II. Factor analysis of the temperature effect on H_2O and D_2O," *The Journal of Chemical Physics* **2008**, 129 (6), 064503, DOI: 10.1063/1.2960583. (Cited on pages 15, 105, 106, 107, and 108).

[111] **Knott, G. D.**, *Interpolating Cubic Splines*. Birkhäuser Boston, New York, 1999, ISBN: 978-0-8176-4100-9. (Cited on page 15).

[112] **Savitzky, A.; Golay, M. J. E.**, "Smoothing and Differentiation of Data by Simplified Least Squares Procedures," *Analytical Chemistry* **1964**, 36 (8), 1627–1639, DOI: 10.1021/ac60214a047. (Cited on page 15).

[113] **DeNoyer, L. K.; Dodd, J. G.**, *Smoothing and Derivatives in Spectroscopy*, in *Handbook of Vibrational Spectroscopy*, Chalmers, J. M.; Griffiths, P. R. (Editors). John Wiley & Sons, Ltd, Chichester, 2006. ISBN: 978-0-471-98847-2, DOI: 10.1002/0470027320.s4501. (Cited on page 15).

[114] **Jones, R. C.**, "A new calculus for the treatment of optical systems," *Journal of the Optical Society of America* **1941**, 31, 488–493. (Cited on pages 16, 20, and 44).

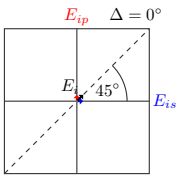

[115] **Stokes, G. G.**, "On the composition and resolution of streams of polarized light from different sources," *Cambridge Philosophical Society Transactions* **1856**, 9, 399–416. (Cited on pages 17 and 20).

[116] **Röseler, A.**, "Problem of polarization degree in spectroscopic photometric ellipsometry (polarimetry)," *Journal of the Optical Society of America A* **1992**, 9 (7), 1124–1131, DOI: 10.1364/JOSAA.9.001124. (Cited on pages 18, 19, and 28).

[117] **Stobie, R. W.; Dignam, M. J.**, "Transmission Properties of Grid Polarizers," *Applied Optics* **1973**, 12 (7), 1390–1391, DOI: 10.1364/AO.12.001390. (Cited on pages 20 and 25).

[118] **den Boer, J. H. W. G.; Kroesen, G. M. W.; Haverlag, M.; de Hoog, F. J.**, "Spectroscopic IR ellipsometry with imperfect components," *Thin Solid Films* **1993**, 234 (1–2), 323–326, DOI: 10.1016/0040-6090(93)90278-W. (Cited on pages 20 and 25).

[119] **Röseler, A.**, "IR spectroscopic ellipsometry: instrumentation and results," *Thin Solid Films* **1993**, 234 (1–2), 307–313, DOI: 10.1016/0040-6090(93)90275-T. (Cited on page 20).

[120] **Müller, H.**, "The foundation of optics," *Journal of the Optical Society of America* **1948**, 38 (7), 661, http://www.opticsinfobase.org/josa/abstract.cfm?uri=josa-38-7-657. Abstract in *Proceedings of the Winter Meeting of the Optical Society of America*. (Cited on page 20).

[121] **Parke III, N. G.**, *Matrix Optics*. PhD thesis, Massachusetts Institute of Technology (MIT), Cambridge, USA, 1948. (Cited on page 20).

[122] **Hinrichs, K.; Gensch, M.; Dittmar, G.; Silaghi, S. D.; Schade, U.; Zahn, D. R. T.; Kröning, S.; Volkmer, R.; Esser, N.**, *IR-Synchrotron Mapping Ellipsometry for Characterization of Biomolecular Films*, in *BESSY – Annual Report 2006*, Godehusen, K. (Editor), pp. 285–287. Berliner Elektronenspeicherring-Gesellschaft für Synchrotronstrahlung m. b. H. (BESSY), Berlin, 2007. (Cited on page 21).

[123] **Sun, G.; Rosu, D. M.; Zhang, X.; Hovestädt, M.; Pop, S.; Schade, U.; Aulich, D.; Gensch, M.; Ay, B.; Holzhütter, H.-G.; Zahn, D. R. T.; Esser, N.; Volkmer, R.; Rappich, J.; Hinrichs, K.**, "Synchrotron infrared spectroscopic ellipsometry for characterization of biofunctional surfaces," *physica status solidi (b)* **2010**, 247 (8), 1925–1931, DOI: 10.1002/pssb.200983945. (Cited on page 21).

[124] **Wold, E.; Bremer, J.**, "Mueller matrix analysis of infrared ellipsometry," *Applied Optics* **1994**, 33 (25), 5982–5993, DOI: 10.1364/AO.33.005982. (Cited on page 26).

[125] **den Boer, J. H. W. G.; Kroesen, G. M. W.; de Zeeuw, W.; de Hoog, F. J.**, "Improved polarizer in the infrared: two wire-grid polarizers in tandem," *Optics Letters* **1995**, 20 (7), 800–802, DOI: 10.1364/OL.20.000800. (Cited on page 26).

[126] **Gensch, M.; Hinrichs, K.; Röseler, A.; Korte, E.-H.; Schade, U.**, "Instrumentation for FT-IR reflection spectroscopy with synchrotron radiation," *Analytical and Bioanalytical Chemistry* **2003**, 376 (5), 626–630, DOI: 10.1007/s00216-003-1985-z. (Cited on page 29).

[127] **Hinrichs, K.; Gensch, M.; Röseler, A.; Korte, E.-H.; Sahre, K.; Eichhorn, K.-J.; Esser, N.; Schade, U.**, "Fourier Transform Infrared Synchrotron Ellipsometry for Studying the Anisotropy of Small Organic Samples," *Applied Spectroscopy* **2003**, 57 (10), 1250–1253, DOI: 10.1366/000370203769699117. (Cited on page 29).

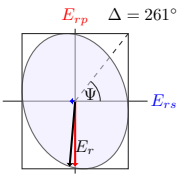

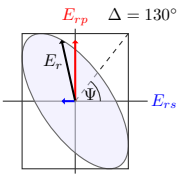

[128] **Gensch, M.; Korte, E.-H.; Esser, N.; Schade, U.; Hinrichs, K.**, "Microfocus-infrared synchrotron ellipsometer for mapping of ultra thin films," *Infrared Physics & Technology* **2006**, 49 (1–2), 74–77, DOI: 10.1016/j.infrared.2006.01.007. (Cited on page 29).

[129] **Tolstoy, V. P.; Chernyshova, I. V.; Skryshevsky, V. A.**, *Handbook of Infrared Spectroscopy of Ultrathin Films*. John Wiley & Sons, Inc., Chichester, 2003, ISBN: 978-0-471-23432-6, DOI: 10.1002/047123432X.ch1. (Cited on pages 29, 74, and 156).

[130] **Claybourn, M.**, *External Reflection Spectroscopy*, in *Handbook of Vibrational Spectroscopy*, Chalmers, J. M.; Griffiths, P. R. (Editors). John Wiley & Sons, Ltd, Chichester, 2006. ISBN: 978-0-471-98847-2, DOI: 10.1002/0470027320.s2201. (Cited on pages 30 and 31).

[131] **Fredericks, P. M.**, *Depth Profiling by Microspectroscopy*, in *Handbook of Vibrational Spectroscopy*, Chalmers, J. M.; Griffiths, P. R. (Editors). John Wiley & Sons, Ltd, Chichester, 2006. ISBN: 978-0-471-98847-2, DOI: 10.1002/0470027320.s2801. (Cited on pages 30 and 31).

[132] **Fitzpatrick, J.; Reffner, J. A.**, *Macro and Micro Internal Reflection Accessories*, in *Handbook of Vibrational Spectroscopy*, Chalmers, J. M.; Griffiths, P. R. (Editors). John Wiley & Sons, Ltd, Chichester, 2006. ISBN: 978-0-471-98847-2, DOI: 10.1002/0470027320.s2302. (Cited on page 30).

[133] "Product Note M28-10/09: A697-G Grazing Angle Objective," Bruker Optics, Bruker, Leipzig, 2009. (Cited on page 31).

[134] **Hinrichs, K.; Furchner, A.; Rappich, J.; Oates, T. W. H.**, "Polarization-Dependent and Ellipsometric Infrared Microscopy for Analysis of Anisotropic Thin Films," *The Journal of Physical Chemistry C* **2013**, 117 (26), 13557–13563, DOI: 10.1021/jp401576r. (Cited on pages 31 and 76).

[135] **Hinrichs, K.; Furchner, A.; Sun, G.; Gensch, M.; Rappich, J.; Oates, T. W. H.**, "Infrared ellipsometry for improved laterally resolved analysis of thin films," *Thin Solid Films, in press 2014*, DOI: 10.1016/j.tsf.2014.02.006. (Cited on page 31).

[136] **Griffiths, P. R.**, *Beer's Law*, in *Handbook of Vibrational Spectroscopy*, Chalmers, J. M.; Griffiths, P. R. (Editors). John Wiley & Sons, Ltd, Chichester, 2006. ISBN: 978-0-471-98847-2, DOI: 10.1002/0470027320.s4601. (Cited on pages 33 and 105).

[137] **Coates, J.**, *Classical Methods of Quantitative Analysis*, in *Handbook of Vibrational Spectroscopy*, Chalmers, J. M.; Griffiths, P. R. (Editors). John Wiley & Sons, Ltd, Chichester, 2006. ISBN: 978-0-471-98847-2, DOI: 10.1002/0470027320.s4602. (Cited on page 33).

[138] **Chalmers, J. M.**, *Mid-infrared Spectroscopy of the Condensed Phase*, in *Handbook of Vibrational Spectroscopy*, Chalmers, J. M.; Griffiths, P. R. (Editors). John Wiley & Sons, Ltd, Chichester, 2006. ISBN: 978-0-471-98847-2, DOI: 10.1002/0470027320.s0104. (Cited on pages 34 and 107).

[139] **Pistorius, A. M. A.; DeGrip, W. J.**, "Deconvolution as a tool to remove fringes from an FT-IR spectrum," *Vibrational Spectroscopy* **2004**, 36 (1), 89–95, DOI: 10.1016/j.vibspec.2004.04.001. (Cited on page 34).

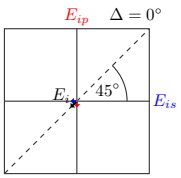

[140] **Max, J.-J.; Chapados, C.**, "Infrared transmission equations in a five media system: gas and liquid," *Journal of Mathematical Chemistry* **2010**, 47 (2), 590–625, DOI: 10.1007/s10910-009-9587-4. (Cited on pages 34 and 107).

[141] **Griffiths, P. R.**, *Introduction to Vibrational Spectroscopy*, in *Handbook of Vibrational Spectroscopy*, Chalmers, J. M.; Griffiths, P. R. (Editors). John Wiley & Sons, Ltd, Chichester, 2006. ISBN: 978-0-471-98847-2, DOI: 10.1002/9780470027325.s8901. (Cited on page 34).

[142] **Palik, E. D.**, *Handbook of Optical Constants of Solids II*. Academic Press, San Diego, 1991, ISBN: 0-12-544422-2. (Cited on pages 34 and 107).

[143] **Masuch, R.; Moss, D. A.**, "Stopped Flow Apparatus for Time-Resolved Fourier Transform Infrared Difference Spectroscopy of Biological Macromolecules in ^1H_2O," *Applied Spectroscopy* **2003**, 57 (11), 1407–1418, DOI: 10.1366/000370203322554581. (Cited on page 35).

[144] **Chalmers, J. M.**, *Mid-infrared Spectroscopy: Anomalies, Artifacts and Common Errors*, in *Handbook of Vibrational Spectroscopy*, Chalmers, J. M.; Griffiths, P. R. (Editors). John Wiley & Sons, Ltd, Chichester, 2006. ISBN: 978-0-471-98847-2, DOI: 10.1002/0470027320.s3101. (Cited on page 35).

[145] **Khanna, V. K.**, *Nanosensors: Physical, Chemical, and Biological*. CRC Press, Taylor & Francis Group, Boca Raton, 2012, ISBN: 978-1-4398-2712-3, DOI: 10.1063/PT.3.1480. (Cited on page 36).

[146] **Jackson, J. D.**, *Classical Electrodynamics*. John Wiley & Sons, Inc., New York, 3 ed., 1999, ISBN: 978-0-471-30932-1. (Cited on pages 37 and 40).

[147] **Tolstoy, V. P.; Chernyshova, I. V.; Skryshevsky, V. A.**, *Absorption and Reflection of Infrared Radiation by Ultrathin Films*, in *Handbook of Infrared Spectroscopy of Ultrathin Films*. John Wiley & Sons, Inc., Chichester, 2003. ISBN: 978-0-471-23432-6, DOI: 10.1002/047123432X.ch1. (Cited on pages 37, 40, and 41).

[148] **Kronig, R. de L.**, "On the theory of dispersion of X-rays," *Journal of the Optical Society of America* **1926**, 12 (6), 547–556, DOI: 10.1364/JOSA.12.000547. (Cited on page 38).

[149] **Kramers, H. A.**, "La diffusion de la lumière par les atomes," in *Atti del Congresso Internazionale dei Fisici, Como-Pavia-Roma*, Vol. 2, pp. 545–557. 1927. (Cited on page 38).

[150] **Bertie, J. E.**, *Optical Constants*, in *Handbook of Vibrational Spectroscopy*, Chalmers, J. M.; Griffiths, P. R. (Editors). John Wiley & Sons, Ltd, Chichester, 2006. ISBN: 978-0-471-98847-2, DOI: 10.1002/0470027320.s0112. (Cited on pages 38, 40, 41, 56, and 62).

[151] **Bertie, J. E.; Eysel, H. H.**, "Infrared Intensities of Liquids I: Determination of Infrared Optical and Dielectric Constants by FT-IR Using the CIRCLE ATR Cell," *Applied Spectroscopy* **1985**, 39 (3), 392–401, DOI: 10.1366/0003702854248575. (Cited on pages 38 and 105).

[152] **Furchner, A.; Aulich, D.**, *Common Polymers and Proteins*, in *Ellipsometry of Functional Organic Surfaces and Films*, Eichhorn, K.-J.; Hinrichs, K. (Editors). Springer Berlin, 2014. ISBN: 978-3-642-40127-5, DOI: 10.1007/978-3-642-40128-2_17. (Cited on page 39).

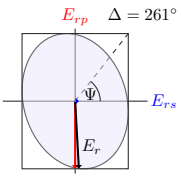

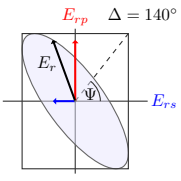

[153] **Furchner, A.; Aulich, D.**, *Organic Materials for Optoelectronic Applications*, in *Ellipsometry of Functional Organic Surfaces and Films*, Eichhorn, K.-J.; Hinrichs, K. (Editors). Springer Berlin, 2014. ISBN: 978-3-642-40127-5, DOI: 10.1007/978-3-642-40128-2_18. (Cited on page 39).

[154] **Palik, E. D.**, *Handbook of Optical Constants of Solids*. Academic Press, San Diego, 1985, ISBN: 0-12-544420-6. (Cited on pages 39, 44, 76, 92, and 111).

[155] **Cauchy, A.-L.**, "Sur la réfraction et la réflexion de la lumière," *Bulletin des Sciences Mathématiques* **1830**, 14, 6–10. (Cited on page 40).

[156] **Steele, D.**, *Infrared Spectroscopy: Theory*, in *Handbook of Vibrational Spectroscopy*, Chalmers, J. M.; Griffiths, P. R. (Editors). John Wiley & Sons, Ltd, Chichester, 2006. ISBN: 978-0-471-98847-2, DOI: 10.1002/0470027320.s0103. (Cited on pages 40 and 71).

[157] **Lorentz, H. A.**, *The theory of electrons and its applications to the phenomena of light and radiant heat*. B. G. Teubner, Leipzig, 1916, ISBN: 978-0-486-49558-3, http://archive.org/details/electronstheory00lorerich. (Cited on page 40).

[158] **Seshadri, K. S.; Jones, R. N.**, "The shapes and intensities of infrared absorption bands—A review," *Spectrochimica Acta* **1963**, 19 (6), 1013–1085, DOI: 10.1016/0371-1951(63)80187-3. (Cited on page 40).

[159] **Bertie, J. E.; Zhang, S. L.**, "Infrared intensities of liquids XXI: integrated absorption intensities of CH_3OH, CH_3OD, CD_3OH and CD_3OD and dipole moment derivatives of methanol," *Journal of Molecular Structure* **1997**, 413–414, 333–363, DOI: 10.1016/S0022-2860(97)00152-X. (Cited on pages 41, 56, and 62).

[160] **De Sousa Meneses, D.; Malki, M.; Echegut, P.**, "Structure and lattice dynamics of binary lead silicate glasses investigated by infrared spectroscopy," *Journal of Non-Crystalline Solids* **2006**, 352 (8), 769–776, DOI: 10.1016/j.jnoncrysol.2006.02.004. (Cited on pages 41, 56, and 62).

[161] **Bruggeman, D. A. G.**, "Berechnung verschiedener physikalischer Konstanten von heterogenen Substanzen. I. Dielektrizitätskonstanten und Leitfähigkeiten der Mischkörper aus isotropen Substanzen," *Annalen der Physik* **1935**, 416 (7), 636–664, DOI: 10.1002/andp.19354160705. (Cited on page 42).

[162] **Aspnes, D. E.**, "Optical properties of thin films," *Thin Solid Films* **1982**, 89 (3), 249–262, DOI: 10.1016/0040-6090(82)90590-9. (Cited on page 42).

[163] **Abelès, F.**, "Recherches sur la propagation des ondes électromagnétiques sinusoidales dans les milieux stratifiés. Application aux couches minces," *Annales de Physique* **1950**, 5, 596–640 and 706–782. (Cited on page 43).

[164] **Berreman, D. W.**, "Optics in Stratified and Anisotropic Media: 4x4-Matrix Formulation," *Journal of the Optical Society of America* **1972**, 62 (4), 502–510, DOI: 10.1364/JOSA.62.000502. (Cited on page 44).

[165] **Schubert, M.**, "Polarization-dependent optical parameters of arbitrarily anisotropic homogeneous layered systems," *Physical Review B* **1996**, 53 (8), 4265–4274, DOI: 10.1103/PhysRevB.53.4265. (Cited on page 44).

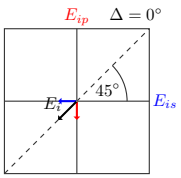

[166] **Max, J.-J.; Chapados, C.**, "Isotope effects in liquid water by infrared spectroscopy. III. H_2O and D_2O spectra from 6000 to 0 cm^{-1}," *The Journal of Chemical Physics* **2009**, 131 (18), 184505, DOI: 10.1063/1.3258646. (Cited on pages 44, 76, 105, 106, and 107).

[167] **Jellison, G. E., Jr.**, "Use of the biased estimator in the interpretation of spectroscopic ellipsometry data," *Applied Optics* **1991**, 30 (23), 3354–3360, DOI: 10.1364/AO.30.003354. (Cited on page 46).

[168] **Jellison, G. E., Jr.**, "Data analysis for spectroscopic ellipsometry," *Thin Solid Films* **1993**, 234 (1–2), 416–422, DOI: 10.1016/0040-6090(93)90298-4. (Cited on page 46).

[169] **Jellison, G. E., Jr.**, *Data Analysis for Spectroscopic Ellipsometry*, in *Handbook of Ellipsometry*, Tompkins, H. G.; Irene, E. A. (Editors). William Andrew, Inc., Norwich, 2005. ISBN: 978-0-8155-1499-2, http://www.sciencedirect.com/science/book/9780815514992. (Cited on page 46).

[170] **Press, W. H.; Teukolsky, S. A.; Vetterling, W. T.; Flannery, B. P.**, *Numerial Recipes – The Art of Scientific Computing*. Cambridge University Press, New York, 2007, ISBN: 978-0-521-88068-8. (Cited on page 46).

[171] **Atkins, P.; de Paula, J.**, *Physical Chemistry*. W. H. Freeman and Company, New York, 2006, ISBN: 0-7167-8759-8. (Cited on page 47).

[172] **Lide, D. R.**, *CRC Handbook of Chemistry and Physics, 90th Edition*. CRC Press/Taylor and Francis, Boca Raton, 2009, ISBN: 978-1-4200-9084-0. (Cited on page 48).

[173] **Peters, T., Jr.**, *All about Albumin: Biochemistry, Genetics, and Medical Applications*. Academic Press, Inc., San-Diego, 1995, ISBN: 978-0-12-552110-9, http://www.sciencedirect.com/science/book/9780125521109. (Cited on page 48).

[174] **Dockal, M.; Carter, D. C.; Rüker, F.**, "The Three Recombinant Domains of Human Serum Albumin: Structural Characterization and Ligand Binding Properties," *The Journal of Biological Chemistry* **1999**, 274 (41), 29303–29310, DOI: 10.1074/jbc.274.41.29303. (Cited on page 48).

[175] **Fernández-San Millán, A.; Mingo-Castel, A.; Miller, M.; Daniell, H.**, "A chloroplast transgenic approach to hyper-express and purify Human Serum Albumin, a protein highly susceptible to proteolytic degradation," *Plant Biotechnology Journal* **2003**, 1 (2), 71–79, DOI: 10.1046/j.1467-7652.2003.00008.x. (Cited on page 48).

[176] **Bordbar, A.-K.; Sohrabi, N.; Gharibi, H.**, "Binding Set Analysis for Interaction of Human Serum Albumin with Cethyl Trimethylammonium Bromide," *Bulletin of the Korean Chemical Society* **2004**, 25 (6), 791–795, DOI: 10.5012/bkcs.2004.25.6.791. (Cited on page 48).

[177] **Artali, R.; Bombieri, G.; Calabi, L.; Del Pra, A.**, "A molecular dynamics study of human serum albumin binding sites," *Il Farmaco* **2005**, 60 (6–7), 485–495, DOI: 10.1016/j.farmac.2005.04.010. (Cited on pages 48 and 49).

[178] **Fasano, M.; Curry, S.; Terreno, E.; Galliano, M.; Fanali, G.; Narciso, P.; Notari, S.; Ascenzi, P.**, "The extraordinary ligand binding properties of human serum albumin," *IUBMB Life* **2005**, 57 (12), 787–796, DOI: 10.1080/15216540500404093. (Cited on pages 48 and 49).

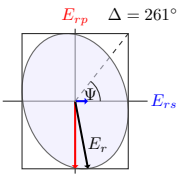

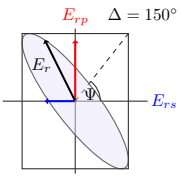

[179] **He, X. M.; Carter, D. C.**, "Atomic structure and chemistry of human serum albumin," *Nature* **1992**, 358 (6383), 209–215, DOI: 10.1038/358209a0. (Cited on page 48).

[180] **Dayhoff, M. O.**, *Atlas of Protein Sequence and Structure*. National Biomedical Research Foundation, Washington, D.C. (Cited on page 48).

[181] **Wallevik, K.**, "Reversible Denaturation of Human Serum Albumin by pH, Temperature, and Guanidine Hydrochloride Followed by Optical Rotation," *The Journal of Biological Chemistry* **1973**, 248 (8), 2650–2655, http://www.jbc.org/content/248/8/2650. (Cited on page 48).

[182] **Wetzel, R.; Becker, M.; Behlke, J.; Billwitz, H.; Böhm, S.; Ebert, B.; Hamann, H.; Krumbiegel, J.; Lassmann, G.**, "Temperature Behaviour of Human Serum Albumin," *European Journal of Biochemistry* **1980**, 104 (2), 469–478, DOI: 10.1111/j.1432-1033.1980.tb04449.x. (Cited on page 48).

[183] **Barbucci, R.; Magnani, A.**, "Conformation of human plasma proteins at polymer surfaces: the effectiveness of surface heparinization," *Biomaterials* **1994**, 15 (12), 955–962, DOI: 10.1016/0142-9612(94)90075-2. (Cited on pages 48 and 129).

[184] **Muzammil, S.; Kumar, Y.; Tayyab, S.**, "Molten globule-like state of human serum albumin at low pH," *European Journal of Biochemistry* **1999**, 266 (1), 26–32, DOI: 10.1046/j.1432-1327.1999.00810.x. (Cited on pages 48 and 130).

[185] **Longsworth, L. G.; Jacobsen, C. F.**, "An Electrophoretic Study of the Binding of Salt Ions by β-Lactoglobulin and Bovine Serum Albumin," *The Journal of Physical and Colloid Chemistry* **1949**, 53 (1), 126–134, DOI: 10.1021/j150466a010. (Cited on page 48).

[186] **Gianazza, E.; Frigerio, A.; Astrua-Testori, S.; Righetti, P. G.**, "The behavior of serum albumin upon isoelectric focusing on immobilized pH gradients," *Electrophoresis* **1984**, 5 (5), 310–312, DOI: 10.1002/elps.1150050512. (Cited on page 48).

[187] **Francis, S. A.; Ellison, A. H.**, "Infrared Spectra of Monolayers on Metal Mirrors," *Journal of the Optical Society of America* **1959**, 49 (2), 131–137, DOI: 10.1364/JOSA.49.000131. (Cited on page 49).

[188] **Sheppard, N.**, *The Historical Development of Experimental Techniques in Vibrational Spectroscopy*, in *Handbook of Vibrational Spectroscopy*, Chalmers, J. M.; Griffiths, P. R. (Editors). John Wiley & Sons, Ltd, Chichester, 2006. ISBN: 978-0-471-98847-2, DOI: 10.1002/0470027320.s0101. (Cited on page 49).

[189] **Kattner, J.; Hoffmann, H.**, *External Reflection Spectroscopy of Thin Films on Dielectric Substrates*, in *Handbook of Vibrational Spectroscopy*, Chalmers, J. M.; Griffiths, P. R. (Editors). John Wiley & Sons, Ltd, Chichester, 2006. ISBN: 978-0-471-98847-2, DOI: 10.1002/0470027320.s2204. (Cited on page 49).

[190] **Chalmers, J. M.; Everall, N. J.**, *Qualitative and Quantitative Analysis of Plastics, Polymers and Rubbers by Vibrational Spectroscopy*, in *Handbook of Vibrational Spectroscopy*, Chalmers, J. M.; Griffiths, P. R. (Editors). John Wiley & Sons, Ltd, Chichester, 2006. ISBN: 978-0-471-98847-2, DOI: 10.1002/9780470027325.s6101.pub2. (Cited on page 49).

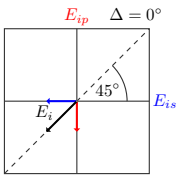

[191] **Guiselin, O.**, "Irreversible Adsorption of a Concentrated Polymer Solution," *Europhysics Letters* **1992**, 17 (3), 225–230, DOI: 10.1209/0295-5075/17/3/007. (Cited on page 51).

[192] **Aubouy, M.; Guiselin, O.; Raphaël, E.**, "Scaling Description of Polymer Interfaces: Flat Layers," *Macromolecules* **1996**, 29 (22), 7261–7268, DOI: 10.1021/ma9604348. (Cited on page 51).

[193] **Ichinose, I.; Kawakami, T.; Kunitake, T.**, "Alternate Molecular Layers of Metal Oxides and Hydroxyl Polymers Prepared by the Surface Sol-Gel Process," *Advanced Materials* **1998**, 10 (7), 535–539, DOI: 10.1002/(SICI)1521-4095(199805)10:7<535::AID-ADMA535>3.0.CO;2-Q. (Cited on page 51).

[194] **Bittrich, E.; Aulich, D.; Eichhorn, K.-J.; Hinrichs, K.; Uhlmann, P.; Luzinov, I.; Stamm, M.**, "Control of Protein Adsorption and Release by Stimuli-Responsive Polymer Brushes," in *Polymeric Materials: Science & Engineering*, no. 101, pp. 930–931. 2009. (Cited on page 51).

[195] **Rosenfeldt, S.; Wittemann, A.; Ballauff, M.; Breininger, E.; Bolze, J.; Dingenouts, N.**, "Interaction of proteins with spherical polyelectrolyte brushes in solution as studied by small-angle x-ray scattering," *Physical Review E* **2004**, 70 (6), 061403, DOI: 10.1103/PhysRevE.70.061403. (Cited on pages 51 and 132).

[196] **Biesheuvel, P. M.; Leermakers, F. A. M.; Cohen Stuart, M. A.**, "Self-consistent field theory of protein adsorption in a non-Gaussian polyelectrolyte brush," *Physical Review E* **2006**, 73 (1), 011802, DOI: 10.1103/PhysRevE.73.011802. (Cited on pages 51 and 132).

[197] **Hollmann, O.; Czeslik, C.**, "Characterization of a Planar Poly(acrylic acid) Brush as a Materials Coating for Controlled Protein Immobilization," *Langmuir* **2006**, 22 (7), 3300–3305, DOI: 10.1021/la053110y. (Cited on pages 51 and 132).

[198] **Hollmann, O.; Gutberlet, T.; Czeslik, C.**, "Structure and Protein Binding Capacity of a Planar PAA Brush," *Langmuir* **2007**, 23 (3), 1347–1353, DOI: 10.1021/la061881b. (Cited on pages 51 and 132).

[199] **Chalmers, J. M.; Griffiths, P. R.**, *Handbook of Vibrational Spectroscopy*. John Wiley & Sons, Ltd, Chichester, 2006, ISBN: 978-0-471-98847-2, DOI: 10.1002/0470027320. (Cited on pages 53 and 146).

[200] **Henbest, H. B.; Meakins, G. D.; Nicholls, B.; Taylor, K. J.**, "Detection of the epoxide group by infrared spectroscopy," *Journal of the Chemical Society* **1957**, (0), 1459–1462, DOI: 10.1039/JR9570001459. (Cited on pages 53 and 55).

[201] **Nyquist, R. A.**, *Interpreting Infrared, Raman and Nuclear Magnetic Resonance Spectra*. Academic Press Inc, San Diego, 2001, ISBN: 978-0-12-523475-7, http://www.sciencedirect.com/science/book/9780125234757. (Cited on pages 53 and 55).

[202] **Nyquist, R. A.; Fiedler, S.**, "Infrared study of styrene oxide and phenylacetylene in various solutions," *Vibrational Spectroscopy* **1994**, 7 (2), 149–162, DOI: 10.1016/0924-2031(94)85025-9. (Cited on pages 53 and 55).

[203] **Coates, J.**, *Interpretation of Infrared Spectra, A Practical Approach*, in *Encyclopedia of Analytical Chemistry*. John Wiley & Sons, Ltd, Chichester, 2000. ISBN: 978-0-470-02731-8, DOI: 10.1002/9780470027318.a5606. (Cited on pages 53, 55, 57, and 71).

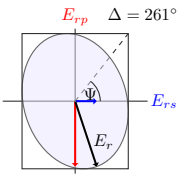

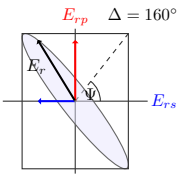

[204] **Miyazawa, T.; Shimanouchi, T.; Mizushima, S.-i.**, "Normal Vibrations of *N*-Methylacetamide," *Journal of Chemical Physics* **1958**, 29 (3), 611–616, DOI: 10.1063/1.1744547. (Cited on pages 55, 57, 64, 68, and 70).

[205] **Cheam, T. C.; Krimm, S.**, "Infrared intensities of amide modes in *N*-methylacetamide and poly(glycine I) from ab initio calculations of dipole moment derivatives of *N*-methylacetamide," *The Journal of Chemical Physics* **1985**, 82 (4), 1631–1641, DOI: 10.1063/1.448395. (Cited on pages 55, 57, 64, and 68).

[206] **Bandekar, J.**, "Amide modes and protein conformation," *Biochimica et Biophysica Acta (BBA) – Protein Structure and Molecular Enzymology* **1992**, 1120 (2), 123–143, DOI: 10.1016/0167-4838(92)90261-B. (Cited on pages 55 and 57).

[207] **Lee, S.-H.; Mirkin, N. G.; Krimm, S.**, "A quantitative anharmonic analysis of the amide A band in α-helical poly(L-alanine)," *Biopolymers* **1999**, 49 (3), 195–207, DOI: 10.1002/(SICI)1097-0282(199903)49:3<195::AID-BIP1>3.0.CO;2-G. (Cited on pages 55, 57, and 68).

[208] **Wu, P.; Siesler, H. W.**, "The assignment of overtone and combination bands in the near infrared spectrum of polyamide 11," *Journal of Near Infrared Spectroscopy* **1999**, 7 (2), 65–76, DOI: 10.1255/jnirs.236. (Cited on pages 55, 57, 70, and 71).

[209] **Maeda, Y.; Nakamura, T.; Ikeda, I.**, "Change in Solvation of Poly(*N*,*N*-diethylacrylamide) during Phase Transition in Aqueous Solutions As Observed by IR Spectroscopy," *Macromolecules* **2002**, 35 (27), 10172–10177, DOI: 10.1021/ma020945w. (Cited on pages 55 and 57).

[210] **Katsumoto, Y.; Tanaka, T.; Sato, H.; Ozaki, Y.**, "Conformational Change of Poly(*N*-isopropylacrylamide) during the Coil–Globule Transition Investigated by Attenuated Total Reflection/Infrared Spectroscopy and Density Functional Theory Calculation," *The Journal of Physical Chemistry A* **2002**, 106 (14), 3429–3435, DOI: 10.1021/jp0124903. (Cited on pages 55, 57, and 65).

[211] **Cheng, X.; Canavan, H. E.; Stein, M. J.; Hull, J. R.; Kweskin, S. J.; Wagner, M. S.; Somorjai, G. A.; Castner, D. G.; Ratner, B. D.**, "Surface Chemical and Mechanical Properties of Plasma-Polymerized *N*-Isopropylacrylamide," *Langmuir* **2005**, 21 (17), 7833–7841, DOI: 10.1021/la050417o. (Cited on pages 55 and 57).

[212] **Chen, X.; Yang, T.; Kataoka, S.; Cremer, P. S.**, "Specific Ion Effects on Interfacial Water Structure near Macromolecules," *Journal of the American Chemical Society* **2007**, 129 (40), 12272–12279, DOI: 10.1021/ja073869r. (Cited on pages 55 and 57).

[213] **Uversky, V. N.; Permyakov, E. A.**, *Methods in Protein Structure and Stability Analysis: Vibrational Spectroscopy*. Molecular Anatomy and Physiology of Proteins. Nova Science Publishers, Inc., New York, 2007, ISBN: 978-1-60021-703-6. (Cited on pages 55, 57, and 64).

[214] **Sun, B.; Lin, Y.; Wu, P.**, "Structure Analysis of Poly(N-isopropylacrylamide) Using Near-Infrared Spectroscopy and Generalized Two-Dimensional Correlation Infrared Spectroscopy," *Applied Spectroscopy* **2007**, 61 (7), 765–771, DOI: 10.1366/000370207781393271. (Cited on pages 55, 57, and 71).

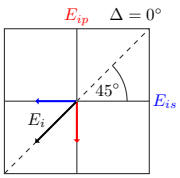

[215] **Barth, A.**, "Infrared spectroscopy of proteins," *Biochimica et Biophysica Acta (BBA) – Bioenergetics* **2007**, 1767 (9), 1073–1101, DOI: 10.1016/j.bbabio.2007.06.004. (Cited on pages 55, 56, 57, 64, 65, 69, 70, 126, 127, and 128).

[216] **Sathyanarayana, D. N.**, *Vibrational Spectroscopy: Theory and Applications*. New Age International (P) Ltd., Publishers, New Delhi, 2004, ISBN: 978-81-224-1517-9. (Cited on page 56).

[217] **Miyamae, T.; Akiyama, H.; Yoshida, M.; Tamaoki, N.**, "Characterization of Poly(*N*-isopropylacrylamide)-Grafted Interfaces with Sum-Frequency Generation Spectroscopy," *Macromolecules* **2007**, 40 (13), 4601–4606, DOI: 10.1021/ma070399c. (Cited on pages 57 and 117).

[218] **Jellison, G. E., Jr.**, "Optical functions of silicon determined by two-channel polarization modulation ellipsometry," *Optical Materials* **1992**, 1 (1), 41–47, DOI: 10.1016/0925-3467(92)90015-F. (Cited on page 58).

[219] **Hall, D. B.; Underhill, P.; Torkelson, J. M.**, "Spin coating of thin and ultrathin polymer films," *Polymer Engineering & Science* **1998**, 38 (12), 2039–2045, DOI: 10.1002/pen.10373. (Cited on page 59).

[220] **Wu, Y.; Meersman, F.; Ozaki, Y.**, "A Novel Application of Hybrid Two-Dimensional Correlation Infrared Spectroscopy: Exploration of the Reversibility of the Pressure- and Temperature-Induced Phase Separation of Poly(*N*-isopropylacrylamide) and Poly(*N*-isopropylmethacrylamide) in Aqueous Solution," *Macromolecules* **2006**, 39 (3), 1182–1188, DOI: 10.1021/ma0521755. (Cited on page 63).

[221] **Buck, M.; Karplus, M.**, "Hydrogen Bond Energetics: A Simulation and Statistical Analysis of *N*-Methyl Acetamide (NMA), Water, and Human Lysozyme," *The Journal of Physical Chemistry B* **2001**, 105 (44), 11000–11015, DOI: 10.1021/jp011042s. (Cited on pages 64 and 72).

[222] **DeCamp, M. F.; DeFlores, L.; McCracken, J. M.; Tokmakoff, A.; Kwac, K.; Cho, M.**, "Amide I Vibrational Dynamics of *N*-Methylacetamide in Polar Solvents: The Role of Electrostatic Interactions," *The Journal of Physical Chemistry B* **2005**, 109 (21), 11016–11026, DOI: 10.1021/jp050257p. (Cited on page 64).

[223] **Mitchell, J. B. O.; Price, S. L.**, "On the relative strengths of amide. . .amide and amide. . .water hydrogen bonds," *Chemical Physics Letters* **1991**, 180 (6), 517–523, DOI: 10.1016/0009-2614(91)85003-F. (Cited on page 64).

[224] **Dixon, D. A.; Dobbs, K. D.; Valentini, J. J.**, "Amide-Water and Amide-Amide Hydrogen Bond Strengths," *The Journal of Physical Chemistry* **1994**, 98 (51), 13435–13439, DOI: 10.1021/j100102a001. (Cited on page 64).

[225] **Katsumoto, Y.; Tanaka, T.; Ihara, K.; Koyama, M.; Ozaki, Y.**, "Contribution of Intramolecular C=O···H−N Hydrogen Bonding to the Solvent-Induced Reentrant Phase Separation of Poly(*N*-isopropylacrylamide)," *The Journal of Physical Chemistry B* **2007**, 111 (44), 12730–12737, DOI: 10.1021/jp0750452. (Cited on pages 65, 66, and 70).

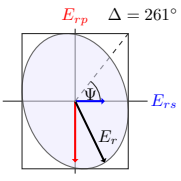

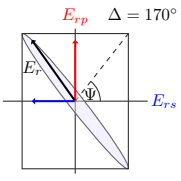

[226] **Richardson, T.; de Gala, S.; Crabtree, R. H.; Siegbahn, P. E. M.**, "Unconventional Hydrogen Bonds: Intermolecular B−H···H−N Interactions," *Journal of the American Chemical Society* **1995**, 117 (51), 12875–12876, DOI: 10.1021/ja00156a032. (Cited on page 66).

[227] **Popelier, P. L. A.**, "Characterization of a Dihydrogen Bond on the Basis of the Electron Density," *The Journal of Physical Chemistry A* **1998**, 102 (10), 1873–1878, DOI: 10.1021/jp9805048. (Cited on page 66).

[228] **Max, J.-J.; Chapados, C.**, "Isotope effects in liquid water by infrared spectroscopy," *The Journal of Chemical Physics* **2002**, 116 (11), 4626–4642, DOI: 10.1063/1.1448286. (Cited on pages 66, 69, 77, 78, 105, 106, 107, 112, and 115).

[229] **Garton, A.; Phibbs, M. K.**, "Some Advances in the Technique of N-deuteration of Polyamides to Measure Amorphous Orientation," *Die Makromolekulare Chemie, Rapid Communications* **1982**, 3 (8), 569–574, DOI: 10.1002/marc.1982.030030808. (Cited on pages 68 and 71).

[230] **Scarpa, J. S.; Mueller, D. D.; Klotz, I. M.**, "Slow Hydrogen–Deuterium Exchange in a Non-α-helical Polyamide," *Journal of the American Chemical Society* **1967**, 89 (24), 6024–6030, DOI: 10.1021/ja01000a006. (Cited on page 68).

[231] **Herrebout, W. A.; Clou, K.; Desseyn, H. O.**, "Vibrational Spectroscopy of *N*-Methylacetamide Revisited," *The Journal of Physical Chemistry A* **2001**, 105 (20), 4865–4881, DOI: 10.1021/jp004396c. (Cited on page 70).

[232] **Maeda, Y.; Yamamoto, H.; Ikeda, I.**, "Effects of ionization on the phase behavior of poly(*N*-isopropylacrylamide-co-acrylic acid) and poly(*N*,*N*-diethylacrylamide-co-acrylic acid) in water," *Colloid and Polymer Science* **2004**, 282 (11), 1268–1273, DOI: 10.1007/s00396-004-1069-4. (Cited on page 70).

[233] **Yamauchi, H.; Maeda, Y.**, "LCST and UCST Behavior of Poly(*N*-isopropylacrylamide) in DMSO/Water Mixed Solvents Studied by IR and Micro-Raman Spectroscopy," *The Journal of Physical Chemistry B* **2007**, 111 (45), 12964–12968, DOI: 10.1021/jp072438s. (Cited on page 70).

[234] **Brzezinski, B.; Zundel, G.**, "Anilides of 6-Methyl-Picolinic Acid N-Oxide Infrared Investigations," *Zeitschrift für Physikalische Chemie* **1977**, 105 (3–4), 125–133, DOI: 10.1524/zpch.1977.105.3_4.125. (Cited on page 70).

[235] **Cannon, C. G.**, "The infra-red spectra and molecular configurations of polyamides," *Spectrochimica Acta* **1960**, 16 (3), 302–319, DOI: 10.1016/0371-1951(60)80092-6. (Cited on page 71).

[236] **Kwac, K.; Cho, M.**, "Molecular dynamics simulation study of *N*-methylacetamide in water. I. Amide I mode frequency fluctuation," *The Journal of Chemical Physics* **2003**, 119 (4), 2247–2255, DOI: 10.1063/1.1580807. (Cited on page 72).

[237] **Maeda, Y.; Nakamura, T.; Ikeda, I.**, "Changes in the Hydration States of Poly(*N*-alkylacrylamide)s during Their Phase Transitions in Water Observed by FTIR Spectroscopy," *Macromolecules* **2001**, 34 (5), 1391–1399, DOI: 10.1021/ma001306t. (Cited on pages 73 and 75).

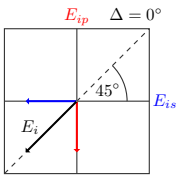

[238] **Gu, Y.; Kar, T.; Scheiner, S.**, "Fundamental Properties of the CH···O Interaction: Is It a True Hydrogen Bond?," *Journal of the American Chemical Society* **1999**, 121 (40), 9411–9422, DOI: 10.1021/ja991795g. (Cited on page 73).

[239] **Max, J.-J.; Chapados, C.**, "Interpolation and Extrapolation of Infrared Spectra of Binary Ionic Aqueous Solutions," *Applied Spectroscopy* **1999**, 53 (12), 1601–1609, DOI: 10.1366/0003702991946064. (Cited on pages 78 and 140).

[240] **Wang, X.; Qiu, X.; Wu, C.**, "Comparison of the Coil-to-Globule and the Globule-to-Coil Transitions of a Single Poly(*N*-isopropylacrylamide) Homopolymer Chain in Water," *Macromolecules* **1998**, 31 (9), 2972–2976, DOI: 10.1021/ma971873p. (Cited on pages 81 and 82).

[241] **Saunders, B. R.**, "On the Structure of Poly(*N*-isopropylacrylamide) Microgel Particles," *Langmuir* **2004**, 20 (10), 3925–3932, DOI: 10.1021/la036390v. (Cited on page 84).

[242] **van Krevelen, D. W.; te Nijenhuis, K.**, *Properties of Polymers – Their Correlation with Chemical Structure; their Numerical Estimation and Prediction from Additive Group Contributions*. Elsevier, Amsterdam, The Netherlands, 2009, ISBN: 978-0-08-054819-7. (Cited on page 84).

[243] **Iyer, K. S.; Luzinov, I.**, "Effect of Macromolecular Anchoring Layer Thickness and Molecular Weight on Polymer Grafting," *Macromolecules* **2004**, 37 (25), 9538–9545, DOI: 10.1021/ma0493168. (Cited on pages 84, 87, and 88).

[244] **Iyer, K. S.; Zdyrko, B.; Malz, H.; Pionteck, J.; Luzinov, I.**, "Polystyrene Layers Grafted to Macromolecular Anchoring Layer," *Macromolecules* **2003**, 36 (17), 6519–6526, DOI: 10.1021/ma034460z. (Cited on pages 87 and 88).

[245] **Yim, H.; Kent, M. S.; Satija, S.; Mendez, S.; Balamurugan, S. S.; Balamurugan, S.; Lopez, G. P.**, "Evidence for vertical phase separation in densely grafted, high-molecular-weight poly(*N*-isopropylacrylamide) brushes in water," *Physical Review E* **2005**, 72 (5), 051801, DOI: 10.1103/PhysRevE.72.051801. (Cited on pages 90, 91, and 111).

[246] **Elliott, L. C. C.; Jing, B.; Akgun, B.; Zhu, Y.; Bohn, P. W.; Fullerton-Shirey, S. K.**, "Loading and Distribution of a Model Small Molecule Drug in Poly(*N*-isopropylacrylamide) Brushes: a Neutron Reflectometry and AFM Study," *Langmuir* **2013**, 29 (10), 3259–3268, DOI: 10.1021/la305088k. (Cited on pages 90, 91, and 111).

[247] **Laukkanen, A.; Valtola, L.; Winnik, F. M.; Tenhu, H.**, "Formation of Colloidally Stable Phase Separated Poly(*N*-vinylcaprolactam) in Water: A Study by Dynamic Light Scattering, Microcalorimetry, and Pressure Perturbation Calorimetry," *Macromolecules* **2004**, 37 (6), 2268–2274, DOI: 10.1021/ma035124l. (Cited on page 97).

[248] **Liu, M.; Bian, F.; Sheng, F.**, "FTIR study on molecular structure of poly(*N*-isopropylacrylamide) in mixed solvent of methanol and water," *European Polymer Journal* **2005**, 41 (2), 283–291, DOI: 10.1016/j.eurpolymj.2004.09.008. (Cited on page 97).

[249] **Martin, P. E.; Barker, E. F.**, "The Infrared Absorption Spectrum of Carbon Dioxide," *Physical Review* **1932**, 41 (3), 291–303, DOI: 10.1103/PhysRev.41.291. (Cited on page 98).

[250] **Maréchal, Y.**, "Infrared spectra of water. I. Effect of temperature and of H/D isotopic dilution," *The Journal of Chemical Physics* **1991**, 95 (8), 5565–5573, DOI: 10.1063/1.461630. (Cited on pages 105, 106, and 108).

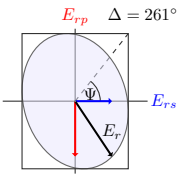

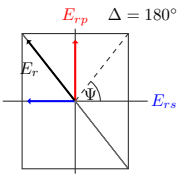

[251] **Libnau, F. O.; Toft, J.; Christy, A. A.; Kvalheim, O. M.**, "Structure of Liquid Water Determined from Infrared Temperature Profiling and Evolutionary Curve Resolution," *Journal of the American Chemical Society* **1994**, 116 (18), 8311–8316, DOI: 10.1021/ja00097a043. (Cited on page 105).

[252] **Iwata, T.; Koshoubu, J.; Jin, C.; Okubo, Y.**, "Temperature Dependence of the Mid-Infrared OH Spectral Band in Liquid Water," *Applied Spectroscopy* **1997**, 51 (9), 1269–1275, DOI: 10.1366/0003702971942196. (Cited on page 105).

[253] **Wagner, R.; Benz, S.; Möhler, O.; Saathoff, H.; Schnaiter, M.; Schurath, U.**, "Mid-infrared Extinction Spectra and Optical Constants of Supercooled Water Droplets," *The Journal of Physical Chemistry A* **2005**, 109 (32), 7099–7112, DOI: 10.1021/jp051942z. (Cited on page 105).

[254] **Zelsmann, H. R.**, "Temperature dependence of the optical constants for liquid H_2O and D_2O in the far IR region," *Journal of Molecular Structure* **1995**, 350 (2), 95–114, DOI: 10.1016/0022-2860(94)08471-S. (Cited on pages 106 and 108).

[255] **Deutsch, T. F.**, "Absorption coefficient of infrared laser window materials," *Journal of Physics and Chemistry of Solids* **1973**, 34 (12), 2091–2104, DOI: 10.1016/S0022-3697(73)80057-5. (Cited on page 107).

[256] **Harris, F. J.**, "On the use of windows for harmonic analysis with the discrete Fourier transform," *Proceedings of the IEEE* **1978**, 66 (1), 51–83, DOI: 10.1109/PROC.1978.10837. (Cited on pages 107 and 146).

[257] **Leviton, D. B.; Frey, B. J.; Madison, T. J.**, "Temperature-dependent refractive index of CaF_2 and Infrasil 301," in *Society of Photo-Optical Instrumentation Engineers (SPIE) Conference Series, Proceedings SPIE 6692, Cryogenic Optical Systems and Instruments XII*, Vol. 6692, p. 669204. 2007. DOI: doi:10.1117/12.735594. (Cited on page 107).

[258] **Dousseau, F.; Therrien, M.; Pézolet, M.**, "On the Spectral Subtraction of Water from the FT-IR Spectra of Aqueous Solutions of Proteins," *Applied Spectroscopy* **1989**, 43 (3), 538–542, DOI: 10.1366/0003702894202814. (Cited on page 110).

[259] **Rahmelow, K.; Hübner, W.**, "Infrared Spectroscopy in Aqueous Solution: Difficulties and Accuracy of Water Subtraction," *Applied Spectroscopy* **1997**, 51 (2), 160–170, DOI: 10.1366/0003702971940080. (Cited on page 110).

[260] **Bouhekka, A.; Bürgi, T.**, "In situ ATR-IR spectroscopy study of adsorbed protein: Visible light denaturation of bovine serum albumin on TiO2," *Applied Surface Science* **2012**, 261, 369–374, DOI: 10.1016/j.apsusc.2012.08.017. (Cited on page 110).

[261] **Fukuda, T.; Kohara, N.; Onogi, Y.; Inagaki, H.**, "Swelling of Poly(glycidyl Methacrylate) Gel Particles by Organic Solvents," *Journal of Applied Polymer Science* **1991**, 43 (12), 2201–2205, DOI: 10.1002/app.1991.070431207. (Cited on page 113).

[262] **Deshmukh, S. A.; Sankaranarayanan, S. K. R. S.; Suthar, K.; Mancini, D. C.**, "Role of Solvation Dynamics and Local Ordering of Water in Inducing Conformational Transitions in Poly(*N*-isopropylacrylamide) Oligomers through the LCST," *The Journal of Physical Chemistry B* **2012**, 116 (9), 2651–2663, DOI: 10.1021/jp210788u. (Cited on page 120).

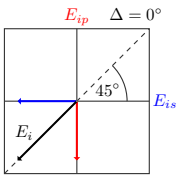

[263] **Hobabi, M.-R.; Hassanzadeh, D.; Azarmi, S.; Entezami, A. A.**, "Effect of synthesis method and buffer composition on the LCST of a smart copolymer of *N*-isopropylacrylamide and acrylic acid," *Polymers for Advanced Technologies* **2007**, 18 (12), 986–992, DOI: 10.1002/pat.951. (Cited on pages 122 and 131).

[264] **Yu, Q.; Zhang, Y.; Chen, H.; Wu, Z.; Huang, H.; Cheng, C.**, "Protein adsorption on poly(*N*-isopropylacrylamide)-modified silicon surfaces: Effects of grafted layer thickness and protein size," *Colloids and Surfaces B: Biointerfaces* **2010**, 76 (2), 468–474, DOI: 10.1016/j.colsurfb.2009.12.006. (Cited on page 124).

[265] **Matsuzaka, N.; Nakayama, M.; Takahashi, H.; Yamato, M.; Kikuchi, A.; Okano, T.**, "Terminal-Functionality Effect of Poly(*N*-isopropylacrylamide) Brush Surfaces on Temperature-Controlled Cell Adhesion/Detachment," *Biomacromolecules* **2013**, 14 (9), 3164–3171, DOI: 10.1021/bm400788p. (Cited on page 124).

[266] **Heyes, C. D.; Groll, J.; Möller, M.; Nienhaus, G. U.**, "Synthesis, patterning and applications of star-shaped poly(ethylene glycol) biofunctionalized surfaces," *Molecular BioSystems* **2007**, 3 (6), 419–430, DOI: 10.1039/B700055N. (Cited on page 124).

[267] **Yoshikawa, C.; Goto, A.; Tsujii, Y.; Fukuda, T.; Kimura, T.; Yamamoto, K.; Kishida, A.**, "Protein Repellency of Well-Defined, Concentrated Poly(2-hydroxyethyl methacrylate) Brushes by the Size-Exclusion Effect," *Macromolecules* **2006**, 39 (6), 2284–2290, DOI: 10.1021/ma0520242. (Cited on page 124).

[268] **Yoshikawa, C.; Goto, A.; Ishizuka, N.; Nakanishi, K.; Kishida, A.; Tsujii, Y.; Fukuda, T.**, "Size-Exclusion Effect and Protein Repellency of Concentrated Polymer Brushes Prepared by Surface-Initiated Living Radical Polymerization," *Macromolecular Symposia* **2007**, 248 (1), 189–198, DOI: 10.1002/masy.200750220. (Cited on page 124).

[269] **Inoue, Y.; Nakanishi, T.; Ishihara, K.**, "Elastic Repulsion from Polymer Brush Layers Exhibiting High Protein Repellency," *Langmuir* **2013**, 29 (34), 10752–10758, DOI: 10.1021/la4021492. (Cited on page 124).

[270] **Li, L.; Hitchcock, A. P.; Robar, N.; Cornelius, R.; Brash, J. L.; Scholl, A.; Doran, A.**, "X-ray Microscopy Studies of Protein Adsorption on a Phase-Segregated Polystyrene/Polymethyl Methacrylate Surface. 1. Concentration and Exposure-Time Dependence for Albumin Adsorption," *The Journal of Physical Chemistry B* **2006**, 110 (33), 16763–16773, DOI: 10.1021/jp062442o. (Cited on page 124).

[271] **Li, L.; Hitchcock, A. P.; Cornelius, R.; Brash, J. L.; Scholl, A.; Doran, A.**, "X-ray Microscopy Studies of Protein Adsorption on a Phase Segregated Polystyrene/Polymethylmethacrylate Surface. 2. Effect of pH on Site Preference," *The Journal of Physical Chemistry B* **2008**, 112 (7), 2150–2158, DOI: 10.1021/jp076583h. (Cited on page 124).

[272] **Kumar, N.; Parajuli, O.; Gupta, A.; Hahm, J.-i.**, "Elucidation of Protein Adsorption Behavior on Polymeric Surfaces: Toward High-Density, High-Payload Protein Templates," *Langmuir* **2008**, 24 (6), 2688–2694, DOI: 10.1021/la7022456. (Cited on page 124).

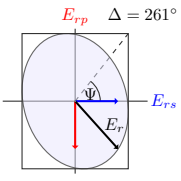

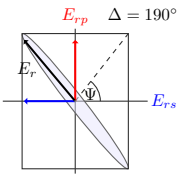

[273] **Wörz, A.; Berchtold, B.; Moosmann, K.; Prucker, O.; Rühe, J.**, "Protein-resistant polymer surfaces," *Journal of Materials Chemistry* **2012**, 22 (37), 19547–19561, DOI: 10.1039/C2JM30820G. (Cited on page 124).

[274] **Reichelt, S.; Eichhorn, K.-J.; Aulich, D.; Hinrichs, K.; Jain, N.; Appelhans, D.; Voit, B.**, "Functionalization of solid surfaces with hyperbranched polyesters to control protein adsorption," *Colloids and Surfaces B: Biointerfaces* **2009**, 69 (2), 169–177, DOI: 10.1016/j.colsurfb.2008.11.025. (Cited on page 124).

[275] **Barth, A.; Zscherp, C.**, "What vibrations tell about proteins," *Quarterly Reviews of Biophysics* **2002**, 35 (04), 369–430, DOI: 10.1017/S0033583502003815. (Cited on pages 126, 128, and 129).

[276] **Baszkin, A.; Norde, W.**, *Physical Chemistry of Biological Interfaces*. Marcel Dekker, Inc., New York, 1999, ISBN: 978-0-8247-7581-0. (Cited on page 127).

[277] **Dickinson, E.**, *Food Colloids: Interactions, Microstructure and Processing*. The Royal Society of Chemistry, Cambridge, 2004, ISBN: 0-85404-638-0. (Cited on page 127).

[278] **Vogler, E. A.**, "Protein adsorption in three dimensions," *Biomaterials* **2012**, 33 (5), 1201–1237, DOI: 10.1016/j.biomaterials.2011.10.059. (Cited on pages 127, 128, and 131).

[279] **Mora, M. F.; Wehmeyer, J. L.; Synowicki, R.; Garcia, C. D.**, "Investigating Protein Adsorption via Spectroscopic Ellipsometry," in *Biological Interactions on Materials Surfaces*, Puleo, D. A.; Bizios, R. (Editors), pp. 19–41. Springer US, 2009. ISBN: 978-0-387-98160-4, DOI: 10.1007/978-0-387-98161-1_2. (Cited on page 127).

[280] **Chou, D. H.; Morr, C. V.**, "Protein-water interactions and functional properties," *Journal of the American Oil Chemists' Society* **1979**, 56 (1), A53–A62, DOI: 10.1007/BF02671785. (Cited on page 127).

[281] **Krishnan, A.; Liu, Y.-H.; Cha, P.; Allara, D.; Vogler, E. A.**, "Interfacial energetics of globular-blood protein adsorption to a hydrophobic interface from aqueous-buffer solution," *Journal of The Royal Society Interface* **2006**, 3 (7), 283–301, DOI: 10.1098/rsif.2005.0087. (Cited on page 127).

[282] **Foster, J. F.**, *Binding properties of albumin*, in *Albumin Structure, Function and Uses*, Rosenoer, V. M.; Oratz, M.; Rothschild, M. A. (Editors). Pergamon Press, Oxford, 1977. ISBN: 0080196039. (Cited on page 129).

[283] **Steger, E.; Herzog, K.**, "Zum Schwingungsspektrum der Phosphorsäure. I. Infrarot- und RAMAN-Spektren von Phosphatlösungen," *Zeitschrift für anorganische und allgemeine Chemie* **1964**, 331 (3–4), 169–182, DOI: 10.1002/zaac.19643310308. (Cited on page 131).

[284] **Ataman, M.**, "Properties of aqueous salt solutions of poly(ethylene oxide). Cloud points, θ temperatures," *Colloid and Polymer Science* **1987**, 265 (1), 19–25, DOI: 10.1007/BF01422658. (Cited on page 131).

[285] **Ishida, N.; Biggs, S.**, "Salt-Induced Structural Behavior for Poly(*N*-isopropylacryamide) Grafted onto Solid Surface Observed Directly by AFM and QCM-D," *Macromolecules* **2007**, 40 (25), 9045–9052, DOI: 10.1021/ma071878e. (Cited on page 131).

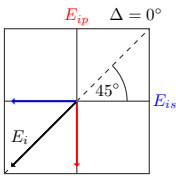

[286] **Zhang, L.; Wang, L.; Kao, Y.-T.; Qiu, W.; Yang, Y.; Okobiah, O.; Zhong, D.**, "Mapping hydration dynamics around a protein surface," *Proceedings of the National Academy of Sciences* **2007**, 104 (47), 18461–18466, DOI: 10.1073/pnas.0707647104. (Cited on page 131).

[287] **Ebbinghaus, S.; Kim, S. J.; Heyden, M.; Yu, X.; Heugen, U.; Gruebele, M.; Leitner, D. M.; Havenith, M.**, "An extended dynamical hydration shell around proteins," *Proceedings of the National Academy of Sciences* **2007**, 104 (52), 20749–20752, DOI: 10.1073/pnas.0709207104. (Cited on page 131).

[288] **Biesheuvel, P. M.; Wittemann, A.**, "A Modified Box Model Including Charge Regulation for Protein Adsorption in a Spherical Polyelectrolyte Brush," *The Journal of Physical Chemistry B* **2005**, 109 (9), 4209–4214, DOI: 10.1021/jp0452812. (Cited on pages 132 and 142).

[289] **Wu, T.; Gong, P.; Szleifer, I.; Vlcek, P.; Subr, V.; Genzer, J.**, "Behavior of Surface-Anchored Poly(acrylic acid) Brushes with Grafting Density Gradients on Solid Substrates: 1. Experiment," *Macromolecules* **2007**, 40 (24), 8756–8764, DOI: 10.1021/ma0710176. (Cited on pages 132, 137, and 138).

[290] **Gong, P.; Wu, T.; Genzer, J.; Szleifer, I.**, "Behavior of Surface-Anchored Poly(acrylic acid) Brushes with Grafting Density Gradients on Solid Substrates: 2. Theory," *Macromolecules* **2007**, 40 (24), 8765–8773, DOI: 10.1021/ma071018y. (Cited on pages 132, 133, 136, 137, and 140).

[291] **Dong, R.; Lindau, M.; Ober, C. K.**, "Dissociation Behavior of Weak Polyelectrolyte Brushes on a Planar Surface," *Langmuir* **2009**, 25 (8), 4774–4779, DOI: 10.1021/la8039384. (Cited on pages 132, 136, 137, and 138).

[292] **Lyatskaya, Y. V.; Leermakers, F. A. M.; Fleer, G. J.; Zhulina, E. B.; Birshtein, T. M.**, "Analytical Self-Consistent-Field Model of Weak Polyacid Brushes," *Macromolecules* **1995**, 28 (10), 3562–3569, DOI: 10.1021/ma00114a009. (Cited on page 133).

[293] **Dukhin, S. S.; Zimmermann, R.; Werner, C.**, "Surface Conductivity Reveals Counterion Condensation within Grafted Polyelectrolyte Layers," *The Journal of Physical Chemistry B* **2007**, 111 (5), 979–981, DOI: 10.1021/jp065585j. (Cited on page 133).

[294] **Currie, E. P. K.; Norde, W.; Cohen Stuart, M. A.**, "Tethered polymer chains: surface chemistry and their impact on colloidal and surface properties," *Advances in Colloid and Interface Science* **2003**, 100–102, 205–265, DOI: 10.1016/S0001-8686(02)00061-1. (Cited on page 134).

[295] **de Feijter, J. A.; Benjamins, J.; Veer, F. A.**, "Ellipsometry as a tool to study the adsorption behavior of synthetic and biopolymers at the air–water interface," *Biopolymers* **1978**, 17 (7), 1759–1772, DOI: 10.1002/bip.1978.360170711. (Cited on page 139).

[296] **Max, J.-J.; Chapados, C.**, "Infrared Spectroscopy of Aqueous Carboxylic Acids: Comparison between Different Acids and Their Salts," *The Journal of Physical Chemistry A* **2004**, 108 (16), 3324–3337, DOI: 10.1021/jp036401t. (Cited on page 139).

[297] **Zundel, G.**, "Hydration Structure and Intermolecular Interaction in Polyelectrolytes," *Angewandte Chemie International Edition in English* **1969**, 8 (7), 499–509, DOI: 10.1002/anie.196904991. (Cited on page 140).

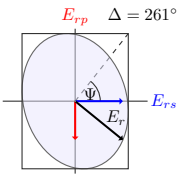

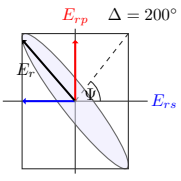

[298] **Henzler, K.; Haupt, B.; Lauterbach, K.; Wittemann, A.; Borisov, O.; Ballauff, M.**, "Adsorption of β-Lactoglobulin on Spherical Polyelectrolyte Brushes: Direct Proof of Counterion Release by Isothermal Titration Calorimetry," *Journal of the American Chemical Society* **2010**, 132 (9), 3159–3163, DOI: 10.1021/ja909938c. (Cited on page 142).

[299] **de Vos, W. M.; Leermakers, F. A. M.; de Keizer, A.; Cohen Stuart, M. A.; Kleijn, J. M.**, "Field Theoretical Analysis of Driving Forces for the Uptake of Proteins by Like-Charged Polyelectrolyte Brushes: Effects of Charge Regulation and Patchiness," *Langmuir* **2010**, 26 (1), 249–259, DOI: 10.1021/la902079u. (Cited on page 142).

[300] **Fellgett, P. B.**, *Theory of Infra-Red Sensitivities and its Application to Investigations of Stellar Radiation in the Near Infra-Red.* PhD thesis, University of Cambridge, Cambridge, United Kingdom, 1951. (Cited on page 145).

[301] **Jacquinot, P.**, "The Luminosity of Spectrometers with Prisms, Gratings, or Fabry-Perot Etalons," *Journal of the Optical Society of America* **1954**, 44 (10), 761–765, DOI: 10.1364/JOSA.44.000761. (Cited on page 145).

[302] **Connes, J.; Connes, P.**, "Near-Infrared Planetary Spectra by Fourier Spectroscopy. I. Instruments and Results," *Journal of the Optical Society of America* **1966**, 56 (7), 896–910, DOI: 10.1364/JOSA.56.000896. (Cited on page 145).

[303] **Jackson, R. S.**, *Continuous Scanning Interferometers for Mid-infrared Spectrometry*, in *Handbook of Vibrational Spectroscopy*, Chalmers, J. M.; Griffiths, P. R. (Editors). John Wiley & Sons, Ltd, Chichester, 2006. ISBN: 978-0-471-98847-2, DOI: 10.1002/0470027320.s0204. (Cited on pages 145 and 146).

[304] **Bretzlaff, R. S.; Bahder, T. B.**, "Apodization effects in Fourier transform infrared difference spectra," *Revue de Physique Appliquée (Paris)* **1986**, 21 (12), 833–844, DOI: 10.1051/rphysap:019860021012083300. (Cited on page 146).

[305] **Hanssen, L. M.; Zhu, C.**, *Wavenumber Standards for Mid-infrared Spectrometry*, in *Handbook of Vibrational Spectroscopy*, Chalmers, J. M.; Griffiths, P. R. (Editors). John Wiley & Sons, Ltd, Chichester, 2006. ISBN: 978-0-471-98847-2, DOI: 10.1002/0470027320.s0701. (Cited on page 146).

[306] **Herres, W.; Gronholz, J.**, "Understanding FT-IR data processing. Part 1: Data acquisition and Fourier transformation," *Computer applications in the laboratory (CAL)* **1984**, 2 (4), 216–220, http://d-nb.info/01210910X. (Cited on page 146).

[307] **Gronholz, J.; Herres, W.**, "Understanding FT-IR data processing. Part 2: Details of the spectrum calculation," *Instruments & Computers* **1985**, 6 (10), 6–12. (Cited on page 146).

[308] **McNaughton, D.**, *Instrumentation and Methods for High-resolution Gas-phase Spectroscopy*, in *Handbook of Vibrational Spectroscopy*, Chalmers, J. M.; Griffiths, P. R. (Editors). John Wiley & Sons, Ltd, Chichester, 2006. ISBN: 978-0-471-98847-2, DOI: 10.1002/0470027320.s0215. (Cited on page 146).

[309] **den Boer, J. H. W. G.**, *Spectroscopic IR ellipsometry with imperfect components.* PhD thesis, Technische Universiteit Eindhoven, Eindhoven, The Netherlands, 1993. ISBN: 90-386-0017-8. (Cited on page 148).

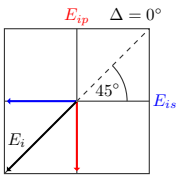

[310] **Furman, Sh. A.; Tikhonravov, A. V.**, *Basics of optics of multilayer systems.* Editions Frontières, Gif-sur-Yvette, France, 1992, ISBN: 2-86332-110-2. (Cited on page 153).

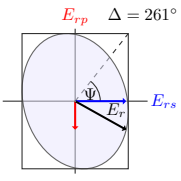

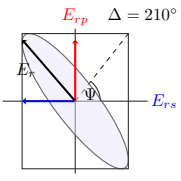

List of figures

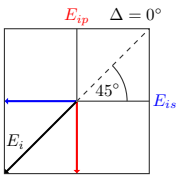

3. Results and discussion

3.1. Thick spin-coated polymer films

3.2. Optical properties of thin brushes

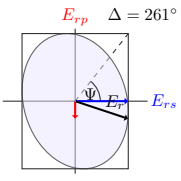

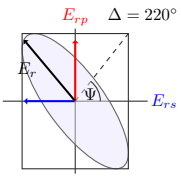

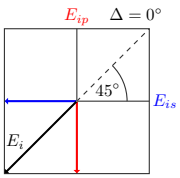

Appendices

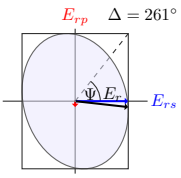

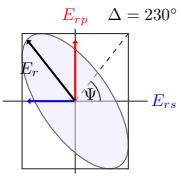

List of tables

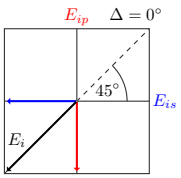

Nomenclature

List of abbreviations:

AA, AB, AI, AII, ...	Amide A, B, I, II, ... bands of undeuterated PNIPAAm
AA', AII', ...	Amide bands of deuterated PNIPAAm
AFM	Atomic force microscopy
ATR	Attenuated total reflection
BaF_2	Barium fluoride
BSA	Bovine serum albumin
CaF_2	Calcium fluoride
DFT	Density Functional Theory
DTGS	Deuterated triglycine sulfate
EMA	Effective-medium approximation
FFT	Fast-Fourier transform
IEP	Isoelectric point
IPF Dresden	Leibniz Institute of Polymer Research Dresden
IR-SE	Infrared-spectroscopic ellipsometry
K–K	Kramers–Kronig
KBr	Potassium bromide
KRS-5	Thallium bromoiodide
LCST	Lower critical solution temperature
MCT	Mercury cadmium telluride
mEMA	Modified effective-medium approximation
NIPAAm	*N*-isopropylacrylamide
NMA	*N*-methylacetamide
P2VP	Poly(2-vinylpyridine)
PDI	Polydispersity index
PEG	Poly(ethylene glycol)
PHEMA	Poly(2-hydroxyethyl methacrylate)
PID	Proportional-integral-derivative
PMMA	Poly(methylmethacrylate)
PN56k	PNIPAAm with $\overline{M}_n = 56\,000$ g/mol
PN94k	PNIPAAm with $\overline{M}_n = 94\,000$ g/mol
PN132k	PNIPAAm with $\overline{M}_n = 132\,000$ g/mol
PS	Polystyrene
QCM	Quartz crystal microbalance
S/N	Signal-to-noise
VIS	Visible
ZnSe	Zinc selenide

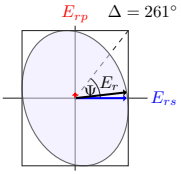

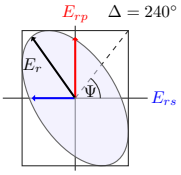

List of polymers, proteins, and chemicals:		Purchased from
PAA	Poly(acrylic acid)	Polymer Source, Inc.
PGMA	Poly(glycidylmethacrylate)	Polymer Source, Inc.
PNIPAAm	Poly(*N*-isopropylacrylamide)	Polymer Source, Inc.
HSA	Human serum albumin, defatted	Sigma-Aldrich
$CHCl_3$	Chloroform (99%+)	Acros Organics
D_2O	Heavy water (99.99 atom% D)	Sigma-Aldrich
EtOH	Absolute ethanol (99%)	Sigma-Aldrich
H_2O	Purified water	
H_2O_2	Hydrogen peroxide (33%)	Sigma-Aldrich
H_2SO_4	Concentrated sulfuric acid	Sigma-Aldrich
Na_2HPO_4	Disodium hydrogen phosphate	Sigma-Aldrich
NaH_2PO_4	Monosodium dihydrogen phosphate	Sigma-Aldrich
NH_4OH	Ammonium hydroxide (25%)	Acros Organics
PBS	Phosphate buffered saline	Sigma-Aldrich
THF	Tetrahydrofuran (99.98%)	Acros Organics

List of mathematical symbols:

A	Absorbance
a_0, a_2, a_4, a_{-2}	Coefficients of the Cauchy dispersion relation
c	Concentration
$c_i = \cos 2\vartheta_i$	Degree of polarization of the i-th polarizer
d	Layer thickness
$\tilde{d}$	Swollen-film thickness, swollen-brush thickness
d_{Cell}	Path length of a transmission cell
d_{chain}	Length of a fully stretched polymer chain
d_{dry}	Dry-state layer thickness
d_{g}	Distance between grafting sites
d_{wet}	Wet-state layer thickness
$\vec{E}$	Electric field vector
E_{ip}, E_{is}, E_{rp}, E_{rs}	Incident/reflected electric-field-vector components in p/s direction
F, $\tilde{F}$	Oscillator strengths of Lorentzian and Gaussian oscillators
f_{H_2O}, f_{Water}, f_{D_2O}	H_2O (D_2O) content of a swollen/collapsed polymer brush or film
k	Extinction coefficient
l_{mono}	Monomer length
$\overline{M}_n$	Number-average molecular weight
$\overline{M}_w$	Weight-average molecular weight
N	Complex refractive index
N_{mono}	Monomer number
N_p	Number of dipole moments per unit volume

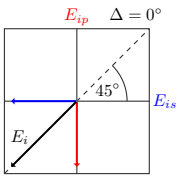

n	Real refractive index
n_∞	High-frequency refractive index
P	Degree of polarization
P_{ph}	Degree of phase polarization
$\vec{P}$	Macroscopic polarization density
$\vec{p}$	Microscopic polarization, electric dipole moment
R	Reflectivity
R_{C}	Radius of a collapsed polymer chain
R_{F}	Flory radius
R_{g}	Radius of gyration
r_p, r_s	Reflection coefficients in p and s direction
S	Stokes vector
S^{D}	Detector intensity
s_0, s_1, s_2, s_3	Stokes parameters
$\tilde{s}_0$, $\tilde{s}_1$, $\tilde{s}_2$, $\tilde{s}_3$	Stokes parameters with retarder in the optical train
$\bar{\mathrm{s}}_0$, $\bar{\mathrm{s}}_1$, $\bar{\mathrm{s}}_2$, $\bar{\mathrm{s}}_3$	Stokes parameters of radiation in front of the first polarizer
$s_i = \sin 2\vartheta_i$	Sine corresponding to $c_i = \cos 2\vartheta_i$
T	Temperature
$\overline{T}$	Transmittance
t	Time
t_p, t_s	Transmission coefficients in p and s direction
z	Surface topography measured with AFM
$\mathcal{E}(\alpha_1, \alpha_2)$	Empty-channel detector intensity without retarder
$\mathcal{I}(\alpha_1, \alpha_2)$	Detector intensity of sample without retarder
$\widetilde{\mathcal{I}}(\alpha_1, \alpha_2)$	Detector intensity of sample with retarder
$\mathcal{M}_j$	Müller matrix of the j-th optical element
$\mathcal{P}$	Cauchy principal value
$\mathcal{R}$	Rotator matrix
$\mathcal{R}(\alpha_1, \alpha_2)$	Empty-channel detector intensity with retarder
$\mathcal{T}_j$	Transfer matrix of the sample's j-th layer
$\hat{\alpha}$	Microscopic polarizability
α_1, α_2	Azimuths of polarizer and analyzer
Γ	Surface concentration
$\tilde{\Gamma}$	Reparameterized dampening constant of a Lorentzian oscillator
γ	Dampening constant of a Lorentzian oscillator
γ_{as}	Asymmetric deformation vibration
γ_{s}	Symmetric deformation vibration
Δ	Phase difference between p- and s-polarized reflection coefficients
δ	Bending vibration
δ_{as}	Asymmetric bending vibration

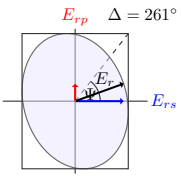

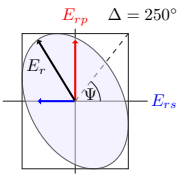

δ_i	Phase shift in the i-th polarizer
δ_{ip}	In-plane bending vibration
δ_{op}	Out-of-plane bending vibration
δ_p	Phase shift of p-polarized light upon reflection/transmission
δ_{Ret}	Phase shift of retarder
δ_s	Phase shift of s-polarized light upon reflection/transmission
δ_{s}	Symmetric bending vibration
ε	Dielectric function
ε_0	Vacuum permittivity
ε_1	Real part of the dielectric function
ε_2	Imaginary part of the dielectric function
$\varepsilon_{\mathrm{eff}}$	Effective dielectric function
ε_∞	High-frequency dielectric constant
λ	Wavelength
ν	Stretching vibration
ν_{as}	Asymmetric stretching vibration
ν_{L}	Libration vibration
ν_{s}	Symmetric stretching vibration
$\tilde{\nu}$	Wavenumber
$\tilde{\nu}_0$	Oscillator center frequency
ρ	Rocking vibration
ρ	Ellipsometric ratio between p- and s-polarized reflection coefficients
ϱ	Density
σ	Grafting density
$\tilde{\sigma}$	Dampening constant of a Gaussian oscillator
$\bar{\sigma}$	Experimental error
τ	Transmittance of polarizer or retarder
φ_0	Angle of incidence
$\bar{\varphi}_0$	Average angle of incidence
$\tilde{\varphi}_0$	Internal angle of incidence at the silicon-wedge/sample interface
χ	Biased estimator (reduced chi-squared)
χ_{e}	Electric susceptibility
$\tan\Psi$	Amplitude ratio between p- and s-polarized reflection coefficients
$\tan\psi_{\mathrm{Ret}}$	Amplitude ratio between transmission coefficients of the retarder
ω	Wagging vibration

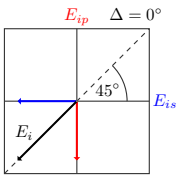

Acknowledgements

First and foremost, I would like to express my deepest gratitude to my advisor and mentor PD Dr. Karsten Hinrichs. Not only did he provide constant support and encouragement throughout the whole 3.5-year experience, but his positive attitude and tireless efforts to discuss and share insights were truly inspiring and motivating, and made this thesis possible. I am truly grateful that he gave me the opportunity to work on this very interesting topic, and also to present the results at several national as well as international conferences.

I deeply thank Prof. Dr. Norbert Esser for giving me the chance to pursue my research and consequently prepare this thesis at ISAS Berlin. I am indebted to Prof. Dr. Norbert Esser and Prof. Dr. Svetlana Santer who agreed to review this work.

Many thanks go to our colleagues Dr. Eva Bittrich, Dr. Sebastian Rauch, Dr. Klaus-Jochen Eichhorn, and Dr. Petra Uhlmann at the IPF Dresden. Especially to Eva and Sebastian who prepared and pre-characterized all polymer samples investigated in this work, and who also kindly shared their knowledge concerning the physical and chemical properties of these material systems. I am indebted to Eva who performed additional in-situ visible ellipsometry on polymer brushes and provided me with the results of the quantitative evaluation.

Special thanks go to my *roommates* Dr. Dennis Aulich, Annika Kroning, and Dr. Simona Pop. To Dennis for the numerous interesting discussions and for introducing me to our ellipsometer set-ups during my first months at the institute; to Annika whose expertise in chemistry was essential for many parts of this work; and to Simona whose calm nature ensured a tranquil and relaxing working atmosphere. Funny thanks go to Özgür Savas, our most reliable coffee drinker. He also kindly performed many of the AFM measurements and offered important assistance at the infrared microscope. I would also like to thank Dr. Tom Oates for many inspiring conversations. Many thanks also to Dr. Guoguang Sun who provided significant knowledge about several chemical cleaning processes and chemistry in general.

I am deeply thankful for Sebastian Geisler's input concerncing the construction of a new temperature-controlled sample stage for our infrared in-situ cell. This made it possible to perform very accurate and reproducible temperature-dependent in-situ measurements. In this respect, I would also like to thank Carsten Roland, Ilona Fischer, Rainer Sorge, and Uwe Dahlke who helped with experimental set-ups and construction issues. I am also grateful to our in-house workshop, in particular to Ralf Herzlieb, Gerhard Hinte, and Annika Michalik who built a new adjustable sample holder for the in-situ cell.

All colleagues at ISAS Berlin and ISAS Dortmund are specially acknowledged for providing a very pleasant and enjoyable working environment. I also want to thank the merciless team of proofreaders for valuable comments on the manuscript. Lastly, but very importantly, I deeply thank my family and friends for their constant support and encouragement.

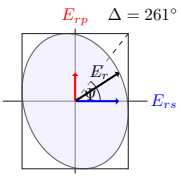

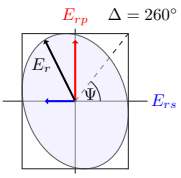

Statement of authorship

This doctoral thesis has been submitted for the degree of Doctor rerum naturalium. I hereby certify that it has been composed by myself, and describes my own work, unless otherwise acknowledged in the text. All references have been quoted, and all sources of information have been specifically acknowledged. The thesis does not contain work extracted from a thesis, dissertation, or research paper previously presented for another degree at this or any other university. I have prepared this thesis specifically for the degree of Dr. rer. nat., while under supervision at the Leibniz-Institut für Analytische Wissenschaften – ISAS – e. V. between July 2010 and December 2013.

Berlin, December 20, 2013

Andreas Furchner